UNIVERSITY OF SOUTHAMPTON

The Control of Gold and Latex Particles on Optical Waveguides

by

John Patrick Hole, MEng.

A thesis submitted in partial fulfillment for the degree of Doctor of Philosophy

in the
Faculty of Engineering, Science and Mathematics
Optoelectronics Research Centre

December 2005

UNIVERSITY OF SOUTHAMPTON

ABSTRACT

FACULTY OF ENGINEERING, SCIENCE AND MATHEMATICS
OPTOELECTRONICS RESEARCH CENTRE

Doctor of Philosophy

THE CONTROL OF GOLD AND LATEX PARTICLES ON OPTICAL WAVEGUIDES

by John Patrick Hole, MEng.

The trapping of microparticles by optical methods using a focussed laser beam, known as optical tweezers, has evolved rapidly in the last thirty years. However this process is limited to the trapping of a small number of particles. Evanescent wave trapping allows simultaneous trapping of many particles due to the long length over which a strong intensity gradient is present. A channel waveguide used to produce such an evanescent wave can be photolithographically defined on a flat substrate and thus can be integrated with other micron scale processes. This therefore has potential applications in the lab-on-a-chip field that is currently proving so successful, particularly in biochemical areas where evanescent wave manipulation is ideal for its properties of being cheap, robust, contaminant-free and designed for use with aqueous solutions.

This thesis describes both a theoretical and experimental study into the optical trapping and propulsion of gold nanoparticles and latex microparticles above caesium ion-exchanged waveguides. Gold particles of radii varying from 50nm to 250nm and latex particles varying from 1.5μm to 7.5μm were propelled above a waveguide in an aqueous medium. The evanescent field of the channel waveguide was used to both optically trap and propel these particles and speeds of up to 500μm/s were achieved, a full order of magnitude faster than has previously been reported.

The optical forces on the particles were derived and used to predict the trapping ability and the speed of particles and physical, electric, and thermophoretic forces, that also affect the particles were described. In addition, modelling allowed the theoretical optimisation of the waveguides for this process.

Using a counter-propagating wave it is demonstrated that it is possible to both render particles stationary and position them at any point along the waveguide. In addition, devices were fabricated that allow particles to be automatically sorted down either branch of a Y-junction waveguide. These results demonstrate, that evanescent wave based, integrated optical devices for trapping are feasible and it is anticipated that this will lead to devices for real-life applications being realised.

Contents

List of Accompanying Material xvi

Declaration of Authorship xvii

List of Publications xviii

Acknowledgements xx

Nomenclature xxi

1 Introduction 1
- 1.1 Aims and motivation . . . 1
- 1.2 An historical background . . . 2
- 1.3 The single beam trap . . . 3
- 1.4 Alternative configurations and beam shapes . . . 4
- 1.5 Applications of optical trapping . . . 5
- 1.6 Evanescent wave trapping and the novel contributions to this field . . . 7
- 1.7 Structure of thesis and important notes . . . 8

2 Theory of Optical Forces on a Particle 11
- 2.1 Introduction . . . 11
- 2.2 Mie theory . . . 12
  - 2.2.1 Derivation . . . 12
    - 2.2.1.1 The vector harmonic functions, **M** and **N** . . . 12
    - 2.2.1.2 The generating function, ψ . . . 13
    - 2.2.1.3 Expansion of a plane wave . . . 16
    - 2.2.1.4 Solving the internal and scattered fields . . . 17
    - 2.2.1.5 Scattering cross sections/efficiences . . . 19
    - 2.2.1.6 Application to evanescent wave excitation . . . 19
    - 2.2.1.7 Rayleigh approximation to Mie theory . . . 20
  - 2.2.2 Theoretical Mie results . . . 21
    - 2.2.2.1 Cross sectional areas and efficiencies . . . 21
    - 2.2.2.2 Comparison of Mie theory to Rayleigh theory . . . 23
- 2.3 Forces on a Rayleigh particle . . . 25
  - 2.3.1 Derivation . . . 25
  - 2.3.2 Electromagnetic description of an evanescent field . . . 26
  - 2.3.3 Rayleigh forces on a nanoparticle in an evanescent wave . . . 27
    - 2.3.3.1 The scattering force . . . 27

2.3.3.2 The gradient and absorption forces 28
2.3.4 Polarisability of gold 30
2.3.4.1 Wavelength dependence of permittivity of gold 30
2.3.4.2 Effective volume of gold particle 31
2.3.5 Theoretical results for optical Rayleigh forces 33
2.4 Summary and conclusions 35

3 Theory and Modelling of Ion-Exchanged Optical Waveguides 37
3.1 Introduction 37
3.2 Theory of optical waveguides 37
3.2.1 Introduction 37
3.2.2 Three-layer planar waveguides 38
3.2.3 Multilayered waveguides 41
3.2.4 Effective index method 44
3.2.5 Beam propagation method 44
3.3 Diffusion theory 46
3.4 Numerical analysis of waveguide modes 48
3.4.1 Three-layer model 48
3.4.2 Multilayer model 48
3.4.3 Modelling graded-index profiles 49
3.4.4 The beam propagation method model 52
3.5 Theoretical results 53
3.5.1 Introduction 53
3.5.2 Determination of diffusion profile 53
3.5.3 Comparison of analytical and numerical models 58
3.5.4 Modelling of measurable waveguide parameters 60
3.5.4.1 Effective refractive indices 60
3.5.4.2 Spot-sizes and the field profile 61
3.5.4.3 Waveguide cut-off wavelengths 64
3.5.5 Theoretical waveguide optimisation for trapping and propulsion . . 66
3.6 Conclusions 71

4 Non-optical Forces on Particles 73
4.1 Introduction 73
4.2 Gravity and buoyancy 73
4.3 Drag force 74
4.4 Brownian motion 75
4.5 Electrostatic and van der Waals forces 78
4.5.1 Introduction 78
4.5.2 Derivations 78
4.5.2.1 The van der Waals force 78
4.5.2.2 The double-layer force 80
4.5.2.3 Derjaguin, Landau, Verwey and Overbeek theory 83
4.5.3 Results from DLVO theory 84
4.5.4 Summary 87
4.6 Fluid-flow due to convection 87
4.6.1 Introduction 87

4.6.2 Heat diffusion theory . . . 88
4.6.3 Modelling method and parameters . . . 89
4.6.3.1 Gold absorption . . . 89
4.6.3.2 Glass absorption . . . 89
4.6.4 Modelling results . . . 90
4.6.4.1 Temperature profile due to gold absorption . . . 90
4.6.4.2 Temperature profile due to glass absorption . . . 90
4.6.5 Discussion . . . 92
4.7 Balance of forces . . . 93
4.7.1 Ability to trap particles . . . 93
4.7.2 Propulsion speed of particles . . . 96
4.8 Conclusions . . . 96

5 Background, Fabrication and Characterisation of Waveguides 99
5.1 Introduction . . . 99
5.2 Optical waveguides . . . 99
5.2.1 Channel waveguides . . . 100
5.2.2 Diffused ion-exchanged waveguides . . . 101
5.3 Waveguide fabrication . . . 103
5.3.1 Inspection and cleaning of substrate . . . 104
5.3.2 Evaporation of aluminium . . . 104
5.3.3 Photolithography and etching . . . 105
5.3.4 Ion-exchange . . . 105
5.3.5 Post-exchange treatment . . . 105
5.4 Waveguide characterisation methods . . . 106
5.4.1 Composition measurements . . . 106
5.4.2 Effective refractive index measurements . . . 107
5.4.3 Loss measurements . . . 109
5.4.4 Spot-size measurements . . . 111
5.5 Characterisation results . . . 112
5.5.1 Composition measurements . . . 112
5.5.2 Effective refractive index results . . . 112
5.5.3 Spectral attenuation results . . . 117
5.5.4 Spot-size measurements . . . 121
5.6 Conclusion . . . 123

6 Propulsion of Particles on Channel Waveguides 125
6.1 Introduction . . . 125
6.2 The experimental apparatus and procedure for trapping . . . 125
6.2.1 Optical apparatus . . . 126
6.2.2 Fluidic apparatus . . . 126
6.2.3 Imaging apparatus . . . 129
6.3 Gathering and analysis of images . . . 131
6.3.1 Data acquisition . . . 131
6.3.2 Analysis of data . . . 132
6.3.2.1 Making a movie . . . 133
6.3.2.2 Identification of position of particles . . . 133

6.3.2.3 Particle tracking analysis . . . 134
6.3.2.4 Checking, collection and presentation of results . . . 135
6.4 Non-optical experimental results . . . 136
6.4.1 Brownian motion of particles . . . 136
6.4.2 The effect of ion concentration . . . 138
6.4.3 The minimization of drift on the surface . . . 140
6.5 Particle propulsion results . . . 141
6.5.1 Positional propulsion results . . . 141
6.5.2 Power and polarisation dependence on particle speed . . . 146
6.5.3 The effect of particle size . . . 148
6.6 Summary . . . 150

7 Sorting of Particles along Optical Waveguides 151
7.1 Introduction . . . 151
7.2 Choice of separation method . . . 151
7.3 Bend loss measurements . . . 153
7.4 Routing light in Y-junctions by varying input coupling . . . 155
7.4.1 Modelling of Y-junctions . . . 155
7.4.2 Experimental results . . . 158
7.5 Particle meandering above a multimode waveguide . . . 159
7.6 Sorting of latex particles along a Y-branch . . . 161
7.6.1 Characterisation of sorting . . . 161
7.6.2 Programmable sorting of latex particles . . . 163
7.7 Sorting of gold particles along a Y-branch . . . 165
7.8 Conclusion and discussion . . . 166

8 Control of Particles using a Counter-propagating Wave 168
8.1 Introduction . . . 168
8.2 Theory for particles in a standing wave . . . 169
8.2.1 Introduction . . . 169
8.2.2 Intensity of a standing wave . . . 169
8.2.3 Effect of standing wave on optical forces . . . 171
8.3 Experimental methods . . . 173
8.3.1 Introduction . . . 173
8.3.2 Dielectric mirror method . . . 174
8.3.3 Optically diffused loop method . . . 174
8.3.4 Bi-coupling fibre method . . . 175
8.4 Experimental results . . . 175
8.4.1 Dielectric mirror results . . . 175
8.4.2 Optically diffused loop results . . . 180
8.4.3 Bi-coupling fibre results . . . 181
8.5 Conclusion . . . 183

9 Conclusion and Future Work 185
9.1 Summary . . . 185
9.2 Future work . . . 189

Appendix A: Screenshot of Labview Program 191

Bibliography **191**

List of Figures

2.1 Diagram of the physical system being solved by Mie theory. 14

2.2 a) $P_n^m(\cos\theta)$ of the zeroth (n=0) (■), first (n=1) (■) and second (n=2), degree (■) for orders m=0 (—), m=1 (- -) and 2 (- ·) and b) Spherical Bessel functions of the first, j_n, (■) and second kind, y_n, (■) for orders n=1 (—) and 2 (- -). 15

2.3 Scattering cross sectional areas for a latex particle in a) air and b) water and their respective scattering efficiencies, c) and d). The highest areas (-) represent the sum of the first 20 modes whilst for air, (··) represent the sum of first 10 modes. The lower four cross sectional areas show the first four modes with the arrow indicating increasing mode number. . . . 22

2.4 a) The scattering cross sectional area and b) efficiency for a latex particle in water using the sum of the first 80 modes. 22

2.5 The a) scattering and b) absorption cross sectional areas for a gold particle in water and their respective efficiencies c) and d). In all cases of the highest plot is the sum of the first 10 modes and the lower four lines show the first four modes with the arrow indicating increasing mode number. . 23

2.6 Scattering a) cross sectional area and b) efficiency comparing the case of the Rayleigh approximation (- -) and the Mie theory (–), for the case of a latex particle in water. The solid lines represent (in increasing values at χ=2) the first Mie order, the second Mie order and the total Mie value. 24

2.7 Scattering a) cross sectional area and c) efficiency and absorption b) cross sectional and d) efficiency, comparing the case of the Rayleigh approximation (- -) and the Mie theory (–), for the case of a latex particle in water. The solid lines represent (in increasing values at χ=2) the first Mie order, the second Mie order and the total Mie value. 24

2.8 Schematic for Rayleigh approximation of a sphere with a radius, a, to a dipole with separation, d, and a charge of $\pm Q$. 25

2.9 The a) real and b) imaginary parts of gold permittivity. 30

2.10 The a) real and b) imaginary parts and the c) absolute value of the Clausius-Mossotti factor. 31

2.11 The penetration depth of gold as a function of wavelength. 32

2.12 The normalised effective volume of a gold sphere of radius a) 10nm (■), b) 50nm (■) and c) 125nm (■). The volumes are normalised to the volume of a particle of the same radius with infinite penetration depth. These are $4.1 \times 10^{-24} m^3$, $4.7 \times 10^{-22} m^3$ and $6.2 \times 10^{-21} m^3$ respectively. 32

2.13 The normalised polarisabilities of a gold sphere of radius 10nm (■), 50nm (■) and 125nm (■). The graphs are normalised to the peak parts of polarisability. 33

2.14 a) The maximum Rayleigh forces on a particle of radius, a in the evanescent field of a channel waveguide with a 1W modal power and assuming a surface intensity of 6×10^9 at a wavelength of 1066nm. The lines represent the following forces: transverse gradient, (■), lateral gradient, (■), scattering (■), absorption, (■) and axial gradient (■). b) As with a) but plotted on a log-log scale. 34
2.15 a) The maximum Rayleigh forces on a 100nm radius, gold particle in the evanescent field of a channel waveguide as a function of the wavelength of light used. A 1W modal power and a surface intensity of $6\times10^9 W/m^2$ is assumed. The lines represent the transverse gradient, (■), lateral gradient, (■), scattering (■) and absorption, (■) forces. 35

3.1 Model of a slab waveguide with examples of the fundamental and first order transverse electric modes in the waveguide schematically shown. . . 38
3.2 Model of a slab waveguide with M layers. 42
3.3 The effective index method; a) the refractive index model, b) first find effective indices of multilayer slab structure, c) replace the middle section with the effective index and find the new effective index. 45
3.4 Schematic diagrams showing a) interpretation of Fick's first diffusion law and b) derivation of Fick's second law. 47
3.5 Various refractive index profiles for w=2, 4 and $6\mu m$ and $d = 2\mu m$ (as defined in equations in 3.45). In all cases the arrow indicates increasing w. 50
3.6 The effect of d on the Fermi function in equation 3.45 for values of d=0.5, 1 and $2\mu m$ and w=$4\mu m$. The arrow indicates increasing d. 50
3.7 Graph showing the fit (–) used to model various profiles ($\cdots$) using 5 steps. It uses the parameters defined in equations 3.45 of $\Delta n = 0.04$, w=$2\mu m$ and $d = 0.5\mu m$. 51
3.8 Graph showing fit (–) used to model various profiles ($\cdots$) using 30 steps. It uses the parameters defined in equations 3.45 of $\Delta n = 0.04$, w=$2\mu m$ and $d = 0.5\mu m$. 52
3.9 The effect of different mode profiles on the effective refractive indices of a planar waveguide. The profiles are a step index (■), the Fermi function (■), the complementary error function (■) and an exponential function (■). Solid lines show the fundamental, dashed, the first, alternate dotted/dashed, the second and dotted, the third order modes. 54
3.10 The Fermi (■), complementary error (■) and exponential (■) function fits and the measured effective refractive indices (×) of a planar waveguide ion-exchanged for 24 hours at 500^0C for the case of a) TE polarisation and b) TM polarisation. 56
3.11 The Fermi (■), complementary error (■) and exponential (■) function fits and the measured effective refractive indices (×) of a planar waveguide ion-exchanged for 96 hours at 450^0C for the case of a) TE polarisation and b) TM polarisation. 56
3.12 TE effective indices for channel waveguides at 1066nm as calculated by the multilayer and effective index methods (–) and by Beamprop BPM package (- -). The graphs are for the case of w=1, 1.5, 2 and 3μm. 58
3.13 The refractive index profiles of a waveguide a) with and b) without isotropic diffusion. 59

3.14 BPM analysis as in figure 3.12 with lateral diffusion. Fundamental TE modes are shown at a wavelength of 1066nm (–) and 633nm (– –). The lines represent waveguide depths, w, of 1, 1.5, 2, 3μm with the higher values representing the greater depths. 60
3.15 Analytical solution to two asymmetric slab waveguides with $n_{sup} = 1$, $\Delta n = 0.03$, $n_{sub} = 1.5$ at a wavelength of 1066nm. The waveguide depth, w, is 1μm for the left plots and 2.8μm for the right plots. The plots show TE (■) and TM (■) fundamental (solid lines) and first order (dashed lines) modes. The y-axis labels refer firstly to the TE fields and secondly to the TM fields. 62
3.16 Graph showing the field for the fundamental TE mode at 633nm. The profiles are a step index (■), the Fermi function (■), the complementary error function (■) and an exponential function (■). 62
3.17 The mode profile of a diffused channel waveguide as predicted by the BPM package. 63
3.18 The normalised field a) normal to and b) parallel to the surface of the substrate through the peak intensity of the mode profile, as calculated by the BPM method. 64
3.19 Waveguide spot-sizes as a function of the waveguide width, dy, for light of wavelength 1066nm. The transverse spot-sizes for an a) air and b) water superstrate and the lateral spot-sizes for the c) air and d) water superstrate. The lines represent w=1 (■), 1.5 (■), 2 (■), 2.5 (■) and 3 μm (■). 65
3.20 Waveguide cut-off wavelengths as a function of the waveguide width, dy, for an air superstrate. The lines represent w= 1.5 (■), 1.1 (■), 1 (■) and 0.9μm (■). 65
3.21 Fraction of modal power in the superstrate with a cover of a) air and b) water as a function of dy. The lines represent w= 0.9 (■), 1 (■), 1.1 (■), 1.5 (■), 2.5μm (■). 66
3.22 Graphs showing parameters concerning cross sections taken vertically (left) and horizontally (right) through the field at the surface as a function of the waveguide width, dy. The parameters from top to bottom are the maximum intensity gradients (G_x, G_y), the intensity at these points (I_s, $I_{gr,y}$), the length over which this force is roughly constant (L_x, L_y) and the product of the gradient and the length, GL. The different lines represent w= 0.9 (■), 1 (■), 1.1 (■), 1.5 (■), 2.5 (■) μm. Results for 1066nm in air. 68
3.23 Graphs showing parameters concerning cross sections taken vertically (left) and horizontally (right) through the field at the surface as a function of the waveguide width, dy. The parameters from top to bottom are the maximum intensity gradients (G_x, G_y), the intensity at these points (I_s, $I_{gr,y}$), the length over which this force is roughly constant (L_x, L_y) and the product, GL. The different lines represent w= 0.9 (■), 1 (■), 1.1 (■), 1.5 (■), 2.5 (■) μm. Results for 1066nm with a cover of *water* 69
3.24 Series of cross sections of the intensity on the surface of a waveguide in water at 1066nm with width, dy. The depth of the waveguide w is 1μm and all other parameters are as described in figure 3.23. 71

4.1 Increased viscosity due to presence of boundary for a 100nm particle (■) and a 3μm (■) particle. 76

4.2 Models used to calculate electrostatic interaction between a) a molecule and a wall and b) particle and a wall. 79
4.3 Interaction energy as a function of distance for varying surface energies for a particle approaching a surface in an electrolyte. The arrow indicates decreasing surface energies. 83
4.4 a) The double-layer (- -) and van der Waals (- ·) forces of the DLVO theory between a glass surface and a 200nm gold particle in water with a 5×10^{-5}M concentration of monovalent ions and the sum of these forces(■). Also plotted are the sums of the forces for concentrations of 1×10^{-4}M (■), 5×10^{-4}M (■), and 1×10^{-3}M (■). Plot b) shows the log of these forces (where positive). 86
4.5 a) The double-layer (- -) and van der Waals (- ·) forces of the DLVO theory between a glass surface and a 3μm polystyrene particle in water with 5×10^{-5}M concentration of monovalent ions and the sum of these forces(■). Also plotted are the sums of the forces for concentrations of 1×10^{-4}M (■), 5×10^{-4}M (■), and 1×10^{-3}M (■). Plot b) shows the log of these forces (where positive). 86
4.6 Schematic of the model and geometry used for glass absorption. 90
4.7 A vertical cross section of the temperature profile caused by absorption by a gold sphere through the centre of the particle. 91
4.8 Temperature profile caused by heat generation due to the waveguide absorbing laser radiation. The total simulated area shown here 5mm (width)×2.18mm(height). 91
4.9 A vertical cross section through figure 4.8 showing the temperature profile through the centre of the waveguide. 91
4.10 a) Transverse and b) lateral analysis of Rayleigh forces and Brownian motion. The lines represent gradient (■) and gravitational/buoyancy (■) forces and equivalent forces required to overcome Brownian motion with values of τ/d (see equation 4.49) of 10 (■), 5 (■) and 1 (■). 94
4.11 Predicted speed for a gold particles with varying radii on an a) linear and b) logarithmic scale. The modal power here is 1W at a wavelength of 1066nm. 97

5.1 Various geometries for producing optical channel waveguides. These are a) a fibre b) a diffused waveguide and c) a ridge waveguide. 100
5.2 The waveguide fabrication process. a) A glass substrate is inspected and cleaned, b) 200nm of Al are deposited, c) photoresist is spun on the Aluminium (Al), d) a chrome mask is pressed to the photoresist and exposed to UV light, e) the photoresist is developed, f) the Al is etched, g) the substrate immersed in melt and h) the sample is cleaned polished and the aluminium coating removed. 103
5.3 Hand polishing method. a) The cut substrate, b) a sharp wedge is cut, followed by c) successively less sharp wedges until d) the end is polished flat. 106
5.4 Experimental apparatus used for prism coupling 108
5.5 Diagram of angles and refractive indices required to measure the effective indices of a waveguide by the prism coupling method. 109
5.6 Experimental apparatus used for white light measurements also showing data interconnects (– →). 111

5.7 Composition of a range of glasses listed in order of sodium composition. SiO_2, the major component in all the glasses is omitted for clarity, the proportion of the Na (□), K (■), Mg (■), Al (■), Ca (■), B (■), Ba (■), Zn (■), Pb (■) and Ti (■) oxides is shown. 113
5.8 An EDX linescan scanned laterally across a Cs^+ ion-exchanged waveguide. The normalised proportions of Na (■) and Cs (■) are shown as a function of the position across the waveguide. 113
5.9 Increase in TM effective refractive indices of K^+ waveguides with respect to the substrate index for a variety of widths at a wavelength of 633nm. Results show Menzel waveguides ion-exchanged at 350^0C for 12(♦), 9(♦), 6(♦), 4(♦) and 2(♦) hours and in BK7 at 400^0C for 4(♦) hours. 115
5.10 Increase in TM effective refractive indices of Cs^+ waveguides for a variety of widths at a wavelength of 633nm. Results show Menzel waveguides ion-exchanged at 450^0C for $9^{(1)}$ (♦), 8.5 (♦), 10(♦), $9^{(2)}$ (♦), 6(♦) and 7 (♦) hours. 116
5.11 TM effective indices for K^+ ion-exchanged waveguides in Menzel at 1066nm at 350^0C and with times 12 (♦), 9 (♦), 6 (♦) and 4 (♦) hours. 116
5.12 Results from a K^+ ion-exchanged waveguide ion-exchanged at 400^0C for 1 hour in a BK7 substrate with nominal openings of 3 (■),7 (■) and 12 μm(■). Dashed lines represents TE loss whereas solid lines represent TM modes. 117
5.13 TE cut-off wavelengths for K^+ ion-exchanged waveguides in Menzel glass ion-exchanged at 350^0C for 9(♦), 6(♦), 4(♦) and 2(♦) hours and in BK7 at 400^0C for 4(♦) and 1(♦) hours. 118
5.14 Typical waveguide spectral loss plots for a Cs^+ ion-exchanged waveguides. This Menzel substrate was ion-exchanged at 450^0C for 11 hours with nominal openings of 4 (■), 6 (■) and 11μm (■). TM polarisation results are shown as solid lines, TE polarisation are dashed. 119
5.15 TM cut-off wavelengths for Cs^+ ion-exchanged waveguides in Menzel at 450^0C (with TM Δn_{eff} at a wavelength of 633nm) for $9^{(1)}$(Δn_{eff}=0.0237)(♦), 8.5 (0.0188)(♦), 10 (0.0151)(♦), $9^{(2)}$(0.0138)(♦) and 7(0.0082) hours (♦) as a function of their width. 120
5.16 a) Fundamental mode profile of a K^+ ion-exchanged, 6μm opening, channel waveguide at 350^0C for 6 hours. The normalised b) lateral and c) transverse cross sections through the peak. b) and c) show the experimental data (■) and the Gaussian fit (■), whilst the vertical lines show the points at which the Gaussian has value of $1/e^2$. 121
5.17 Spot-sizes at a wavelength of 1066nm for TM polarisation for K^+ ion-exchanged waveguide in Menzel at 350^0C for 9 (♦), 6(♦) and 4(♦) hours and in a BK7 substrate at 400^0C for 4 hours (♦). In all cases the dashed line represents the spot-size perpendicular to the surface, whereas the solid line shows the beam spot-sizes in the plane of the surface (and perpendicular to the waveguide). 122
5.18 Spot-sizes at a wavelength of 1066nm for TM polarisation for Cs^+ ion-exchanged waveguide at 450^0C (with TM Δn_{eff} at a wavelength of 633nm) for $9^{(1)}$ (Δn_{eff}=0.0237) (♦), 8.5 (0.0188) (♦), 10 (0.0151) (♦), $9^{(2)}$ (0.0188) (♦) and 6 (0.0101) (♦) hours. In all cases the dashed line represents the spot-size perpendicular to the surface, whereas the solid line shows the spot-sizes in the plane of the surface (and perpendicular to the waveguide). 123

6.1 Schematic diagram of the experimental setup used for trapping. The arrows (→) indicates a degree of freedom offered by a manipulator in that dimension. Coloured lines indicate the optical path of the laser beam (■), the imaging path of the microscope (■) and a data link to a PC (■). . . . 126
6.2 Fabrication and use of PDMS cell. a) Mould is made by gluing a coverslip, microscope slide, and petri dish together, b) PDMS is poured over mould, degassed, baked and cut, c) the cell can be pulled out of the mould and d) the cell is applied to the substrate. Tubes can then be pushed into the cell to allow the pumping of fluid over the waveguides. 128
6.3 Fabrication and use of cell using UV-curing glue. a) Segments of coverslip are glued to the substrate, b) a cut-out sheet of Parafilm is laid over coverslips, c) the microscope slide fixed to top by heating the substrate and pressing together and d) the tubes glued in with superglue. 129
6.4 Fabrication method for a cell using sputtered silica. a) Photoresist is defined, b) silica is sputtered and lifted-off where the photoresist previously was, c) a cut-out sheet of Parafilm laid over coverslips and d) a microscope slide is fixed to top by heating the substrate and pressing together. Tubes can subsequently be glued in with superglue. 130
6.5 Particle images of 6μm, 3μm, 250nm, 150nm and 100nm from the top down respectively, with the left images being the raw images and the right images being the background-corrected images. Images inverted for clarity. 137
6.6 All displacements of all particles in a 50ms time interval recorded over 5000 frames for a) 3μm particles and b) 250nm particles. 137
6.7 Comparison of Brownian motion experimentally measured (×) compared to that calculated theoretically (–) for particles of different radii. 138
6.8 The proportion of particles free after 200 (▲) and 400 (⧫) seconds. 139
6.9 The first image of a movie (drift.avi) showing 250nm gold particles drifting due to convection currents caused by absorption of laser radiation. 141
6.10 First image of a movie (goldprop.avi) showing particles above a 3μm wide, single-mode waveguide. The movie shows the motion of the particles - some of which are propelled along the waveguide. 142
6.11 a) Three consecutive images of three 250nm gold particles propelled along the waveguide b) A typical trace of a particle initially traveling randomly due to Brownian motion until it is propelled along the waveguide c) the velocity diagram of the particle in b. 143
6.12 Position of propelled particles for a) a single mode waveguide b) a dual-moded waveguide. 144
6.13 Plot of lateral position against speed of particles for a) single mode waveguide b) dual-moded waveguide, and their respective beam profiles c),d). . 145
6.14 A typical speed histogram of the trapped particles, with a Gaussian best fit curve (–) and its equation shown. 147
6.15 Plot of particle speed against power output for the two polarisations, TE and TM and the best fit lines for these. 147
6.16 Plot of particle speed against power for a range of particle sizes and their lines of best fit. The sizes are 15μm, (⧫), 10μm, (⧫), 7μm, (⧫), 5μm, (⧫), 3μm and (⧫) latex particles and 500nm, (⧫) and 250nm, (⧫) gold particles. 149

7.1 Two methods for optically sorting particles. a) The power in perpendicular waveguides is modulated in order to separate desired particles. b) The power can be modulated down either of two branches by controlling the beat pattern with either input fibre position or wavelength. 152
7.2 Sorting of particles. In a) the beat pattern guides the particles to travel down the lower branch, in b) the wavelength is lowered to introduce an extra half wavelength and the particles are sorted into the upper branch and in c) the position of the input is shifted to a symmetrically opposite position on the other side of the waveguide, the beat pattern is now opposite to that in a) and the particles are sorted to the upper branch. . . 153
7.3 Two masks used to obtain an indication of the bend losses for a) K^+ and b) Cs^+ ion-exchanged waveguides. 154
7.4 An indication of a K^+ ion-exchanged waveguides' bend losses at 1066nm (■) and 632nm (▲). 154
7.5 The two designs used to separate particles - a) has a 6μm opening, whilst b) has a 10μm opening. 156
7.6 Mode profiles of the a) zeroth, b) first and c) second order modes of a 10μm waveguide and the d) zeroth and e) first modes of a 6μm waveguide. 156
7.7 Propagation of the beam with the input beam positioned at a) y=+1.75μm and b) y=-1.75μm with respect to the centre of a 6μm waveguide. 157
7.8 Propagation of the beam with the input beam positioned at a) y=+3.5μm and b) y=-3.5μm with respect to the centre of a 10μm waveguide. 157
7.9 Proportions of light propagating in the left (■) and right (■) branches as a function of the fibre position for the case of a) a 6μm and b) a 10μm width trunk. 158
7.10 The output power of the upper branch (■) and the lower branch (▲) of the Y-junction as the fibre is traversed across the input of the multimode waveguide. 159
7.11 Position of latex particles travelling on multimode waveguide showing a) an interpolated speed map showing that particles on either side of the waveguide alternatively travel faster and b) the positions from which a) was formed. 160
7.12 Traces of all the particles viewed in figure 7.11. (•) represents the end of a trail where the next position of the particle was uncertain. 160
7.13 The instantaneous axial speed as a function of the lateral position of the particles represented in figure 7.11. 161
7.14 The first image of the start of a movie (latsort1.avi) that shows latex particles travelling down the branches. In this movie the power is not controlled. 162
7.15 The powers in the upper (■) and lower (■) waveguide for a greater duration than shown in the above movie. 162
7.16 A plot showing the particles that were sorted into the upper branch (■) and those that were sorted to the lower branch (♦) as a function of the powers in these waveguides at the instant the particle crossed the junction. 163
7.17 The controlled sorting of a particle, a) shows the first image of movie (latsort2.avi) whilst b) simultaneously shows the power in the upper (■) and lower (■) branches as a function of the time. The vertical bar in the movie represents the time point that is being shown in the movie. 164

7.18 Trace of 250nm gold nanoparticles with the a) lower branch and b) upper branch more strongly coupled to. 165
7.19 The position of particles travelling at least 30μm/s with a) the left branch and b) the right branch illuminated. c) shows the two images superimposed on each other for clarity. 166

8.1 Geometry for evanescent standing wave analysis of a lossy waveguide. . . 170
8.2 Intensity as a function of position for the partial standing wave (■). Included are the incident (■) and reflected (■) waves and the sum of the incident and reflected waves (■). 171
8.3 Comparison of scattering (■), gradient (■) and absorption (■) axial forces on a 125nm radius gold particle in an evanescent standing wave of a waveguide. 172
8.4 Design for production of a standing wave using a loop. The width of all waveguiding parts was 3μm 174
8.5 Creation of a standing wave by injecting light from the laser into both ends of the waveguide. 175
8.6 First image of a movie (mirroroff.avi) showing the scattered light from a trapped latex sphere. The attached mirror is knocked off at t=247seconds. 176
8.7 a) The 'x' position in the image and b) the speed of particle as a function of time. The × represents the point at which the mirror was knocked off. 177
8.8 Diagram showing the approximate positions of scattering lobes on a latex particle for the case of a) no reflection and b) some reflection at the output of the waveguide. f and b refer to the bulbs caused by the forward travelling and backwards travelling wave respectively where the direction of forward propagating light is from left to right. 177
8.9 The speed (left axis) of particles plotted as a function of their distance from the end of the waveguide with the mirror on (■), and removed (■). The right axis shows the ratio between the intensity of forward 'bulb' and the rear 'bulb' (♦). The best fit curves are also shown. 178
8.10 The axial speed histogram for gold particles above a single mode waveguide with a mirror attached to (■)and after knocking off (■) the output end of the waveguide. 180
8.11 The $\log_{10}$ of the ratio of the brightness of the front to backward lobes as a function of the distance (along the waveguide) from the Y-junction split. 181
8.12 First image from a movie (matched.avi) showing the scattering from seven latex particles with equal forward and backward components of intensity. At t=31s the fibre at the left hads side is moved. 182
8.13 The axial speed of particles as a function of the ratio of the intensity of the forward to backward scattering 'bulbs'. 182
8.14 The first image of a movie (latcont.avi) showing the axial control of the latex particle indicated by the black arrow. 183

9.1 A screenshot of the Labview program used for the acquisition of images and experimental conditions. 192

List of Tables

2.1 Peak values of polarisability for a 10, 50 and 125nm gold particle. 33
2.2 Constant used for predicting optical forces. 33

3.1 Measured area enclosed by equation 3.45 with conditions as in figure 3.8 for the case of 30 steps. 52
3.2 Measured effective refractive indices of planar Cs^+ ion-exchanged waveguide for a) 24 hours at 500^0C and b) 96 hours at 450^0C. 55

3.3 The optimised profile parameters to match the effective indices of the planar Cs^+ ion-exchanged waveguide, ion-exchanged for 24 hours at 500^0C. 55

3.4 The optimised profile parameters to match the effective refractive indices of a planar Cs^+ ion-exchanged waveguide, ion-exchanged for 96 hours at 450^0C. 56

4.1 Gravity, buoyancy and resultant forces for a range of particles. 74
4.2 Expected RMS Brownian motion of a range of gold and latex particles for a range of times. 77
4.3 Individual Hamaker constants for materials used. 84
4.4 Zeta potentials of the materials used for DLVO calculations. 86
4.5 Parameters used to model heating. All values are given in SI units. 89
4.6 Parameters used for predicting the ability to trap a gold particle. 94
4.7 Radii at which values of τ would be obtained for various powers in both the transverse (x) and lateral (y) dimensions ('-' indicates the value is greater than 250nm). 95

5.1 Ion sizes along with reported surface refractive index increases in different glasses for the group I metals and silver and thallium ions. In all cases the ion being exchanged is Na^+ except in the case of * where K^+ is the ion exchanged. 102
5.2 Measured effective indices of planar waveguides at 633nm in a range of glasses along with substrate indices that were all taken from literature apart from that of Menzel glass which was measured (at 633nm). An x indicates that a waveguide was not formed in these glasses. 114

7.1 A summary of waveguide lengths and losses (at a wavelength of 1066nm) for Cs^+ and K^+ ion-exchanged waveguides. 155
7.2 Effective refractive indices of the modes for a 6μm and 10μm waveguide. . 156

List of Accompanying Material

The accompanying material for this thesis is:

- One compact disc

The compact disc (CD) contains six movie files. These are (in order of reference):

- drift.avi (page 141)
- goldprop.avi (page 142)
- latsort1.avi (page 162)
- latsort2.avi (page 164)
- mirroroff.avi (page 176)
- matched.avi (page 182)
- latcont.avi (page 183)

The audio video interleave (.avi) file format used is highly portable and may be viewed on Macintosh or Windows-based personal computers. Free software to view these files include Windows Media Player and QuickTime Player.

Declaration of Authorship

I, John Patrick Hole, declare that the thesis entitled 'The control of gold and latex particles on optical waveguides' and the work presented in it are my own. I confirm that:

- this work was done wholly while in candidature for a research degree at this University;
- where any part of this thesis has previously been submitted for a degree or any other qualification at this University or any other institution, this has been clearly stated;
- where I have consulted the published work of others, this is always clearly attributed;
- where I have quoted from the work of others, the source is always given. With the exception of such quotations, this thesis is entirely my own work;
- I have acknowledged all main sources of help;
- where the thesis is based on work done by myself jointly with others, I have made clear exactly what was done by others and what I have contributed myself;
- parts of this work have been published as shown in the List of Publications

Signed: .....

Date:...../...../.....

List of Publications

Listed in reverse chronological order:

1. J.S. Wilkinson, O.G. Hellesø, J.P. Hole, and K. Grujic. Optical waveguide manipulation of micro- and nano-spheres. In *PERS'06 Progress in Electro-magnetics Research Symposium*, Cambridge, Ma, 2006.

2. J. Tschmelak, G. Proll, J. Riedt, J. Kaiser, K. Kräemmer, L. Barzaga, J.S. Wilkinson, P. Hua, J.P. Hole, R. Nudd, M. Jackson, R. Abuknesha, D. Barcelo, S. Rodriguez-Mozaz, M.J. Lopez de Alda, F. Sacher, J. Stien, J. Slobodnik, P. Oswald, H. Kozmenko, E. Korenkova, L. Tothova, Z. Krascsenits, and G. Gauglitz. Biosensors for unattended, cost-effective and continuous monitoring of environmental pollution: Automated water analyser computer supported system (AWACSS) and river analyser (RIANA). *International Journal of Environmental Analytical Chemistry*, 85(12-13):837–852, 2005.

3. J.P. Hole, J.S. Wilkinson, O.G. Hellesø, and K. Grujic. Guiding and sorting of micro and nano-particles with integrated optics. In *CLEO Europe*, ICM, Munich, Germany, 2005.

4. K. Grujic, O.G. Hellesø, J.P. Hole, and J.S. Wilkinson. Microsphere chain formation in the evanescent field of an optical waveguide. In *ECIO*, Grenoble, France, 2005.

5. J.P. Hole, J.S. Wilkinson, K. Grujic, and O.G. Hellesø. Velocity distribution of gold nanoparticles trapped on an optical waveguide. *Optics Express*, 13(10):3896, 2005.

6. P. Hua, J.P. Hole, J.S. Wilkinson, G. Proll, J. Tschmelak, G. Gauglitz, M.A. Jackson, R. Nudd, H.M.T. Griffith, R.A. Abuknesha, J. Kaiser, and P. Kräemmer Integrated optical fluorescence multisensor for water pollution. *Optics Express*, 13(4):1124, 2005.

7. K. Grujic, O.G. Hellesø, J.P. Hole, and J.S. Wilkinson. Sorting of polystyrene microspheres using a Y-branched optical waveguide. *Optics Express*, 13(1):1, 2005.

8. J. Tschmelak, G. Proll, J. Riedt, J. Kaiser, P. Kräemmer, L. Barzaga, J.S. Wilkinson, P. Hua, J.P. Hole, and R. Nudd. Automated water analyser computer supported system (AWACSS) part I: Project objectives, basic technology, immunoassay development, software design and networking. *Biosensors and Bioelectronics*, 20(8):1509, 2005.

9. J. Tschmelak, G. Proll, J. Riedt, J. Kaiser, P. Kräemmer, L. Barzaga, J.S. Wilkinson, P. Hua, J.P. Hole, and R. Nudd. Automated water analyser computer supported system (AWACSS): Part II: Intelligent, remote-controlled, cost-effective, on-line, water-monitoring measurement system. *Biosensors and Bioelectronics*, 20(8):1516, 2005.

10. P. Hua, J.P. Hole, J.S. Wilkinson, G. Proll, J. Tschmelak, G. Gauglitz, M.A. Jackson, R. Nudd, R. Abuknesha, J. Kaiser, and P. Kräemmer. Integrated optical immunofluoresence multisensor for river pollution. In *EWOFS'04 Second European Workshop on Optical Fibre Sensors*, Santander, Spain, 2004.

11. K. Grujic, O.G. Hellesø, J.S. Wilkinson, and J.P. Hole. Optical propulsion of microspheres along a channel waveguide produced by Cs^+ ion-exchange in glass. *Optics Communications*, 239(4-6):227–235, 2004.

Acknowledgements

I would like to thank a great number of people who have made this thesis both possible and enjoyable. Firstly I would like to thank the integrated optics group in the ORC including Ping for her help both in waveguide fabrication and with the work we did on the AWACSS project. I would also like to thank Neil for his help with the SEM and, with Dave Sager, for their help in the cleanroom. I thank Tracy for her advice on the biochemical aspects of the project. I also thank Anna, Andy, Charlie, Vasilis, Huabing and Larysa for always being willing to help and for enlivening the group meetings!

I spent two of my years in Southampton in a shared house with Laurie, Anna and Pete and I thank them greatly for being fun and for their tolerance.

Olav Gaute Hellesø and Katarina Grujic from the Institutt for Fysikk at the Universitetet i Tromsø both spent long periods working with me in the ORC and it is to them that I owe much of my understanding and thoughts, through countless conversations. Much more than that, they were great company in an otherwise fairly isolated project. In addition to their visits, I was a guest of theirs in Norway for four months and find myself thanking them again for looking after me far better than I believe I looked after them! I especially thank Olav for skiing trips and cooking, Katarina for her lengthy conversations and for introducing me to everyone, and all the other friends I made there for making the visit thoroughly enjoyable. I also thank the Norwegian Government for granting me a scholarship to fund this period of my study.

My family have always supported me and I thank Mum, Dad, Alison and Dave for their understanding and advice.

Despite being 50 miles away from Ellie for most of my study (or a couple of thousand kilometers whilst in Norway) she has put up with me for the last four years and for that I am very grateful. I thank her whole-heartedly for all the support, encouragement and advice that she has given me. I cannot begin to describe my gratefulness for always having her there to talk to.

James has (as I believe he does for all of his students) taken extra-special care of me. His commitment has been total, and despite always being busy, he has always been willing to see me or to read through work promptly. It is these factors along with his far-reaching knowledge and calming manner that has made this project most enjoyable and I am extremely grateful to him.

Nomenclature

$_{i,int,s}$	Subscripts for incident, internal and scattered fields
$_{sca,abs,ext}$	Subscripts for scattering, absorption and extinction
α	Complex polarisability, α= α'+iα"
β	Propagation constant
γ	Field attenuation constant
δ	Penetration depth of waveguide or particle
ϵ	Permittivity
η	Viscosity
θ	Azimuthal angle in spherical coordinates
κ	Debye length
λ	Free space wavelength
μ	Permeability
ρ	Density
σ	Surface charge density
τ	Trapping parameter
ϕ	Polar angle in spherical coordinates
χ	Size parameter
ψ	Scalar generating function
ω	Angular velocity (=$2\pi f$) (also beam waist size)
a	Particle radius
a_n, b_n	Coefficients used for the incident and scattered fields of the nth mode
A	Hamaker constant
B	Magnetic field
c	speed of light in vacuum
c_n, d_n	Coefficients used for the internal field of the nth mode
C	Cross-sections of scattering, absorption and extinction respectively
d	Sharpness of Fermi function
D	Diffusion constant
E	Electric field vector
F	Force
g	Acceleration due to gravity (=9.81ms^{-2})
h_n	Hankel function of the first or second kind

$\mathbf{H}$	Magnetic field vector
I	Intensity
I_0, I_f, I_b	Peak surface and forward and backward propagating intensities
j_n, y_n	Spherical Bessel functions of the first and second kind respectively of order n
J_n, Y_n	Bessel functions of the first and second kind respectively of order n
k	Free space wavenumber (given by $\frac{2\pi}{\lambda}$)
m	ratio of refractive index of particle to medium (also the order of a Legendre)
$\mathbf{M}$,$\mathbf{N}$	Vector spherical functions
n_{eff}	effective refractive index of a waveguide mode
N_m	Refractive index of medium
$\mathbf{p}$	Dipole moment
P	Power
P_n^m	Legendre function of degree n and order m
Q	Cross-sectional area efficiency (also charge)
r	Radial component in spherical coordinates
R	Field reflection coefficient
t	Time
T	Temperature
V	Volume
w	Depth of waveguide
W	Energy rate
z_n	Undefined Bessel function

Chapter 1

Introduction

1.1 Aims and motivation

The aims of this project are to obtain an understanding of the optical forces that are required for the trapping and propulsion of spherical particles in the evanescent field of a channel waveguide and to use this knowledge to trap and propel both latex and gold particles above a channel waveguide device. This is expected to pave the way for integrated optical devices to be fabricated and optimised allowing this technology to become applicable to a practical system. Any application will clearly depend on the amount of control that can be gained over the particles and the type of devices that can be produced. This thesis therefore concentrates on these two factors.

Whilst the aims of this work are to obtain a better understanding of evanescent optical trapping and to determine what is feasible with this technology it is useful to have an overview of potential applications.

One example of a potential application that this technology could address is in the separation and counting of populations of certain target DNA sequences. One way in which this could be carried out is as follows. Oligonucleotides (short segments of single-stranded DNA) of one type would be attached to the surface of gold particles of a uniform size. These particles would also be tagged with fluorophores. A second oligonucleotide sequence would be attached to a different gold particle size with a different colour fluorophore. A sample containing DNA would be heated to separate the two intertwined strands of DNA. The oligonucleotide- and fluorescently-labelled particles would be mixed with the sample. If present, the single-stranded DNA would hybridise to the oligonucleotides containing the complementary sequence. This sample would be injected over the waveguide and the differing gold particles separated optically by size. By illuminating the end sample and optically filtering the concentration and level of cross-contamination could be measured. This could also be used as a preliminary step for purifying a DNA sample for subsequent polymerase chain reaction (PCR).

Using a channel waveguide configuration gives the advantage of being able to manipulate many particles at once. This will thus be a significant advantage if high throughput separation were required (as would be normal for a biological application such as this device could address). The use of optical forces ensures no contamination whilst the use of a channel waveguide geometry will mean that many processes may be integrated in a lab-on-a-chip type format.

Although this may appear to be a convoluted method for DNA measurement and purification, much of the science for this process has already been studied and developed. For example the tagging of gold beads with oligonucleotides and fluorophores has been possible for many years [1, 2]. A concern is that the high optical density would lead to damage of either the biological material or the fluorophore. However, as was shown in the experiments by Ashkin, particles can be trapped with sufficiently low powers so as to not damage biological material. With regard to the fluorophore, although it has been noted that photobleaching can occur, this is not total [3] and sufficient light will still be collectable. In addition it is possible that instead of fluorophores, quantum dots, which have much longer lifetimes could be used [4, 5]. These would also have to be sufficiently separated from the gold to reduce the effect of quenching by the gold.

This process could equally well be carried out using dye doped or quantum dot loaded latex particles with DNA attached. However the disadvantage of this approach is that the latex particles required would be larger, thus reducing the ratio of sample-to-carrier volume, which may reduce the throughput of the process.

1.2 An historical background

Radiation pressure is the force caused by a change in the momentum of light when reflected or refracted at an interface. The concept of this force has been known since 1619 when Johannes Kepler explained the fact that the tails of comets are always directed away from the sun by the "pressure" of the sunlight [6]. Later in 1873 Maxwell confirmed that his electromagnetic approach predicted such a force and he was also able to predict theoretically, what was already known practically, that it was an extremely small force [6]. This force can now be readily explained by the de Broglie wavelength or wave-particle duality put forward by de Broglie in 1924 [7]. This is the theory that every particle has an associated wavelength, and conversely that light with a certain wavelength has an associated momentum. Thus if light is reflected/refracted then its associated change in momentum must be transferred to an object. Despite knowledge of the force that light could exert on an object it was impossible to utilise it in any practical way at that time due to the absence of a suitably intense light source. Thus with the exception of the demonstration of radiation pressure on macroscopic objects and absorbing glasses in 1901 [8, 9] the forces were considered of little relevance to terrestrial affairs. This

remained the case until the critical invention of the first laser (Light Amplification by Stimulated Emission of Radiation) in the 1960s [10].

1.3 The single beam trap

With the use of this new tool that produces an intense coherent beam of light, progress in optical trapping has been rapid.

Arthur Ashkin was the first to demonstrate optical trapping in 1970 [11]. In this paper he showed that latex particles in water could be propelled and attracted into a focussed laser beam, and that with an opposing laser beam, particles could be stably trapped. He then showed that particles could be trapped with just one laser beam [12] by illuminating from below using gravity to counteract the forwards scattering force. In 1975 he demonstrated the levitation of particles in a vacuum [13] and was able to use this to observe Mie resonances in liquid droplets [14, 15]. In the late 1980's he proposed [16] and demonstrated [17] the optical focussing of neutral atoms using radiation pressure. He later showed the optical gradient force could be a method for self-focussing light in an artificial Kerr medium [18, 19]. More recently he has looked at the biological applications of optical trapping by trapping viruses and bacteria [20], single cells [21] and the cytoplasm strands within cells [22]. He has also written three comprehensive reviews on optical trapping [23, 24, 25].

Optical trapping is typically suitable for trapping particles in the size region of tens of nanometers to tens of microns. The physical reason for this is that the wavelength of light loosely spans the range from hundreds of nanometers to twenty microns and a typical diffraction limited spot is the order of a few microns. The type of trapping that Ashkin pioneered, using a collimated Gaussian beam from a laser focussed down tightly, has formed the core of optical trapping applications and research. This is chosen for trapping experiments as this form of field is simple to produce and requires relatively low powers of light (several milliWatts, typically). In this case a particle will typically be trapped just the far side of the focal point of the beam. This beam exerts two forces on the particle. The first is the scattering force that acts in the direction of the beam and is due to the scattering of the beam by the particle. This force is often referred to as radiation pressure. The second force acting on the particle is the gradient force. This is directed up an optical intensity gradient towards the position of maximum intensity of the beam and is due to the interaction of the internal field induced in the particle and the external field. These forces are discussed in more detail in chapter 2. This configuration is given many different names but here the term single-beam trap (SBT) is used.

Since Ashkin's first paper much has been done in the field of optical trapping, especially in the last ten years. The single beam trap has been used to trap many different spherical

particle types and sizes [11, 15, 26, 27, 28, 29, 30, 31, 32, 33]. Most commonly trapped are latex particles of sizes ranging from about 100nm to about 10μm diameter [17, 26, 30, 31, 34, 35, 36, 37]. In addition silica [32, 37], oil [15], gold [27, 28, 31, 36, 38, 39], silver [27, 29], platinum and bronze [27] have also successfully been trapped.

Metallic particles are harder to trap in a SBT due to higher absorption and thus the forward axial forces are often stronger than the gradient force that acts to trap the particle. However Svoboda and Block [31] trapped Rayleigh gold particles of size 36nm in a SBT and compared this to the trapping of 38nm latex particles using 1047nm wavelength radiation. They noted that the ratio of the magnitude of the polarisabilities and the trapping strength were similar, the gold particles being trapped approximately 6.6 times more effectively. Sato et al. [27] trapped 2μm bronze, silver and gold particles with both the TEM_{00} and TEM_{01} modes depending on the position of the waist of the beam compared to particle. However these were only trapped in two dimensions, pushed against the cell. Furukawa and Yamaguchi [28] also trapped particles in two dimensions explaining this by a 'creeping wave' theory whereby the particle is trapped the on near side of the focal point to explain the trapping of 0.5-3.0μm gold particles with 515nm radiation.

1.4 Alternative configurations and beam shapes

Recently much of the research into the field of optical trapping has been focussed on forming different intensity distributions, other than that from a focussed Gaussian beam. This is generally done to allow multiple particles to be trapped. An example of this is the holographic optical tweezer (HOT) that is programmable with the use of a spatial light modulator (SLM) [40, 41]. Garces-Chavez et al. have described a method of using Bessel fields to trap multiple particles in one beam separated by relatively large distances (up to 3mm) [42]. These self-reconstructing beams have the advantage of remaining narrow in the axial dimension over a longer distance, compared to the Gaussian beam that diverges rapidly. These beams are also controllable in terms of their periodicity and power. Macdonald et al. [43] have shown how an interference between two different modes of the same laser produces a pattern in which particles will become trapped in the peak flux areas. They also demonstrated the stacking of six 53μm latex particles on top of each other in the Bessel field. Flynn et al. [26] have shown that by using an array of vertical cavity surface emitting lasers (VCSELs) that they are able to trap 5μm and 10μm polystyrene spheres and various biological samples. In addition, by modulating the lasers, they can move the particles into different set positions. Another method of creating an array of microparticles has been demonstrated by Tam et al. [44] by illuminating a fibre bundle where each fibre terminates with a focussing element so that each fibre is able to trap a particle. Another method of trapping multiple particles simultaneously is by time-sharing a single focussed Gaussian over many positions by

scanning it rapidly from point-to-point as demonstrated by Sasaki amongst others [45]. Four orthogonal fibres were used to hold a latex bead very stably at the centre of a $200\times200\mu$m cell with no use of lenses [46].

The last form of field described here is that of the evanescent wave that is used in this project. The term evanescent wave is used to describe a field that is exponentially decaying with distance. These waves are described by the Helmholtz equation where the field is non-zero at a boundary but no power is transferred to the medium of lower refractive index. The evanescent wave travels parallel to the interface in the medium of lower refractive index. The evanescent wave trap has been used previously for trapping and is formed either by reflection of a beam at a surface [37, 47, 48, 49], or as the superstrate to a channel waveguide [35, 36, 38, 39]. The rapid decay of field with distance from the interface means the resulting intensity gradient is well suited to trapping particles. Evanescent wave optical trapping is more thoroughly reviewed later in this chapter.

1.5 Applications of optical trapping

So far the discussion has only considered what is physically possible in terms of trapping. In this section the uses of optical trapping are discussed in more detail.

One of the main advantages of optical trapping is that no physical entity comes into physical contact with the particle as a result of the trapping, since it is only the presence of an intensity gradient that is required, and this is formed by lenses etc. remote to the sample. This therefore has the advantage of there being no chance of contaminating the sample. In addition, if the particle and medium in which it is held are transparent, then it will not be heated and thus damaged.

There are very many different types of applications for which optical trapping has shown potential and a few of these will be described below. For a more complete study of the applications of laser radiation pressure see reviews by Brown and Brown [50], Chu [51], Molloy et al. [52], Ashkin [23, 24] and Grier [53].

One of the first uses of optical trapping was when it was realised that atoms could also be slowed by two opposing TEM_{00} modes carefully tuned to the resonance of the atoms (sodium in this case) [16, 17]. There has been much work done on this since 1978 but the essence of the trapping has not changed. Essentially atoms are slowed by detuning the wavelength of the laser to just either side of the resonance peak. The force applied to the atom will then be dependent on the Doppler shifted wavelength of the particle relative to the laser source. This has also been proposed in a channel waveguide geometry [54] and demonstrated with a prism [55] where the evanescent waves produce a minimum energy for the ions.

Optical trapping has been used to produce a small probe that can be used as a near-field scanning optical microscope (NSOM). The principle was shown by Kawata et al. [30] in 1994 and this was further optimised by Gu and Ke [29] by comparing the use of gold, silver and polystyrene spheres to make up the probe. This method has the advantage over normal NSOM, with a pointed tip, of being less likely to either damage the tip or sample as the particle can be forced out of the weak trap in the case of a collision.

Optical traps have been rotated and propelled in various configurations of particles. A spinning micromotor has been produced using two latex particles attached to each other with one face of one of the particles being coated with reflective material where speeds of up to 800rpm were obtained [56]. A rotor fabricated by laser photopolymerisation has been demonstrated that is held in an optical trap and rotates at a frequency up to 2Hz with the direction of rotation set by the relative position of the rotor to the focal point of the beam. An optical trap has been combined with eight electromagnetic arms where a superparamagnetic bead was held optically and rotated magnetically [33]. By time-sharing trapping of four particles a pump was constructed in a micro channel pumping up to 1nl/hour in a controllable manner [32]. Holographic optical tweezers mentioned above have been used for optical peristalsis, dragging glass particles through water [57]. Experiments have also demonstrated how by varying the polarisation of light, torque can be applied to a particle [58] as was first predicted by Ashkin [13].

Optical traps have been also used in the process of measuring various parameters. These include particle size by Mie resonances [13], and by their ability to be trapped [59], the medium's viscosity [60], a waveguides' evanescent field [61] and various biological properties discussed below.

As has already been mentioned optical trapping has also been used in biological experiments with Ashkin demonstrating the trapping of single cells [21], and viruses and bacteria [20] in 1987. In 1989 he demonstrated the ability to examine filaments of cytoplasm from a plant cell demonstrating intracellular manipulation [22]. Much work has also been done in finding the power of myosin motors (that act in muscles) [62, 63, 64]. This is normally done by either trapping the myosin or the actin and finding the minimum power required to counteract the force of the other component on the system. Although DNA molecules have been trapped by themselves the more usual way of doing this is to first attach a latex bead to the DNA and trap this instead [65]. Cell or particle sorters have been demonstrated by various methods [34, 66]. The force which was required to stretch DNA has also been monitored by the use of optical tweezers [67]. For more details on the earlier biological optical applications of optical traps, see the review by Svoboda and Block [6].

General reviews of the applications of the optical forces can be found in [25, 51, 53].

1.6 Evanescent wave trapping and the novel contributions to this field

Very little work has been done on using an evanescent wave for optical trapping, however a few published papers are discussed briefly below.

Kawata and Sugiura [37] were the first to show trapping in the evanescent field in 1992. They illuminated a half cylinder sapphire prism directly with a Nd:YAG (1064nm, 150mW) laser to create the evanescent wave by total internal reflection (TIR). They propelled both glass (2 and 8μm diameter) and latex particles (1, 6.8 and 27μm diameter) above the prism and showed that for the 6.8μm latex particles TE polarisation propelled particles faster than TM polarisation. They also suggested that particles 'bounced' along the surface from the evidence of scattering fringes observed.

In 1996 Kawata and Tani [36] used a Nd:YLF (1047nm) laser, this time using a channel waveguide to propel latex particles with velocities up to 14μm/s for an 80mW output power. They also demonstrated propulsion of gold (0.5μm) and platinum (1μm) spheres and stated that the gold spheres travelled faster than the latex spheres for an output power of just 11mW. This was contrary to the existing theoretical belief that metallic particles should not be trapped in this way as they had refractive indices lower than the medium in which they were held (thus a repulsive force was predicted). However they pointed out that this theory was only applicable to particles with a wholly real refractive index, and that the absorbtivity of the particles must also be taken into account. This was later confirmed in a comprehensive paper by Brevik et al. [68].

In 2000 Tanaka and Yamamoto [35] used a Nd:YLF laser to excite various modes in an Ag^+ ion-exchanged channel waveguide. By setting the power of the output of the waveguide to 6mW and exciting different modes they showed that 4μm latex particles were propelled more slowly with increasing modal number. Later they used the same apparatus with 14mW output modal power to verify this trend [69]. They also showed that the particles meander following the beat pattern along the optical waveguide.

Ng et al. [38, 39] also used a Nd:YLF laser to propel 20nm diameter gold particles using a K^+ ion-exchanged waveguide. They compare the velocity for waveguides fabricated with different widths (between 3.5 and 5.5μm) and at both polarizations. The velocity of the particles was shown to be greater for the narrower waveguides and for TM polarised light. They also pointed out that the speeds they obtained (up to 4μm/s) were approximately 30 times greater than would be theoretically predicted. A potential explanation of this was the agglomeration of the gold spheres to form a larger structure.

Thus the work in the field of evanescent wave trapping has so far been limited. The most comprehensive work having been done by Ng where the effects of power, polarisation and waveguide width on the speed of particles were all investigated.

This thesis adds substantially to that work by examining many thousands of displacement vectors for each analysis using self-written, semi-automated, image acquisition, particle identification and tracking algorithms. Analysis of more than a few particles has not been performed in this field previously and its use has allowed accurate data regarding the position and speed distributions of particles propelled on the waveguide to be obtained where previously a maximum or mean speed of a few particles was measured. This has allowed comparisons to be made with theory, both in terms of the experimentally determined speeds of propelled particles and in the wavelength of the beat pattern between two modes of observed propelled particles. In addition, directly comparable results of the speeds of latex and gold particles have been obtained.

The Cs^+ ion-exchanged waveguides used for the trapping and propulsion have, for the first time, been experimentally characterised and modelled using the beam propagation method. This allowed the optimisation of various parameters important to the trapping and propulsion of particles and guides the fabrication of waveguides suitable for this application.

For the first time integrated optical devices have been designed and fabricated for use with evanescent wave trapping allowing particles to be sorted down Y-branched waveguides which is a necessary step towards the potential application of sorting DNA tagged samples.

Also for the first time a counter-propagating wave was introduced in the waveguide, which was shown to allow good positional control of the latex particles along a waveguide. It is anticipated that this may lead to an integrated optical method of controlling particle position.

In addition to the experimental work the optical forces on the particles have been derived theoretically using Rayleigh theory and these have been evaluated for gold particles leading to predictions and comparisons concerning particle velocities and the ability to trap particles.

The double-layer and van der Waals forces and an absorption induced, natural convective flow, that are well-known in other fields, have also been investigated here to determine their likely effect to this field of research. These phenomena have also been indirectly observed experimentally in this project.

1.7 Structure of thesis and important notes

The structure of this thesis is separated approximately between three mainly theoretical chapters followed by four mainly experimental chapters.

The next two chapters concentrate on calculating the optical forces that act on the particles. The **second** chapter is devoted purely to a derivation of these optical forces analytically where the importance of both the polarisability of the particle and the intensity profile of the field are stressed. Both the Mie theory and Rayleigh theory are derived (the Rayleigh theory being an approximation to the more complex Mie theory).

The **third** chapter investigates this intensity profile by analysing the fields of modes in an optical channel waveguide. This chapter is used to theoretically predict the characteristics of a waveguide that can then be used to design optimised waveguides.

The **fourth** chapter investigates the non-optical forces on the particles. These are the gravitational and buoyancy force, Brownian motion and a Stokes' drag force, the DLVO theory that encompasses the van der Waals force and the double-layer force, and a force predicted by modelling of the temperature profile caused by absorption of the laser radiation. It then brings these forces together with the optical forces and discusses the relevance of each of them.

The **fifth** chapter concentrates on the fabrication and characterisation of the waveguides used. It describes results from both K^+ and Cs^+ ion-exchanged waveguides in a range of substrates. It includes the characterisation of the composition of the substrates, effective index measurements, modal cut-off wavelengths and modal sizes.

The **sixth** chapter discusses in detail the experimental apparatus and programs used to analyse and record the data. It also shows a range of results for particles being trapped along straight waveguides.

The **seventh** chapter uses waveguides fabricated in the shape of a Y-junction and shows how these can be used to sort both gold and latex particles.

The **eighth** chapter introduces a counter-propagating wave and shows how this can be used to control the position of latex particles axially along the waveguide.

Finally in the **ninth** chapter the conclusions from the thesis are given and suggestions of future work in the area are put forward.

Throughout this thesis there are a small number of conventions that are used to make the reading of the thesis more fluent. Firstly when a **particle size** is referred to it should be taken to be referring to a spherical particle with the value being the particle diameter. Where the terms **transverse**, **lateral** and **axial** are used these refer to the dimensions normal to the substrate, in the plane of the substrate and normal to the waveguide and along the axis of the waveguide, respectively.

This project largely involves quantifying the motion of particles and it was felt that great benefit and understanding could be achieved for the reader by the use of animated **movies** of particles' motion. A number of movies are therefore included and a CD

ROM is enclosed inside the back cover of this thesis. The reader is directed to the supplementary material section for details on how to access and use these movies. In all cases in the text a figure of the first frame is shown and it is made clear that there is a movie available for viewing.

Chapter 2

Theory of Optical Forces on a Particle

2.1 Introduction

To aid the understanding of how to improve the trapping and propulsion of particles this chapter studies the theory involved in the interaction of light and spherical particles. There are three potential analytical methods for analysing optical trapping forces on a particle. These are Rayleigh theory, Mie theory and a ray optics approach. The theory that should be applied depends upon the size of the particle [70].

The factor that determines which theory should be used for a certain particle is called the size parameter, χ, and is given as:

$$\chi = \frac{2\pi a N_m}{\lambda} \tag{2.1}$$

where a is the radius of the particle, N_m is the refractive index of the surrounding medium and λ is the wavelength of light in a vacuum.

Although Mie theory is theoretically accurate for all size parameters it is unsuited to very small or very large particles. For particles much larger than the wavelength of light it is generally better to use the ray optics approach. This is because the Mie series uses a sum of an infinite series. This may be approximated by fewer terms, where the number of terms required increases with χ. If the number of terms is very large this can lead to small rounding errors introduced mounting up. For very small particles the Rayleigh theory can be used. This assumes a dipole is induced in the particle and is thus both conceptually and computationally much simpler. A guideline for the size range applicable to each theory is that for a$\ll \frac{\lambda}{N_m}$ the Rayleigh theory may be used, for a$> 20\lambda$, geometrical theory can be used [71] and Mie theory should be used for particles between these approximate limits.

This chapter discusses both the Rayleigh and Mie theories. Although the particles used in this project would mainly fall into the size regime for which the Mie theory is the most suited, the Rayleigh theory is simpler, more intuitive and much less computationally demanding. The ray optics method is omitted as it would only be applicable to particles larger than those used in the project.

In the first section the Mie theory is derived for a plane wave and results for gold and latex particles are shown that give exact results for this case. The method to extend this to an evanescent wave is briefly outlined. An approximation to Mie theory is used to obtain the Rayleigh theory and the two are then compared to highlight the size limitations of the Rayleigh theory. The Rayleigh theory is derived by a more intuitive method and the importance of the polarisability of a particle is discussed. The form of the evanescent wave is applied to the theory to obtain expressions for the optical Rayleigh forces upon a particle in an evanescent wave. Values are estimated and used to demonstrate the trends and relative size of these forces.

2.2 Mie theory

The method for the derivation of the fields surrounding a spherical particle in a plane wave is summarised as follows. Vector functions, **M** and **N** are introduced that both satisfy the vector wave equation and have zero divergence. These vector functions are functions of a scalar function called the generating function, ψ. The solutions to the generating function can be obtained by the conditions that it must satisfy both the scalar wave equation and the boundary conditions of space. The plane wave is manipulated into a form where it is described by a sum of the vector waves, **M** and **N**. The internal and scattered fields are obtained by solution of the boundary conditions at the surface of the sphere.

In this section the theory is derived briefly following the method of Bohren and Huffman [70] and results using this theory are presented and discussed.

2.2.1 Derivation

2.2.1.1 The vector harmonic functions, M and N

A time harmonic electromagnetic field is required that satisfies the wave equation in linear, isotropic, homogeneous media. The wave equation is given as:

$$\nabla^2\mathbf{E} + k^2\mathbf{E} = 0 \tag{2.2}$$

$$\nabla^2\mathbf{H} + k^2\mathbf{H} = 0 \tag{2.3}$$

where $k^2 = \omega^2\epsilon\mu$ and $\mathbf{E}$ and $\mathbf{H}$ are the electric and magnetic field vectors respectively and have zero divergence.

A scalar function, ψ, is introduced that can generate a vector function, $\mathbf{M}$ by:

$$\mathbf{M} = \nabla \times (\mathbf{c}\psi) \tag{2.4}$$

where $\mathbf{c}$ is a vector constant.

This can be manipulated into the form:

$$\nabla^2\mathbf{M} + k^2\mathbf{M} = \nabla \times [\mathbf{c}(\nabla^2\psi + k^2\psi)] \tag{2.5}$$

Thus $\mathbf{M}$ satisfies the vector wave equation if ψ is a solution to the scalar wave equation

$$\nabla^2\psi + k^2\psi = 0 \tag{2.6}$$

In addition, as the divergence of a vector function is zero:

$$\nabla.\mathbf{M} = 0 \tag{2.7}$$

Another vector, $\mathbf{N}$, can also be constructed that is given by:

$$\mathbf{N} = \frac{\nabla \times \mathbf{M}}{k} \tag{2.8}$$

and it can be shown that this also has zero divergence and satisfies the vector wave equation. Therefore if a solution to ψ can be found then the vectors $\mathbf{M}$ and $\mathbf{N}$ (that can be generated from ψ) satisfy the required conditions for an electromagnetic wave.

2.2.1.2 The generating function, ψ

Here the physical system, geometry and coordinate systems used in this method are introduced. Figure 2.1 shows the case of a sphere centred on the origin with a plane wave incident upon it. Both the Cartesian and spherical coordinate systems are shown.

As a sphere has symmetry in both the ϕ and θ dimensions, the vector $\mathbf{c}$ is chosen to be $\mathbf{r}$, the radial vector outwards from the origin of the sphere. From equation 2.4:

$$\mathbf{M} = \nabla \times (\mathbf{r}\psi) \tag{2.9}$$

The scalar wave equation in spherical coordinates is

$$\frac{1}{r^2}\frac{\partial}{\partial r}(r^2\frac{\partial\psi}{\partial r}) + \frac{1}{r^2\sin\theta}\frac{\partial}{\partial\theta}(\sin\theta\frac{\partial\psi}{\partial\theta}) + \frac{1}{r^2\sin\theta}\frac{\partial^2\psi}{\partial\phi^2} + k^2\psi = 0 \tag{2.10}$$

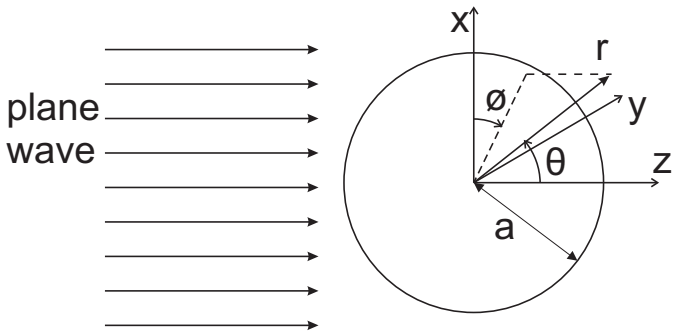

FIGURE 2.1: Diagram of the physical system being solved by Mie theory.

For simplicity, a solution of the following form is sought:

$$\psi(r,\theta,\phi) = R(r)\Theta(\theta)\Phi(\phi) \tag{2.11}$$

By separating variables it is required that:

$$\frac{d^2\Phi}{d\phi^2} + m^2\Phi = 0 \tag{2.12}$$

$$\frac{1}{\sin\theta}\frac{d}{d\theta}(\sin\theta\frac{d\Theta}{d\theta}) + [n(n+1) - \frac{m^2}{\sin^2\theta}]\Theta = 0 \tag{2.13}$$

$$\frac{d}{dr}(r^2\frac{dR}{dr}) + [k^2r^2 - n(n+1)]R = 0 \tag{2.14}$$

m and n are constants that can be determined by the requirement to satisfy ψ. Solutions to each of the three independent equations are now described below.

A requirement on ψ is that $\psi(\phi) = \psi(\phi + 2C\pi)$ where C is an integer. From equation 2.12 this requires m to be an integer and the positive integers are able to describe the complete set of solutions. This gives two possible solutions:

$$\Phi_e = \cos m\phi \tag{2.15}$$

$$\Phi_o = \sin m\phi \tag{2.16}$$

where e,o are used to denote even and odd functions, respectively.

For equation 2.13 to have wholly finite solutions, the first kind of associated Legendre functions, $P_n^m(\cos\theta)$ are required where n is the degree and m is the order and where $n = m, m+1, ...$

Finally the solution to equation 2.14 that gives linearly independent functions are the Bessel functions of the first, J_v, and second, Y_v, kind. More precisely the solutions are spherical Bessel functions where v is the order and $v = n + \frac{1}{2}$. For convenience, these

are written as:

$$j_n(\rho) = \sqrt{\frac{\pi}{2\rho}} J_{n+1/2}(\rho) \tag{2.17}$$

$$y_n(\rho) = \sqrt{\frac{\pi}{2\rho}} Y_{n+1/2}(\rho) \tag{2.18}$$

Thus the solution to the generating function is given by:

$$\psi_{emn} = \cos m\phi P_n^m(\cos\theta) z_n(kr) \tag{2.19}$$

$$\psi_{omn} = \sin m\phi P_n^m(\cos\theta) z_n(kr) \tag{2.20}$$

where z_n can represent j_n, y_n, $h_n^{(1)}$ or $h_n^{(2)}$ where $h_n^{(1,2)} = j_n \pm i y_n$. If the form of z_n is determined then a superscript of (1),(2),(3) or (4) will be used to describe each of the four functions respectively. In the undetermined form there will be no superscript. This complete notation set will also be used for the vector spherical functions, **M** and **N**, so, for example, $\mathbf{M}_{e12}^{(3)}$ represents the vector generated by a generating function, ψ, which was even in terms of ϕ, using the first degree of a second order Legendre function and using the first order of a Hankel function of the first type.

The form of the cos and sin functions are well known, however Legendre and Bessel functions are less common. The first two orders of these functions are shown below in figure 2.2.

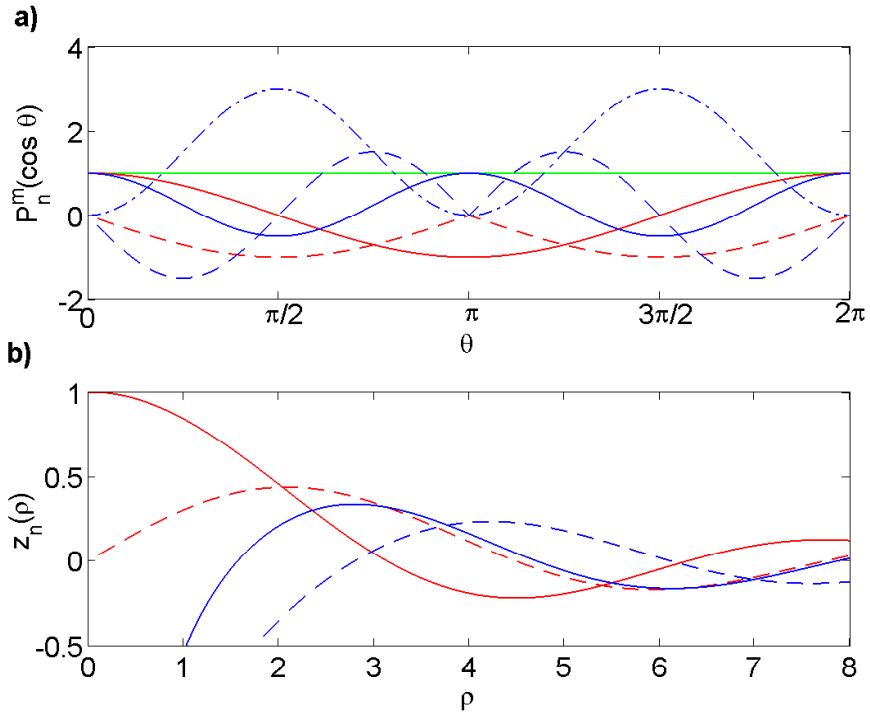

FIGURE 2.2: a) $P_n^m(\cos\theta)$ of the zeroth (n=0) (■), first (n=1) (■) and second (n=2), degree (■) for orders m=0 (—), m=1 (- -) and 2 (- ·) and b) Spherical Bessel functions of the first, j_n, (■) and second kind, y_n, (■) for orders n=1 (—) and 2 (- -).

From the Legendre functions showing the dependence on θ it can be seen that at multiples of π when the vector is perpendicular to the z axis the function is zero. Parallel to the z axis the alternating orders go through a zero or a maximum. Most importantly concerning the Bessel functions that describe the generating function in terms of the distance from the origin, are that the second kind all tend to -∞ at ρ=0 and that the first kind are all zero at ρ=0 apart from the first order which is 1.

2.2.1.3 Expansion of a plane wave

The generating function, ψ, gives the transfer function of the system that is used to calculate the field due to the sphere caused by an input field. In this section the input field is considered. The analysis studies the most common case of the plane wave, and this may subsequently be modified for the case of an evanescent wave. The function ψ was necessarily obtained in spherical coordinates. Therefore a lengthy manipulation of the plane wave into a spherical form is required. Rather than give the full algebraic solution of how this is done the important conceptual steps are outlined.

A plane x-polarised wave has form

$$\mathbf{E_i} = E_0 \exp(ikr\cos\theta)\hat{\mathbf{e_x}} \tag{2.21}$$

in spherical coordinates $\hat{\mathbf{e}}_\mathbf{x}$ is given by:

$$\hat{\mathbf{e}}_\mathbf{x} = \sin\theta\cos\phi\hat{\mathbf{e}}_\mathbf{r} + \cos\theta\cos\phi\hat{\mathbf{e}}_\theta - \sin\phi\hat{\mathbf{e}}_\phi \tag{2.22}$$

This field needs to be manipulated into the following form:

$$\mathbf{E_i} = \sum_{m=0}^{\infty}\sum_{n=m}^{\infty}(B_{emn}\mathbf{M_{emn}} + B_{omn}\mathbf{M_{omn}} + A_{emn}\mathbf{N_{emn}} + A_{omn}\mathbf{N_{omn}}) \tag{2.23}$$

where A_{xxx} and B_{xxx} are constants. It can be shown that all of the vector harmonics ($\mathbf{M_{xxx}}$ and $\mathbf{N_{xxx}}$) are orthogonal to all other vector harmonics.

By integrating over the surface of an arbitrary shape the coefficient, B_{emn} can therefore be written as

$$B_{emn} = \frac{\int_0^{2\pi}\int_0^{\pi} E_i \cdot \mathbf{M_{emn}} \sin\theta d\theta d\phi}{\int_0^{2\pi}\int_0^{\pi} \mid \mathbf{M_{emn}} \mid^2 \sin\theta d\theta d\phi} \tag{2.24}$$

Similar expressions can be written for each of the other coefficients. Fortunately equation 2.23 can be greatly simplified. Firstly B_{emn}, A_{omn} are zero for all m and n as are the remaining coefficients for $m \neq 1$ due to their mutual orthogonalities. The radial form of ψ was allowed to take one of four forms (see equations 2.19 and 2.20), however due to the requirement that the field be finite at the origin, j_n is selected as it is the only Bessel function that satisfies this condition and thus the superscript (1) is used.

This leaves a much simplified version of equation 2.23 as:

$$\mathbf{E_i} = \sum_{n=1}^{\infty} (B_{o1n}\mathbf{M^{(1)}_{o1n}} + A_{e1n}\mathbf{N^{(1)}_{e1n}}) \tag{2.25}$$

Using some specialised integrating theorems it is possible to evaluate the coefficients described by equation 2.24 and its analogues to solve for these remaining coefficients. This therefore gives expressions for the field as:

$$\mathbf{E_i} = E_0 \sum_{n=1}^{\infty} i^n \frac{2n+1}{n(n+1)} (\mathbf{M^{(1)}_{o1n}} - i\mathbf{N^{(1)}_{e1n}}) \tag{2.26}$$

$$\mathbf{H_i} = \frac{-k_0}{\omega\mu} E_0 \sum_{n=1}^{\infty} i^n \frac{2n+1}{n(n+1)} (\mathbf{M^{(1)}_{e1n}} + i\mathbf{N^{(1)}_{o1n}}) \tag{2.27}$$

where μ is the permeability of the medium.

2.2.1.4 Solving the internal and scattered fields

Having expanded the incident plane wave as shown above, it is now possible to examine the internal field of the particle. This will be an expansion of the same form as the plane wave, however it will have different constants:

$$\mathbf{E_{int}} = \sum_{n=1}^{\infty} E_n (c_n \mathbf{M^{(1)}_{o1n}} - id_n \mathbf{N^{(1)}_{e1n}}) \tag{2.28}$$

$$\mathbf{H_{int}} = \frac{-k_0}{\omega\mu_1} \sum_{n=1}^{\infty} E_n (c_n \mathbf{M^{(1)}_{e1n}} + id_n \mathbf{N^{(1)}_{o1n}}) \tag{2.29}$$

where μ_1 is the permeability of the particle and where $E_n = i^n E_0 (2n+1)/n(n+1)$. The scattered field has form:

$$\mathbf{E_s} = \sum_{n=1}^{\infty} E_n (ia_n \mathbf{N^{(3)}_{e1n}} - b_n \mathbf{M^{(3)}_{o1n}}) \tag{2.30}$$

$$\mathbf{H_s} = \frac{-k_0}{\omega\mu} \sum_{n=1}^{\infty} E_n (ib_n \mathbf{N^{(3)}_{o1n}} + a_n \mathbf{M^{(3)}_{e1n}}) \tag{2.31}$$

Where the superscript (3) represents a Hankel function of the first kind and is due to the scattered field not being required to satisfy the condition of finiteness at the origin. In order to solve these coefficients the boundary conditions at the surface of the sphere

(r=a) are applied. These are:

$$E_{i\theta} + E_{s\theta} = E_{int\theta} \tag{2.32}$$

$$E_{i\phi} + E_{s\phi} = E_{int\phi} \tag{2.33}$$

$$H_{i\theta} + H_{s\theta} = H_{int\theta} \tag{2.34}$$

$$H_{i\phi} + H_{s\phi} = H_{int\phi} \tag{2.35}$$

These four equations lead to the solutions of the constants as:

$$a_n = \frac{\mu m^2 j_n(m\chi)[\chi j_n(\chi)]' - \mu_1 j_n[m\chi j_n(m\chi)]'}{\mu m^2 j_n(m\chi)[\chi h_n^{(1)}(\chi)]' - \mu_1 h_n^{(1)}[m\chi j_n(m\chi)]'} \tag{2.36}$$

$$b_n = \frac{\mu j_n(m\chi)[\chi j_n(\chi)]' - \mu j_n(\chi)[m\chi j_n(m\chi)]'}{\mu_1 j_n(m\chi)[\chi h_n^{(1)}(\chi)]' - \mu_1 h_n^{(1)}[m\chi j_n(m\chi)]'} \tag{2.37}$$

$$c_n = \frac{\mu_1 j_n(\chi)[\chi h_n^{(1)}(\chi)]' - \mu_1 h_n^{(1)}(\chi)[\chi j_n(\chi)]'}{\mu_1 j_n(m\chi)[\chi h_n^{(1)}(\chi)]' - \mu h_n^{(1)}[m\chi j_n(m\chi)]'} \tag{2.38}$$

$$d_n = \frac{\mu_1 m j_n(\chi)[\chi h_n^{(1)}(\chi)]' - \mu_1 m h_n^{(1)}(\chi)[\chi j_n(\chi)]'}{\mu m^2 j_n(m\chi)[\chi h_n^{(1)}(\chi)]' - \mu_1 h_n^{(1)}[m\chi j_n(m\chi)]'} \tag{2.39}$$

where $'$ represents differentiation with respect to the argument of the Bessel function, m is the relative refractive index of the sphere to that of the surrounding medium (not the order of a Legendre function) and χ is the size parameter. For the common case of $\mu = \mu_1$ and by introducing the factors $\psi_n(\rho) = \rho j_n(\rho)$ and $\xi_n(\rho) = \rho h_n^{(1)}(\rho)$ it is possible to simplify these equations to those shown below:

$$a_n = \frac{m\psi_n(m\chi)\psi_n'(\chi) - \psi_n(\chi)\psi_n'(m\chi)}{m\psi_n(m\chi)\xi_n'(\chi) - \xi_n(\chi)\psi_n'(m\chi)} \tag{2.40}$$

$$b_n = \frac{\psi_n(m\chi)\psi_n'(\chi) - m\psi_n(\chi)\psi_n'(m\chi)}{\psi_n(m\chi)\xi_n'(\chi) - m\xi_n(\chi)\psi_n'(m\chi)} \tag{2.41}$$

$$c_n = \frac{m\psi_n(\chi)\xi_n'(\chi) - m\xi_n(\chi)\psi_n'(\chi)}{\psi_n(m\chi)\xi_n'(\chi) - m\xi_n(\chi)\psi_n'(m\chi)} \tag{2.42}$$

$$d_n = \frac{m\psi_n(\chi)\xi_n'(\chi) - m\xi_n(\chi)\psi_n'(m\chi)}{m\psi_n(m\chi)\xi_n'(\chi) - \xi_n(\chi)\psi_n'(m\chi)} \tag{2.43}$$

To summarise, the incident plane wave has been expanded as an infinite sum of spherical waves as shown in equation 2.26. The constants to the spherical waves are simple and thus included directly in this equation. The vector spherical waves, **M** and **N** can be solved by equations 2.8 and 2.9 given the generating function, ψ. The function ψ has been solved and has the form of either equation 2.19 or 2.20. Finally the internal and scattered fields are described by equations 2.28-2.31 where the constants are less simple than in the case of the incident field but can be solved and are given by equations 2.40-2.43.

2.2.1.5 Scattering cross sections/efficiences

By integrating over an infinitely large sphere, information regarding the proportion of light that is scattered or absorbed can be calculated. The net rate at which electromagnetic energy crosses this infinitely large sphere is given by

$$W_a = -\int_A S \cdot \hat{e}_r dA \tag{2.44}$$

Where S denotes the Poynting vector, and A is the surface area of the sphere over which the field is being integrated. Similar expressions can be written for the work done by the incident field, W_i, the scattered field, W_s and the electromagnetic energy arising from the interaction of the incident field and the scattered field, W_{ext}. The balance of these energies is:

$$W_{abs} = W_i - W_s + W_{ext} \tag{2.45}$$

where W_{abs} is the absorption by the sphere. W_{abs} must account for W_a if the medium in which the plane wave is travelling is non-absorbing, i.e. W_i is zero. W_{ext} and W_s can be written as:

$$W_{ext} = \frac{1}{2}\int_0^{2\pi}\int_0^{\pi}(E_{i\phi}H^*_{s\theta} - E_{i\theta}H^*_{s\phi} - E_{s\phi}H^*_{i\phi} + E_{s\phi}H^*_{i\theta})r^2\sin\theta d\theta d\phi \tag{2.46}$$

$$W_s = \frac{1}{2}\int_0^{2\pi}\int_0^{\pi}(E_{s\theta}H^*_{s\phi} - E_{s\phi}H^*_{s\theta})r^2\sin\theta d\theta d\phi \tag{2.47}$$

Terms for $E_{i\theta}$, $E_{i\phi}$,$E_{s\theta}$ and $E_{s\phi}$ have already been shown, by an expansion in spherical form (equations 2.28 and 2.30). By integrating these equations term-by-term, expressions for the scattering and extinction cross-sectional areas, C_{sca} and C_{ext}, which are defined as the ratio of these energy rates to the incident intensity, I_i, are readily obtained. These are given below:

$$C_{sca} = W_s/I_i = \frac{2\pi}{k^2}\sum_{n=1}^{\infty}(2n+1)(|a_n|^2 + |b_n|^2) \tag{2.48}$$

$$C_{ext} = W_{ext}/I_i = \frac{2\pi}{k^2}\sum_{n=1}^{\infty}(2n+1)Re[|a_n|^2 + |b_n|^2] \tag{2.49}$$

$$C_{abs} = W_{abs}/I_i = C_{ext} - C_{sca} \tag{2.50}$$

In addition, efficiencies, denoted Q_{ext}, Q_{sca} and Q_{abs} can be calculated, by dividing the above cross sectional areas by the cross-sectional area of a sphere (πa^2).

2.2.1.6 Application to evanescent wave excitation

In this project, particles will not be subjected to a plane wave, but an evanescent wave. The application of Mie theory to an evanescent wave generally considers a plane wave

internally incident on a prism at an angle greater than the critical angle of the interface. The angle of the refracted wave, θ_k, is given by Snell's law and is complex, therefore describing an evanescent wave. This complex angle may be used in equation 2.21 describing a plane wave. Conceptually therefore the plane wave may be expanded in the same manner as shown in section 2.2.1.3. However mathematically this expansion is much more complex due to the mutual orthogonality relations of the Legendre functions used in the expansion of the plane wave not being valid for complex angles. The theory is therefore more complex, but a number of studies have recently been carried out in this area [68, 72, 73].

2.2.1.7 Rayleigh approximation to Mie theory

By making suitable approximations about the size of the particle being analysed, it is possible to greatly simplify the theory. The basis of this simplification is outlined briefly below.

The first and second types of spherical Bessel functions can be expanded as:

$$j_n(\rho) = \frac{\rho^n}{1 \cdot 3 \cdot 5 \cdots (2n+1)}[1 - \frac{\frac{1}{2}\rho^2}{1!(2n+3)} + \frac{(\frac{1}{2}\rho^2)^2}{2!(2n+3)(2n+5)} - \cdots] \tag{2.51}$$

$$y_n(\rho) = \frac{1 \cdot 3 \cdot 5 \cdots (2n-1)}{\rho^{n+1}}[1 - \frac{\frac{1}{2}\rho^2}{1!(-2n)} + \frac{(\frac{1}{2}\rho^2)^2}{2!(1-2n)(3-2n)} - \cdots] \tag{2.52}$$

This allows the functions ψ and ξ (defined in section 2.2.1.4) to be expanded. The first two orders alone are required to expand these functions of χ to order χ^6. From these the scattering constants $a_{1,2}$ and $b_{1,2}$ may be written as:

$$a_1 = -\frac{i2\chi^2}{3}\frac{m^2-1}{m^2+2} - \frac{i2\chi^5}{5}\frac{(m^2-2)(m^2-1)}{(m^2+2)^2} + \frac{4\chi^6}{9}\frac{(m^2-2)^2}{(m^2+2)^2} + O(\chi^7) \tag{2.53}$$

$$b_1 = -\frac{i\chi^5}{45}(m^2-1) + O(\chi^7) \tag{2.54}$$

$$a_2 = -\frac{i\chi^5}{15}\frac{m^2-1}{2m^2+3} + O(\chi^7) \tag{2.55}$$

$$b_2 = O(\chi^7) \tag{2.56}$$

As can be seen if $|m|\chi << 1$ then all but the first term of a_1 can be omitted, giving a cross sectional area (as defined by equations 2.48 and 2.49):

$$C_{sca} = \frac{6\pi}{k_m^2}[\frac{2\chi^3}{3}|\frac{m^2-1}{m^2+2}|]^2 \tag{2.57}$$

$$C_{ext} = \frac{6\pi}{k_m^2} Im[\frac{-i2\chi^3}{3}\frac{m^2-1}{m^2+2}] \tag{2.58}$$

Here the substitution may be made for the complex polarisability $\alpha = \alpha' + i\alpha''$ where α is:

$$\alpha = 3V\frac{m^2 - 1}{m^2 + 2} \tag{2.59}$$

This greatly simplifies the expressions for the cross sectional areas to

$$C_{sca} = \frac{k_m^4}{6\pi}|\alpha|^2 \tag{2.60}$$

$$C_{ext} = k_m\alpha' \tag{2.61}$$

2.2.2 Theoretical Mie results

2.2.2.1 Cross sectional areas and efficiencies

From the constants a and b, plots of both the scattering and extinction cross sectional areas and efficiencies can be calculated as a function of particle size. Such plots are shown below for the cases of a latex sphere in air (figure 2.3a and c), a latex sphere in water (figures 2.3b and d and 2.4), and a gold sphere in water (figure 2.5). Figures 2.3 and 2.5 show the first four orders of these functions along with the sum of the first 10 and 20 orders. The resolution in χ used for these plots was 10^{-3}.

As can be seen, the higher order modes only start to have a significant effect above a certain radius, hence it is possible to approximate the complete series by only considering a number of modes. This number was shown by Wiscombe, to be approximately $\chi + 4\chi^{\frac{1}{3}} + 1$ [74].

From figure 2.3 it can be seen that there is a vast difference between a particle being in a medium of air compared to water. Due to the greater contrast in refractive indices a particle in air exhibits an envelope with many local peaks in the range of χ shown. In the case of the particle being in water, the smaller index contrast means that the local peaks do not occur until much higher values of χ as seen in figure 2.4. These peaks become more sharp as χ increases. As χ is a function of both a and λ these peaks can be observed by small changes in particle radius or wavelength used (or indeed the refractive index of the medium). Latex particles have no absorption, as the refractive index is wholly real. Figure 2.4 also shows the scattering efficiency of latex particles in water having risen sharply for very small particles, peaks at a value of 3.6 for 2.5μm particles and oscillates tending towards a value of two for larger particles. This apparent oddity is explained by the diffraction of the sphere past its physical boundaries [70].

In contrast, for the case of a gold particle shown in figure 2.5 there is a small absorption at the wavelength considered (1066nm) due to the imaginary part of the refractive index. This is approximately 45 times less than the scattering cross sectional area however at a wavelength closer to the gold resonance (400nm) where the refractive index has changed

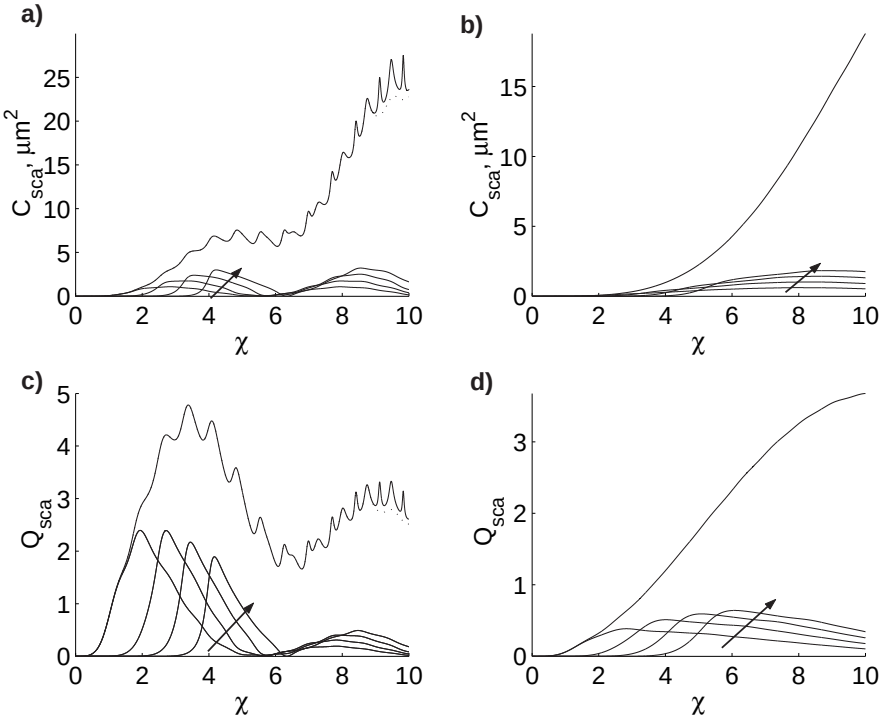

FIGURE 2.3: Scattering cross sectional areas for a latex particle in a) air and b) water and their respective scattering efficiencies, c) and d). The highest areas (-) represent the sum of the first 20 modes whilst for air, (··) represent the sum of first 10 modes. The lower four cross sectional areas show the first four modes with the arrow indicating increasing mode number.

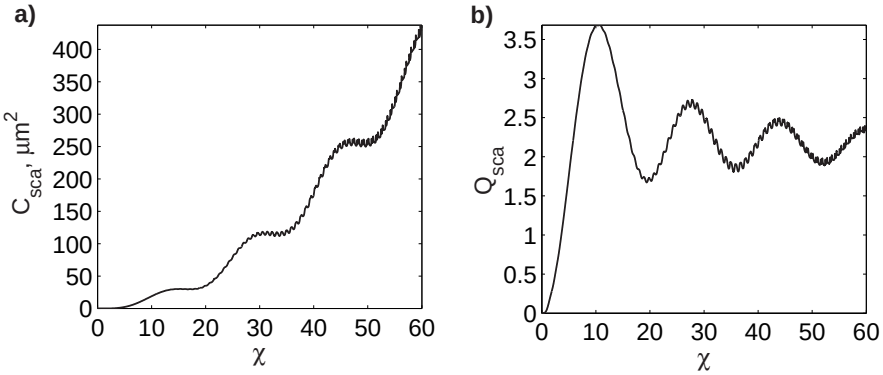

FIGURE 2.4: a) The scattering cross sectional area and b) efficiency for a latex particle in water using the sum of the first 80 modes.

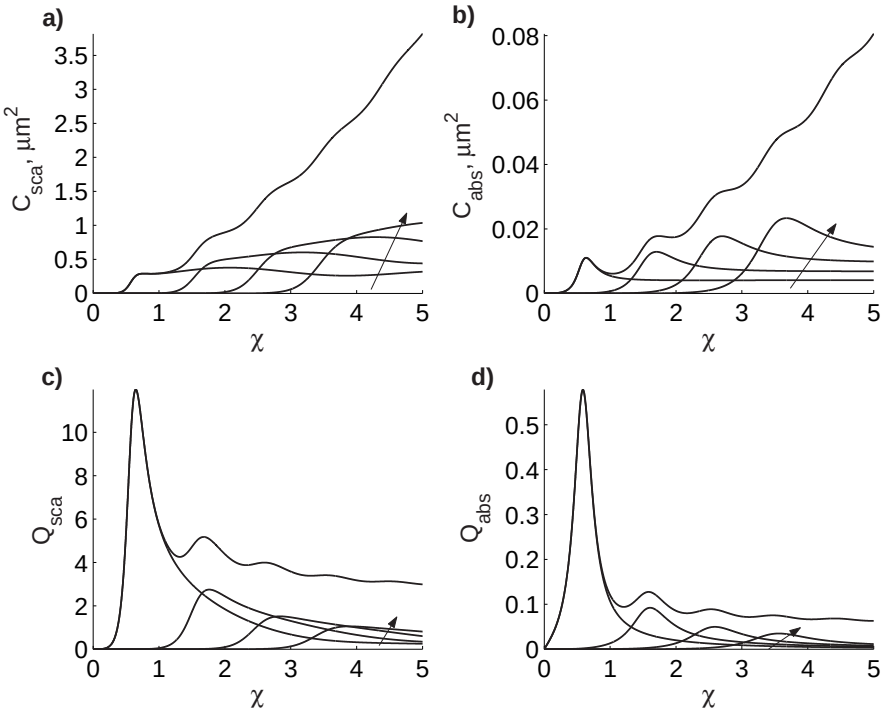

FIGURE 2.5: The a) scattering and b) absorption cross sectional areas for a gold particle in water and their respective efficiencies c) and d). In all cases of the highest plot is the sum of the first 10 modes and the lower four lines show the first four modes with the arrow indicating increasing mode number.

from 0.26+6.98i to 1.47+1.95i this factor reduces to approximately 1.75. The scattering from the gold is much greater than that from the latex for a particle of a given size due to the larger index contrast.

To give some feeling for the ranges of χ relevant to this project, the latex particles used ranged in size from 1μm to 15μm. In water at a wavelength of 1066nm these values represent a range of χ from 3.9 to 59. For gold the particle sizes used were between 100nm and 500nm, which represents a range of χ from 0.39 to 1.96. Therefore whereas for latex particles clearly many orders are required to describe the effects of even the smallest latex particles used, the gold can adequately be described by the first two orders. At $\chi = 1.96$ the first order value is approximately 42% of the total cross sectional area as calculated by the Mie theory. For $\chi = 0.98$, representing 250nm particles (which were more commonly used), the first order comprised 99.5% of the cross sectional area.

2.2.2.2 Comparison of Mie theory to Rayleigh theory

This section compares the scattering and absorption and scattering cross sectional areas and efficiencies to determine the applicability of Rayleigh theory to the latex and gold particles used in this project.

The comparison of the cross-sectional areas and efficiencies as calculated by Mie theory (equation 2.48 and 2.49) and the basic Rayleigh theory (equations 2.60 and 2.61) can be seen below in figures 2.6 and 2.7 for the cases of latex and gold particles in water, respectively.

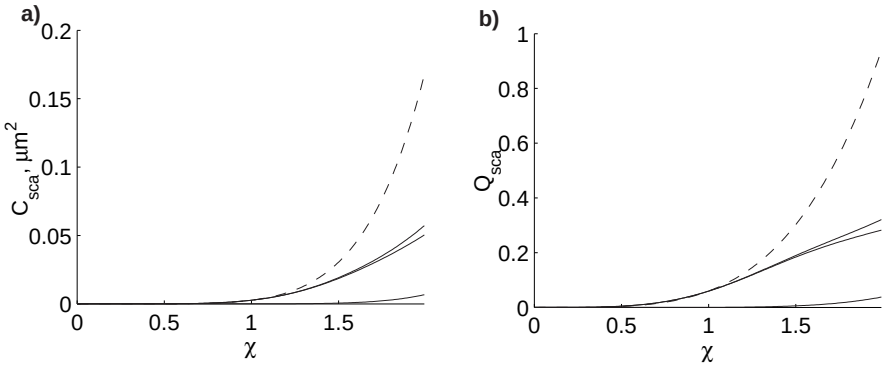

FIGURE 2.6: Scattering a) cross sectional area and b) efficiency comparing the case of the Rayleigh approximation (- -) and the Mie theory (–), for the case of a latex particle in water. The solid lines represent (in increasing values at χ=2) the first Mie order, the second Mie order and the total Mie value.

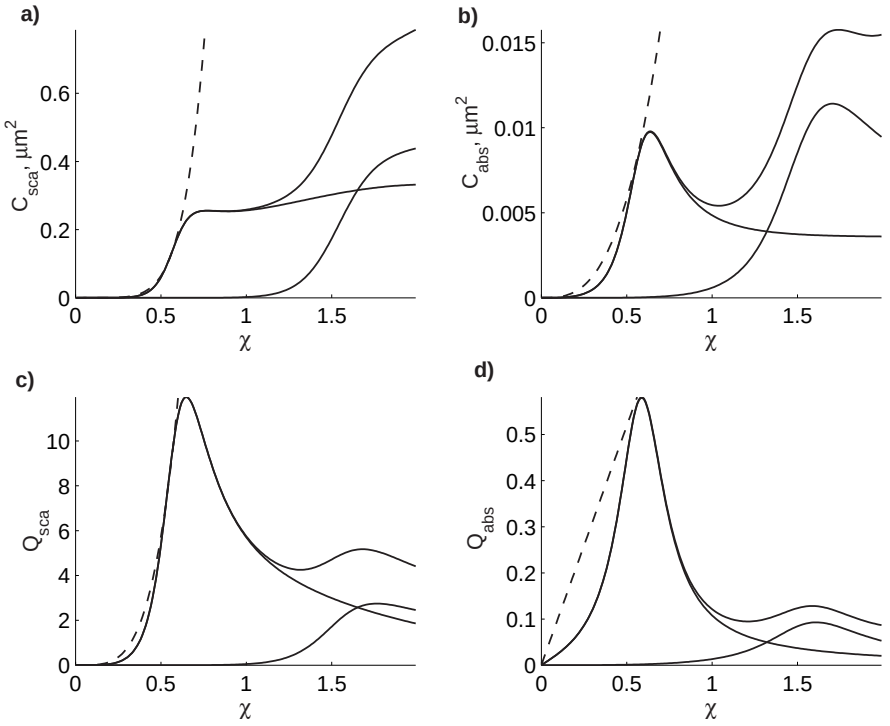

FIGURE 2.7: Scattering a) cross sectional area and c) efficiency and absorption b) cross sectional and d) efficiency, comparing the case of the Rayleigh approximation (- -) and the Mie theory (–), for the case of a latex particle in water. The solid lines represent (in increasing values at χ=2) the first Mie order, the second Mie order and the total Mie value.

As can be seen the Rayleigh and Mie theories agree well up to a certain value of χ and diverge thereafter. For a latex particle this point is at approximately χ=1.1, and at χ=0.61 for gold which represent radii of approximately 123nm and 70nm respectively.

Therefore the Rayleigh theory cannot be used for latex particles and should be used with caution with the gold particles. This is the case for the plane wave excitation of the spheres. For evanescent excitation, differing values are found and these are discussed below.

2.3 Forces on a Rayleigh particle

2.3.1 Derivation

The Rayleigh theory should strictly only be used if the field across the particle may be assumed to be approximately constant, i.e. where the diameter of the particle is less than a fraction of a wavelength, as the theory only allows for a dipole to be induced in the particle. In this case the particle can be approximated to a single dipole at the centre of the particle (see figure 2.8). To explain the origin of the force on a dipole in an electromagnetic field, the derivation of Stenholm [75, 76] and Ng [77] is followed.

For a dipole of +Q and -Q separated by $\mathbf{r} = \mathbf{r_1} - \mathbf{r_2}$ the balance between the mechanical and electromagnetic forces is given by:

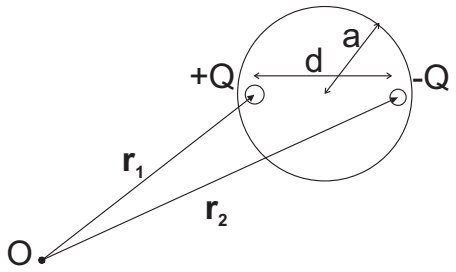

FIGURE 2.8: Schematic for Rayleigh approximation of a sphere with a radius, a, to a dipole with separation, d, and a charge of $\pm Q$.

$$m_1 \ddot{\mathbf{r_1}} = Q[\mathbf{E}(\mathbf{r_1}, t) + \dot{\mathbf{r_1}} \times \mathbf{B}(\mathbf{r_1}, t)] + \mathbf{F} \tag{2.62}$$

$$m_2 \ddot{\mathbf{r_2}} = -Q[\mathbf{E}(\mathbf{r_2}, t) + \dot{\mathbf{r_2}} \times \mathbf{B}(\mathbf{r_2}, t)] - \mathbf{F} \tag{2.63}$$

Where $m_{1,2}$ are the masses of the charge carriers, $\mathbf{E}$ and $\mathbf{B}$ are the applied electric and magnetic fields, respectively and F is the (mechanical) binding force between the two particles. The centre of mass of this dipole is:

$$\mathbf{R} = \frac{m_1}{M}\mathbf{r_1} + \frac{m_2}{M}\mathbf{r_2} \tag{2.64}$$

Where $M = m_1 + m_2$. Substituting equation 2.64 in equation 2.62 and expanding about $\mathbf{r}$:

$$\begin{aligned} m_1\ddot{\mathbf{R}} + m_r\ddot{\mathbf{r}} =& Q\{\mathbf{E}(\mathbf{R},t) + \frac{m_2}{M}\mathbf{r}.\nabla\mathbf{E}(\mathbf{R},t) \\ &+ [\dot{\mathbf{R}} + \frac{m_2}{M}\dot{\mathbf{r}}] \times [\mathbf{B}(\mathbf{R},t) + \frac{m_2}{M}\mathbf{r}.\nabla\mathbf{B}(\mathbf{R},t)]\} + \mathbf{F} + O(r^2) \end{aligned} \tag{2.65}$$

$$\begin{aligned} m_2\ddot{\mathbf{R}} - m_r\ddot{\mathbf{r}} =& Q\{\mathbf{E}(\mathbf{R},t) - \frac{m_1}{M}\mathbf{r}.\nabla\mathbf{E}(\mathbf{R},t) \\ &+ [\dot{\mathbf{R}} - \frac{m_1}{M}\dot{\mathbf{r}}] \times [\mathbf{B}(\mathbf{R},t) - \frac{m_1}{M}\mathbf{r}.\nabla\mathbf{B}(\mathbf{R},t)]\} - \mathbf{F} + O(r^2) \end{aligned} \tag{2.66}$$

Where

$$m_r = \frac{m_1 m_2}{M} \tag{2.67}$$

Adding equations 2.65 and 2.66 gives:

$$M\ddot{\mathbf{R}} = Q[\mathbf{r}.\nabla(\mathbf{E}(\mathbf{R},t) + \mathbf{v} \times \mathbf{B}(\mathbf{R},t)] + \mathbf{v} \times [\mathbf{p}.\nabla\mathbf{B}(\mathbf{R},t)] \tag{2.68}$$

Where the dipole moment of the dipole, $\mathbf{p} = Q\mathbf{r}$ and $\mathbf{v} = \dot{\mathbf{r}}$ has been used. This can be manipulated into the form shown below [76]:

$$\mathbf{F}_{e,n} = [\nabla(\mathbf{E} + \mathbf{v} \times \mathbf{B})].\mathbf{p} + \frac{d(\mathbf{p} \times \mathbf{B})}{dt} \tag{2.69}$$

The subscripts e and n refer to the force on the electron (-Q charge), nucleus (+Q charge) respectively. This is the Rayleigh force and in section 2.3.3 it is broken down into the constituent terms along single dimensions, in order to observe the effect this force will have on a gold Rayleigh particle in an evanescent field.

2.3.2 Electromagnetic description of an evanescent field

In order to simplify the Rayleigh force, and to understand its physical meaning, first the form of an evanescent wave is examined. The field in the superstrate of a single mode slab waveguide can be modelled as (see chapter 3):

$$E(x) = E_0 e^{-qx} e^{i\psi} \tag{2.70}$$

Where E_0 is the peak electric field at the waveguide-superstrate interface, x is in the direction perpendicular to the substrate-superstrate interface, positive z is in the direction of the propagation of the wave and where $\psi = \beta z - \omega t$. The intensity of a wave is given by [7]:

$$I = \frac{n_{eff} c \epsilon_0}{2} |E^2| \tag{2.71}$$

In addition the waveguide may have a propagation loss. This will introduce an extra factor of $e^{-\gamma z}$ in the field term or $e^{-2\gamma z}$ in the intensity term and I_0 and E_0 are now

defined to be at the start of the waveguides. Substituting equation 2.71 into 2.70 gives an intensity profile:

$$I_{x,z} = n_2\epsilon_0 c\frac{|E_0|^2}{2}e^{-2qx}e^{2i\psi}e^{-2\gamma z} \tag{2.72}$$

$$= I_0 e^{-2qx}e^{2i\psi}e^{-2\gamma z} \tag{2.73}$$

Where I_0 is the peak intensity at the waveguide-superstrate interface.

Lastly it is necessary to include an expression for how the field varies laterally (y dimension), as this is important in determining the lateral force on a particle. Here the approximation that the beam is Gaussian laterally in the superstrate is used. Thus in the y dimension:

$$I_y = I_0 e^{\frac{-2y^2}{\pi\omega_y^2}} \tag{2.74}$$

where ω_y is the beam radius. This approximation is improved upon in the next chapter.

2.3.3 Rayleigh forces on a nanoparticle in an evanescent wave

Using the general Rayleigh force (equation 2.69) and the electromagnetic description of the evanescent wave (equation 2.70) it is now possible to obtain the forces applied to a small particle in an evanescent wave.

By closer examination of equation 2.69 it is possible to simplify the Rayleigh force by observing that the $\mathbf{v}\times\mathbf{B}$ term is a correction to the electromagnetic field which is much smaller (by a factor of the order of v/c) than the electric field and is thus discarded [75].

2.3.3.1 The scattering force

The last term in equation 2.69 is the scattering force arising from the change in momentum of the electromagnetic wave. This scattering force is given by [77, 78]:

$$F_{scat} = \frac{n_{eff}}{6\pi c}\beta_0^4|\alpha|^2 I \tag{2.75}$$

where n_{eff} is the effective refractive index of the mode and $\beta_m(=\frac{2\pi}{n_{eff}})$.

The scattering force is therefore given as:

$$F_{scat,z} = \frac{n_{eff}k^4}{6\pi c}|\alpha|^2 I_0 e^{-2qx}e^{-2\gamma z} \tag{2.76}$$

where α is the polarisability.

2.3.3.2 The gradient and absorption forces

The first term in equation 2.69, $(\nabla \mathbf{E}).\mathbf{p}$, is the gradient or Lorentz force acting on the induced dipole. As mentioned above, $\mathbf{p}$ is the dipole moment which can be expressed as

$$\mathbf{p} = \epsilon_0 \epsilon_1 \alpha \mathbf{E} \tag{2.77}$$

where ϵ_0 is the permittivity of free space and ϵ_1 is the relative permittivity of the medium in which the dipole is embedded. In fast varying fields the dipole will lag the electric field, therefore the polarisability is complex with the real part describing the in-phase component and the imaginary part describing the component $\pi/2$ out-of phase with the electric field. The polarisability may therefore be rewritten as:

$$\alpha = \alpha' + i\alpha" = |\alpha| e^{i\theta} \tag{2.78}$$

The average force due to the first term of equation 2.69 can therefore be written as:

$$\overline{\mathbf{F}_{e,n}} = \overline{\epsilon_0 \epsilon_1 [(\nabla \mathbf{E}).\alpha \mathbf{E}]} \tag{2.79}$$

For one spatial component of a plane wave, substituting $\mathbf{E} = E_x e^{i(\phi - \omega t)}$ for the field where ϕ is the phase and using $\overline{AB} = \frac{1}{2}\Re[AB^*]$:

$$\begin{aligned}
\overline{\mathbf{F}_{e,n(x)}} &= \frac{1}{2}\epsilon_0 \epsilon_1 \Re[\frac{\partial E_x}{\partial x} e^{i(\phi-\omega t)} |\alpha^*| E_x^* e^{-i(\phi - \omega t + \theta)} + i E_x \frac{\partial \phi}{\partial x} e^{i(\phi - \omega t)} |\alpha^*| E_x^* e^{-i(\phi - \omega t + \theta)}] \\
&= \frac{1}{2}\epsilon_0 \epsilon_1 \Re[\frac{\partial E_x}{\partial x} E_x |\alpha| e^{-i\theta} + i E_x^2 \frac{\partial \phi}{\partial x} |\alpha| e^{-i\theta}] \\
&= \frac{1}{2}\epsilon_0 \epsilon_1 \Re[\frac{\partial E_x}{\partial x} E_x |\alpha| \cos\theta + E_x^2 \frac{\partial \phi}{\partial x} |\alpha| \sin\theta] \\
&= \frac{1}{2}\epsilon_0 \epsilon_1 \Re[\frac{\partial E_x}{\partial x} E_x \alpha' + E_x^2 \frac{\partial \phi}{\partial x} \alpha"]
\end{aligned} \tag{2.80}$$

Using $(\nabla E)E = \frac{1}{2}\nabla E^2$:

$$\overline{\mathbf{F}_{e,n(x)}} = \frac{1}{2}\epsilon_0 \epsilon_1 \Re[\frac{1}{2}\frac{\partial E_x^2}{\partial x}\alpha' + E_x^2 \frac{\partial \phi}{\partial x}\alpha"] \tag{2.81}$$

The other two spatial components are entirely analogous therefore the complete expression:

$$\overline{\mathbf{F}_{e,n}} = \epsilon_0 \epsilon_1 \Re[\frac{1}{4}\alpha' \nabla \mathbf{E^2} + \frac{1}{2}\alpha" \mathbf{E^2} \nabla \phi] \tag{2.82}$$

The first component of this force is one which varies proportionally to the gradient of E^2 or the intensity and is therefore termed the gradient force. The second term varies with the imaginary part of the polarisability and with the spatial variation of phase. This is called the dissipative or absorption force as it is related to the amount of radiation that the particle absorbs due to the lagging of polarisation compared to the applied field.

This gives:

$$\mathbf{F_{grad}} = \frac{1}{4}\epsilon_0\epsilon_1\alpha'\nabla|E^2| \tag{2.83}$$

$$= \frac{1}{2}\epsilon_0\epsilon_1\alpha'\nabla I \tag{2.84}$$

for the gradient force and

$$\mathbf{F_{abs}} = \frac{1}{2}\epsilon_0\epsilon_1\alpha"|E^2|\nabla\phi \tag{2.85}$$

for the absorption force.

Substituting the expression for the evanescent field including the loss (equation 2.73) into these equations gives [77]:

$$F_{grad,x} = -\frac{1}{2}\epsilon_0\epsilon_1 q\alpha' E_0^2 e^{-2qx}e^{-2\gamma z} \tag{2.86}$$

$$= -\frac{\epsilon_1}{n_{eff}c}q\alpha' I_0 e^{-2qx}e^{-2\gamma z} \tag{2.87}$$

$$F_{grad,z} = -\frac{1}{2}\epsilon_0\epsilon_1\gamma\alpha' E_0^2 e^{-2qx}e^{-2\gamma z} \tag{2.88}$$

$$= -\frac{\epsilon_1}{n_{eff}c}\gamma\alpha' I_0 e^{-2qx}e^{-2\gamma z} \tag{2.89}$$

and:

$$F_{abs,z} = \frac{1}{2}\epsilon_0\epsilon_1\beta_0\alpha" E_0^2 e^{-2qx}e^{-2\gamma z} \tag{2.90}$$

$$= \frac{\epsilon_1}{n_{eff}c}\beta_0\alpha" I_0 e^{-2qx}e^{-2\gamma z} \tag{2.91}$$

and from 2.74:

$$F_{grad,y} = -\frac{1}{2\omega_y}\epsilon_0\epsilon_1\alpha' E_0^2 e^{-2qx}e^{-2\gamma z}e^{\frac{-2y^2}{\omega_y^2}} \tag{2.92}$$

which has a maximum at $y = \pm\omega_y/2$ and thus a maximum force of:

$$F_{grad,y,max} = -\frac{\epsilon_1}{n_{eff}c\omega_y}\alpha' e^{-\frac{1}{2}} I_0 e^{-2qx}e^{-2\gamma z} \tag{2.93}$$

Thus there are gradient forces acting in the negative x-direction that will act to hold the particle transversely to the waveguide, in the y direction that will act to restore the particle laterally above the waveguide, and in the negative z direction that will act to slow the particle down.

In addition there are scattering (equation 2.76) and absorption forces (equation 2.90) that act to accelerate the particle along the direction of the propagation of light.

2.3.4 Polarisability of gold

The above theory has shown how polarisability, α is an important parameter for the trapping and propulsion of Rayleigh particles. In this section the wavelength dependence of the permittivity of gold, the Clausius-Mossotti factor and the effective volume of a spherical particle will be examined. This is of interest as the permittivity of gold is highly dependent on wavelength and thus the ease of trapping of a particle is strongly dependent on the wavelength.

As stated above the polarisability of a particle is given as [70]:

$$\alpha = 3V\frac{\epsilon_1 - \epsilon_2}{\epsilon_1 + 2\epsilon_2} \tag{2.94}$$

where ϵ_2 is the complex permittivity of the particle and the factor $\frac{\epsilon_1-\epsilon_2}{\epsilon_1+2\epsilon_2}$ is termed the Clausius-Mossotti factor.

2.3.4.1 Wavelength dependence of permittivity of gold

The wavelength dependence of the permittivity of gold is shown below in figure 2.9. The crosses show experimental data from [79] whereas the line shows a cubic spline fit to the data and this fit is used to obtain the values of ϵ used for the results in this project. Although there are various other papers published with data on the permittivity of gold [80, 81], [79] was chosen being the most often cited in this field.

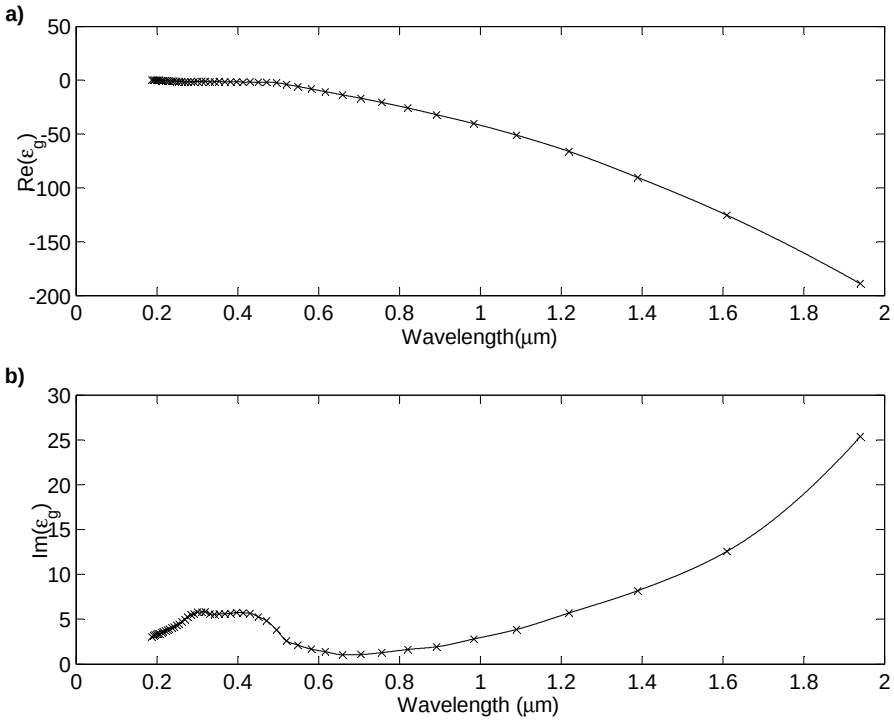

FIGURE 2.9: The a) real and b) imaginary parts of gold permittivity.

For the experiments the superstrate in which the particles are held is water and for this a real permittivity of $1.33^2 = 1.77$ is used. Recall that the polarisability of a particle is proportional to the Clausius-Mossotti factor and the volume (equation 2.94). Figure 2.10 shows the wavelength dependence of the Clausius-Mossotti factor, using the data shown in figure 2.9.

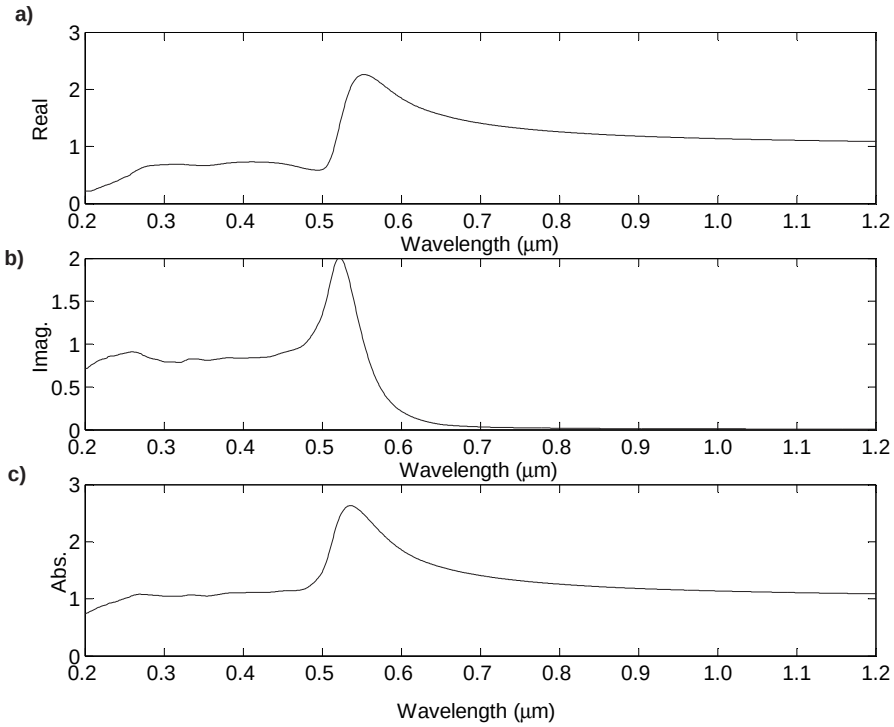

FIGURE 2.10: The a) real and b) imaginary parts and the c) absolute value of the Clausius-Mossotti factor.

2.3.4.2 Effective volume of gold particle

The volume that should be used to calculate the polarisability of a sphere is dependent on the absorption of light by the particle. This factor is described by the penetration depth, δ, given by

$$\delta = \frac{\lambda}{2\pi Im(\varepsilon_g)} \tag{2.95}$$

Figure 2.11 shows this penetration depth as a function of wavelength for gold. Thus at a wavelength of $1\mu m$ the penetration depth given by of the light is only 55nm. It is clear therefore that a constant electric field cannot act equally on the centre of a 250nm gold particle as at the edge. A modification to the standard $\frac{4}{3}\pi a^3$ equation for the volume of a sphere is therefore used given as [36]:

$$V = 4\pi \int_0^a r^2 e^{(r-a)/\delta} dr \tag{2.96}$$

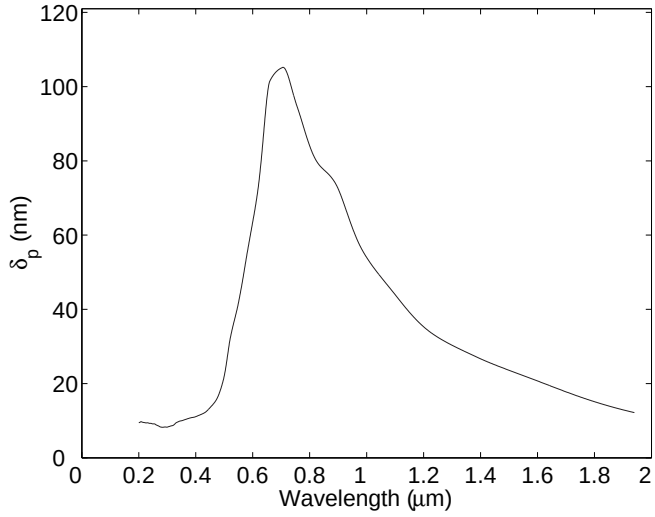

FIGURE 2.11: The penetration depth of gold as a function of wavelength.

It should be noted that the predicted velocity of particles is strongly affected by this value of the skin depth, δ. As is seen by equation 2.95, δ is inversely proportional to $\mathrm{Im}(\varepsilon_g)$. However $\mathrm{Im}(\varepsilon_g)$ has been reported as ranging from 3.6-5.9 for bulk gold [79, 80, 81] at 1066nm (and is not reported experimentally for particles in the relevant size range and wavelength).

The effective volume used in this thesis is given below in figure 2.12 for three sizes.

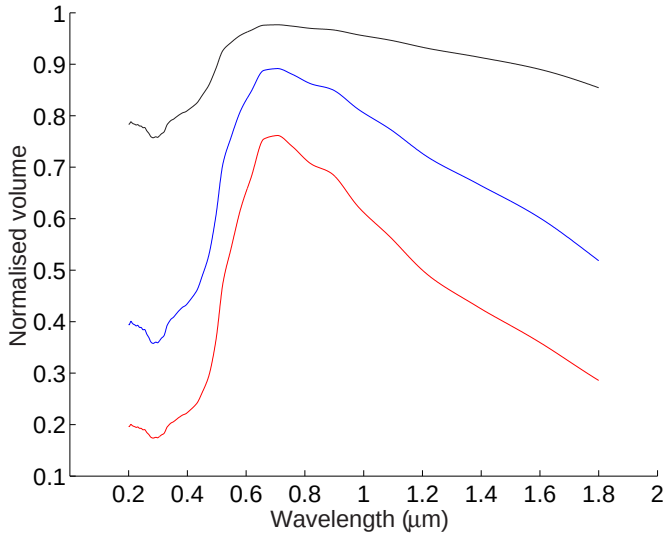

FIGURE 2.12: The normalised effective volume of a gold sphere of radius a) 10nm (■), b) 50nm (■) and c) 125nm (■). The volumes are normalised to the volume of a particle of the same radius with infinite penetration depth. These are $4.1 \times 10^{-24} m^3$, $4.7 \times 10^{-22} m^3$ and $6.2 \times 10^{-21} m^3$ respectively.

By multiplying the Claussius-Mossotti factor and the effective volume the polarisability of a particle is obtained and is shown in figure 2.13. The peak values to which the values in the graph are normalised are shown in table 2.1.

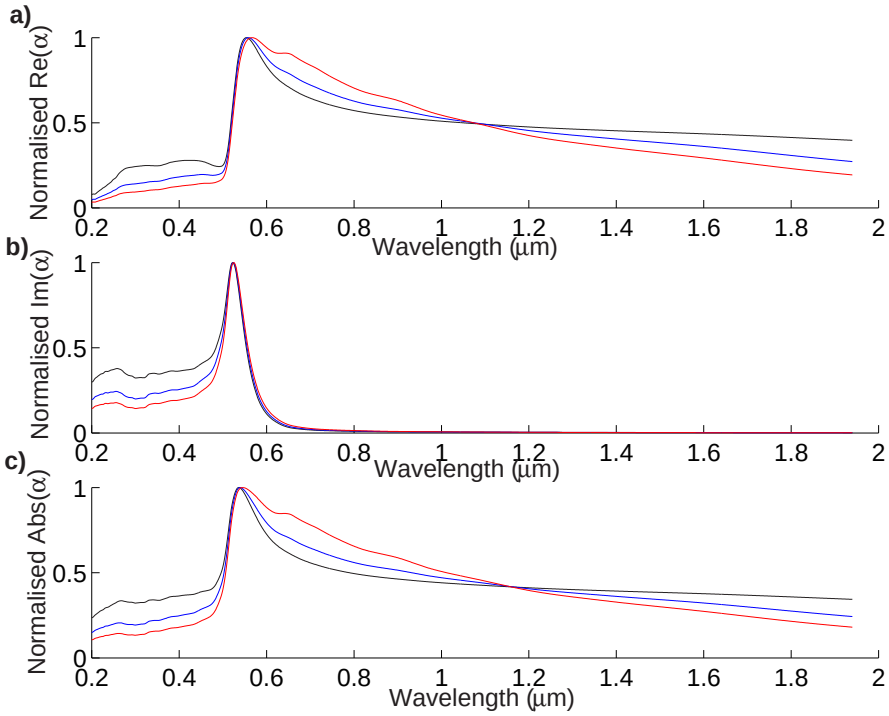

FIGURE 2.13: The normalised polarisabilities of a gold sphere of radius 10nm (■), 50nm (■) and 125nm (■). The graphs are normalised to the peak parts of polarisability.

Size (nm)	Real (m^3)	Imaginary (m^3)	Absolute (m^3)
10	2.7×10^{-23}	2.3×10^{-23}	3.1×10^{-23}
50	2.7×10^{-21}	2.2×10^{-21}	3.1×10^{-21}
125	3.1×10^{-20}	2.4×10^{-20}	3.4×10^{-20}

TABLE 2.1: Peak values of polarisability for a 10, 50 and 125nm gold particle.

Variable	symbol	value	units
Superstrate index	n_c	1.33	-
Gold index	n_g	0.2579+6.9679i	-
Peak intensity	I_0	6	GW/m^2
Waveguide effective index	n_{eff}	1.512	-
Modal power	P	1	W
Waveguide loss	γ	2	dB/cm
Beam waist	w	6	μm

TABLE 2.2: Constant used for predicting optical forces.

2.3.5 Theoretical results for optical Rayleigh forces

Using the forces derived above in equations 2.87 to 2.93 it is possible to plot the magnitudes of these forces for some typical conditions. The values that are used are listed in table 2.2.

Figure 2.14a shows the optical forces using these parameters and shows that the forces are all very small, with the maximum predicted force for any of the components being

about 100pN. However the forces are calculated for particles of size up to 0.5μm. To give some concept of this force if it were scaled up linearly with volume to a particle of size 1cm this would represent a force of 800N and, unrestrained, would cause an acceleration of 8km/s^2.

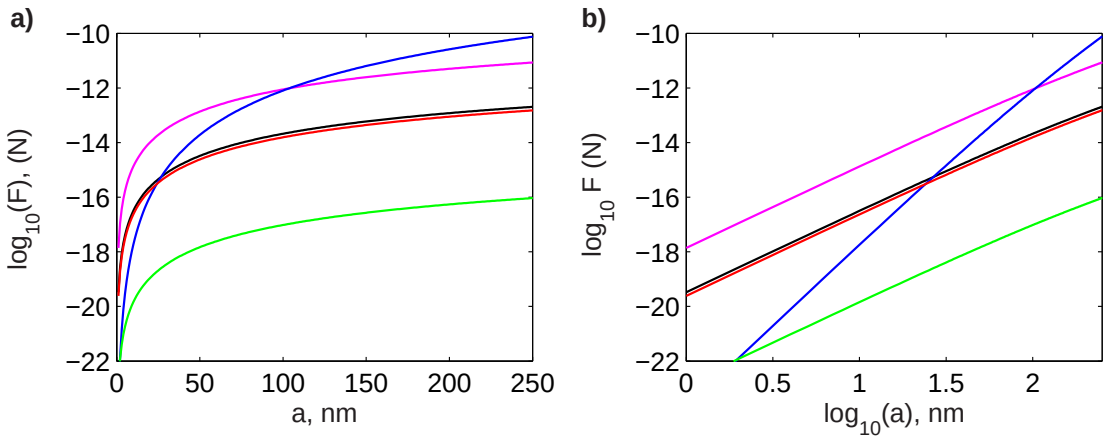

FIGURE 2.14: a) The maximum Rayleigh forces on a particle of radius, a in the evanescent field of a channel waveguide with a 1W modal power and assuming a surface intensity of 6×10^9 at a wavelength of 1066nm. The lines represent the following forces: transverse gradient, (■), lateral gradient, (■), scattering (■), absorption, (■) and axial gradient (■). b) As with a) but plotted on a log-log scale.

More importantly however figure 2.14 allows a prediction concerning which are the more important forces to be optimised and what trends would be expected for particles of different sizes. For example, the smallest force for most of the size range considered is the gradient force in the axial (z) direction. This was the force caused by a 2dB/cm propagation loss in the waveguide. As shall be shown in chapter 5 this was greater than the loss encountered for the waveguides. The fact that this force is approximately four orders of magnitude smaller than the scattering force (which also acts in the axial direction), suggests it may be disregarded. The absorption force on gold particles is also much smaller, almost two orders of magnitude, hence the scattering force is the dominant axial force. Figure 2.14a shows that the gradient force in the transverse, x, direction is almost two orders of magnitude larger than the lateral, y, dimension.

Figure 2.14b illustrates some of the important points regarding the trends of the forces with respect to the radius of the particle. The slope (gradient) of the scattering force is approximately 6 decades/decade for lower values of a, but will approach a slope of 4 decades/decade at higher values. At smaller radii this rate is due to the force being proportional to square of the polarisability, which itself is proportional to the cube of the radius. The reduction in slope is due to the penetration depth of the gold reducing the polarisability to a squared relationship with radius. The slopes (gradients) of all the other forces are 3 decades/decade due to their being proportional to a component of the polarisability, and this decreases to 2 decades/decade for larger particles.

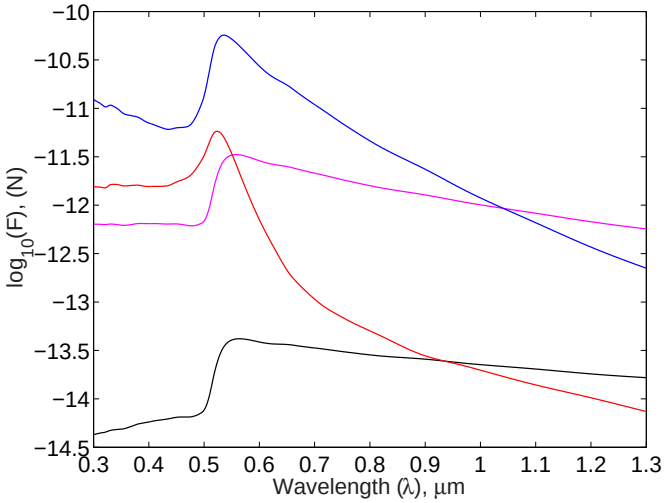

FIGURE 2.15: a) The maximum Rayleigh forces on a 100nm radius, gold particle in the evanescent field of a channel waveguide as a function of the wavelength of light used. A 1W modal power and a surface intensity of 6×10^9W/m^2 is assumed. The lines represent the transverse gradient, (■), lateral gradient, (■), scattering (■) and absorption, (■) forces.

Figure 2.15 shows how the Rayleigh forces vary with wavelength for a gold particle of radius 100nm. The forces all have a maximum at a wavelength of approximately 550nm, due to the gold plasmon resonance. It also shows that the two gradient forces have the same form. Although the absolute value of polarisability decreases at a similar rate to the real part, as the scattered force is proportional to the square of polarisability, this decreases more rapidly with wavelength than the gradient forces. The absorption force decays more rapidly with wavelength due to it being proportional to the imaginary part of polarisability.

It is important to note here that there are caveats to the interpretation of these graphs. The limits here are threefold: the limit of applicability of Rayleigh theory, the limit of the theoretical model, and the limits to the accuracy of the parameters in table 2.2. As was discussed in section 2.2.2.2 Rayleigh and Mie theory start to diverge at radii of around 70nm for gold and 120nm for latex particles. Despite this, it is not anticipated that the forces will be highly inaccurate thus physically reasonable conclusions about the relative magnitudes of the forces can be drawn. The effect of the evanescent field excitation and the parameters used will be considered in more detail in chapter 4.

2.4 Summary and conclusions

This chapter has derived and discussed the two main theories that govern the interaction of light with spheres of diameter comparable to and smaller than the wavelength of light. It has shown that particles with size comparable to the wavelength of light (and thus governed by Mie theory) have multipole resonances that must be taken into account.

Evanescent wave excitation for particles of this size is much more complex and is the subject of further work. In a plane wave, however, the resonances of latex particles were shown to be greatly damped in a medium of water, compared to those of an air medium.

The Rayleigh theory was compared to the Mie theory and, for the smaller gold particles used, has been shown to be a good approximation for particle sizes up to 140nm. Using Rayleigh theory all of the physical phenomena and the basic trends have been demonstrated with this simpler but physically more appealing theory. It was shown that Rayleigh theory can be separated into three forces: a gradient force, that acts to force particles up an intensity gradient, and an absorption and scattering force, that will accelerate particles in the direction of the propagating evanescent wave. The gradient force is the force that acts to trap particles above the waveguide and is substantially greater in the transverse direction compared to the lateral direction. This is due to the evanescent wave decaying much more rapidly away from the surface than it does in the lateral dimension that was approximated to a Gaussian profile. The gradient force in the axial direction, due to the loss of the waveguide, was much smaller than that of the scattering force and is therefore omitted.

The scattering force was shown to increase much more rapidly with radius, due to its dependence on $|\alpha^2|$ and was shown to be the dominant axial force for particles larger than a few nanometers radius. The polarisability, which is complex for gold particles, and was shown to be a common factor to all the optical forces, is dependent not only on the volume of the particle but also its complex permittivity. The permittivity of gold varies greatly in the optical domain, with the real part peaking at a wavelength of approximately 550nm and the imaginary part at approximately 530nm. The imaginary part of the permittivity also defines directly the penetration depth of light into the particle, and this value was critical in calculating the effective volume to be used for the calculation of the polarisability.

Chapter 3

Theory and Modelling of Ion-Exchanged Optical Waveguides

3.1 Introduction

The design of the waveguide used to trap and propel particles is critical. By modelling the waveguides used it is shown that theoretically they may be optimised for the application of evanescent wave trapping. The basic electromagnetic theory of a three-layer asymmetric slab waveguide is described as a basis for explaining multilayer slab waveguide theory using a transfer matrix approach. An approximation is then used to make the method applicable to a channel waveguide. In addition the basic diffusion theory is derived, to understand the form of the refractive index profile expected. The results from the analytical method are compared to a commercial beam propagation method (BPM) package and shown to give good agreement allowing analysis of more complex structures relatively simply using this BPM package with confidence. The design parameters of the waveguide are then investigated to see how they affect the expected trapping ability of the waveguide and the optimum conditions are obtained.

3.2 Theory of optical waveguides

3.2.1 Introduction

This section describes four distinct methods of analysis of waveguiding in a guide having a refractive index profile that is constant along the direction of propagation. Firstly the three-layer slab index method, used to describe a slab of finite depth extending

infinitely in the other two dimensions and sandwiched between two semi-infinite slabs, is discussed. This is extended to a multilayer case where the middle slab can be replaced by any number of slabs of differing indices allowing a more complex planar model to be described. To allow channel waveguides to be modelled the effective index method is described. Finally the theory behind the beam propagation method (BPM) for which a commercial package is used which allows a greater range of refractive index profiles and waveguide structures to be modelled is briefly described.

3.2.2 Three-layer planar waveguides

Although this model is extended to the case of a multilayered waveguide below where a gradient index waveguide may be approximated in a step-wise fashion, it is worth first considering the simplest case of a homogeneous three-layer slab waveguide. Many of the fundamental rules to produce optimised waveguides apply equally well to three-layer waveguides as to more complex models. In addition, the three-layer model is used directly in the effective index method (section 3.2.4) which allows an estimation of the properties of a channel waveguide. The derivation of this model also helps describe the method and the notation for the more complex multilayer method.

In this model three parallel layers with real refractive indices, n_1, n_2 and n_3 are used. The two outer layers continue to infinity in the perpendicular direction, x, whilst the inner layer has thickness, d. The three layers all extend infinitely in the z and y dimensions, as shown in figure 3.1. The direction of propagation of the light is in the positive z direction.

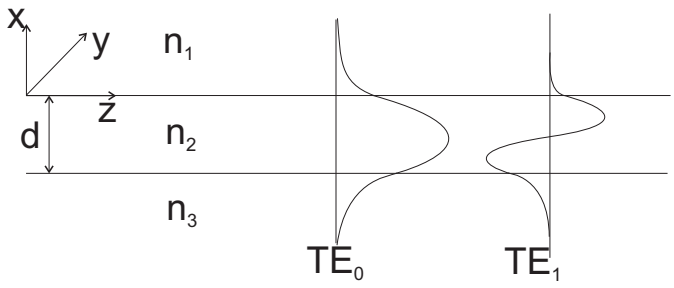

FIGURE 3.1: Model of a slab waveguide with examples of the fundamental and first order transverse electric modes in the waveguide schematically shown.

In order to anlayse this model the wave equation, which must be satisfied at every point in space and time, is applied. This is derived from Maxwell's equations and the general materials' equations and applies to the case of time-harmonic fields. The current density, J, and charge density, ρ, are both set at zero for dielectric waveguides. The homogenous

wave equation states that [82]:

$$\nabla^2\mathbf{E}(\mathbf{r},t) - \frac{\mu\epsilon}{c^2}\ddot{\mathbf{E}}(\mathbf{r},t) = 0 \tag{3.1}$$

$$\nabla^2\mathbf{H}(\mathbf{r},t) - \frac{\mu\epsilon}{c^2}\ddot{\mathbf{H}}(\mathbf{r},t) = 0 \tag{3.2}$$

where **E** and **H** are the electric and magnetic fields, **r** is the position vector, μ and ϵ are the permeability and permittivity of the material and are assumed isotropic here and c is the speed of light in vacuum. A general monochromatic wave has an electric field of the form [82]:

$$\mathbf{E} = \Re\{\mathbf{E}_0 \exp[-i(\mathbf{k}.\mathbf{r} + \delta)]exp(i\omega t)\} \tag{3.3}$$

Here $\mathbf{E}_0$ is the amplitude of the field, δ describes the initial phase and $\Re\{...\}$ represents the real part and demonstrates that the field has a purely real value. The $exp(i\omega t)$ factor is the fast time variation of the wave at a fixed point in space where $\omega(= 2\pi f)$ is the angular frequency. The time variation, initial phase and the real part notation will all be omitted for clarity in all further analyses. **k** is the wave vector which has a magnitude equal to $\frac{n\omega}{c}$, where n is the refractive index, which describes the ratio of the speed of light in a vacuum to that in the material.

It is convenient here to apply a Cartesian coordinate system due to the boundary conditions of the model in figure 3.1. Thus **k** and **r** are written as:

$$\mathbf{k} = k_x\hat{\mathbf{x}} + k_y\hat{\mathbf{y}} + k_z\hat{\mathbf{z}} \tag{3.4}$$

$$\mathbf{r} = x\hat{\mathbf{x}} + y\hat{\mathbf{y}} + z\hat{\mathbf{z}} \tag{3.5}$$

A condition of a mode is that it should maintain its transverse distribution whilst propagating in the z direction thus there is a dependence on z in the form $e^{-i\beta z}$. This gives a solution with form:

$$\mathbf{E(r)} = \mathbf{E}(x,y)e^{-i\beta z}e^{i\omega t} \tag{3.6}$$

where β is the propagation constant and is related to the effective refractive index, n_{eff} by the relationship:

$$\beta = k_0 n_{eff} \tag{3.7}$$

In addition $\mathbf{E}(x,y)$ should not be a function of y as the slab is invariant in that dimension, thus is replaced by $\mathbf{E}(x)$. Substituting equation 3.6 into equation 3.1 gives:

$$\frac{\partial^2}{\partial x^2}\mathbf{E}(x) + (k_0^2 n_i^2 - \beta^2)\mathbf{E}(x) = 0, \text{ i=1, 2 or 3} \tag{3.8}$$

where $k_0^2 = \omega^2\mu_0\epsilon_0$. The assumption has been made here that the material is non-magnetic ($\mu_r = 1$).

This form of differential equation gives rise to two types of solution. If the factor $k_0^2 n_i^2 - \beta^2$ is positive the solution is of the sinusoidal form, whereas if $k_0^2 n_i^2 - \beta^2$ is negative the

solution is of the exponential form. In order to limit the energy flow the fields in the outer two media must vanish to zero. Thus there is the requirement that $k_0^2 n_i^2 - \beta^2 < 0$ for the outer media and that the exponents must also be negative i.e. the field should approach zero at x=$\pm\infty$. In order that the intermediate layer satisfies the field boundary conditions the internal layer must have a sinusoidal form.

To simplify the situation (when matching boundary conditions) the fields are separated into a transverse electric (TE) wave (which has non-zero field components of E_y, H_z and H_x only) and a transverse magnetic (TM) wave (with non-zero field components of H_y, E_z and E_x only). As these waves are mutually orthogonal any polarisation can be expressed as a linear combination of the two, thus this manipulation in no way limits the model.

For the case of TE modes, by solving equation 3.8 and applying the boundary conditions, that the tangential electric and magnetic field should be continuous across the boundaries, the electric field in each of the three media is obtained as follows [83]:

$$E_y = C\exp[-jk_z z]\begin{cases} \exp(-h_1 x) & 0 \le x \le \infty \\ \{\cos(h_2 x) - \frac{h_1}{h_2}\sin(h_2 x)\} & -d \le x \le 0 \\ \{\cos(h_2 d) - \frac{h_1}{h_2}\sin(h_2 d)\}\exp[h_3(x+d)] & -\infty \le x \le -d \end{cases} \tag{3.9}$$

where

$$h_1 = \sqrt{\beta^2 - n_1^2 k_0^2} \tag{3.10}$$

$$h_2 = \sqrt{n_2^2 k_0^2 - \beta^2} \tag{3.11}$$

$$h_3 = \sqrt{\beta^2 - n_3^2 k_0^2} \tag{3.12}$$

and C is a constant that is dependent on the power carried by the mode. It is noted here that penetration depth, δ in the superstrate of a waveguide is given by $1/h_1$. This is the distance by which the field has fallen to e^{-1} and the intensity has fallen to e^{-2} of their respective peak values at the superstrate/waveguide interface.

In solving the boundary equations one extra equation is obtained which may be used to solve for β. This is:

$$\frac{h_3}{h_2}(h_2\cos h_2 d + h_1 \sin h_2 d) = h_2 \sin h_2 d - h_1 \cos h_2 d \tag{3.13}$$

This may be solved by manipulation into the form [83]:

$$0 = h_2 d - \arctan\frac{h_1}{h_2} - \arctan\frac{h_3}{h_2} - m\pi \tag{3.14}$$

In this equation the right hand side can be iteratively evaluated for a certain value of β and m (given the refractive indices of the layers, the thickness of the middle layer and the wavelength of light used). The physical interpretation of m is as the mode number whose solution is being found, viz figure 3.1 (i.e. for m=0 the solution of the effective index of the fundamental mode). If there is no solution for this then there cannot be a solution for higher order modes. Therefore this function is solved for values of m starting at zero and incrementing by one until no solution is found.

From equation 3.9 H_x and H_z can then be obtained directly by the relationship [83]:

$$-j\omega\mu\mathbf{H} = \nabla \times \mathbf{E} \tag{3.15}$$

These give:

$$H_x = \frac{k_z}{\omega\mu_0} C \exp[-jk_z z] \begin{cases} \exp(-h_1 x) & 0 \leq x \leq \infty \\ \{\cos(h_2 x) - \frac{h_1}{h_2}\sin(h_2 x)\} & -d \leq x \leq 0 \\ \{\cos(h_2 d) - \frac{h_1}{h_2}\sin(h_2 d)\}\exp[h_3(x+d)] & -\infty \leq x \leq -d \end{cases} \tag{3.16}$$

and

$$H_z = C \exp[-jk_z z] \begin{cases} \{-h_1 \exp(-h_1 x)\} & 0 \leq x \leq \infty \\ \{h_2 \sin(h_2 x) + h_1 \cos(h_2 x)\} & -d \leq x \leq 0 \\ \{\cos(h_2 d) - \frac{h_1}{h_2}\sin(h_2 d)\}h_3 \exp[h_3(x+d)] & -\infty \leq x \leq -d \end{cases} \tag{3.17}$$

The fields in the case of TM modes are solved in exactly the same way, with the only difference being in the boundary conditions.

3.2.3 Multilayered waveguides

The previous section examined the solution of the fields for the case of a three-layer structure. The analysis is now extended to more accurately analyse the refractive index profile used in this project. The following analysis allows the profile to be of any form by using an unlimited number of layers (limited only by computational time). The method used is a transfer matrix approach where the coefficients of the phase and amplitude of the forwards and backwards travelling wave are matched. Knowledge that the outermost layers must be of evanescent form provides sufficient conditions to recursively solve for the effective index and therefore the fields, as before.

The model used is shown in figure 3.2 below and shows an example with M layers. The layers 1,2,...,M have refractive indices $n_1, n_2, ..., n_M$ and thicknesses of ∞, d_2, d_3,..., d_{M-1}, ∞ respectively. The x-axis is again defined as perpendicular to the layers with the origin at interface 1 and direction into the second layer. The wave is again propagating in the (positive) z direction. The interfaces have positions given by:

$$x_m = \begin{cases} 0 & \text{m=1} \\ -\sum_{i=2}^{m} d_i & \text{m=2:M} \end{cases} \tag{3.18}$$

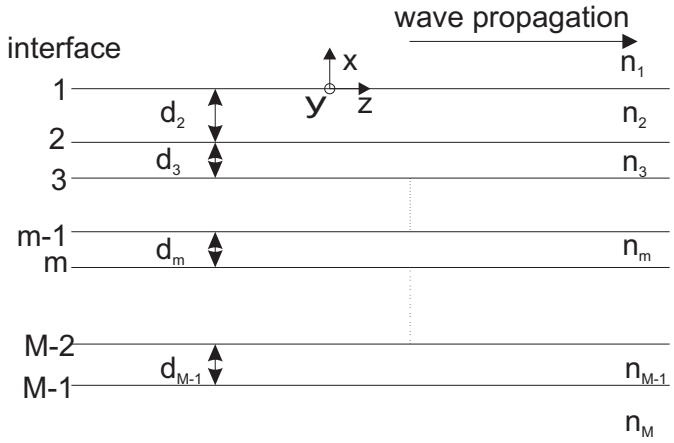

FIGURE 3.2: Model of a slab waveguide with M layers.

This analysis follows the method of Walpita [84] with different notations and axes. Here the case of the TE modes is solved. The adjustment for TM modes is explained at the end of the analysis.

For each layer, m, K is given by:

$$K_{z,m} = i\beta = ik_0 n_m \cos\theta \tag{3.19}$$

$$K_{x,m} = k_0 n \sin\theta = (\beta^2 - k_0^2 n_m^2)^{1/2} \tag{3.20}$$

where β is the wave vector, $k_0 (= 2\pi/\lambda)$, the free space wave vector, n, the refractive index as before and θ being the angle that the notional 'bouncing' ray makes with the z-axes.

To satisfy Maxwell's equations:

$$\nabla \times E_{p,m} = \sum_q -i\omega\mu_{pq,m}\mu_0 H_{q,m} \tag{3.21}$$

$$\nabla \times H_{p,m} = \sum_q i\omega\epsilon_{pq,m}\epsilon_0 E_{q,m} \tag{3.22}$$

where the subscripts, q and m refer to orthogonal directions perpendicular to propagation. In the TE case again the same three non-zero components of the field, E_y, H_z

and H_x are present. All layers are assumed non-magnetic, hence $\mu_{mpq} = 1$ and isotropic ($\epsilon_{pqm} = \epsilon_m$). This gives the field components:

$$E_{y,m} = A_m \exp[-K_{x,m}(x - x_{m-2})] + B_m \exp[K_{x,m}(x - x_{m-2})] \tag{3.23}$$

$$i\omega\mu_0 H_{z,m} = -A_m K_{x,m} \exp[-K_{x,m}(x - x_{m-2})] + B_m K_{x,m} \exp[K_{x,m}(x - x_{m-2})] \tag{3.24}$$

$$i\omega\mu_0 H_{x,m} = A_m K_{z,m} \exp[-K_{x,m}(x - x_{m-2})] + B_m K_{z,m} \exp[K_{x,m}(x - x_{m-2})] \tag{3.25}$$

where A and B are the coefficients representing the magnitude of the forward (positive x direction) and backward (negative x direction) travelling wave respectively.

As can be seen from equations 3.23 and 3.25, E_y and H_x are proportional to each other. Therefore in order to satisfy these three equations only the first two fields are required. Writing these fields in matrix form gives:

$$\begin{bmatrix} E_{y,m} \\ i\omega\mu_0 H_{z,m} \end{bmatrix} = \begin{bmatrix} \exp[-K_{x,m}(x - x_{m-2})] & \exp[K_{x,m}(x - x_{m-2})] \\ -K_{x,m} \exp[-K_{x,m}(x - x_{m-2})] & K_{x,m} \exp[K_{x,m}(x - x_{m-2})] \end{bmatrix} \begin{bmatrix} A_m \\ B_m \end{bmatrix} \tag{3.26}$$

By balancing these fields at the interface (x=x_m) the following condition is obtained:

$$\begin{bmatrix} E_{y,m}(x_m) \\ H_{z,m}(x_m) \end{bmatrix} = \begin{bmatrix} E_{y,m+1}(x_m) \\ H_{z,m+1}(x_m) \end{bmatrix} \tag{3.27}$$

At the interface 1:

$$\begin{bmatrix} 1 & 1 \\ -K_{x,1} & K_{x,1} \end{bmatrix} \begin{bmatrix} A_1 \\ B_1 \end{bmatrix} = \begin{bmatrix} 1 & 1 \\ -K_{x,2} & K_{x,2} \end{bmatrix} \begin{bmatrix} A_2 \\ B_2 \end{bmatrix} \tag{3.28}$$

and at interface 2:

$$\begin{bmatrix} \exp[-K_{x,2}d_1] & \exp[K_{x,2}d_1] \\ -K_{x,2} \exp[-K_{x,2}d_1] & K_{x,2} \exp[K_{x,2}d_1] \end{bmatrix} \begin{bmatrix} A_2 \\ B_2 \end{bmatrix} = \begin{bmatrix} 1 & 1 \\ -K_{x,3} & K_{x,3} \end{bmatrix} \begin{bmatrix} A_3 \\ B_3 \end{bmatrix} \tag{3.29}$$

By manipulation and substitution it is seen that:

$$\begin{bmatrix} A_3 \\ B_3 \end{bmatrix} = \begin{bmatrix} 1 & 1 \\ -K_{x,3} & K_{x,3} \end{bmatrix}^{-1} \begin{bmatrix} \exp[-K_{x,2}d_1] & \exp[K_{x,2}d_1] \\ -K_{x,2} \exp[-K_{x,2}d_1] & K_{x,2} \exp[K_{x,2}d_1] \end{bmatrix} \begin{bmatrix} 1 & 1 \\ -K_{x,2} & K_{x,2} \end{bmatrix}^{-1} \begin{bmatrix} 1 & 1 \\ -K_{x,1} & K_{x,1} \end{bmatrix} \begin{bmatrix} A_1 \\ B_1 \end{bmatrix} \tag{3.30}$$

This process can be repeated for all the interfaces such that a transfer matrix is obtained. This matrix relates the forward and backward travelling constants in the superstrate to

the substrate as follows:

$$\begin{bmatrix} A_M \\ B_M \end{bmatrix} = \begin{bmatrix} a & b \\ c & d \end{bmatrix} \begin{bmatrix} A_1 \\ B_1 \end{bmatrix} \tag{3.31}$$

The boundary conditions are now applied (namely that the waves in the superstrate and substrate be evanescent). This implies that there can be no forward travelling wave in the superstrate (i.e. $A_1 = 0$) and no backward travelling wave in the substrate (i.e. $B_M = 0$). This gives

$$\begin{bmatrix} A_M \\ 0 \end{bmatrix} = \begin{bmatrix} a & b \\ c & d \end{bmatrix} \begin{bmatrix} 0 \\ B_1 \end{bmatrix} \tag{3.32}$$

which can only be solved if

$$d = 0. \tag{3.33}$$

It is this factor, d, therefore that is iteratively solved for. As only the inverse of 2×2 matrices are required this method is not excessively computationally demanding.

In order to modify the equations to solve the case of TM modes, the only change that is required is that $K_{x,m}$ should be replaced by $K_{x,m}/n_m^2$ when *not* within an exponential term.

3.2.4 Effective index method

The effective index method is a simple, approximate method that aims to make the slab waveguide approach applicable to channel waveguides. The method is described and reviewed in [85] and is shown below in figure 3.3. The effective indices of the slab waveguide (single or multilayer) are found as described above. The other dimension that is normal to the propagation direction (y in this model) is then modelled as a symmetric slab waveguide. The slab waveguide used for this method consists of two semi-infinite slabs with refractive indices of the substrate either side of a slab with effective index as calculated by the multilayer/slab waveguide method. In addition, the polarisations used in the calculations of the effective indices should be switched between the two (due to the evaluated dimension being orthogonal) however this is assumed to have negligible effect in the calculations below (see section 3.5.4.2).

The theory for this method has already been shown in the three-layer slab waveguide model (section 3.2.2).

3.2.5 Beam propagation method

The fundamental difference in application between the beam propagation method (BPM) and the methods described above is that the BPM method requires a starting field as an input. This could be, for example, a Gaussian beam from a fibre. This input field

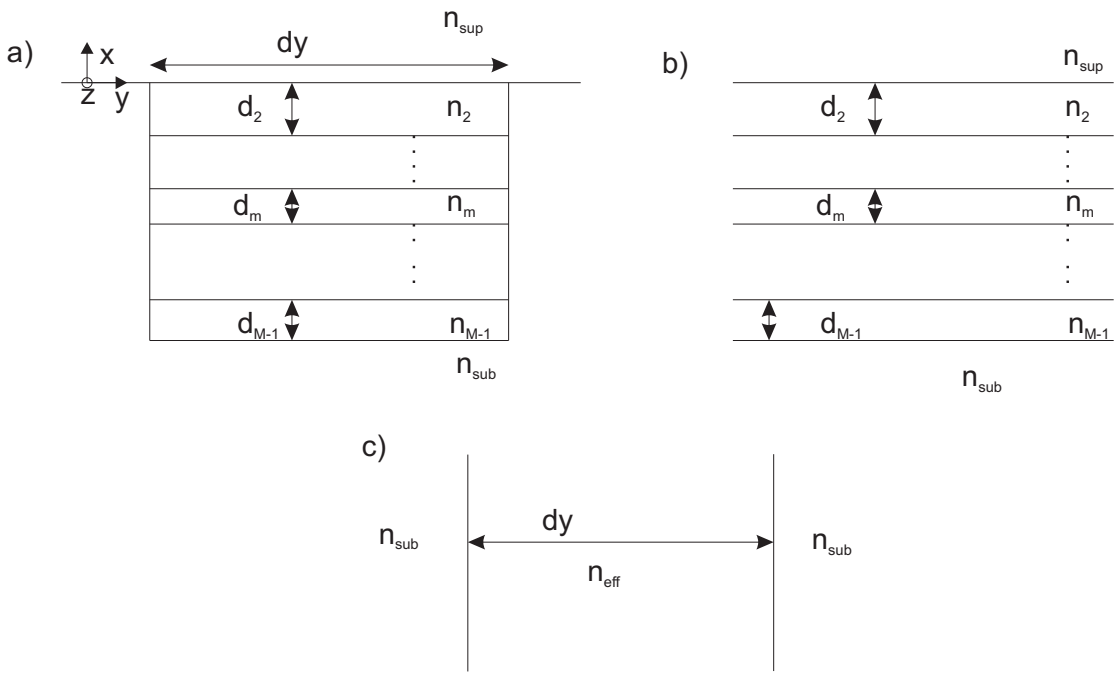

FIGURE 3.3: The effective index method; a) the refractive index model, b) first find effective indices of multilayer slab structure, c) replace the middle section with the effective index and find the new effective index.

is carried through the defined refractive index distribution and the field calculated at regular steps in the z-direction. Due to this propagation of the beam in finite steps of z the solutions are not exact (although can be *very* accurate) and (generally) the computational time required is longer.

To carry out this analysis a commercial software package, Beamprop, is used. Unfortunately due to the software being proprietary, not all details of the package are explained. However the fundamental theory on which it is based is well known and is explained below.

The method starts as before with the monochromatic wave (or Helmholtz) equation, see equation 3.1. Here it is written as:

$$\frac{\partial^2\phi}{\partial x^2} + \frac{\partial^2\phi}{\partial y^2} + \frac{\partial^2\phi}{\partial z^2} + k(x,y,z)^2\phi = 0 \tag{3.34}$$

where ϕ is the field. The substitution:

$$\phi(x,y,z) = u(x,y,z)e^{i\beta z} \tag{3.35}$$

is now made where $\beta = k_0 n_{eff}$ as before. This substitution uses the fact that the fastest varying component of equation 3.34 is the phase variation with z. It gives [86]:

$$\frac{\partial^2 u}{\partial z^2} + 2i\beta\frac{\partial u}{\partial z} + \frac{\partial^2 u}{\partial x^2} + \frac{\partial^2 u}{\partial y^2} + (k^2 - \beta^2)u = 0 \tag{3.36}$$

It is now assumed that the variation of u with z is slow enough so as to make the first term above, zero. This is effectively a paraxial approximation and gives:

$$\frac{\partial u}{\partial z} = \frac{i}{2\beta}[\frac{\partial^2 u}{\partial x^2} + \frac{\partial^2 u}{\partial y^2} + (k^2 - \beta^2)u] = 0 \tag{3.37}$$

This is the fundamental equation for the BPM method; by separating out the fast varying phase the assumption can be made that as the propagation is principally in the z direction, the field will not change rapidly in this direction. The effect of this assumption is to vastly reduce the processing time required (as iteration or eigenvalue solutions are not required). The disadvantages are due to the limitations the assumption places on the model. These are principally that paraxial rays should be used, only forward travelling waves can be modelled and that polarisation effects are not modelled.

Beamprop has produced partial solutions to all of these problems at an additional computational cost, but as this project rarely requires it these are not used in the analyses.

3.3 Diffusion theory

Having obtained the methods by which a refractive index profile may be analysed, the expected form of this refractive index profile is now considered.

Ion-exchanged waveguides are used throughout this thesis, where the ions enter the glass substrate by diffusion. The refractive index distribution to be modelled may therefore be determined by considering diffusion theory. Diffusion is governed by two central equations (Fick's first and second laws) [87].

Fick's first law states that if an interface with differing concentrations of mobile particles of the same type either side of the interface, C_1 and C_2 (figure 3.4a), then, if the particles' motion is random there will be a flow of particles from the higher to the lower concentration side. This flow (or flux) will be proportional to the concentration difference. This is more formally stated as:

$$F = -D\frac{\partial C}{\partial x} \tag{3.38}$$

where F is the flux of particles and D is the diffusion constant that takes into account many other factors such as temperature, the energy required to move the particle across the boundary, the frequency with which particles will attempt to move across the boundary etc.

Although this equation is universally applicable under the condition of steady-state, this is rarely the case. Thus an equation is required for the time-dependent case. To derive

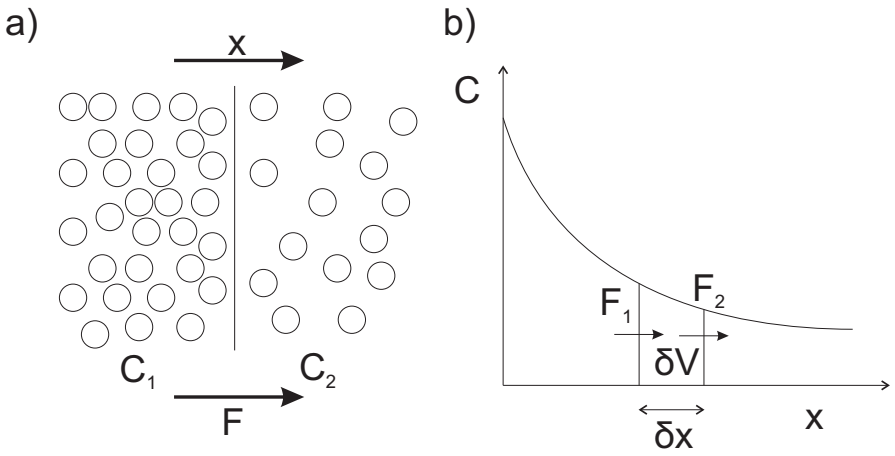

FIGURE 3.4: Schematic diagrams showing a) interpretation of Fick's first diffusion law and b) derivation of Fick's second law.

this an elemental volume, δV, in a planar structure with area, A is considered (figure 3.4b).

By conservation of matter:

$$\Delta C_V A \Delta x = (F_1 - F_2) A \Delta t \tag{3.39}$$

where C_V is the concentration in volume, δV. For very small Δx:

$$F_2 = F_1 + \frac{\partial F}{\partial x} \Delta x \tag{3.40}$$

By substitution of equation 3.40 into equation 3.39 and taking the limit of Δx and Δt tending to zero, Fick's second law is obtained:

$$\frac{\partial C_V}{\partial t} = -\frac{\partial F}{\partial x} \tag{3.41}$$

$$= \frac{\partial}{\partial x}(D \frac{\partial C_V}{\partial x}) \tag{3.42}$$

$$= D \frac{\partial^2 C_V}{\partial x^2} \tag{3.43}$$

Note here that the last step assumes that D is independent of C_V.

As with the wave equation, the solution depends on the boundary conditions of the problem. As the equation is a partial differential equation it is not possible to find all the possible solutions, however for the boundary conditions here a solution can be obtained.

In this project a melt saturated with Cs^+ ions is used. By the following approximate calculation it can be seen that the melt will not be depleted. The melt is approximately 500g weight therefore containing approximately 1.5×10^{24} Cs^+ ions, the total surface area of the glass sample is $5 \times 10^{-3} m^2$ and the maximum depth the Cs^+ ions reach is

about 10μm and can obtain a maximum concentration of about 10% (weight) in the glass. Using the glass density of $1700kg/m^3$ gives an upper limit of diffusion of 4.1×10^{19} Cs^+ ions per ion exchange being diffused into the substrate which is an insignificant proportion of the total. The initial concentration of Cs^+ ions in the substrate is zero (see section 5.5.1).

The solution for this case is given by the complementary error function [87]:

$$C(x,t) = \frac{C_0}{2(\pi Dt)^{\frac{1}{2}}} \int_x^\infty \exp \frac{-y^2}{4Dt} dy = \frac{C_0}{2}[1 - erf(\frac{x}{2\sqrt{Dt}})] \tag{3.44}$$

Another solution that can be obtained from this function is, for example, the Gaussian function. This is the solution to the case of a fixed amount of material being available for diffusion, for example, if the substrate were coated with a thin layer of Cs^+ ions, then heated to the point where the source becomes exhausted by diffusion into the substrate [87].

3.4 Numerical analysis of waveguide modes

3.4.1 Three-layer model

Matlab programs were written to solve the effective indices, n_{eff}, in the three-layer model using equation 3.14 (and an analogous equation for the TM modes). These were used to solve all the modes in both polarisations. The right hand side of equation 3.14 was evaluated for a range of effective indices between the substrate index and the maximum refractive index of all the layers (the range within which propagating modes must lie). It was necessary that the test points have a small enough separation such that it was impossible to have two modes between a pair of test points as this could lead to modes being missed. Typically an incremental effective index of 10^{-4} was used, which is reasonable as, for the most part, the fundamental and first order modes (where the modal spacing is greater than higher order modes) are being considered.

3.4.2 Multilayer model

Similarly programs were written in Matlab to create the transfer equation (equation 3.31). The function in equation 3.33 is solved to obtain the modes for the multilayer model.

The model was checked against the simpler model of the three-layer waveguide and was found to give the same effective refractive indices. The effective refractive indices were also calculated and checked against results published by Chilwell and Hodgkinson [88]

(for a 5 layer coupler). The values calculated gave exactly the same effective refractive indices as those published for both polarisations (indices given to 5 significant figures).

Using the calculated effective refractive indices, it is then possible to plot all the fields in the waveguide as defined in equations 3.9,3.16 and 3.17. It is also simple to use the effective index method described in section 3.2.4 to calculate the effective refractive indices of a channel waveguide mode.

3.4.3 Modelling graded-index profiles

As has been discussed in section 3.3 a step planar refractive index profile is not expected, however it is a useful profile to use as a standard for comparison. Here three other refractive index profiles are studied and it is shown how they can be approximated by a multilayer method. These functions are the Fermi function, an exponential function and the expected complementary error function. Whilst the exponential function is included as it is a simple function, it is not expected to give a good fit but may be used to compare the effect of the refractive index profile. The Fermi function is included as a number of papers have referred to a function like this being obtained mostly in the case of field assisted ion-exchanges [89] but also from the small amount of previous work on cesium ion exchange [90, 91], where the form of the obtained refractive index profile appears similar to that of a Fermi function. The characteristic equations of these are shown below:

$$n(x) = \begin{cases} n_s + \Delta n u(w-x) & \text{Step function} \\ n_s + \Delta n[1+\exp(\frac{x-w}{d})]^{-1} & \text{Fermi function} \\ n_s + \Delta n \exp(\frac{-x}{w}) & \text{Exponential function} \\ n_s + \Delta n \ \text{erfc}(\frac{x}{w}) & \text{Complementary error function} \end{cases} \tag{3.45}$$

where $u(x) = 0$ for $x < 0$ and 1 for $x \geq 0$ and where the functions are defined for $x > 0$.

The effects on the functions of both n_s, the substrate refractive index and Δn, the peak change in refractive index, are obvious. Figure 3.5 below shows both the form of these functions and the effect of increasing w. As can be seen from figure 3.5 the parameter w describes the 'depth' to which the index is modified and the depth of the waveguide therefore refers to this parameter.

For the Fermi function there is an additional parameter, d. Figure 3.6 shows that d describes the steepness of the refractive index profile centred at depth, w.

For a graded index waveguide, the profile is better modelled by sampling at regular intervals of n, rather than x. The type of fit used is shown in figure 3.7, in this case

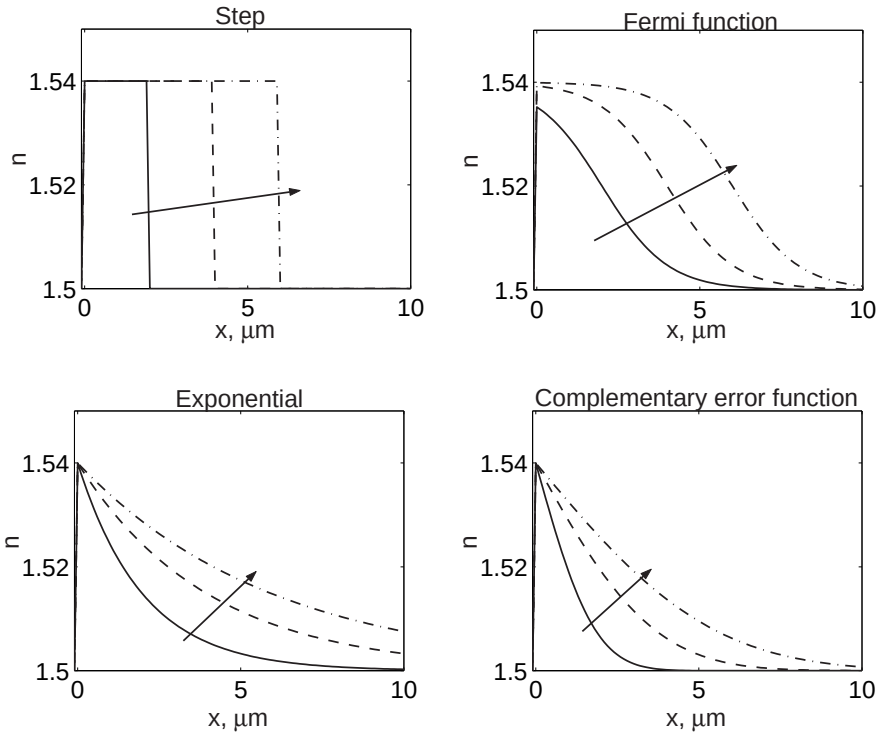

FIGURE 3.5: Various refractive index profiles for w=2, 4 and 6μm and $d = 2\mu m$ (as defined in equations in 3.45). In all cases the arrow indicates increasing w.

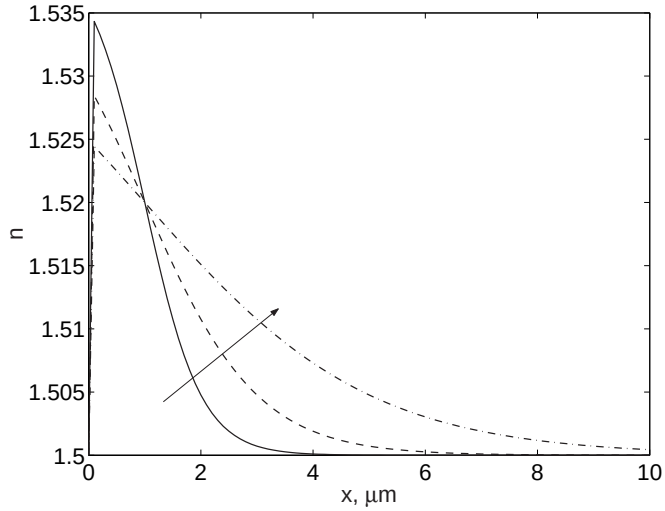

FIGURE 3.6: The effect of d on the Fermi function in equation 3.45 for values of d=0.5, 1 and 2μm and w=4μm. The arrow indicates increasing d.

with 5 steps for the purpose of illustration. The refractive index profiles are segmented into M-2 layers spaced Δn/(M-2) apart and starting at $n_s + 0.5 \times \Delta n/(M-2)$. The first and M^{th} layers are the superstrate and substrate respectively. The inverse of the function is used to obtain the value of x at the required value of n. The first interface is at x_1=0. The positions (x_i) of the intermediate interfaces are calculated as the mean of the calculated x values either side of the interface. Finally the interface with highest value of x has a width twice the difference between the last calculated x value and the previous interface.

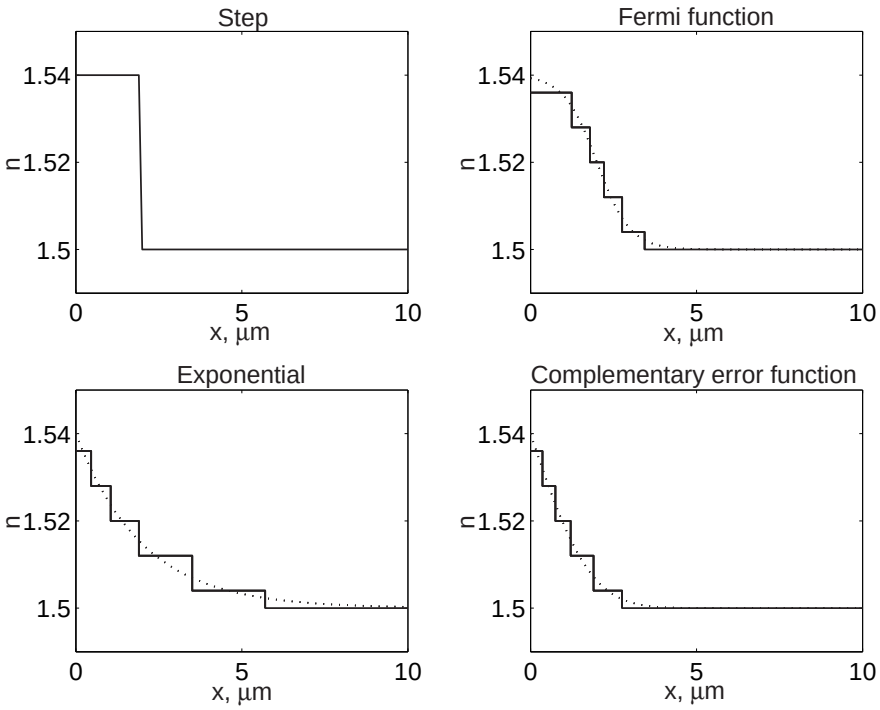

FIGURE 3.7: Graph showing the fit (–) used to model various profiles ($\cdots$) using 5 steps. It uses the parameters defined in equations 3.45 of $\Delta n = 0.04$, w=$2\mu m$ and $d = 0.5\mu m$.

The fit is poor in this illustration using five steps, however if the number of steps is increased to 30 a far better fit is obtained as seen in figure 3.8, and this has been used in subsequent calculations.

In order to attempt like-for-like comparisons of the effect of the profile types on the properties of the waveguide, w is set whilst varying Δn in order to make the integral $\int_0^\infty (n(x) - n_s)dx$ the same for each model. The aim is, that by using this condition, the same number of ions are diffused into the substrate for each profile.

For the conditions described in figure 3.8 the sum of the increase in refractive index is given by $\sum_{i=1}^{30}[n(x_i) - n_s](x_i - x_{i-1})$ and the values of this for the four profiles are shown in table 3.1. Therefore to model a constant number of ions exchanged for the differing

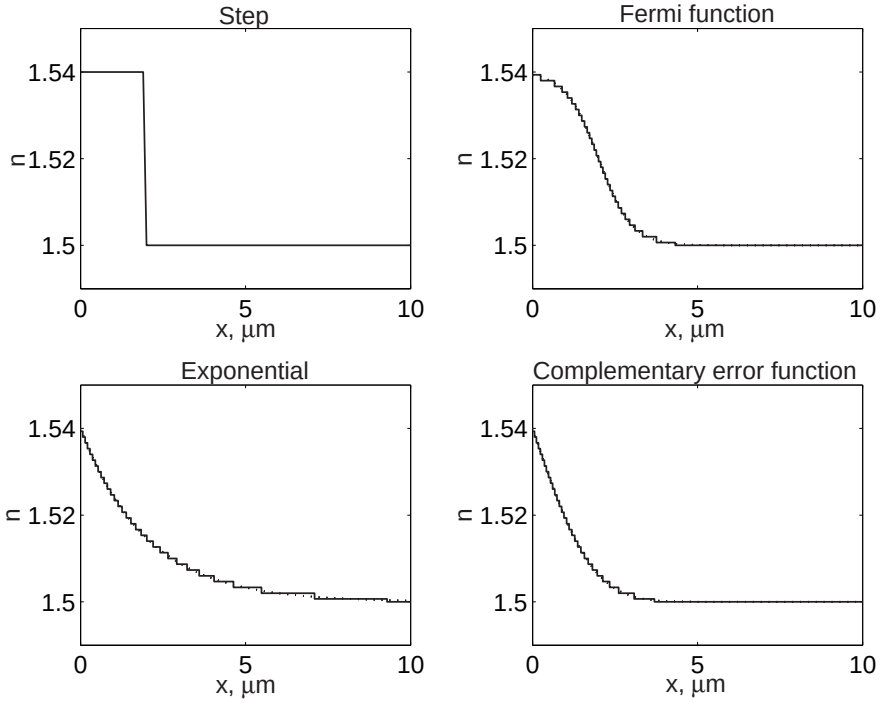

FIGURE 3.8: Graph showing fit (–) used to model various profiles ($\cdots$) using 30 steps. It uses the parameters defined in equations 3.45 of $\Delta n = 0.04$, w=$2\mu m$ and $d = 0.5\mu m$.

Function	$\int_0^\infty(\Delta n)\mathrm{dx}$ (μm)
Step	4
Fermi	4.01
Exponential	3.99
Complementary error	2.26

TABLE 3.1: Measured area enclosed by equation 3.45 with conditions as in figure 3.8 for the case of 30 steps.

profiles, in future calculations the refractive index change, Δn, for the complementary error function is increased by a factor of 4/2.26.

3.4.4 The beam propagation method model

Beamprop required five stages of programming to solve a given model. Firstly global parameters, such as the substrate index, the superstrate index, the maximum index change and the model type (BPM, FDTD, TE, TM polarisation etc.) and the wavelength of light had to be set. Then the geometry of the model could be constructed in a CAD program (a straight waveguide, for the analysis in this chapter). A user-configurable refractive index profile was defined for the region of the waveguide. Depending on the type of calculation, an initial field may also be required. Finally the simulation parameters such as the output required, the resolution and size of the grid, the step-size in the z direction etc. were defined. In all the cases below the resolution of the model used was 0.1μm in the y-direction and 0.05μm in the x-direction. This was sufficiently

accurate that the results did not change appreciably for changes in the resolution, whilst also not being overly time consuming. The size of the modelling area used was typically 18μm in the y-dimension (centred on the waveguide) and 14μm in the x-dimension with the substrate/superstrate interface positioned 2μm from the top of the modelled area. This was because much more of the field propagated in the substrate than the superstrate, as shall be seen later.

3.5 Theoretical results

3.5.1 Introduction

The first aim of this section is to produce a realistic model of the waveguides. This is done using data supplied by Dr. O.G. Hellesø from the University of Tromsø to predict the refractive index profile of planar waveguides. Secondly this refractive index profile is used to predict characteristics of the waveguide modes such as spot-sizes, effective indices and cut-off wavelengths. Finally, the requirements for the optimal waveguide in terms of both trapping and propulsion are examined within the constraints of the model. The parameters that are required for this are discussed and then results that lead to the choice of an optimised waveguide are shown.

In all the models used, the waveguides are assumed perfect (in that the profile does not change with z). This may not necessarily be the case due to the roughness of photolithography, defects or other practical issues. It is also assumed that the refractive index profile is not wavelength dependent (i.e. non-dispersive). This allows results obtained at 633nm and 1066nm to be relatively simply compared, and is believed to be a reasonable approximation.

3.5.2 Determination of diffusion profile

In this section it is first shown that there is a significant difference in the properties of the waveguide when comparing the different refractive index profiles. Some validation of the BPM package is carried out. A particular refractive index profile is chosen in agreement both with preliminary data and the literature.

The multilayer program was used to solve the modes for a range of waveguide depths, w, for each of the four index profiles described above in section 3.4.3. The effect of the different index profiles on the effective refractive indices is shown below in figure 3.9. Arbitrarily values of $\Delta n = 0.04$, d=0.5μm and $\lambda = 1066nm$ are used whilst w is varied between 0.1μm and 4μm. The figure shows the effective indices of up to the first four modes. In order to confirm agreement between the two methods the waveguide was also simulated using the BPM package. These results are not plotted as they are virtually

indistinguishable from those modelled by the analytical method with differences in n_{eff} of less than 0.0001 being observed. This confirms that for modelling planar waveguides both methods are good. It also shows that the number of refractive index layers chosen (30) is likely to be sufficient for the multilayer method. For the BPM method the resolution used in the x-direction was 50nm.

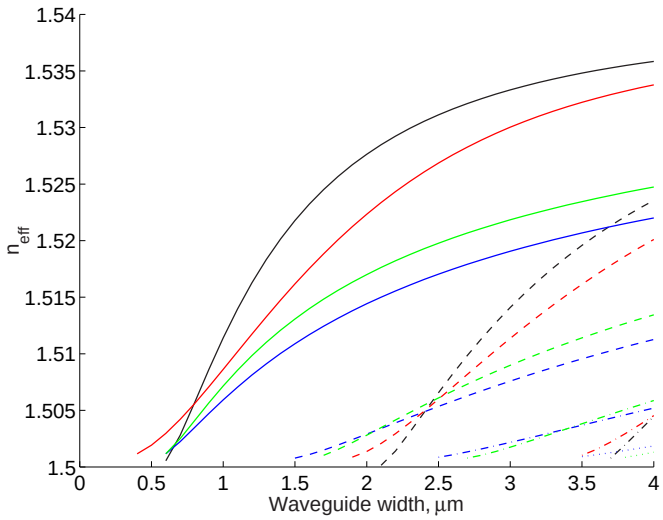

FIGURE 3.9: The effect of different mode profiles on the effective refractive indices of a planar waveguide. The profiles are a step index (■), the Fermi function (■), the complementary error function (■) and an exponential function (■). Solid lines show the fundamental, dashed, the first, alternate dotted/dashed, the second and dotted, the third order modes.

As can be seen from figure 3.9 the type of profile that should be used is of great importance in the modelling as the effective index elevation above the substrate index, Δn_{eff}, for the step function profile can be over twice that caused by the exponential function. Apart from very near cut-off (where the waveguide ceases to be able to confine the light) the step-index waveguide generally gives the largest effective index. This is because its penetration into the substrate is least. Whereas the exponential function which, due to its sharp decay at the surface, penetrates much further into the substrate, generally has modes with the lowest effective refractive indices.

In order to identify the form of refractive index profile that should be used in the case of caesium ion-exchange in Menzel glasses, a process called the inverse WKB method, first devised by White and Heidrich [92], is used. In order to derive a best fit refractive index profile to the measured effective refractive indices of the modes of a waveguide, for each type of profile, these effective indices were used in a program that optimised the parameters from equations 3.45 in order to minimise the error. This is an inverse process to that first described by Hocker and Burns [93] (and used for example in [89]).

The method works by predicting a depth of the 'grazing' angle of the mode for a supplied refractive index profile [93]. In this method a refractive index profile may be obtained by minimizing some function describing the error of the profile. White and Heidrich

mode	a) TE	TM	b) TE	TM
0	1.5380	1.5384	1.5368	1.5374
1	1.5353	1.5361	1.5270	1.5271
2	1.5318	1.5323	1.5126	1.5123
3	1.5265	1.5270	-	-
4	1.5202	1.5204	-	-
5	1.5124	1.5126	-	-

TABLE 3.2: Measured effective refractive indices of planar Cs^+ ion-exchanged waveguide for a) 24 hours at 500^0C and b) 96 hours at 450^0C.

Method	$\Delta n(\times 10^{-2})$	w (μm)	d(μm)	fit
TE				
Fermi	2.9	6.28	0.22	0.15
Complementary Error	5.1	6.76	-	18.1
Exponential	6.5	3.08	-	24.5
TM				
Fermi	2.9	6.32	0.13	0.0048
Complementary Error	5.2	6.76	-	18.5
Exponential	6.7	3.08	-	24.8

TABLE 3.3: The optimised profile parameters to match the effective indices of the planar Cs^+ ion-exchanged waveguide, ion-exchanged for 24 hours at 500^0C.

used a function describing the curvature to define the error [92], thus they obtained the smoothest profiles that fit the measured effective refractive indices. In this project, the errors of the refractive index profiles from the functions in equation 3.45 are minimized. The step index profile could not be fitted due to its discontinuity in refractive index profile within the substrate.

In the results below a superstrate refractive index of 1 is used, to represent air (the condition in which the waveguides were characterised). A substrate refractive index of 1.5098 is used to represent the bulk refractive index of the Menzel substrate at 633nm, the wavelength used to measure the effective refractive indices (see chapter 5).

Preliminary results from two waveguides were provided by Dr. O.G. Hellesø from the University of Tromsø. These were a slab waveguide ion-exchanged for 24 hours at 500^0C giving 6 modes for both TE and TM polarisation and a slab waveguide ion-exchanged for 96 hours at 450^0C giving 3 modes in both polarisations. The effective refractive indices of these modes measured (by the prism coupling method, see chapter 5) at a wavelength of 633nm are listed in table 3.2. The optimised parameters for the first waveguide are shown in table 3.3, whilst those for the second waveguide are in table 3.4. The best fit curves for the different functions for both these waveguides are plotted below in figures 3.10 and 3.11 respectively along with the points of the measured effective indices plotted as a function of their predicted depths.

Method	$\Delta n(\times 10^{-2})$	w (μm)	d(μm)	fit
TE				
Fermi	3.0	2.89	0.12	0.00001
Complementary Error	5.6	2.83	-	1.06
Exponential	7.2	1.27	-	1.46
TM				
Fermi	3.1	2.87	0.17	0.001
Complementary Error	5.9	2.75	-	1.04
Exponential	7.8	1.21	-	1.45

TABLE 3.4: The optimised profile parameters to match the effective refractive indices of a planar Cs^+ ion-exchanged waveguide, ion-exchanged for 96 hours at 450^0C.

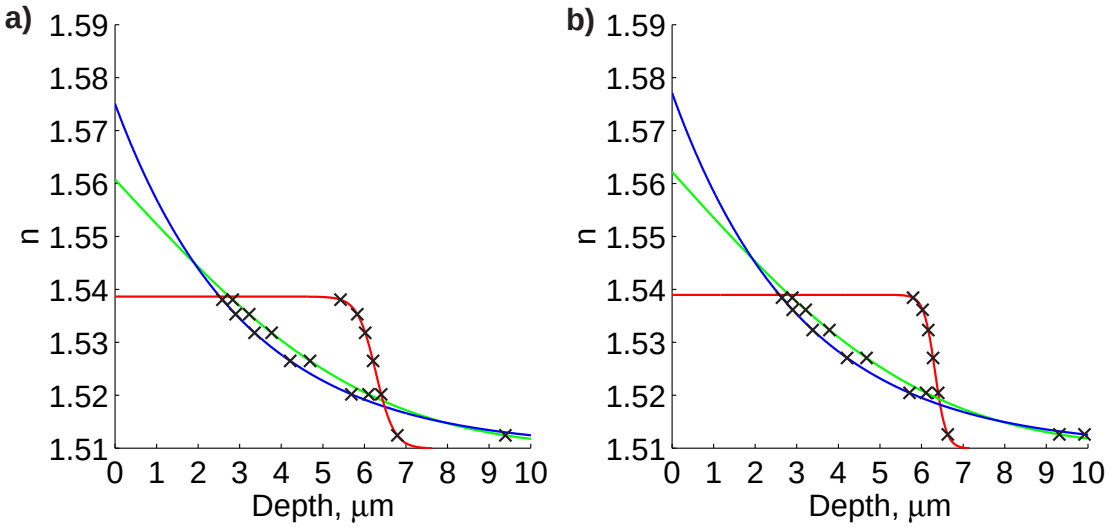

FIGURE 3.10: The Fermi (■), complementary error (■) and exponential (■) function fits and the measured effective refractive indices (×) of a planar waveguide ion-exchanged for 24 hours at 500^0C for the case of a) TE polarisation and b) TM polarisation.

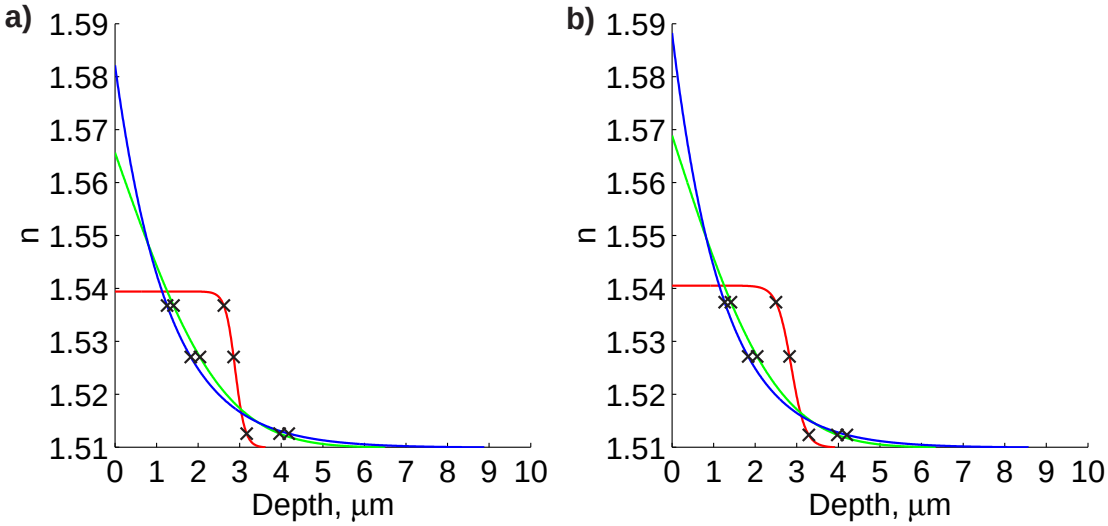

FIGURE 3.11: The Fermi (■), complementary error (■) and exponential (■) function fits and the measured effective refractive indices (×) of a planar waveguide ion-exchanged for 96 hours at 450^0C for the case of a) TE polarisation and b) TM polarisation.

From the data in the tables, it seems clear that the best fit is a Fermi function. However there are a number of points that should first be considered:

1. The Fermi function has three parameters that can be optimised in order to fit the modes. Therefore this function will almost inevitably give the lowest fitting error. For the second waveguide there are only 3 modes, thus the three parameters should fit perfectly (limited only by the tolerance of the fit).
2. The Fermi function is not the result as predicted by Fick's diffusion laws (see section 3.3).
3. Ideally a waveguide supporting many modes should be used in order to get a meaningful fit. Therefore a much longer ion-exchange time was used to create a larger number of modes than will be used to make the (mostly monomode) waveguides used for trapping.
4. To make a waveguide that supports even more modes is hard without moving to a lower wavelength where there are increased risk of dispersion becoming significant. Also as the depth of the waveguide increases with only the square root of the ion-exchange time, and increasing the temperature would risk the decomposition of the melt.

In the literature, there are few papers that deal with caesium ion-exchange in glass [90, 94, 95, 96]. However the paper by Neuman et al. [90], uses a similar glass (i.e. a soda-lime glass) and ion-exchange conditions to the experiment above. It also uses the WKB method to try to identify the refractive index profile and produces Fermi like profiles. In addition, they also achieve a Δn of approximately 0.03 as is predicted by the results above for the case of the Fermi model. They give the explanation that this profile is due to the so called 'double alkali effect'. Following equation 3.42 the assumption was made that the concentration of the molecule being considered had no effect on its diffusion rate, D. However the process being considered, (Cs^+ ions diffusing into the glass and substituting native Na^+ ions), has a significantly varying diffusion constant as a function of both the Cs^+ and Na^+ local ion concentration. Neuman et al. [90] state that initially the mobility of the Na^+ ions is much greater than that of the Cs^+ ions. However the large concentration gradient enhances the diffusion of Cs^+ ions into the substrate. As the concentration of Cs^+ ions in the substrate increases so too does the self diffusion constant of the Cs^+ ions, whilst the self-diffusion constant of the Na^+ ions is decreasing. As this is a very strong effect the diffusion will be immediately halted and will only move forward into the substrate again once the Cs^+ ion concentration has obtained this critical concentration at that boundary. This explanation is backed up with the data in [96] about the diffusion constants of Cs^+ ions in glasses.

This explains the deviation in profile from the expected complementary error profile and justifies the use of a Fermi function refractive index profile. Therefore a Fermi profile

using the parameters Δn=0.03 and d=0.125μm is adopted for this work. Although the value for d is not strongly established, in both cases there was a much better fit for one polarisation over the other. The model takes the average of these best fits (0.12μm and 0.13μm). The value for w will depend on the length of the ion-exchange and therefore the results below are shown as a function of this parameter.

3.5.3 Comparison of analytical and numerical models

In order to verify the validity of the numerical program, Beamprop, the effective refractive indices for a range of waveguide depths and widths are calculated by both the analytical and numerical methods.

Having decided on a Fermi function refractive index profile to model the waveguides, theoretical plots are now predicted based on this model.

The effective indices are shown below in figure 3.12 for the case of λ=1066nm and with d=0.125μm. The width, dy, of the opening in the aluminium through which the ions are allowed to diffuse (see chapter 5) on the effective index of the fundamental mode is examined, considering various values of w. This is calculated both with the effective index method (in conjunction with the multilayer method) and the Beamprop program.

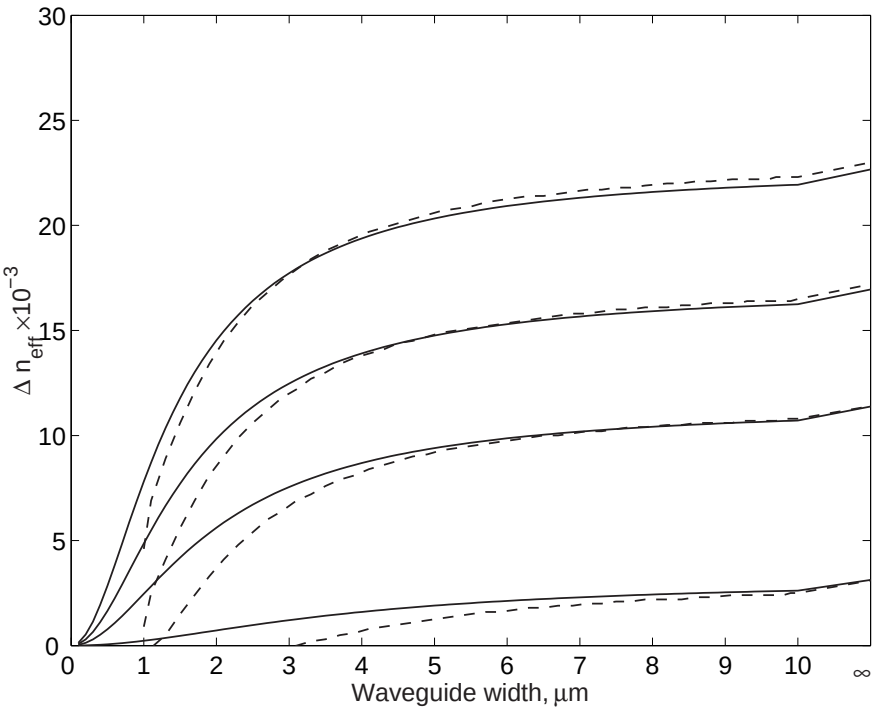

FIGURE 3.12: TE effective indices for channel waveguides at 1066nm as calculated by the multilayer and effective index methods (–) and by Beamprop BPM package (- -). The graphs are for the case of w=1, 1.5, 2 and 3μm.

The minimum value of w (1μm) was chosen because waveguides with this value are close to the depth at which they cannot guide (cut-off), identifiable in figure 3.12 from the intercept of the effective index change with zero. The maximum value of w was chosen based on the data from the very long ion-exchanges used to determine the profile type. As the 96 hour waveguide at 450^0C gave a value of w=2.9μm it is not considered necessary to choose values higher than this. As can be seen there is good agreement between the models for the higher values of dy. For narrower waveguides there is a marked difference in the values calculated using the effective index method compared to those using Beamprop due to the waveguide being modelled by a symmetrical profile laterally in the effective index method. Here therefore the results calculated from the Beamprop model are considered more reliable. Having confirmed that the multilayer model is accurate, by comparison to published refractive indices in section 3.4.2, it is therefore reasonable to assume that the Beamprop method is also reliable. This model is therefore used exclusively in the rest of this chapter due to its increased flexibility and better accuracy.

In comparing the effective index method to the BPM package it was necessary to model the same structure (that shown in figures 3.3a and 3.13a). Now that the the BPM package only is being used a more complex refractive index profile can be considered that also takes into account lateral diffusion. For this it was assumed that the diffusion into the glass is isotropic. Therefore rather than zero index difference for $|y| > dy/2$ the index profile change is given by the relevant Fermi function. However the value used for x is now the closest point that is not masked. The effect of this is shown below in figure 3.13b for the case of w=2μm, d=0.125μm and dy=4μm.

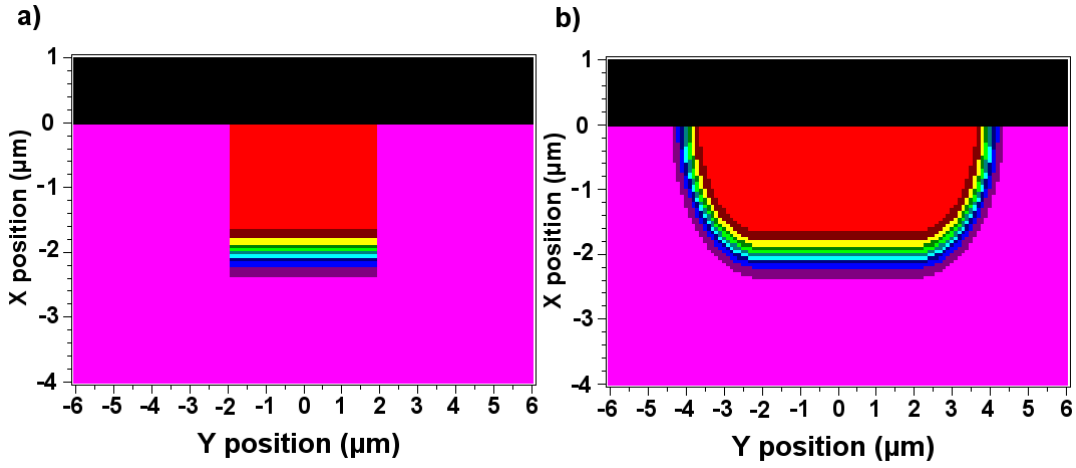

FIGURE 3.13: The refractive index profiles of a waveguide a) with and b) without isotropic diffusion.

The effect that this change has can be large. Consider a waveguide with dy=1μm and w=3μm. With no lateral diffusion the effective index is modified up to a width of just

1μm. However taking into account lateral diffusion, the width of substrate modified is around 7μm. This is of course an extreme case, but makes an important point.

3.5.4 Modelling of measurable waveguide parameters

3.5.4.1 Effective refractive indices

Having changed the form of the refractive index profile to take into account the lateral diffusion, it is necessary to recalculate the effective refractive indices. These are shown below in figure 3.14 using the same conditions as in section 3.5.3, but for wavelengths of both 1066nm and 633nm.

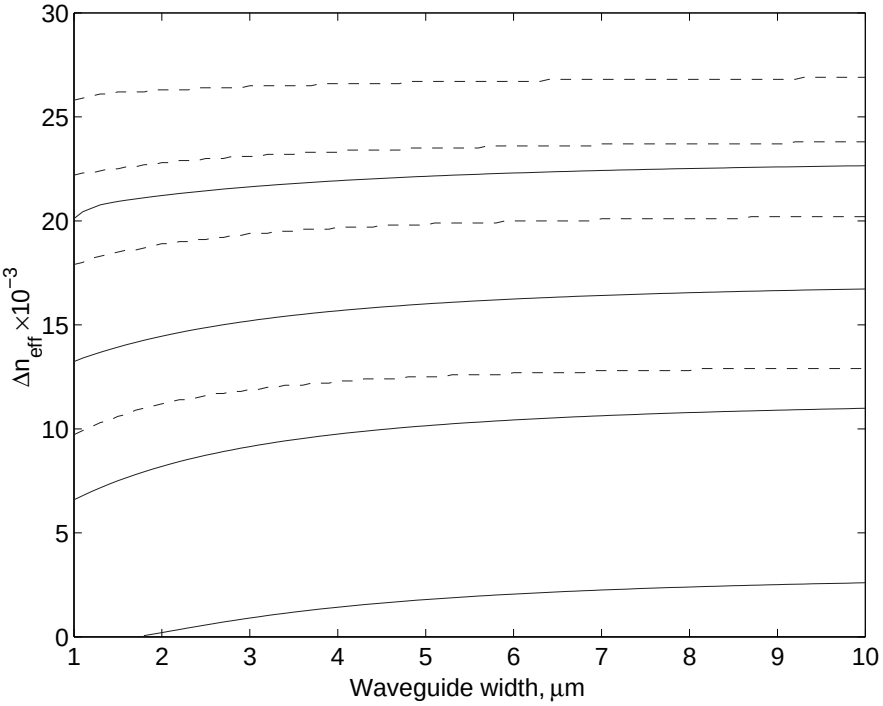

FIGURE 3.14: BPM analysis as in figure 3.12 with lateral diffusion. Fundamental TE modes are shown at a wavelength of 1066nm (–) and 633nm (– –). The lines represent waveguide depths, w, of 1, 1.5, 2, 3μm with the higher values representing the greater depths.

Figure 3.14 shows that, as expected, there is a significant difference between the effective refractive indices predicted previously in figure 3.12 without lateral diffusion and here with lateral diffusion. This is especially evident for narrower waveguides where lateral diffusion means the sharp decrease in Δn_{eff} is not observed. There is also a larger difference between an effective refractive index measured at a wavelength of 1066nm and that measured at 633nm. At 1066nm for w=1μm the waveguide is close to being cut-off for all widths (i.e. the planar waveguide is almost cut-off with an expected index increase of only 0.003) and that it only starts to guide with a waveguide width greater than 1.7μm. However at 633nm the planar waveguide will guide with a significant

effective refractive index change (0.006) at w=1μm. This is because the modal spot-size at 633nm is significantly smaller than that at 1066nm for a given mode. Lastly it can be seen from the results that for a waveguide width greater than about 4μm the effective refractive index does not increase greatly. This is especially evident when considering the results for a waveguide of width 10μm and a planar waveguide (width=∞).

3.5.4.2 Spot-sizes and the field profile

In this section the fields of the waveguide are considered in order to predict the intensity distribution of both planar and channel waveguides. These results can then be used to extract a number of useful parameters that are required to theoretically optimise the waveguide used and also to compare to experimental results.

First the fields of the very simplest type, a three-layer, assymetric slab waveguide, will be discussed to highlight some important points about modal fields. The three components for the fields for both the TE and TM polarisations are shown below in figure 3.15. The fields are normalised by dividing by the integral of the field. The waveguides analysed model a Menzel glass at a wavelength of 1066nm ($n_{sub} = 1.5$) with air cladding ($n_{sup} = 1$) and with a step refractive index change (Δn) of 0.03. The graphs show the case of two waveguides. A single mode waveguide with a depth, w=1μm and a multimode waveguide with depth, w=2.8μm.

In order to simplify future plots and in confirmation of well-known waveguide properties the following points are noted:

1. The E and H fields are continuous across the boundaries except the E_x field where D, the electric displacement, is continuous.
2. The E and H fields perpendicular to the direction of propagation are simply related to each other. In future field plots of only one of the fields is plotted.
3. The field in the z direction does not contribute to the power travelling along the waveguide. This therefore holds no additional useful information and is omitted below.
4. The difference between the case of TE and TM polarisation is small. In figure 3.15 the highest supported modes are close to their cut-off depth, where the difference in the fields for the different polarisations is greatest. Henceforth the TE E_y field will be shown and termed 'the field'.

Having examined the form of the fields travelling in a three-layer waveguide the fields for the profiles defined in section 3.5.2 with the parameters d=0.125μm, w=2μm, $\Delta n = 0.03$ and $\lambda = 1066nm$ are shown below in figure 3.16 using the same normalisation as above.

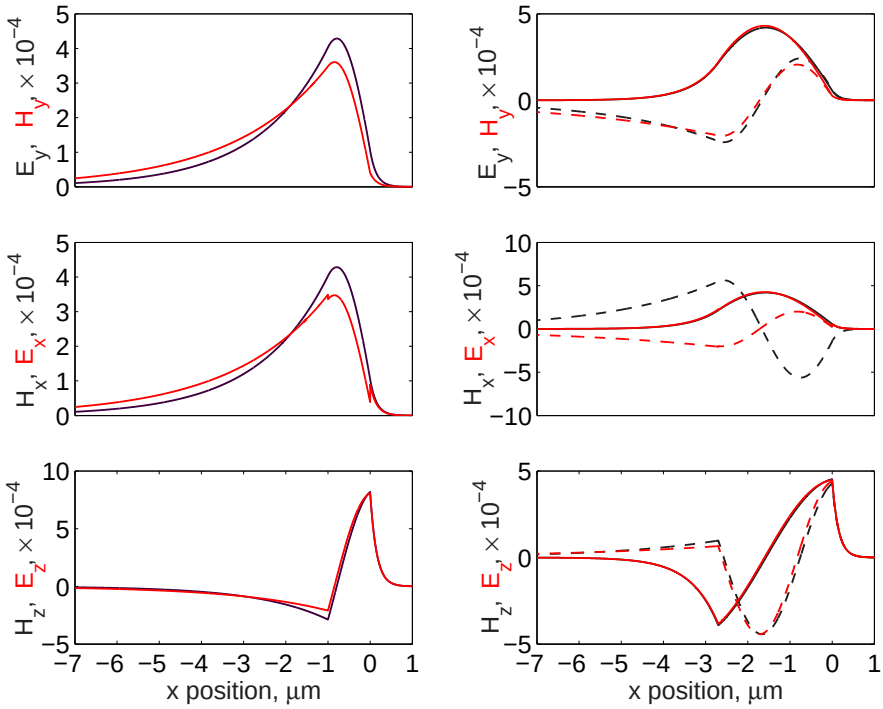

FIGURE 3.15: Analytical solution to two asymmetric slab waveguides with $n_{sup} = 1$, $\Delta n = 0.03$, $n_{sub} = 1.5$ at a wavelength of 1066nm. The waveguide depth, w, is 1μm for the left plots and 2.8μm for the right plots. The plots show TE (■) and TM (■) fundamental (solid lines) and first order (dashed lines) modes. The y-axis labels refer firstly to the TE fields and secondly to the TM fields.

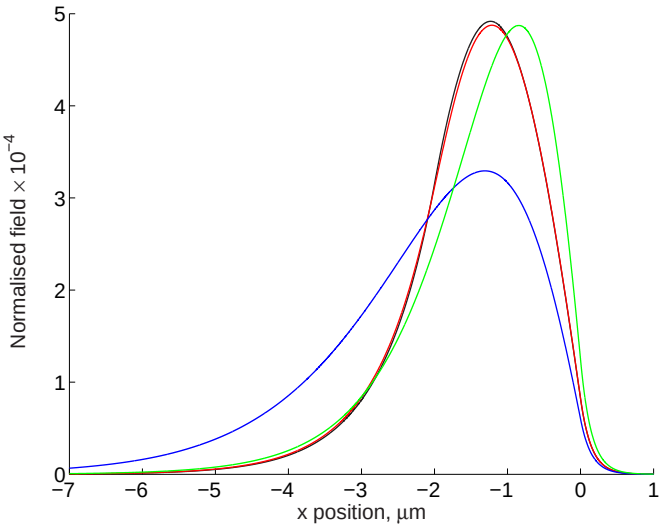

FIGURE 3.16: Graph showing the field for the fundamental TE mode at 633nm. The profiles are a step index (■), the Fermi function (■), the complementary error function (■) and an exponential function (■).

The curves in figure 3.16 show that, for these conditions, the field for the Fermi function and step function are very similar. As the profiles themselves are similar, this is expected. It also shows that the field of the exponential function penetrates much deeper into the substrate. This can be explained by the fact that in the exponential fit, the refractive index is modified much deeper into the substrate. In the other functions, most of the change in refractive index is concentrated near the surface. Finally it shows that a complementary error function would have a field slightly more concentrated towards the superstrate, and thus a higher intensity in the superstrate, for a given number of ions diffused into the substrate.

The fields for a channel waveguide are now considered. In particular the field normal to the surface through the centre of the waveguide is of great interest as this will be the field that will trap the particle transversely to the waveguide. The BPM package can calculate a complete 3-d field as shown in figure 3.17 and so cross sections may be taken in both dimensions and normalised in the same way as in figure 3.15. The parameters used for the Fermi function are d=0.125μm, w=1.5μm and Δn=0.03, dy is 3μm and the wavelength is 1066nm with an air superstrate.

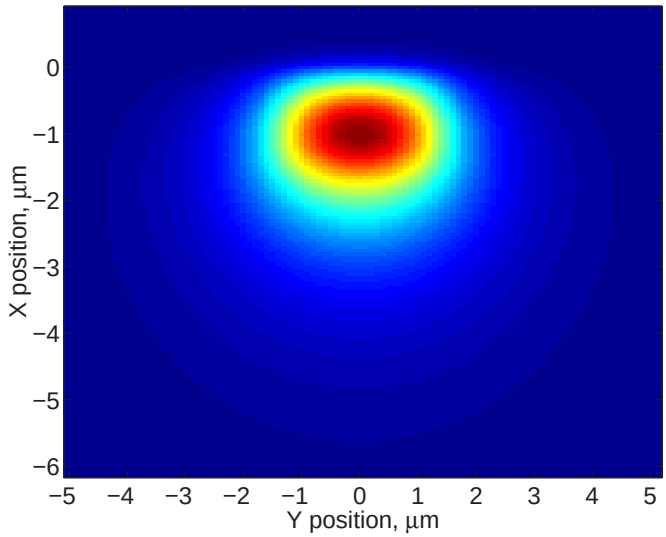

FIGURE 3.17: The mode profile of a diffused channel waveguide as predicted by the BPM package.

Using the field as shown in figure 3.17 the intensity profile, and therefore many important parameters based on this, can be calculated. One such parameter is the spot-size that is defined as the width between the two points on a cross section at which the intensity of the mode has fallen to e^{-2} of the peak intensity.

The spot-size for a range of waveguide widths, dy, and diffusion depths, w, is shown in figure 3.19 below for both lateral and transverse spot-sizes and for an air and water superstrate. Figure 3.19 shows that the spot-size in the lateral dimension, y, increases roughly linearly with the waveguide opening, dy, whereas, apart from at narrow widths where the waveguide is almost cut-off, the spot-size in the vertical direction is approximately

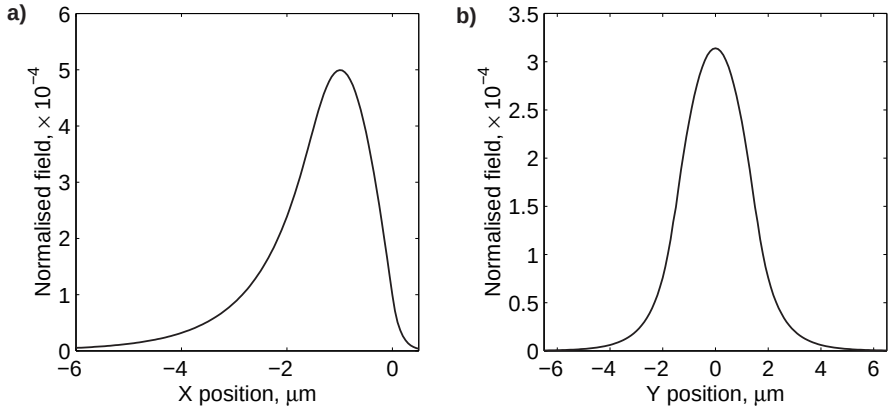

FIGURE 3.18: The normalised field a) normal to and b) parallel to the surface of the substrate through the peak intensity of the mode profile, as calculated by the BPM method.

constant. The spot-size is always greater in the lateral dimension than the transverse dimension as there is diffusion to a width of at least 2w in the lateral dimension whereas only to a depth of w in the transverse dimension.

As can also be seen from figure 3.19 there is very little variation in the width of the fundamental mode with w, until w becomes large (above 2.5μm). The spot-size is larger than dy but appears to approach it asymptotically. In the transverse direction the height of the mode varies greatly with the depth of the profile, w, having a large value at low values of w (close to the cut-off wavelength of the waveguide) decreasing to a minimum at a value of w between 2 and 3μm, and then increasing again with increasing value of w.

3.5.4.3 Waveguide cut-off wavelengths

An asymmetric waveguide will have a wavelength above which it ceases to act as a waveguide. This wavelength is called the cut-off wavelength. As shall be seen in chapter 5, this is a parameter that can be accurately measured (to a resolution of approximately 2nm). Therefore if this value can be theoretically obtained it will be of use in the comparison of experimental measurements.

A plot of the cut-off wavelength of the fundamental mode of a waveguide with a range of parameters is shown below in figure 3.20. It should be noted that in obtaining this graph a certain amount of interpolation was required as the computational time required to scan through a wavelength range at high resolution would be excessive.

It can be seen that as either the depth of the diffusion, w, or the waveguide width, dy, increases so too does the wavelength range that a waveguide will support. Given that the wavelength of laser used in this project is 1066nm, if the cut-off wavelength is below

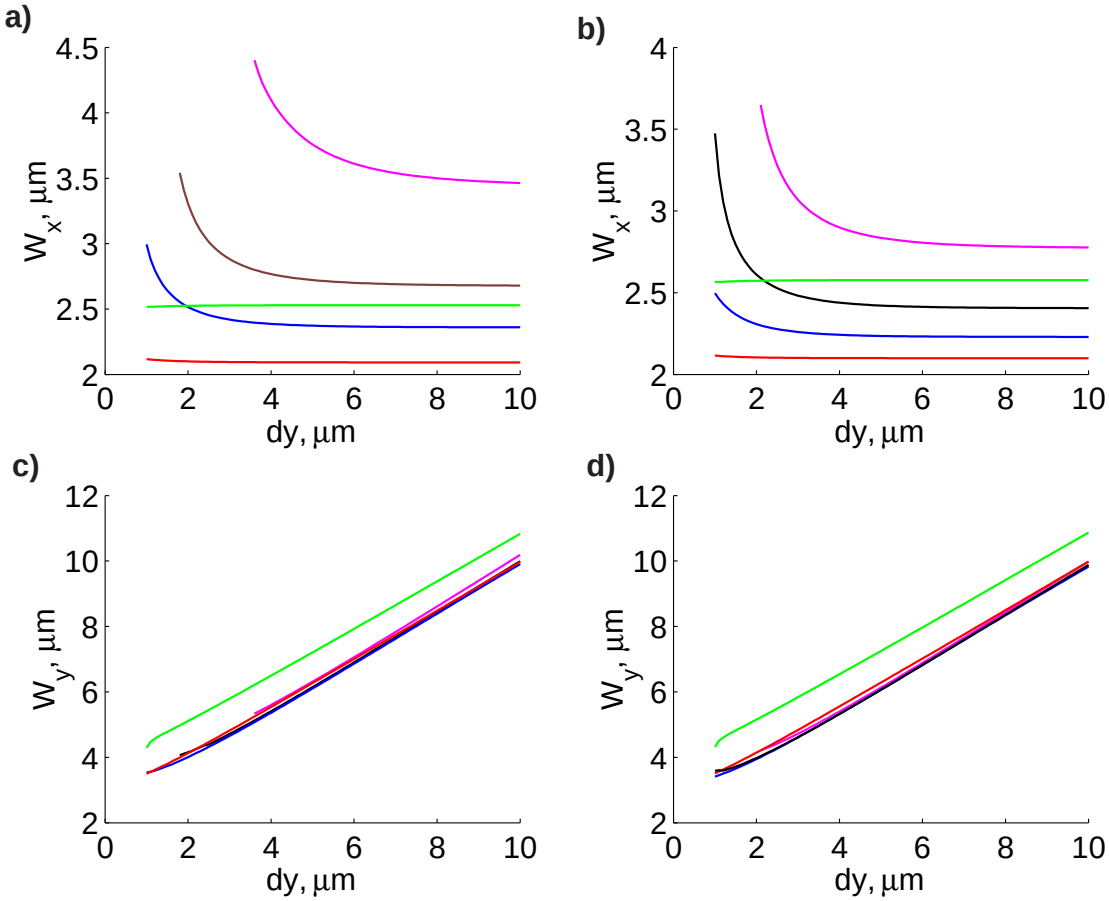

FIGURE 3.19: Waveguide spot-sizes as a function of the waveguide width, dy, for light of wavelength 1066nm. The transverse spot-sizes for an a) air and b) water superstrate and the lateral spot-sizes for the c) air and d) water superstrate. The lines represent w=1 (■), 1.5 (■), 2 (■), 2.5 (■) and 3 μm (■).

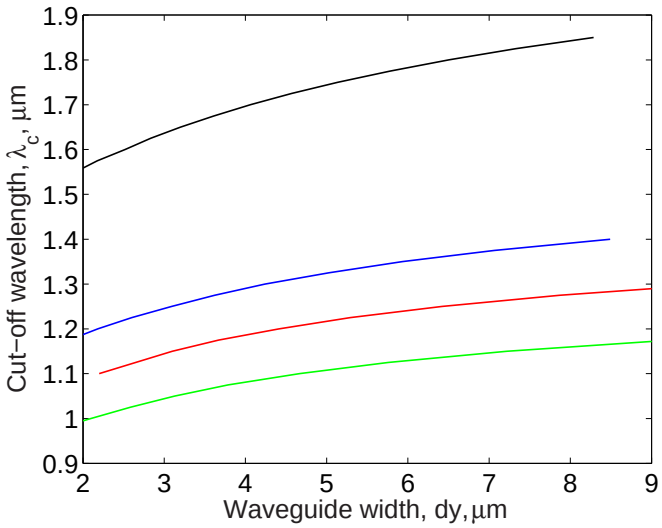

FIGURE 3.20: Waveguide cut-off wavelengths as a function of the waveguide width, dy, for an air superstrate. The lines represent w= 1.5 (■), 1.1 (■), 1 (■) and 0.9μm (■).

this value (as is the case for a waveguide with w=0.9μm and dy<4μm, for example) then this waveguide will not guide in air.

3.5.5 Theoretical waveguide optimisation for trapping and propulsion

In this section the aim is to design a waveguide that is optimised for evanescent trapping. First therefore it is necessary to consider the parameters that will be used for this definition for an optimised waveguide.

The power in the superstrate is one measure of an ideal waveguide for trapping as any light in the superstrate will act to both trap and propel particles. Thus this parameter is plotted below in figure 3.21. It shows that for shallow waveguides as the width of waveguide increases so too does the proportion of light in the superstrate. This is because as the waveguide gets narrower it approaches cut-off. In this case, all the light will be propagating in the substrate (the effective index of the mode being identical to that of the substrate). In the more usual case of the waveguide not being close to the cut-off wavelength, the proportion of light in the superstrate decreases with increasing width. Figure 3.21 also shows that (as expected) a larger proportion of the beam travels in the superstrate of the waveguide if the superstrate is water (up to ~1.3%) compared to an air superstrate (up to ~0.4%).

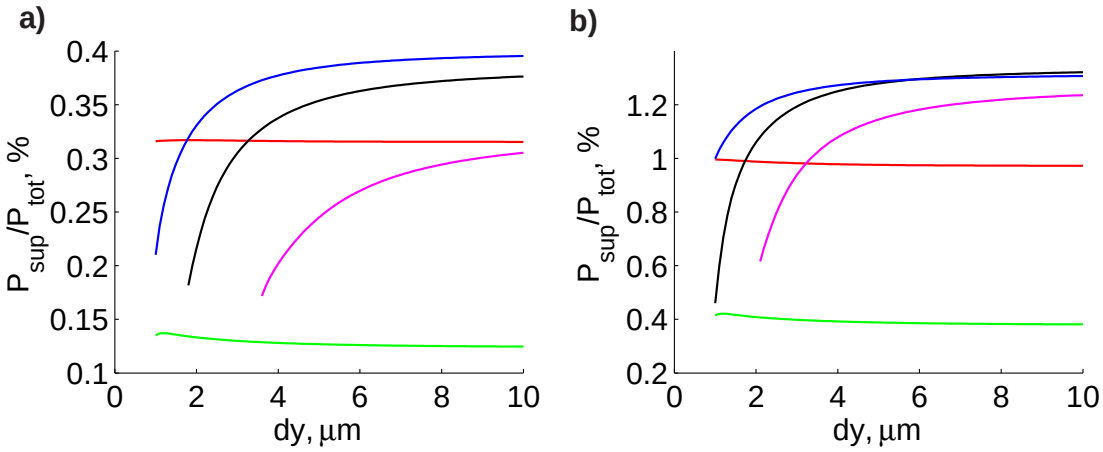

FIGURE 3.21: Fraction of modal power in the superstrate with a cover of a) air and b) water as a function of dy. The lines represent w= 0.9 (■), 1 (■), 1.1 (■), 1.5 (■), 2.5μm (■).

However as has been seen in chapter 2, it is an intensity gradient that causes a trapping force and therefore it is ideal that this be maximised, in both lateral and transverse directions. It is also interesting to note the intensity at which this maximum gradient occurs as the intensity will determine the speed at which a trapped particle is propelled.

As shall be seen in the next chapter a destabilizing force called Brownian motion will always act on the particle. An important factor in overcoming this is the distance

over which the gradient force acts. Effectively the greater this distance, the wider the potential well formed by the trapping force is, thus making it harder for the particle to escape by random motion. Therefore a parameter, L, is introduced, which describes the length over which the intensity is within 20% of the maximum gradient. In chapter 4 it shall be shown that the product of the gradient and L are crucial and this parameter shall be referred to as τ, the trapping parameter.

Figures 3.22 and 3.23 below show graphs of the four parameters described above against the waveguide width. The first shows the case of an air superstrate, as is normally the case when characterising the waveguide, whilst the second shows the case of a water superstrate, used when trapping particles.

Much can be obtained from figures 3.22 and 3.23. Most importantly the value of τ, the trapping factor in water, is found to be a maximum for narrow waveguides with small depths. However there is a limit to this as is shown for the case of w=1μm. To understand this and other factors in the graph a number of comparisons are made.

Firstly the comparison between an air superstrate and a water superstrate is made. Generally, the values for the maximum gradient, the intensity, the length parameter and the trapping parameter are all greater in the case of a water superstrate by factors of (very approximately) 2, 2, 1.5 and 5 respectively. The exceptions to this are that the length factor in the lateral dimension is roughly the same in both cases, as the shape of the roughly Gaussian intensity profile in this dimension will not change significantly. This comparison therefore shows the great advantage that the use of a liquid with refractive index closer to that of the substrate, or a substrate with refractive index closer to that of water, might give.

Next the comparison between the two dimensions is made for the case of a water superstrate. The transverse intensity gradient is a maximum above the centre of the waveguide at the surface whereas in the lateral dimension the maximum is laterally either side of this position. In the transverse direction the gradient exponentially decays with a penetration depth in the order of 250nm whereas the lateral Gaussian-like profile has a much slower decay over several microns (as seen by plots for L_x and L_y). Therefore it is not unexpected that the transverse gradient is over ten times greater than the lateral gradient. The intensity over the centre of the waveguide is approximately twice that at the maximum intensity gradient of the approximately Gaussian profile as would be expected.

The variation with width, dy, is now considered. Generally, as the width of the waveguide increases the intensity and the intensity gradient decrease, whilst the transverse length factor remains constant and the lateral length factor increases. This is explained by the (fundamental) mode generally increasing in size, thus the power is distributed over a larger area and the average intensity decreases. The relative independence of the length factor in the transverse dimension to the width is due to the relatively small change in

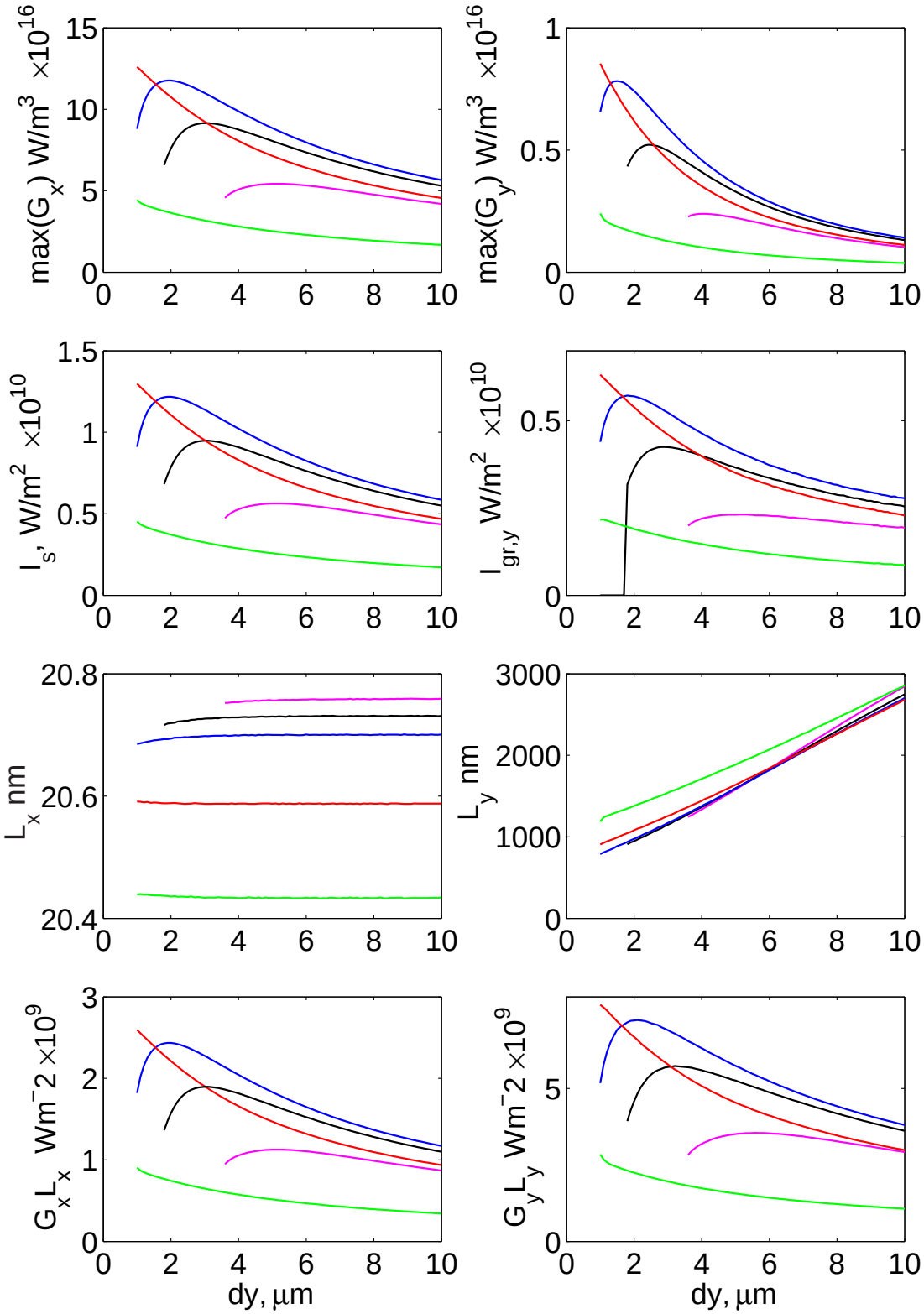

FIGURE 3.22: Graphs showing parameters concerning cross sections taken vertically (left) and horizontally (right) through the field at the surface as a function of the waveguide width, dy. The parameters from top to bottom are the maximum intensity gradients (G_x, G_y), the intensity at these points (I_s, $I_{gr,y}$), the length over which this force is roughly constant (L_x, L_y) and the product of the gradient and the length, GL. The different lines represent w= 0.9 (■), 1 (■), 1.1 (■), 1.5 (■), 2.5 (■) μm. Results for 1066nm in air.

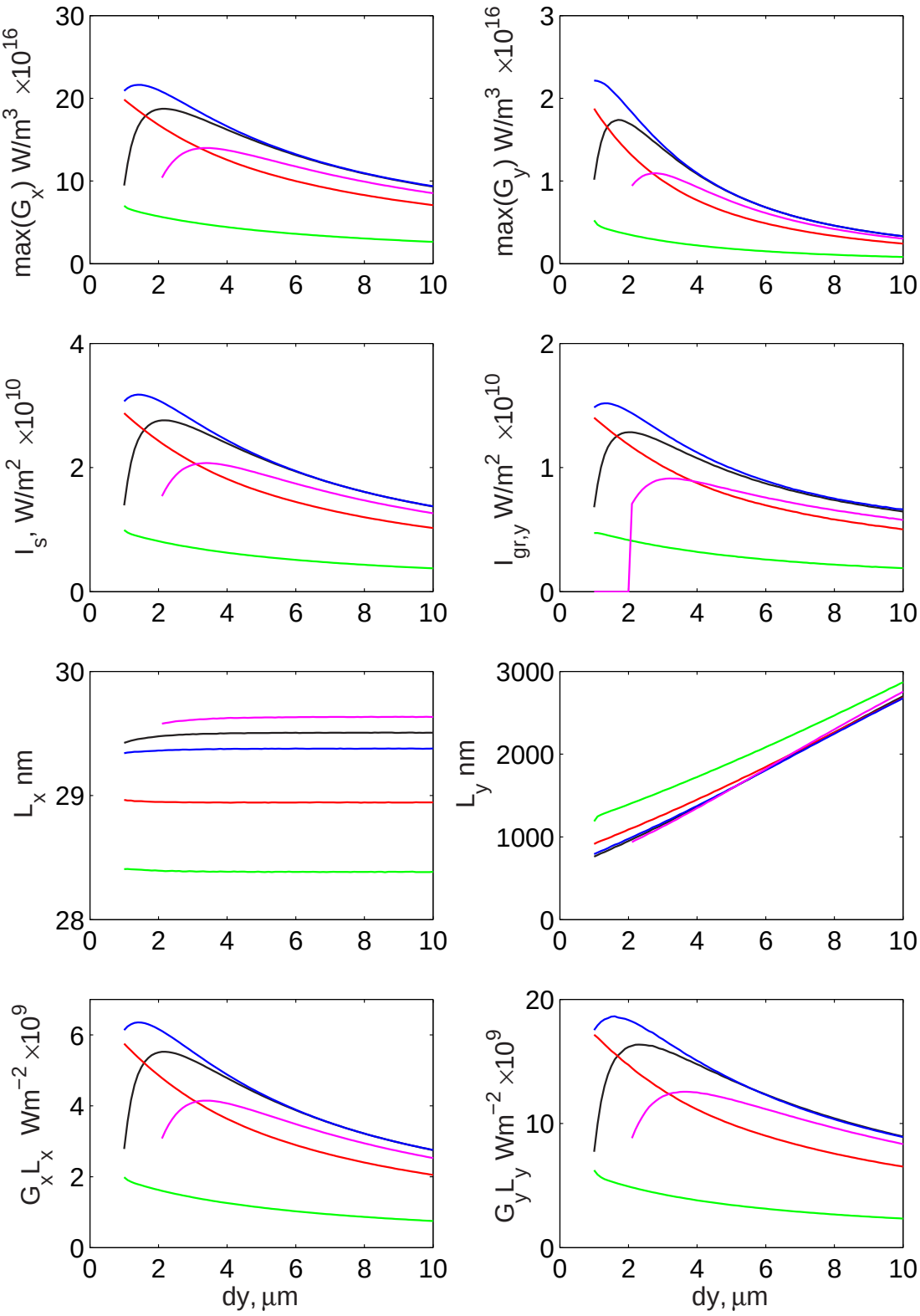

FIGURE 3.23: Graphs showing parameters concerning cross sections taken vertically (left) and horizontally (right) through the field at the surface as a function of the waveguide width, dy. The parameters from top to bottom are the maximum intensity gradients (G_x, G_y), the intensity at these points (I_s, $I_{gr,y}$), the length over which this force is roughly constant (L_x, L_y) and the product, GL. The different lines represent w= 0.9 (■), 1 (■), 1.1 (■), 1.5 (■), 2.5 (■) μm. Results for 1066nm with a cover of *water* .

effective index. The length factor in this dimension is purely a function of the relative indices of the mode and the superstrate, and the wavelength, since these can be used to calculate the form of the exponential decay of the evanescent wave (see section 3.2.2). As has been seen in section 3.5.4.1 the effective refractive index of the fundamental mode does not change by more than approximately 0.002 by varying dy which as a fraction of the effective refractive index of the mode (approximately 1.5) is very small.

Finally the effect of the depth, w, on the parameters that determine trapping strength is explained. Again generally speaking, as w increases the maximum intensity gradients and the intensities at these points, along with the length factors in the lateral dimension decrease, whilst in the transverse dimension the length factors increase. The decreases are again explained by the mode becoming larger as in the case of the increase in width, dy. In addition, more of the power of the mode will reside in the substrate as shall be seen below. The increase in the values of w shown are sufficiently significant to make relatively large changes to the effective refractive indices of the fundamental modes, and this explains the (small) decrease in the transverse length parameter.

As is seen by the case of w=0.9μm these general rules do not always apply. In this case at narrow widths a waveguide is close to its cut-off wavelength (as seen in section 3.5.4.3). As this is approached the mode expands (at the cut-off wavelength, theoretically the mode has an infinite mode size). This leads to the sharp fall-off in both the intensity and intensity gradient at this point.

This phenomenon can be seen below in figure 3.24 showing lateral cross-sections at the surface through the modal intensity distribution for w=1μm for a range of waveguide openings, dy, between 1 and 10μm. It shows that as dy increases so too does the width of the cross-section and the intensity above the centre of the waveguide decreases. It also shows that at values of dy less than approximately 2μm the beam expands slightly and the intensity above the centre decreases.

This combination of these trends implies that for a given width, dy, there is an optimum depth of waveguide, w, in terms of trapping particles in the evanescent superstrate. As there are limitations to the fabrication of the waveguide, a width of 3μm is taken to be the narrowest that may be fabricated. It can be seen that a depth of approximately 1.1μm is optimum in terms of the trapping parameter, τ. This combination will approximately give maximum intensity gradients of 20×10^{16} and 1.5×10^{16}W/m^3, intensities of 3×10^{10} and 1.3×10^{10}W/m^2 and trapping parameters, τ, of 5.5×10^{9} and 17×10^{9}W/m^2 , all per watt of modal power, in the transverse and lateral dimensions respectively.

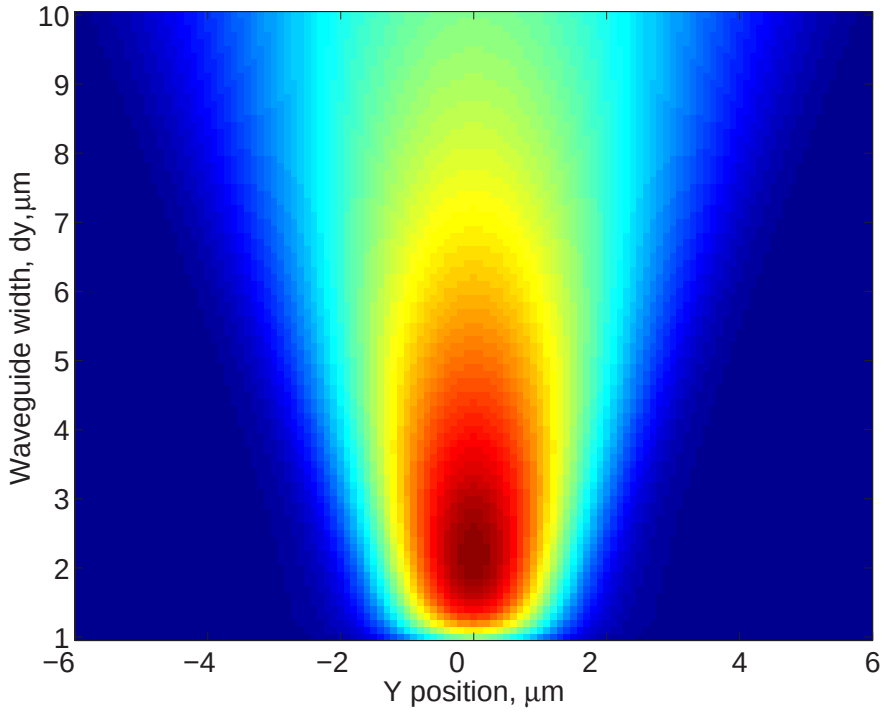

FIGURE 3.24: Series of cross sections of the intensity on the surface of a waveguide in water at 1066nm with width, dy. The depth of the waveguide w is 1μm and all other parameters are as described in figure 3.23.

3.6 Conclusions

This chapter has described and implemented two models to calculate the field for a given refractive index profile. The first was an analytical method, used to check the validity of the second more versatile model; that of a commercial BPM package. Planar waveguides were modelled by both methods and shown to give the same effective refractive indices for a range of forms of index profiles with a range of parameters.

By analysis of planar waveguides using the inverse WKB method, the refractive index profile for long ion-exchanged waveguides was established to be of a form similar to that described by a Fermi function. The parameters for this were calculated, leaving one parameter, w, as a variable that is used to describe differing ion-exchange conditions.

The fields of these planar waveguides were shown to be the same for both methods, and could be adequately described by one field (E_y in the case of TE polarisation and H_y in the case of TM polarisation).

The effective index method was used in conjunction with the multilayer method and the effective indices of channel waveguides were compared to those predicted by the BPM method. These were found to be in good agreement for wide waveguides but were found to vary substantially for narrow waveguides. The reason for this was the breakdown of the validity of the effective index method in these conditions. The refractive index model

of the waveguide was modified to additionally take into account the lateral diffusion into the waveguide using an isotropic diffusion approximation. The BPM package, having been sufficiently validated, was then applied to find the optimum waveguide conditions for trapping particles in water in the evanescent field of the waveguide.

From the complete field output by the BPM package, a range of conditions could be modelled from which much data could be elicited. The effective refractive indices, cut-off wavelengths and modal spot-sizes were modelled for a range of widths and depths. These are measurable parameters of a waveguide and thus may be used to compare to fabricated waveguides. The parameters that are determined by the waveguide and most strongly affect the trapping ability (i.e. the intensity gradient, the intensity at that point and a length factor over which this intensity gradient is roughly constant) were all examined along with the fraction of power in the superstrate. It was found that the refractive index of the superstrate made a large difference to these parameters with water giving much higher values than air.

Optimum conditions for the intensity gradient of a caesium ion-exchanged channel waveguide in soda-lime glass in water and operating at a wavelength of 1066nm were found to be with a waveguide with a diffusion depth of approximately 1.1μm diffused through a mask of approximately 3μm opening. With a depth less than this the effect of approaching cut-off was becoming significant where the waveguide ceased to effectively confine the modes. With depths greater than this, the mode was too well confined within the physical waveguide.

Chapter 4

Non-optical Forces on Particles

4.1 Introduction

In chapter 2 the origin of the optical forces that are used to both trap and propel gold and latex particles in the evanescent field of an optical channel waveguide was discussed. Chapter 3 examined the waveguide design and fabrication parameters that will affect these optical forces. This chapter firstly considers all the non-optical forces that will also act on the particle. It examines forces that would be present in any system containing particles held in a liquid, namely gravity, buoyancy and Brownian motion which are very well understood. It then uses mathematical models to examine forces more specific to this project; the electrostatic forces between the particles and surfaces and a drift induced by heating due to absorption of the laser radiation.

All of these non-optical forces are brought together and compared to the optical forces to predict both the ability to trap and to propel particles on an optical waveguide. Thus the aim of this chapter is to determine which of these forces are significant and thus should be optimised and to obtain some understanding of the particle sizes that may be trapped.

4.2 Gravity and buoyancy

Gravitational and buoyancy forces are widely understood and so are only discussed briefly here. The gravitational force on a particle acts downwards (in the negative x direction) and is given by:

$$F_{gr,x} = -\rho_s V g \tag{4.1}$$

where $g(= 9.81 ms^{-2})$ is the gravitational acceleration, ρ_s is the density and V, the volume of the particle.

Particle type	Radius (μm)	F_{gr} (N)	F_{bu} (N)	$F_{g,x}$ (N)
Gold	0.025	1.24×10^{-17}	6.40×10^{-19}	1.18×10^{-17}
Gold	0.05	9.92×10^{-17}	5.12×10^{-18}	9.41×10^{-17}
Gold	0.10	7.93×10^{-16}	4.10×10^{-17}	7.53×10^{-16}
Gold	0.25	1.24×10^{-14}	6.40×10^{-16}	1.18×10^{-14}
Latex	0.5	5.39×10^{-15}	5.12×10^{-15}	2.72×10^{-16}
Latex	1.5	1.46×10^{-13}	1.38×10^{-13}	7.35×10^{-15}
Latex	3	1.17×10^{-12}	1.11×10^{-12}	5.88×10^{-14}
Latex	6	9.32×10^{-12}	8.85×10^{-12}	4.70×10^{-13}

TABLE 4.1: Gravity, buoyancy and resultant forces for a range of particles.

The buoyancy force acting upwards is given by:

$$F_{bu,x} = \rho_m V g \tag{4.2}$$

where ρ_m is the density of the surrounding medium. The resultant force is therefore:

$$F_{g,x} = (\rho_s - \rho_m) V g \tag{4.3}$$

Table 4.1 shows values of these forces for a range of cases covering the particles used in the project in a medium of water. The values of density used are gold ($\rho_s = 19.31\times 10^3 \text{kgm}^{-3}$) [97], latex ($\rho_s = 1.05 \times 10^3 \text{kgm}^{-3}$) [98] and water ($\rho_m = 0.997 \times 10^3 \text{kgm}^{-3}$) [97].

The resultant force due to gravity and buoyancy is always in the downward direction as the density of both gold and latex are greater than that of water. The force increases with the volume of the particle (hence the cube of the radius). It is also worth noting that due to the density of latex being much closer to water than is gold, a much larger latex particle can have a smaller resultant force downwards. The ratio of the difference in density between gold and water and latex and water is approximately 370. This implies a gold particle has a resultant force equivalent to a latex particle with a radius seven times larger. This can be seen in the case of a 1μm latex particle having the same order of magnitude of force applied to it as 200nm gold particle.

4.3 Drag force

Axial forces due to the absorption and scattering of light were discussed in chapter 2. With no force to oppose these optical forces a trapped particle would continuously accelerate, a physical impossibility. The main force to oppose these optical forces is a drag force. This is caused by the viscosity of the medium in which the particles are held

(i.e. water). For a spherical particle of radius, a, this drag force can shown to be:

$$F_{dr} = 6\pi a\eta v \tag{4.4}$$

where η is the viscosity of the fluid and v is the speed of the particle. This force is called the Stokes' drag force and can be derived by considering the translational flow of fluid around a sphere. The conditions for this relationship to be applicable are that the relative flow be slow, steady and taking place in an unbounded Newtonian fluid [99]. The Reynold's number is given by $Re = VL\rho/\mu$, where V is the velocity, L, the characteristic length (the diameter of the spheres here), ρ the density and μ the dynamic viscosity. This parameter is a measure of flow where a value of much less than one indicates that the flow is slow and steady. This is undoubtedly satisfied for all the spheres used in this project, always having a value less than 10^{-3}.

On the second condition of the medium being unbounded, this is a reasonable approximation in the plane of the substrate, however perpendicular to this, the particle is clearly not unbounded, being within a few hundred nanometers of the waveguide. This has been shown both experimentally [100] and theoretically [101] to modify the diffusion coefficient of the particle, D(z) compared to that in an unbounded medium $D_0(z = \infty)$

$$\frac{D(z)}{D_0(z=\infty)} = 1 - \frac{9}{16}\frac{r}{r+z} + \frac{1}{8}\Big(\frac{r}{r+z}\Big)^3 - \frac{45}{256}\Big(\frac{r}{r+z}\Big)^4 - \frac{1}{16}\Big(\frac{r}{r+z}\Big)^5 \tag{4.5}$$

where r is the radius of the particle and z is the separation of the wall to the lower surface of the particle. Thus if the particle is virtually in contact with the wall, the diffusivity is reduced to about 33% of the unbounded value, thus representing a threefold increase in the effective viscosity compared with the tabulated bulk viscosity values, as the diffusion constant is inversely proportional to viscosity. The function is independent of any of the particle's properties other than its radius. The inverse of this function is plotted below in figure 4.1, showing the ratio η/η_∞ for the case of a 100nm particle and a 3μm particle.

The height that the particle is held above the waveguide is unknown, as shall be seen later in section 4.5. Here a height of approximately 20nm will be used for illustration. At heights much less than this a van der Waals force is likely to cause the particle to be adsorbed onto the surface as shall be seen later. Thus particle velocities observed in this work are likely to be 2-3 times lower than those predicted for an unbounded medium.

4.4 Brownian motion

A particle's Brownian motion is the resultant motion caused by it being randomly and constantly bombarded by many other particles (mainly water molecules in this project). The high rate at which water molecules collide (approximately 10^{11} collisions per second

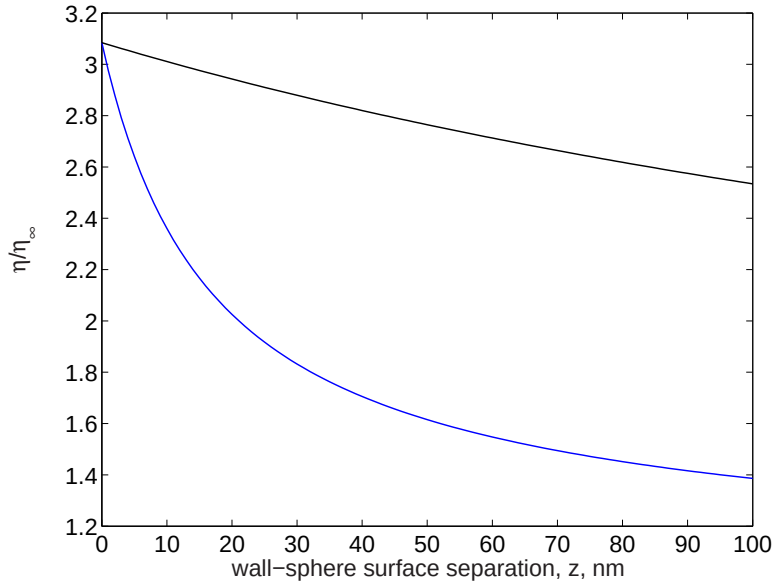

FIGURE 4.1: Increased viscosity due to presence of boundary for a 100nm particle (■) and a 3μm (■) particle.

for a water molecule) means that in the smallest time frame of interest to this project there will be so many collisions so as to make the force caused by these molecules effectively continuous. The force is also random and fast varying (both in terms of direction and magnitude). The form of this force is written as, MA(t) where M is the mass of the particle. The particle is also in a medium with a viscosity that acts to dampen the motion of the particle, as seen above. This force is proportional to the velocity and in the opposite direction of the motion of the particle and is written as, $-\beta M\dot{x}$. The overall force, $M\ddot{x}$, in one dimension is therefore [102]:

$$M\ddot{x} = -\beta M\dot{x} + MA(t) \tag{4.6}$$

By multiplying through by x and using various substitutions it can be shown that this gives:

$$\frac{1}{2}\frac{d^2}{dt^2}x^2 - (\dot{x})^2 = -\frac{\beta}{2}\frac{d}{dt}x^2 + xA(t) \tag{4.7}$$

By equipartition of energies:

$$\overline{(\dot{x})^2} = kT/M \tag{4.8}$$

By substitution of equation 4.8 into equation 4.7 and by integration:

$$\frac{\overline{d(x^2)}}{dt} = \frac{2kT}{M\beta} + Ce^{-\beta t} \tag{4.9}$$

where the bar represents a time-averaged factor and C is a constant. The exponential term describes the damping that would be required to fit an initial velocity and is not required here. Therefore by integrating the simple expression for the expected

Particle type	Radius (μm)	time (s)	RMS displacement (μm)
Gold	0.05	1	2.95
Gold	0.10	1	2.09
Gold	0.25	1	1.32
Gold	0.25	2	1.87
Gold	0.25	5	2.95
Latex	0.5	1	0.93
Latex	1.5	1	0.54
Latex	3.0	1	0.38
Latex	6.0	1	0.27

TABLE 4.2: Expected RMS Brownian motion of a range of gold and latex particles for a range of times.

displacement time first shown by Einstein in 1905 [103] is obtained:

$$\overline{x^2} = \frac{2kT}{M\beta}t \tag{4.10}$$

As above, for the special case of Stokes' law being satisfied:

$$M\beta = 6\pi a\eta \tag{4.11}$$

where a is the sphere's radius and η is the viscosity [102]. Substituting this in equation (4.10)

$$\overline{x^2} = \frac{kTt}{3\pi a\eta} \tag{4.12}$$

Imaging particles in two dimensions as with a standard microscope gives an RMS displacement given by:

$$\overline{(x,y)^2} = \frac{2kTt}{3\pi a\eta} \tag{4.13}$$

and the total displacement (in three dimensions) is:

$$\overline{(x,y,z)^2} = \frac{kTt}{\pi a\eta} \tag{4.14}$$

Examples of predicted root-mean-square (RMS) displacements in one dimension and in an unbounded medium are shown in table 4.2 using the values $k = 1.38 \times 10^{-23} JK^{-1}$, T=298K, $\eta = 1 \times 10^{-3} Pas$ [97].

As can be seen, as either the particle size increases or the duration of observation decreases, the expected displacement decreases. Less predictable are the actual magnitudes of these displacements. As an example if a particle is positioned directly over a waveguide with lateral spotsize of 5μm, then a 100nm particle would be expected to move from the centre to a lateral position where the intensity is $1/e^2$ of the peak intensity of

the evanescent field in 1.56 seconds. This compares to 3.5 seconds for a 500nm particle and 86 seconds for a 12μm particle.

4.5 Electrostatic and van der Waals forces

4.5.1 Introduction

Both latex and gold particles have a negative surface charge to prevent agglomeration. Therefore depending on the charge of the waveguides, the particle may be attracted or repelled. Both of these conditions are unwanted, as, if the waveguide is negatively charged the waveguide and particle will repel, pushing the particle away from the evanescent trapping field. In the case that the two are oppositely charged, they will attract and particles may become permanently attached to the waveguide. The magnitude of these forces with respect to the other forces is therefore of interest, as it is possible that this force could dominate in one of the afore mentioned cases. The electrostatic forces are separated into two parts, the van der Waals force and the double-layer force. The repulsion force described above is the simplest explanation of the double-layer force. The van der Waals force is a different manifestation of the gradient force described in chapter 2. It comes about by individual atoms/molecules inducing a field in close-by atoms/molecules. This fields interacts with the original field and thus the van der Waals forces always causes an attractive force.

The two components of the loosely termed 'electrostatic' forces are derived below following the book by Israelachvili [104]. It is considered important to describe this here to appreciate the approximations used and the relatively long-reaching effect of both forces when compared to that of individual atoms/molecules.

4.5.2 Derivations

4.5.2.1 The van der Waals force

Electrostatic van der Waals energies between two molecules decay with a rate of their separation to the power of six [104]. This would imply that the force was very short ranged. However, for larger bodies the relationship between the force to the distance can be much more gradual. For this project the case of concern is a sphere (the particle) approaching a plane surface (the waveguide). This can be derived by first considering a single molecule near a wall, and then summing over many such molecules. To do this the two geometries shown in figure 4.2 are used.

In the first instance of a single molecule near a wall as shown in figure 4.2a an elemental ring with radius, x is considered. The number of molecules in the ring is $2\pi\rho_1 x dx dz$

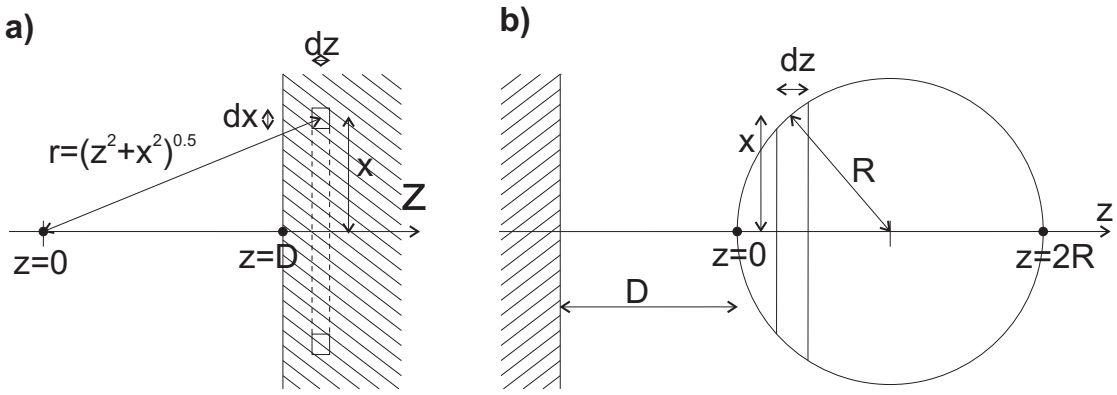

FIGURE 4.2: Models used to calculate electrostatic interaction between a) a molecule and a wall and b) particle and a wall.

where ρ_1 is the number density of molecules in the wall. If two molecules have an interaction energy between them of $w(r) = -C/r^n$ then the interaction energy between the molecule and the wall is given by [104]:

$$w(D) = -2\pi C\rho_1 \int_D^\infty dz \int_0^\infty \frac{xdx}{(z^2+x^2)^{n/2}} = \frac{2\pi C\rho_1}{(n-2)} \int_D^\infty \frac{dz}{z^{n-2}} \tag{4.15}$$

$$= \frac{2\pi C\rho_1}{(n-2)(n-3)D^{n-3}} \quad \text{for n>3} \tag{4.16}$$

for n=6 as in the case of van der Waals forces:

$$w(D) = -\frac{\pi C\rho_1}{6D^3} \tag{4.17}$$

Hence in this case the energy is proportional to $1/D^3$. Applying this to the case shown in figure 4.2b and using some geometrical approximations the case for a sphere of molecules can now be solved.

A section is considered with area, $\pi x^2 dz$. By chord theorem x^2 can be approximated to $(2R-z)z$ for $z \approx R$. This is reasonable as for individual molecules the energy decays with separation to the power of six, hence only the molecules closest to the wall are considered. The interaction energy between sphere and wall, W(D) is given by:

$$W(D) = -\frac{2\pi^2 C\rho_1\rho_2}{(n-2)(n-3)} \int_0^{2R} \frac{(2R-z)z}{(D+z)^{n-3}} dz \tag{4.18}$$

where ρ_2 is the number density of molecules in the sphere. For D$\ll$R, only small values of z contribute. Therefore using z$\approx$D:

$$W(D) = -\frac{2\pi^2 C\rho_1\rho_2}{(n-2)(n-3)} \int_0^\infty \frac{2Rz}{(D+z)^{n-3}} dz \tag{4.19}$$

$$= -\frac{4\pi^2 C\rho_1\rho_2 R}{(n-2)(n-3)(n-4)(n-5)D^{n-5}} \tag{4.20}$$

and for the case of the van der Waals forces (n=6):

$$W(D) = -\frac{\pi^2 C \rho_1 \rho_2 R}{6D} \tag{4.21}$$

Thus in the case of a particle being in the close presence of a wall, the energy only decreases in proportion to $1/D$. The term $\pi^2 C \rho_1 \rho_2$ is termed the Hamaker constant, A, and as can be seen the energy (along with the force) of the van der Waals force is directly proportional to this.

The force can be obtained as the partial differential of the energy with respect to the distance:

$$F = \frac{\partial W(D)}{\partial D} = \frac{\pi^2 C \rho_1 \rho_2 R}{6D^2} \tag{4.22}$$

Thus the van der Waals force is proportional to $1/\mathrm{D}^2$ and is therefore much more long-range than would initially be expected.

4.5.2.2 The double-layer force

The van der Waals forces do not require any charge to be present, however the surface charge on both gold [2] [105] and latex particles [98], [106] is known to be negative. This is a design requirement of the particles, required to stop particles agglomerating by the van der Waals forces described above. In the case of unmodified glass the charge is also typically negative. This is due to hydrogen ions from the water penetrating into the glass and replacing alkali ions by the following process [107, 108]:

$$\equiv Si - ONa + H_2O \quad \rightleftharpoons \quad \equiv Si - OH + Na^+ + OH^- \tag{4.23}$$

At a pH of 7 the silanol groups can deprotonize to form a negative surface due to the O^- ions left at the surface. However the situation for a surface modified by ion-exchange is unknown.

In addition to the charges present on the surface of the solids, the medium in which the particles are held, i.e. water, will partially dissociate to a solution containing 10^{-7}M of $\mathrm{H_3O^+}$ and $\mathrm{OH^-}$ ions, meaning that it must be considered as a (weak) electrolyte [104].

The surface charges attract the oppositely charged ions and repel the like charged ions in the electrolyte, thus at equilibrium a profile of each ion concentration is formed. This profile can readily be described by the following Boltzmann-type expression:

$$\rho_{xi} = \rho_{\infty i} \exp(-\frac{z_i e \psi_x}{kT}) \tag{4.24}$$

where ρ_{xi} is the concentration of the i ions at position x, $\rho_{\infty i}$ is the concentration of i ions in the bulk electrolyte, z_i is the valency of the ions, e, the charge of an electron and ψ_x the electrostatic potential at x.

In addition the Poisson equation is required, giving the net excess charge density at x:

$$ze\rho = -\epsilon\epsilon_0 \frac{d^2\psi}{dx^2} \tag{4.25}$$

Combining equations 4.24 and 4.25 the Poisson-Boltzmann equation is obtained:

$$\frac{d^2\psi}{dx^2} = -\frac{ze\rho_0}{\epsilon\epsilon_0} \exp(-\frac{ze\psi}{kT}) \tag{4.26}$$

For a surface with charge density, σ, the total concentration of ions is given by the Grahame equation:

$$\sum_i \rho_{0i} = \sum_i \rho_{\infty i} + \frac{\sigma^2}{2\epsilon\epsilon_0 kT} \tag{4.27}$$

For a monovalent pair of ions such as H_3O^+/OH^- or Na^+/Cl^- this can be rearranged in terms of σ^2 for the case of NaCl as follows:

$$\sigma^2 = 2\epsilon\epsilon_0 kT(\sum_i \rho_{0i} - \sum_i \rho_{\infty i}) \tag{4.28}$$

$$= 2\epsilon\epsilon_0 kT(\exp(-\frac{e\psi_0}{kT})[Na^+]_\infty + \exp(+\frac{e\psi_0}{kT})[Cl^-]_\infty - [Na^+]_\infty - [Cl^-]_\infty) \tag{4.29}$$

$$= 8\epsilon\epsilon_0 kT[NaCl]\sinh^2(\frac{e\psi_0}{2kT}) \tag{4.30}$$

using $[NaCl]=[Na^+]_\infty=[Cl^-]_\infty$.

This gives the potential gradient (or electric field):

$$\frac{d\psi}{dx} = \sqrt{\frac{8kT\rho_{\infty i}}{\epsilon\epsilon_0}} \sinh\left(\frac{e\psi_x}{2kT}\right) \tag{4.31}$$

integrating using $\int \cosh X\, dX = \ln \tanh(X/2)$ gives:

$$\psi_x = \frac{2kT}{e} \ln\left[\frac{1+\gamma\exp(-\kappa x)}{1-\gamma\exp(-\kappa x)}\right] \tag{4.32}$$

$$\approx \frac{4kT}{e}\gamma\exp(-\kappa x) \tag{4.33}$$

where κ^{-1} is the characteristic decay length of the electric field and is called the Debye screening length and $\gamma = \tanh(ze\psi_0/4kT)$. In the case of two parallel surfaces with the same surface charge, σ, separated by distance, D, the pressure (force per unit area) between the surfaces is given by:

$$P_x(D) - P_x(\infty) = -\frac{1}{2}\epsilon\epsilon_0[(\frac{d\psi}{dx})^2_{x(D)} - (\frac{d\psi}{dx})^2_{x(\infty)}] + kT[\sum_i \rho_{xi}(D) - \sum_i \rho_{xi}(\infty)] \tag{4.34}$$

This can be manipulated similarly into the following form:

$$\begin{aligned} P &= kT\rho_\infty[(\exp(-\frac{e\psi_m}{kT}) - 1) + (\exp(+\frac{e\psi_m}{kT}) - 1)] \\ &\approx \frac{e^2\psi_m^2\rho_\infty}{kT} \end{aligned} \tag{4.35}$$

where ψ_m, is the potential mid-position between the two planes. By substituting for ψ_m using equation (4.33), equation (4.35) can be written as:

$$P = 64kT\rho_\infty\gamma^2\exp(-\kappa D) \tag{4.36}$$

Although the expression was derived for the case of two identical surfaces, for two differing surfaces a similar expression to equation 4.36 is obtained, with γ^2 being replaced by $\gamma_1\gamma_2$.

Integrating equation 4.36 gives an expression for the energy (per unit area) between the two planes of:

$$W = \frac{64kT\rho_\infty\gamma^2}{\kappa}\exp(-\kappa D) \tag{4.37}$$

The force between a sphere and a wall can be calculated from this by the relationship, F(D)=2πRW(D) that is applicable to this geometry [104]. This may then be integrated to give an absolute expression for the energy.

$$F = \frac{128\pi RkT\rho_\infty\gamma^2}{\kappa}\exp^{-\kappa D} \tag{4.38}$$

$$W = \frac{128\pi RkT\rho_\infty\gamma^2}{\kappa^2}\exp^{-\kappa D} \tag{4.39}$$

It is noted then that the force decays exponentially with D and is proportional to the radius of the particle.

The origin of the force could intuitively be believed to be due to the surface charge on the solids electrostatically repelling, however this is not the case. The force is actually entropic with the electrostatic component being attractive. This can be better understood by considering two surfaces with a dielectric liquid between. As can often happen, ions may dissociate to an equilibrium concentration making the surfaces charged, and the liquid an electrolyte. If these two surfaces are now pushed together the dissociated ions are being pushed closer to the surface, contrary to their equilibrium position, but clearly favored by purely electrostatic considerations. Therefore the force opposing this electrostatic attraction is entropic (osmotic).

4.5.2.3 Derjaguin, Landau, Verwey and Overbeek theory

The Derjaguin, Landau, Verwey and Overbeek (DLVO) theory requires no more derivation. It is simply the combination of the double-layer forces and the van der Waals forces discussed in the above two sections and is named after Derjaguin and Landau [109], and Verwey and Overbeek's [110] work on colloidal stability.

There are restrictions to the above derivation. For example it has been found to break down at very small distances. The reason for this is that there are other factors, namely ion-correlation effects (where a highly polarizable, conducting double-layer can have attractive van der Waals forces that are not taken into account here), image forces (in the case of the solid having a lower permittivity that the medium) and steric, solvation and other effects that are not accounted for. In addition, approximations were made in a number of other steps for example the approximation in equation 4.35, where ψ_m is assumed small. The effect that this has is to further reduce the range over which the equations are applicable, to values of D greater than κ.

As has been shown in the two sections above, the van der Waals force is attractive and will overcome the double-layer force for small distances as it obeys a power law with relation to separation whereas the double-layer force has an exponential dependence.

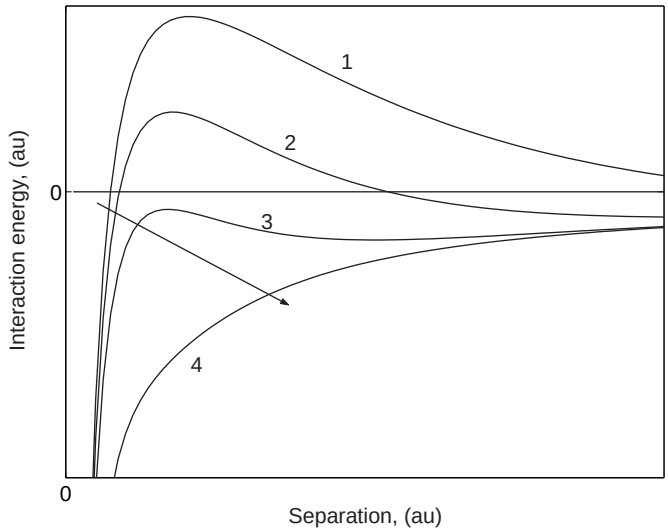

FIGURE 4.3: Interaction energy as a function of distance for varying surface energies for a particle approaching a surface in an electrolyte. The arrow indicates decreasing surface energies.

The combination of these two effects is shown schematically in figure 4.3, showing four cases of a decreasing surface potential (or surface charge). In the first case the energy is positive, until the particle gets close enough to be attracted by the van der Waals force and attach to the surface. Therefore the particle will be repelled from the surface, except in the highly improbable case that it gets very close to the surface, in which case it will be strongly attracted and will adhere. In the second case there is a minimum

Material	Hamaker constant, A, $\times 10^{-20} J$
Gold	40
Polystyrene	6.6
Glass	6.5
Water	3.8

TABLE 4.3: Individual Hamaker constants for materials used.

in the energy curve away from the surface. A particle is attracted to the surface up to this secondary minimum. The height of the energy barrier then determines the expected time for the particle to come into contact with the surface, if at all. If the secondary minimum is very weak the particle will remain dispersed in the solution. If it is very strong the particle will be stably held away from the surface. In the third case, the energy barrier is removed and particles can approach the surface unobstructed. In the final case, the surface charge approaches zero and the particle rapidly comes into contact with the surface.

In this analysis the van der Waals force is kept constant and the surface potential varied, however a similar analysis could be made in the case of the van der Waals force being varied with the surface potential kept constant. This therefore shows that the relative strengths of the van der Waals attractive force and the double-layer repulsive force is critical in determining which of the four cases outlined above occur. The four cases are all distinct, with the ideal case for this project being that of the second case, where the particles are attracted up to a certain point but then an energy barrier inhibits their coming into contact with the surface and thus the risk of adhesion to the surface.

4.5.3 Results from DLVO theory

Although data for the specific case in this project is not available, use can be made of published results for similar cases. The only value that is required for the van der Waals forces is the Hamaker constant, A, which can be roughly estimated from the permittivities of the three individual components (glass, gold and water) as [104]:

$$A_{\text{particle, glass, water}} = (\sqrt{A_{\text{particle}}} - \sqrt{A_{\text{water}}})(\sqrt{A_{\text{glass}}} - \sqrt{A_{\text{water}}}) \tag{4.40}$$

The values used here are calculated from the individual Hamaker constants tabulated in table 4.3 and taken from reference [104]. Using these values in equation 4.40:

$$A_{\text{gold, glass, water}} = 2.63 \times 10^{-20} J \tag{4.41}$$

$$A_{\text{polystyrene, glass, water}} = 0.37 \times 10^{-20} J \tag{4.42}$$

The case of the electric double-layer is somewhat more complicated due it being highly

dependent on the specific conditions. However here the aim is only to obtain an estimate of the forces, not necessarily the exact values. The main requirement is an expression for the potential, ψ, for the surfaces. However, this quantity is not directly measurable. It can be calculated from the surface charge density, σ_0 of a surface if this value is low. However such data is generally not available apart from for polystyrene particles where the surface density of sulphate groups is given by the manufacturers. The data that is available (due to it being a measurable factor) is the zeta potential, ζ, and it is this value that is used as the surface potential. This is a measure of the surface potential a very small distance away from the surface (of the order of 1nm), and is sometimes referred to as the shear potential. This is because it is a measure of the potential at a distance where the ions within the layer are dragged along with the motion of the particle (called the Stern layer).

Table 4.4 lists the zeta potentials for the various materials along with their references. As can be seen in work by Gu and Li [111] the zeta potential of a glass surface is very dependent on the ion concentration in the water and the pH of the water as would be expected. In this analysis, the pH is assumed to remain at pH of 7, however the ion-concentration is varied. The zeta potential of polystyrene is not found to be pH dependent (at least not above a pH of 2) [112].

An important consideration regarding the choice of parameters is that the DLVO theory breaks down for separations less than 1 Debye length. The Debye length for a monovalent ion pair can be approximated as:

$$1/\kappa = 0.304/\sqrt{[\mathrm{H_3O^+}]}nm \tag{4.43}$$

Thus in very pure water ($[\mathrm{H_3O^+}]$=10^{-7}M) a Debye length of almost 1μm is obtained. As the optical field only penetrates 200nm, the theory outlined above is hardly relevant to the case of pure water. However, in the process of gold particle fabrication, gold ions and chloride ions are byproducts of the process [105], thus despite dilution in deionised water, there will still be a concentration of monovalent ions higher than 10^{-7}M. In addition, in the geometry of this project, the thin water layer is in contact with two large glass surfaces, which will immediately dissociate ions e.g. Na^+, into the water, thus further raising the ion concentration. At a still very low concentration of 5×10^{-5}M, the Debye length has reached 135nm, above which DLVO theory is applicable and at a concentration of 10^{-3}M NaCl, the Debye length is just 9.6nm.

Using these values, it is now possible to plot the double-layer and van der Waals forces at a range of ion concentrations and the results are shown in figure 4.4 for the case of a 200nm gold particle and in figure 4.5 for the case of 3μm latex particle.

These plots show that as the concentration of ions in the medium increases, the repulsion force between particle and substrate decreases rapidly for separations greater than about 20nm. This phenomenon is well known and is called 'screening'. It suggests that in

Material	Concentration M	Zeta potential ζ, mV
Gold	-	-47 [113], [114]
Polystyrene	-	-85 [112]
Glass	$5\times\ 10^{-5}$	-35 [111]
Glass	$1\times\ 10^{-4}$	-30 [111]
Glass	$5\times\ 10^{-4}$	-23 [111]
Glass	$1\times\ 10^{-3}$	-22 [111]

TABLE 4.4: Zeta potentials of the materials used for DLVO calculations.

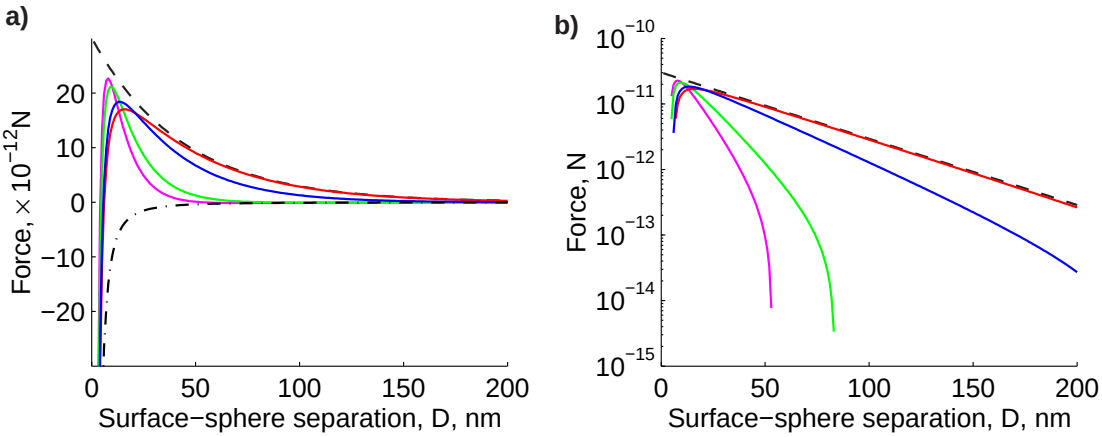

FIGURE 4.4: a) The double-layer (- -) and van der Waals (- ·) forces of the DLVO theory between a glass surface and a 200nm gold particle in water with a $5\times\ 10^{-5}$M concentration of monovalent ions and the sum of these forces(■). Also plotted are the sums of the forces for concentrations of $1\times\ 10^{-4}$M (■), $5\times\ 10^{-4}$M (■), and $1\times\ 10^{-3}$M (■). Plot b) shows the log of these forces (where positive).

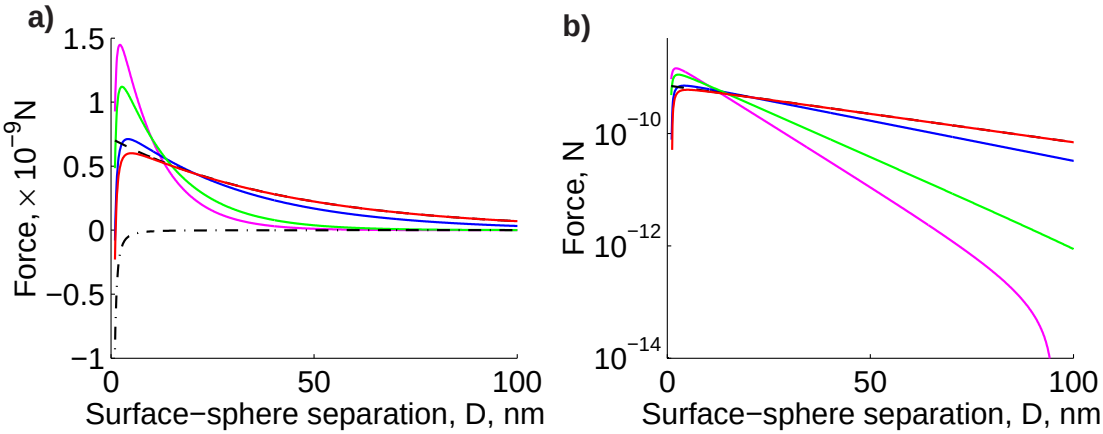

FIGURE 4.5: a) The double-layer (- -) and van der Waals (- ·) forces of the DLVO theory between a glass surface and a 3μm polystyrene particle in water with $5\times\ 10^{-5}$M concentration of monovalent ions and the sum of these forces(■). Also plotted are the sums of the forces for concentrations of $1\times\ 10^{-4}$M (■), $5\times\ 10^{-4}$M (■), and $1\times\ 10^{-3}$M (■). Plot b) shows the log of these forces (where positive).

order to minimize the repulsion forces and allow particles to approach the surface, it is necessary to have ions in the aqueous medium. This has been shown experimentally by Odiachi and Prieve [106] for the case of latex particles approaching a glass wall in water.

In this project therefore the concentration of ions should be as high as possible so as to minimize the energy required for a particle to come close to the surface. However as shall be shown in chapter 6 there is a limit to this, above which particles start to adhere to glass surfaces.

4.5.4 Summary

Whilst there is uncertainty over the values of the parameters used here, rather than go into this in great depth values have been selected, that seem in agreement with several groups. The results shown here should not be used in too predictive a form, but more as indicative of the trends that can be observed. It should also be noted that the gravitational force is not taken into account here that will act to bring the equilibrium height of the particle closer to the surface than implied here.

This section has shown that the effect of the surface charges of the glass and the particle is to cause the two to repel each other. This force is counteracted by the van der Waals force and, at a separation of less than about 10nm the van der Waals force is greater. The implication of this is that for a height of particle above the waveguide of less than 10nm it is likely to be strongly attracted and adhere to the glass surface. If the particle is at a greater separation than this it will be repelled with a force that decays with the separation from the surface. However it was shown that electronic screening, due to ions in the solution in which the particles are held, can vastly reduce the double-layer repulsive force at a separation above approximately 20nm.

4.6 Fluid-flow due to convection

4.6.1 Introduction

The use of a laser for trapping and propelling particles is critical. Due to the very high intensities supplied by a laser, a heat energy study is worthwhile as gold particles have a significant optical absorption. In addition, both the glass of the waveguide and the water through which the evanescent field travels will partially absorb the laser light. If there is some local heating then the density of the water will change [115] leading to convection currents being induced in the water [116]. This section analyses the steady-state temperature profile expected. In doing this some fundamental approximations are used and these are described below.

The first approximation is that the situation is static, i.e. that the temperature distribution is not altered by the fluid flow, and that the particle is stationary. Secondly the heating is modelled by two separate models. These are that the absorption (and thus heating) is caused solely by gold particles on the waveguide and the second is that the absorption is carried out solely by the waveguide.

These are the main approximations, however there are others, to do with the geometry of the situation being modelled, the parameters used (for example most are considered temperature insensitive), scattered light is considered not to be absorbed etc.

4.6.2 Heat diffusion theory

In order to confirm the accuracy of the model an analytical solution is obtained. To simplify the analytical model the case of a gold particle surrounded infinitely by water is used (the glass substrate is omitted from the analysis).

The analytical solution uses diffusion theory with spherical coordinates. Diffusion theory was discussed previously in sections 3.3. In spherical coordinates, the diffusion equation is [87], [110]:

$$\frac{\partial T}{\partial t} = \frac{\alpha}{r^2}\{\frac{\partial}{\partial r}(r^2\frac{\partial T}{\partial r}) + \frac{1}{\sin\theta}\frac{\partial}{\partial\theta}(\sin\theta\frac{\partial T}{\partial\theta}) + \frac{1}{\sin^2\theta}\frac{\partial^2 T}{\partial\phi^2}\} \tag{4.44}$$

where $\alpha = k/\rho c_p$, k is the conductivity, ρ the density and c_p the specific heat capacity.

For conduction only in the radial direction, where the isothermals would be concentric spheres, this reduces to:

$$\frac{\partial u}{\partial t} = \alpha\frac{\partial^2 u}{\partial r^2} \tag{4.45}$$

where the substitution u=Tr has been used. Here the approximation that the sphere generates a constant rate of heat is used. If the particle generates heat at a rate of $\dot{Q}$ per unit volume, has a radius, a, and a conductivity K_0, whilst the medium has no heat generation and a conductivity, K, and the contact (thermal) resistance between the two is R per unit area, then it can be shown that the temperature distribution is given by [110]:

$$\Delta T = \begin{cases} \frac{\dot{Q}}{6K_0}\{a^2 - r^2 + 2RaK_0 + 2a^2(K_0/K)\} & 0 \le r < a, \\ \frac{\dot{Q}a^3}{3Kr} & r > a. \end{cases} \tag{4.46}$$

The value of $\dot{Q}$ is derived from the absorption cross-section and the estimated intensity as described previously by equation 2.50. For a 200nm gold particle C_{abs}=2.5×10^{-15}m^2. The intensity used, 3×10^{10}W/m^2 per watt of modal power, is from the peak value in figure 3.23. Thus if 100mW modal power is used a value of $\dot{Q}$ of 1.79×10^{15}W/m^3 is obtained.

Material	Gold	Water	Glass
Density , ρ	19300	1000	2230
Thermal conductivity, K	310	0.61	1
Heat capacity, c_p	145	4180	800

TABLE 4.5: Parameters used to model heating. All values are given in SI units.

For K=0.61W/m^{0}C a steady-state change of temperature at the surface of the sphere of approximately 9.8^{0}C is expected, and at a distance 2μm from the centre of the sphere, the temperature change in the water is 0.49^{0}C. This result will be used as a check of the numerically modelled results described below.

4.6.3 Modelling method and parameters

The modelling of the temperature profile was carried out using Ansys, a commercial finite element software package. The separate cases of modelling the temperature profile due to gold absorption and due to the waveguide absorption are described below.

4.6.3.1 Gold absorption

The geometry for the case of gold absorption was first constructed making use of the four-way symmetry existing. The origin is at the point of contact of the particle to the waveguide surface. A quarter sphere is therefore used to model the gold particle, and two cubes were used to model the water and glass, the water having the quarter sphere subtracted from it.

Table 4.5 shows the material properties for the three materials used (values from [97]). The heat generation rate for the gold sphere was 1.79×10^{15}W/m^3, as given above.

The objects were meshed into eight-noded blocks. The boundary and initial conditions were that, at the external edges of the cubes, the temperature was taken to be the initial temperature of 25^{0}C. The cubes were made sufficiently large for this to be a reasonable approximation. The model conditions (type of analysis, method of analysis etc.) were set as recommended and the steady-state solution obtained.

4.6.3.2 Glass absorption

Modelling the absorption of laser light by the waveguide is simpler as it may be reduced to two dimensions. Figure 4.6 shows a schematic of the geometry used in the model which was meshed with a four-noded tetrahedral.

For the case of the waveguide absorbing the laser light a loss of 1dB/cm is used. This is an upper limit as most of the propagating loss of the waveguide is expected to be due

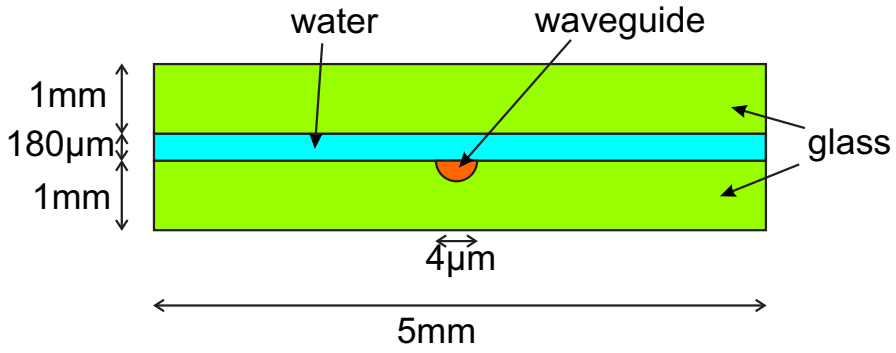

FIGURE 4.6: Schematic of the model and geometry used for glass absorption.

to scattering. For 100mW modal power this gives a loss of approximately 10.8mW/cm. This is lost in an area given by $\pi r^2/2$, which for a waveguide modelled as a semicircle with a radius of 2μm gives an area of 6.3μm^2. This gives a heat generation rate of 1.72×10^{11}W/m^3.

The initial condition is again that all bodies have a temperature of 25^0C. The boundary conditions used here are that heat is lost from the top and bottom surfaces to the surrounding air and at the sides of the model to similar material. All media surrounding the model are assumed fixed at 25^0C. The heat loss to the air is given by use of a film coefficient with a value of $3\text{Wm}^{-2}K^{-1}$ [117].

4.6.4 Modelling results

4.6.4.1 Temperature profile due to gold absorption

A vertical cross-section through the centre of the sphere is shown below in figure 4.7. This was for the case of a 200nm gold particle absorbing energy at a rate, $\dot{Q}$, of 1.79×10^{15}W/m^3.

As can be seen from figure 4.7 the temperature change falls rapidly away from the surface and 2μm from the surface the temperature is just 0.45^0C greater than the background temperature. This is in very good agreement with the analytical value predicted above and shows that the effect of having a glass surface below (with slightly different thermal values) is not significant on this length scale.

4.6.4.2 Temperature profile due to glass absorption

The temperature profile for the case of the waveguide absorbing 1.72×10^{11}W/m^3 is shown below in figure 4.8 where false colours have been used. Figure 4.9 shows the vertical cross-section through the centre of the waveguide.

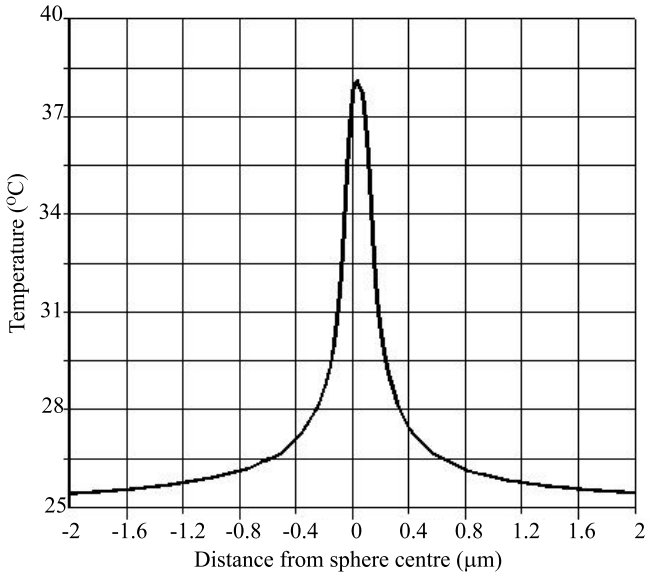

FIGURE 4.7: A vertical cross section of the temperature profile caused by absorption by a gold sphere through the centre of the particle.

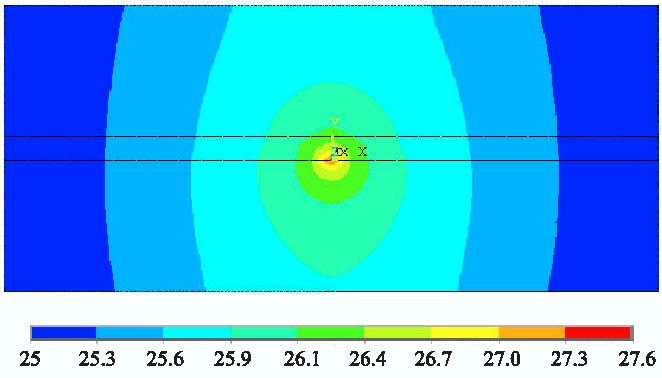

FIGURE 4.8: Temperature profile caused by heat generation due to the waveguide absorbing laser radiation. The total simulated area shown here 5mm (width)×2.18mm(height).

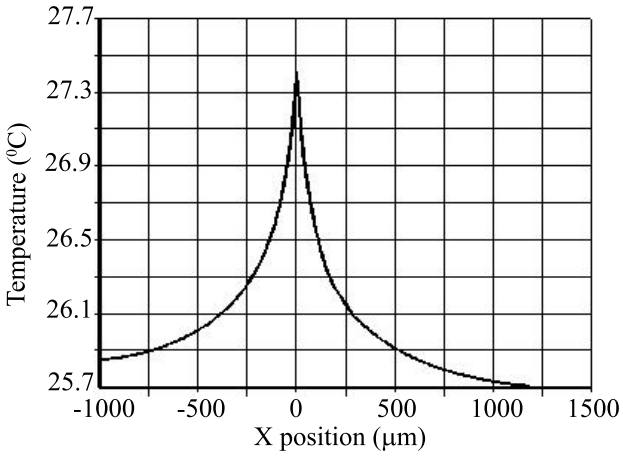

FIGURE 4.9: A vertical cross section through figure 4.8 showing the temperature profile through the centre of the waveguide.

Figures 4.8 and 4.9 show that the peak temperature rise is approximately 2.5^0C for the case described. It also shows that the temperature drop through the 180μm water is greater than that through the glass (as would be expected due to its greater thermal conductivity).

4.6.5 Discussion

This section has examined the heating caused by both a gold particle in the peak intensity evanescent field and by absorption by the waveguide. In both cases a 100mW modal power was assumed. The temperature rise due to the gold particle was greater (approximately 13^0C) compared to that caused by the waveguide (approximately 2.5^0C). However the temperature rise caused by the glass was much further reaching. The temperature rise caused by the waveguide fell to approximately 40% of its peak value over a distance of 500μm whereas that caused by the particle fell to approximately 3.5% its peak value in 2μm. Therefore it is expected that the absorption caused by the waveguide will be likely to cause drift than that of the gold particles. The rate of temperature drop through the water was greater than through glass due to the greater conductivity of water, however this was less apparent on the scale evaluated for absorption by the gold sphere. It should be noted that the situation was modelled as a static case with the steady-state solutions being found, which is not the case for the gold particle. This does however give a value for the maximum temperature difference that could be expected.

The temperature rise would be expected to scale linearly with modal power and thus for a modal power of 1W, temperature changes in the order of 25^0C due the waveguide absorption would be expected. However this power would also cause the water surrounding a gold particle to boil (assuming static fluid conditions).

The paper by Duhr and Braun [116] uses a very similar model to that used here i.e. heating of a wide thin cell of water surrounded by glass and sapphire using a 100mW IR laser (operating at 1405nm). In their case however the beam was focussed into the centre of the chamber and modelled. A temperature of up to 62^0C was predicted due to the absorption of water (which is much greater at this wavelength). In this paper they observed natural flow due to convection, which resulted in a strong build up of 2μm latex particles at the base of the cell to a radius of 200μm.

This effect of natural convection may be beneficial to this project as it would be expected to draw particles towards the waveguide from a greater distance than can be effected by the optical field. The disadvantage of this type of convection flow is that as the particle approaches the waveguide laterally there will be also be a transverse component to the flow which will act to take the particle transversely away from the waveguide.

4.7 Balance of forces

In chapter 2 expressions for the optical forces were examined and some numerical results were given based on typical values expected. In chapter 3, the form of the electromagnetic field in the superstrate was explored in some detail using results from the simulations of a BPM package. In light of the data from these three chapters it is now possible to give a prediction both in terms of how well a particle is trapped and how fast it is likely to travel. This section therefore concentrates on three important parameters. These are the transverse trapping ability, the lateral trapping, and the expected speed in the direction of propagation of gold particles.

4.7.1 Ability to trap particles

The trapping force can be separated into two components. The force in the x direction has four principal components to it, these are the transverse gradient force, gravity, an electrostatic attraction or repulsion and a destabilising Brownian motion. The gravitational and electrostatic forces have no component in the lateral, y direction, but there is still a lateral gradient force and Brownian motion. The electrostatic force has been omitted from the following analysis, due to the complexity of the force and due to the values being uncertain for small separations. The trapping forces are only considered for the case of gold particles as expressions for the optical forces for Mie particles in an evanescent field were not obtained.

Ideally a force would be obtained for Brownian motion that could be directly compared to other forces such as the optical forces and would therefore determine whether a particle would theoretically be trapped. However even with a very large trapping force the particle will still have random motion. The approach taken here is to look at the distance travelled under different force conditions and is a method modified from that of Hughes et al. [118], in their case for the application to dielectrophoretic trapping.

In this approach the time taken, t_{br}, for a particle to be expected to travel a distance, d, in one dimension is calculated as shown in section 4.4. Similarly the time taken, t_{tr}, for the trapping force, F_{tr} to move the particle the same distance, d, is calculated using Stokes' theory.

In the case of an optical trap:

$$t_{br} = \frac{3\pi a \eta d^2}{kT} \tag{4.47}$$

$$t_{tr} = \frac{6\pi a \eta d}{F_{tr}} \tag{4.48}$$

Parameter	Dimension	Value (S.I. units)
Gradient	x	20×10^{16}
Gradient	y	1.5×10^{16}
Length	x	29.3×10^{-9}
Length	y	960×10^{-9}
Modal power	-	1
Wavelength	-	1.066×10^{-6}
Effective index	-	1.51

TABLE 4.6: Parameters used for predicting the ability to trap a gold particle.

For a particle to be trapped clearly t_{tr} should be much less than t_{br}. τ is defined as:

$$\tau = \frac{t_{br}}{t_{tr}} = \frac{F_{tr}d}{2kT} \tag{4.49}$$

The ratio, τ, required for a particle to be 'trapped' is clearly rather arbitrary, and in [118] a factor of 10 is used. This method has the advantage of taking into account the distance over which the force acts. To explain this, consider a large gold particle in water in a cell. Gravity will act on it throughout the cell whilst the optical gradient force in the transverse direction will act only over a distance of a few hundred nanometers. Therefore to consider simply the magnitude of the forces is over-simplistic.

Here the parameter, d, is given by L, the parameter that was introduced in chapter 3. This explains the relevance of the parameter, ∇IL from section 3.5.5 as the trapping force is proportional to ∇I.

From section 3.5.5 values for the maximum intensity gradient and the length over which this is roughly constant are obtained. The values used are detailed in table 4.6.

Values of τ/d are plotted below in figure 4.10 along with the gradient and gravitational forces for a range of particle radii.

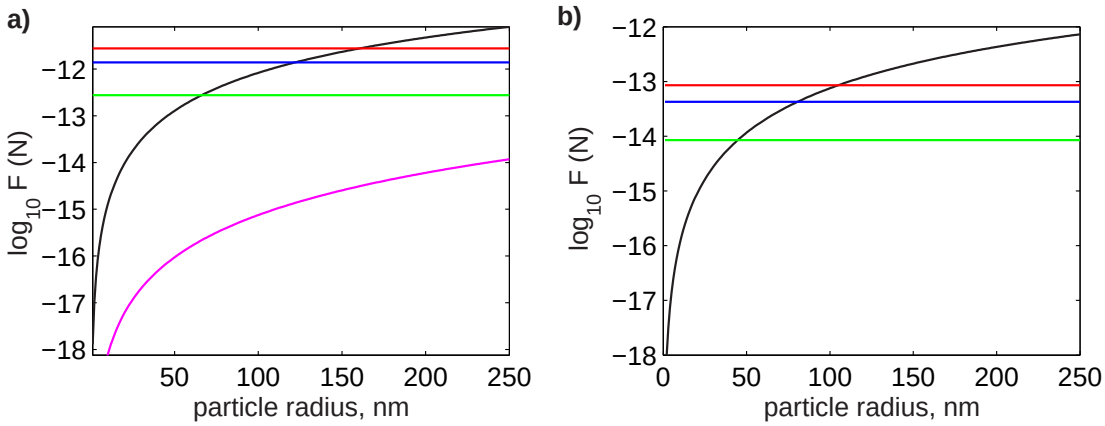

FIGURE 4.10: a) Transverse and b) lateral analysis of Rayleigh forces and Brownian motion. The lines represent gradient (■) and gravitational/buoyancy (■) forces and equivalent forces required to overcome Brownian motion with values of τ/d (see equation 4.49) of 10 (■), 5 (■) and 1 (■).

Power	τ	x intercept, nm	y intercept, nm
1	10	160	105
1	5	122	80
1	1	66	45
0.3	10	-	169
0.3	5	198	128
0.3	1	104	70
0.1	10	-	-
0.1	5	-	200
0.1	1	161	105

TABLE 4.7: Radii at which values of τ would be obtained for various powers in both the transverse (x) and lateral (y) dimensions ('-' indicates the value is greater than 250nm).

Considering figure 4.10 a comment should be made about the resultant gravitational/buoyancy force. The force is shown to be much smaller than the corresponding gradient force for the parameters used, however it should be noted that gravity will act everywhere, in contrast to the gradient force which only acts over 29nm in this case. Figure 4.10 does not take this into account. A possible solution to this is to consider that the requirement for trapping is that the particle remains in the evanescent field of the waveguide. However as the evanescent field, by definition, tends to zero, this solution is not straightforward. An assumption that could be made is that the particle should remain within a distance of $1/e^2$ of the intensity at the surface. This would give a length value over which the gravity could be said to be relevant of the penetration depth, δ, of the waveguide which for the waveguides used in this project is approximately 330nm. This would have the effect of shifting the gravitational forces in figure 4.10 up 1.06 decades.

As can be seen from figure 4.10 due to the parameter L_y being much greater than L_x, the corresponding equivalent force values of τ are much less in the lateral dimension. If the gravity force is omitted, this difference in lengths has the effect that the particle is more likely to be trapped laterally than transversely, despite the transverse force being much greater than the lateral force.

It should be noted that this graph was produced with a modal power of 1W. However in practice powers this high are not readily achieved (see chapter 6). The effect of using different powers is simple, for example, changing the modal power to 100mW (a more reasonable value) simply shifts the optical forces down 1 decade.

Table 4.7 shows the intercepts of the optical forces with the various values of τ for various powers. The gravity force has been omitted as exhibiting a much smaller force even for the case of the weakest power used.

From table 4.7 it can be seen that in all cases the ability to trap laterally is greater than that transversely, therefore the transverse trapping is the limiting case. For very

weak trapping ($\tau = 1$) where the time taken for Brownian motion to move the particle out of the trap is equal to the time required for the optical force to move the particle the same distance, the radii required are 66nm, 104nm and 161nm for modal powers of 1W, 0.3W and 0.1W respectively. Therefore for an optimised waveguide a 100nm gold particle will only be trapped weakly at a modal power approaching 1W whereas a 250nm gold particle could theoretically be trapped weakly by a modal power of 300mW.

In comparing the transverse forces shown here to the electrostatic forces calculated in section 4.5 it can be seen that for a 200nm gold particle the separation at which the optical trapping force is equal to the electrostatic repulsion force is given by 40, 55 and 100nm for a 10^{-3}, 5×10^{-4} and 10^{-4}M ion concentration. Clearly this height will also have an effect on the strength of the Rayleigh gradient force. It should again be noted however that the electrostatic force should not be used too predictively due to the uncertainty in the model.

4.7.2 Propulsion speed of particles

In order to calculate the expected speed only two forces need to be considered. These are the sum of the axial optical forces (the absorption, scattering and gradient force due to loss) and the Stokes' drag force, which is modified due to the proximity to the glass boundary. In this situation a particle will reach terminal velocity almost instantaneously, so only the steady-state case is required. Therefore the predicted speed of a particle is given simply by a rearrangement of equation 4.4 to the following:

$$v = \frac{F_{opt}}{6\pi a\eta} \tag{4.50}$$

Figure 4.11 gives the predicted speeds of gold particles in the evanescent field of a Cs^+ ion-exchanged waveguide carrying a modal power of 1W. The speed will scale linearly with modal power.

From figure 4.11 it can be seen that for a modal power of 1W gold particles with a radius of 250nm would be expected to have a speed of almost 40mm/s, whereas particles with a radius of 100nm would have an expected speed of approximately 1mm/s. The Rayleigh theory is used here, and therefore there is a limit to its applicability for the larger radii particles.

4.8 Conclusions

This chapter has first examined the non-optical forces for a particle in solution in a glass cell. It described the Brownian and buoyancy forces and showed that the resultant force

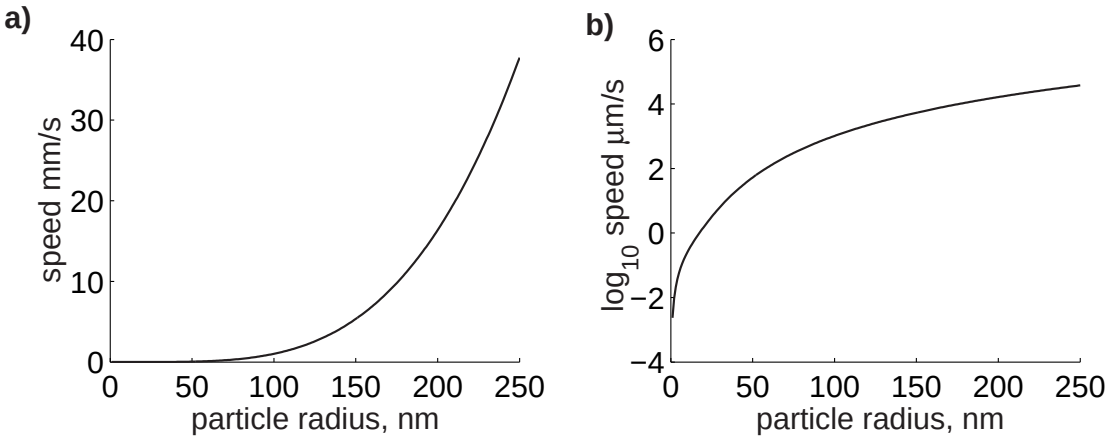

FIGURE 4.11: Predicted speed for a gold particles with varying radii on an a) linear and b) logarithmic scale. The modal power here is 1W at a wavelength of 1066nm.

from these was in the downwards direction for both gold and latex spheres, but that due to the much greater density of gold, the force on a gold particle was equivalent to that on a latex particle with approximately seven times the radius.

It also studied Brownian motion, which is independent of the material properties of the particle and showed that this has a greater effect on smaller particles causing greater RMS speeds. It showed that, for the particle size range used in this project the expected time taken for a particle to move to a position with an intensity $1/e^2$ of the peak surface intensity ranges from 1.56 seconds for a 100nm gold particle to 81 seconds for a 12μm latex particle.

The effect of the surface charges on both the surface of the particles and the glass were studied together with the van der Waals force. It was shown that the effect of the van der Waals force were much further-reaching for bodies compared to that of individual molecules - but that it still was shorter ranging than the double-layer electrostatic force. The ion concentration was found to have a significant effect on the double-layer force even at very low concentrations. Ions act to 'screen' the surface charges, thus reducing the repulsive force.

Modelling was used to investigate the temperature profile caused by the absorption of laser light. It was shown that within a 200nm gold particle, for a modal power of 100mW, a maximum temperature of approximately 37^0C was predicted, however that within 2μm of the centre of the sphere, this had fallen to less than 0.5^0C above the initial temperature. The absorption due to the glass waveguide, although creating a much smaller heat generation rate per unit volume (by a factor of approximately 10^4) had a much further-reaching effect due to the larger cross-sectional area and the fact that heat is generated along the whole length of the waveguide. In this case the peak temperature change was 2.5^0C however this fell to 0.9^0C after a distance of 500μm.

The gravitational, buoyancy, and optical gradient forces were compared to the effect of Brownian motion and it was shown that the effect of gravity was small, despite acting over a longer distance. It was also shown that the particles were more easily trapped laterally than transversely due to the greater length over which the lateral force acts. The limiting force is therefore found to be the transverse gradient force and thus it is this force along with distance over which it acts that should be maximised in future waveguide designs. The speed of gold particles were also predicted and were found to obtain a value of almost 40mm/s for 500nm gold particles. This is expected to be an over prediction due to the breakdown of the Rayleigh theory for this particle size.

Having investigated theoretically all the forces acting on a particle above a waveguide, the design and fabrication of the waveguides used are considered.

Chapter 5

Background, Fabrication and Characterisation of Waveguides

5.1 Introduction

The waveguides used in this project are a critical component of the device required to trap particles. Glass ion-exchanged waveguides were selected early on in the project for a number of reasons. This chapter gives an overview of potential waveguiding structures that could be used and explains the choice of an ion-exchanged waveguide. It then describes the ion-exchange process in glass and highlights some of the important considerations from a theoretical point of view.

The processes required for the fabrication of these waveguides that are especially sensitive to surface conditions used for trapping are then described. Having been fabricated, various parameters of the waveguide were characterised. Some of the processes for characterisation are non-trivial and the methods for this are therefore described. The results obtained are used to compare waveguides to each other and to the simulated results of chapter 3. This helps in the choice of the optimum waveguide according to the conclusions drawn in chapter 3. Other practical restrictions of the waveguides used are also highlighted in this chapter.

5.2 Optical waveguides

Ion-exchanged waveguides are one of many forms of waveguiding structure. Therefore this section discusses briefly optical waveguides and gives some explanation of the choice of ion-exchanged waveguides that are used in this project. It then examines the relationship between the local concentration of (diffused) ions and the local refractive index.

This relationship was assumed linear in chapter 3 and the validity of this is examined here.

First the distinction must be made between planar waveguides and channel waveguides. Planar waveguides confine light in only one dimension, thus the light is allowed to propagate and diffract in the other direction unrestricted. Channel waveguides confine light in the two orthogonal dimensions normal to the direction of propagation. The project requires high intensities over a length of several millimetres thus a confined wave is required. In addition the aim is to guide the particles, therefore a channel waveguide was required.

5.2.1 Channel waveguides

Optical channel waveguides come in a number of forms, classified mainly by their shape. The common forms are shown below in figure 5.1.

Fibre waveguides are formed by pulling a large glass preform with a doped core into a thin fibre. In this project the aim is to produce a lab-on-a-chip type solution that can be patterned to make integrated devices, this option is therefore discarded.

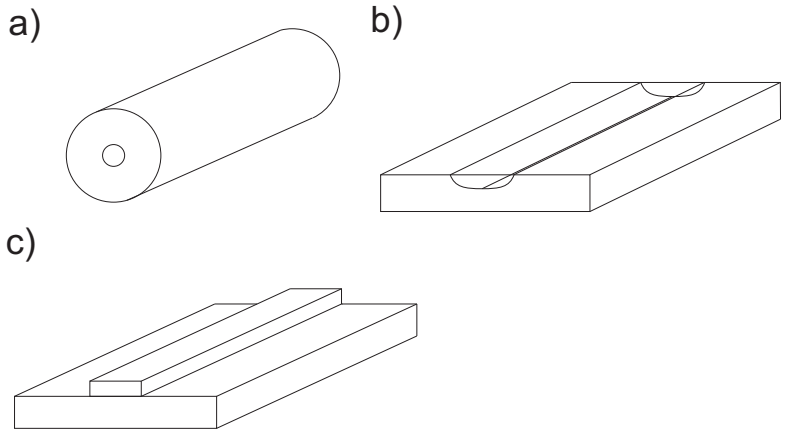

FIGURE 5.1: Various geometries for producing optical channel waveguides. These are a) a fibre b) a diffused waveguide and c) a ridge waveguide.

The next form of waveguide is a ridge waveguide, generally formed by depositing one or more layers by, for example, the various forms of chemical vapour deposition (CVD) including metal organic CVD (MOCVD), radio frequency (RF) sputtering, evaporation, molecular beam epitaxy (MBE) etc. Typically a layer would be deposited on a flat substrate (generally silicon, glass or sapphire) and photolithographically defined channels etched out. This structure stands proud of the substrate and therefore is not ideal for the control of particles. This is because particles located either side of the waveguide may not be able to mount the waveguide thus restricting the ability to manipulate particles (for example in sorting particles, see chapter 7).

The final option is that of a diffused ion-exchanged waveguide. This produces a flat surface and may be easily integrated with other processes. In addition, features of few microns can be photolithographically defined giving great flexibility in the fabrication of waveguides devices. Diffused waveguides are physically hard and the flat surface of the glass gives access to the evanescent field of the waveguide. This glass surface can be integrated with biological systems, where measurements are routinely carried out in the presence of glass surfaces. In addition, although the time required for the production of a single, patterned, ion-exchanged waveguide is high ($\sim$ 8 hours in addition to the ion-exchange time) the average time may be vastly reduced by batch processing of multiple substrates. Lastly, given the availability of the necessary equipment, the cost to produce the waveguides is not high as the materials' cost are low with substrates costing between approximately 20 pence and 20 pounds.

5.2.2 Diffused ion-exchanged waveguides

There is a large range of potential ion-exchanged waveguides that could be used. This section aims to highlight the available choices and explain the decisions that were made for the waveguides used in this project.

In producing ion-exchanged waveguides, there are two fundamental choices that must be made; the choice of the substrate and the choice of the ion that will be diffused into the substrate. In this project a silica-based glass substrate is used which has a large range of ions that can be exchanged into the glass. In addition there are a wide range of commercial glass substrates that can be used [119].

An important parameter in the choice of a suitable waveguide for evanescent trapping is the refractive index change that can be induced in the glass. This is because a larger refractive index change means the size of the waveguide required to guide a certain wavelength is smaller. Thus to obtain a high surface intensity the waveguide should be as small as possible.

In most cases the Na^+ ions in the glass are substituted with Li^+ [120], K^+ [121, 122, 123], Ag^+[121], Cs^+ [94, 95], Rb^+ [90], Cu^+ [124, 125] or Tl^+ [126]. In addition K^+ ions can also be substituted by Cs^+ ions to produce a waveguiding layer [91]. Reviews of the ion exchange theories and results can be found in papers by Ramaswamy [127], Findakly [128], Opilski [129], Doremus [108], Abouelleil [130] and Terai and Hayami [131].

K^+ ion exchange with Na^+ ions in a glass is very well established, and produces low-loss waveguides, however the refractive index change is not high. Ag^+ ion exchange is also well-established, but is known to have a problem with silver ions combining, with time, to form atomic silver and causing high losses [132], and is therefore not considered ideal. This has also been mentioned for Cu^+ ion-exchanged waveguides [124, 133]. Tl^+ ion-exchanged waveguides give a large refractive index change, however thallium is

Ion	Ion size, Å	Δn
Li	0.68	0.012
Na	0.97	-
K	1.33	0.008
Rb	1.47	0.013
Cs	1.67	0.043
Cs*	1.67	0.03
Ag	1.26	0.13
Tl	1.47	0.1

TABLE 5.1: Ion sizes along with reported surface refractive index increases in different glasses for the group I metals and silver and thallium ions. In all cases the ion being exchanged is Na^+ except in the case of * where K^+ is the ion exchanged.

very toxic, and the process would require very strict safety considerations and therefore expensive facilities. Cs^+ ion-exchanged waveguides give a refractive index change approximately three times greater than those of K^+ ion-exchanged waveguides. It has also been reported to have losses as low as 0.48dB/cm at 633nm and does not have such stringent safety requirements as Tl^+ ion-exchanged waveguides. It was on these grounds therefore that Cs^+ ions were chosen as the ions to diffuse into the glass.

In chapter 3 it was assumed that the concentration profile mapped linearly to the refractive index profile. Here this assumption is examined more closely. The refractive index change obtained by the diffusion of the ion into the glass is a strong function of its size. This is shown in table 5.1 where the maximum obtainable refractive index change (at the surface) increases with the size of the group I alkali metal used to diffuse into the substrate [128]. In addition, the data for silver and thallium ion exchange are shown as they are also common ions used in glass ion-exchange.

The relationship between the refractive index change and the ion is not solely dependent upon its size. Instead it is caused by three physical processes; ionic polarizability, molar volume (or density) and stress state [134]. It can be shown that the refractive index change due to these first two terms is given by [134]:

$$\Delta n = \frac{(n^2+2)^2}{6nV}[\Delta R - (\frac{n^2-1}{n^2+2})\Delta V] \tag{5.1}$$

where n is the refractive index, V, the molar volume and R the molar refraction given by $\frac{N_0}{3\epsilon_0}\alpha$ where N_0 is Avogadro's number and α is the polarisability. The first part of equation 5.1 is the polarisability effect and the second part the effect of the molar volume difference. The polarisability is proportional to the concentration of diffused ions. The molar volume part produces a constant negative index change [134]. The stress term can produce birefringence in the glass and the anisotropy from which the stress can be estimated has been measured to be small in Cs^+/Na^+ ion system [135]. Thus if the molar volume difference is also small then the refractive index change will be approximately proportional to the concentration. Although there has been no data

published regarding this factor it has been shown that the refractive index profile and the Cs^+ ion concentration profile are of similar form [136] and thus the assumption (that the refractive index profile and Cs^+ ion concentration is linear) is reasonable.

In experiments previously carried out for particle propulsion using a channel waveguide, a number of these ion-exchanges have been used. Kawata and Tani make no mention of the type of waveguide used [36]. Tanaka and Yamamota [35, 69] use potassium ion-exchanged waveguides as do Ng et al. [39, 38]. Finally the work done here and in collaboration with the University of Tromsø in Norway have used Cs^+ ion-exchanged waveguides [137, 66, 61].

A range of glass substrates was evaluated in this project as described in section 5.5.1. The choice for substrate was based mainly on the ability to produce a large refractive index change in the glass.

5.3 Waveguide fabrication

Waveguide fabrication is a multi-step technique and these steps are described below in the order in which they are carried out. Different substrate materials were used in the project with a range of compositions or surface qualities. However in all cases the substrate used was approximately square with sides of length between 4cm and 6cm and with a thickness between 1mm and 2mm. The method for waveguide fabrication was virtually the same in all cases, and the process is summarized in figure 5.2.

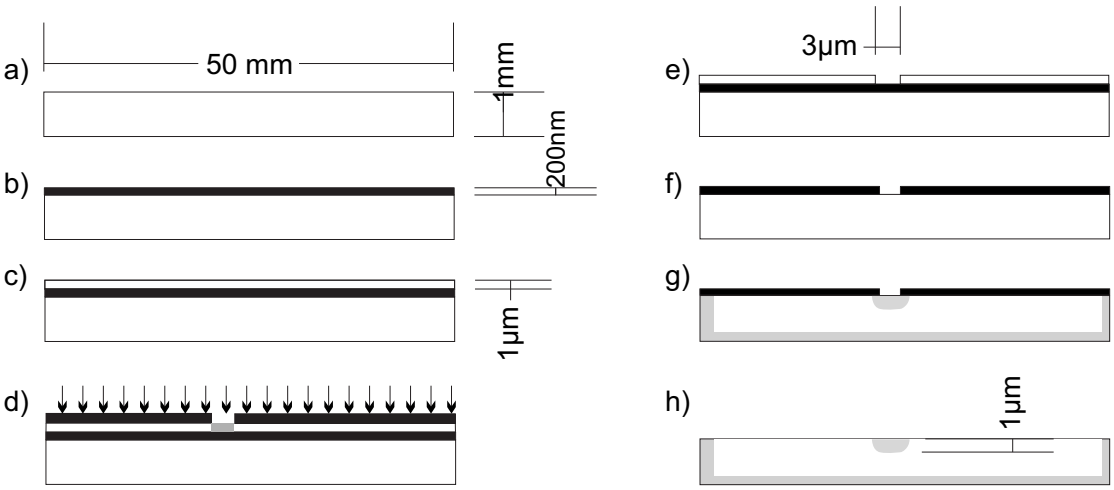

FIGURE 5.2: The waveguide fabrication process. a) A glass substrate is inspected and cleaned, b) 200nm of Al are deposited, c) photoresist is spun on the Aluminium (Al), d) a chrome mask is pressed to the photoresist and exposed to UV light, e) the photoresist is developed, f) the Al is etched, g) the substrate immersed in melt and h) the sample is cleaned polished and the aluminium coating removed.

5.3.1 Inspection and cleaning of substrate

In order to create a smooth and homogenous surface to which aluminium can adhere well, it is necessary to have a thoroughly cleaned substrate. The substrate is first inspected, and if there are any large scratches or apparent blemishes the sample is immediately rejected. The yield was highly dependent on the type of material. For example, fewer than 1 in 20 polished BK7 substrates were rejected compared to more than 1 in 2 for the soda-lime Menzel float-glass.

An accepted substrate was cleaned by firstly rubbing with a cotton bud in an acetone bath. This removes large particles or thick films that could be attached to the substrate. It is then washed in an ultrasonic bath in acetone at 55°C for 20 minutes removing organic contaminants from the surface. The substrate must be handled by gloved hands and tweezers in the fabrication process from this point on, to prevent grease adhering to the surfaces. The substrate is removed from the acetone bath and immediately rinsed with cool acetone followed by isopropanol (IPA) and deionised water. It is then dried using compressed nitrogen. The use of the IPA and a water rinse is to completely remove the acetone that would leave a residue on the surface.

The substrate is then placed in piranha solution to further remove organic contaminants. Hydrogen peroxide and sulphuric acid are mixed in a volume ratio of 1:4 and the sample immersed at a temperature of 50°C for 5 minutes. Another part of hydrogen peroxide is then added to make best use of the sulphuric acid. This is done in two stages to prevent too violent a reaction at the outset due to the very high temperature reached by the highly exothermic reaction. It is then thoroughly rinsed in deionized water and dried with compressed nitrogen.

The sample is placed in a bath of fuming nitric acid, which attacks metals and metal alloys at room temperature for five minutes before being removed and rinsed and dried again. It is then baked in an oven at 120°C to thoroughly dry the sample (figure 5.2a).

5.3.2 Evaporation of aluminium

Aluminium is used as a masking layer for the substrate as it can be evaporated and adheres well without any primer. In addition there is a good aluminium etchant available and the aluminium withstands the temperature reached in the furnace. A 1mm thick aluminium wire is wrapped around a tungsten filament and is evaporated by passing a high current through the tungsten filament at a pressure below 2×10^{-6} bar. The aluminium should be totally melted before releasing the shutter to prevent an erratic deposition rate. A thickness of approximately 200nm is deposited at a rate of approximately 1 ± 0.2 nm/s (figure 5.2b). The current may be altered to maintain the rate to within these bounds.

5.3.3 Photolithography and etching

Photoresist (S1813, Shipley) is spun on top of the aluminium layer at a speed of approximately 5500revs/min for 60 seconds resulting in a resist layer of approximately 1μm thickness (figure 5.2c). The substrate is soft baked at 90°C for 30 minutes. A custom-designed chrome mask (produced by Rutherford Appleton Labs by an electron beam) is used as the master. This is inverted, aligned with the substrate, and forced into hard contact with the photoresist. It is then exposed to UV light for 4 seconds (figure 5.2d). This is then developed in the recommended developer (MF319, Shipley) for one minute, washed thoroughly with deionised water and examined under the microscope (figure 5.2e). The substrate is then hard baked at 120°C for 30 minutes to completely set the photoresist. The sample is then placed in aluminium etchant (a mixture of sulphuric, nitric and hydrochloric acids) at 50°C for 1 minute and the features examined under the microscope for defects. Further etching may be necessary (figure 5.2f).

5.3.4 Ion-exchange

The ion-exchange salt, either $CsNO_3$ (Aldrich 99.99%) or KNO_3 (Aldrich, 99.99%) is placed in the oven and the substrate is suspended over the salt using a long, hooked steel wire to support another steel wire bent to hold two opposite corners of the substrate. The oven is heated to the required temperature, directly monitoring the melt temperature, and left to stabilize for 30 minutes. The substrate is then lowered into the melt and left for the required ion-exchange time (typically between 4 and 24 hours). The substrate is lifted out of the melt, the oven turned off and the substrate allowed to cool slowly. The sample is rinsed in water, to remove all the salt, and dried (figure 5.2g).

5.3.5 Post-exchange treatment

In order to get good end-faces both input and output edges are polished. This gives a very flat surface along the edges perpendicular to the waveguides and allows high coupling efficiencies into the waveguides. The substrate was polished by one of two methods.

The first method was to set the substrate in wax and cut it to remove approximately 1mm of the aluminium coated area. It is then lapped with 9μm Al_2O_3 particles (Logitech) to flatten the surface. This is monitored by marking the end face at the start with a permanent marker, total absence of the permanent marker indicates the face is flat. A further 200μm is then removed and the edge is inspected under the microscope. After this it is lapped with 3μm Al_2O_3, removing a further 50μm of glass and re-inspected. It is then chemically polished using syton solution (SF1, Logitech) for at least 30 minutes until the edge perpendicular to the waveguide is straight enough to be judged acceptable.

The wax is then removed; initially by gentle wiping of the surface, followed by immersion in Ecoclear, either overnight at room temperature or for a few minutes at 50°C. Finally the substrate is placed in aluminium etchant (Rockwood Electronic Materials) at 50°C until all aluminium is visibly removed (figure 5.2h).

The second method of polishing was by hand and had the advantage of being (potentially) much quicker. This is especially true if only one sample is required to be polished (the machine polish described above could polish up to 4mm of glass i.e. four 1mm substrates simultaneously). Two millimetres of the substrates edges perpendicular to the waveguides were cut off. A coarse (e.g. P400) paper was used to lap a $\sim 45^0$ wedge into the substrate as shown in figure 5.3b. New wedges were lapped at successively shallower angles with successively finer grade paper (figure 5.3c). Finally the edge is polished with P2400 paper perpendicular to the waveguides (figure 5.3d).

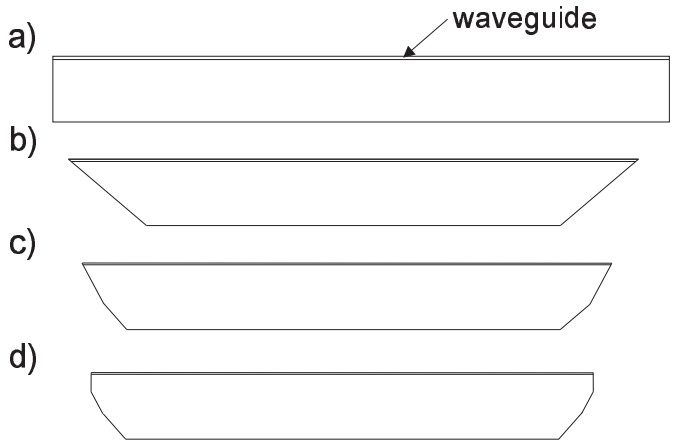

FIGURE 5.3: Hand polishing method. a) The cut substrate, b) a sharp wedge is cut, followed by c) successively less sharp wedges until d) the end is polished flat.

5.4 Waveguide characterisation methods

Chapter 3 dealt with the theoretical aspects of a diffused waveguide, allowing determination of how various parameters e.g. Δn_{eff} theoretically affect the factors that are important for trapping. This section describes the methods that were used to measure some of these parameters.

5.4.1 Composition measurements

Glass contains a former (SiO_2 in this case), intermediates (such as Al, Zn and Ti) and modifiers (most group 1 and 2 metals and some of the transition metals). The composition of a glass determines many of its physical properties. For example, Al in glass acts as a stabilizer due to its high bond energy with oxygen, thus glasses with a

higher aluminium content are generally stronger [138]. There are a vast range of glasses commercially available [119] and a selection of these with a varied range of compositions was chosen in order to see how well they could produce K^+ or Cs^+ ion-exchanged waveguides. Although the name suggests the type of composition the glass may have, the quantitative composition is not given. Therefore to understand the behaviour of a glass in forming waveguides the bulk composition of the substrates was measured.

Energy dispersive X-ray (EDX) analysis using an adapted scanning electron microscope (SEM) was used to obtain the compositions of a range of glasses. A small sample of each glass (approximately 5mm square) was cut and coated with a thin layer of carbon (approx. 30nm) using a evaporating carbon coater. This was then mounted on a holder and silver paste used to create a low impedance route from the sample surface to the holder to prevent electron build up on the dielectric surface. The samples were mounted in the SEM and an area of the glass imaged. The area should contain no scratches or visible contaminants. The EDX was calibrated using a cobalt target. X-rays were collected until sufficient data had been obtained to make the energy peaks easily identifiable. X-rays from a bulb-shaped volume with a radius of approximately 2μm and penetrating to a depth of approximately 3μm were collected. Peaks in X-ray energy counts were highlighted and an element selected based on the position and relative height of other peaks. In some cases, it was necessary to select an element based on the elements that were expected to be present in the glass.

By slowly sweeping the sample across the X-ray beam a line-scan could be obtained that showed the change of composition as a function of the position of the sample. By sweeping the sample perpendicular to a waveguide it is therefore possible to identify the ions that have been exchanged.

5.4.2 Effective refractive index measurements

The effective refractive indices, n_{eff}, of the modes of a waveguide are of great interest as they can give a good indication of the peak index change possible by the ion-exchange process. This is a critical parameter of the waveguide as shown in section 3.5.4.1. Shorter ion-exchanges can then be compared to simulations to predict waveguides' other characteristics. Measuring the effective index of the modes also gives the number of modes at a given wavelength and can thus help with characterisation.

In order to measure the effective refractive index of a planar or channel waveguide mode, the prism coupling method is used. This relies on the accurate measurement of an angle at which light is coupled into a specific mode of a waveguide. In a multimode waveguide with more than 3 modes, it can also be used to calculate an approximate refractive index profile [92] as seen in section 3.5.2. The apparatus (see figure 5.4) uses a prism pressed hard against the substrate sample being measured. The contact has to be such

that optical coupling is made. When optical contact is achieved there is an overlap in the evanescent fields of the prism and substrate and an area of greater transparency is apparent.

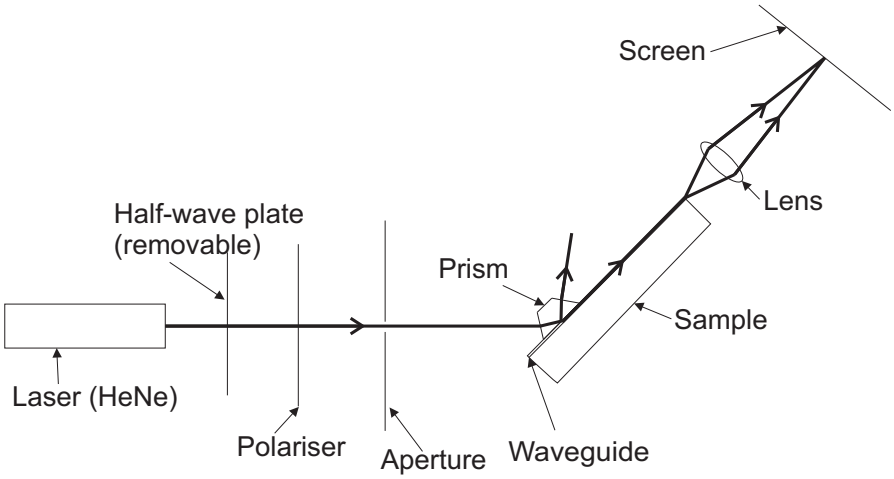

FIGURE 5.4: Experimental apparatus used for prism coupling

The prism, substrate and imaging lens are all mounted on a digital rotation stage with an accuracy less than 0.001°. The prism and substrate could be translated together in two dimensions and rotated in two dimensions. The sample is clamped to the prism. The apparatus is initialised by rotating the prism in the two dimensions until the reflection from the input face of the prism is incident on the laser aperture and the rotation stage is zeroed. The prism is manipulated to give good overlap between the point of optical contact and the beam. The prism is rotated until the light was coupled into the waveguide, visible as a small mode-shaped profile for a channel waveguide or a line in the case of a planar waveguide, and the angle recorded.

In the case of measuring the infra-red (IR) effective refractive indices of a waveguide, a collimated IR beam was aligned to intersect the HeNe beam, a mirror was inserted at the point of intersection and angled such that the IR beam and the HeNe beam were coincident on the prism. The HeNe beam could then be used for much of the alignment simplifying measurement of the IR effective refractive indices.

Figure 5.5 shows the angles necessary to calculate the effective index of a waveguide mode. In the diagram n_p is the refractive index of the prism, n_{eff} is the effective index of the mode, θ_p is the internal angle of the prism made by the faces parallel to the substrate and that the laser beam is initially incident upon. θ_m is the angle that the beam makes to the normal of the prism face and changes for each waveguide mode.

Using Snell's law and basic trigonometry it can be shown that the effective refractive index of the mode is given by [92]:

$$n_{eff} = n_p \sin(\theta_p + \arcsin \frac{\sin \theta_m}{n_p}) \tag{5.2}$$

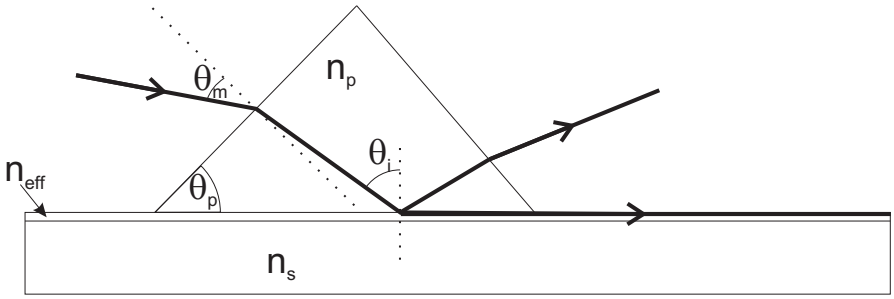

FIGURE 5.5: Diagram of angles and refractive indices required to measure the effective indices of a waveguide by the prism coupling method.

It is also possible to measure the refractive index of a substrate using this method. In this case light can be refracted into the substrate from the prism up to a certain angle, above this angle light will be totally reflected within the prism. This angle is used as θ_m in equation 5.2 to give the substrate refractive index.

5.4.3 Loss measurements

In this section waveguide loss and the factors that affect it are described. Why this is important and various ways that it can be measured are also discussed; including finally a description of the white light method used to measure a waveguide's cut-off wavelength.

Losses of channel waveguides can be separated into two types of loss. The first type is the coupling loss suffered in coupling external light into the waveguide. This is made up of three parts; a mode mismatch between the input beam and the shape of the mode being considered, a diffuse reflection and refraction due to imperfect end-face polishing and a specular Fresnel reflection at the interface due to the change in refractive index. The second type of loss is the propagation loss. This is due to absorption or scattering of the guided beam in the waveguide and is proportional to the length of the sample (measured in dB/cm).

In this project, the larger the propagation loss of the waveguide, the more limited the length of the waveguide that can be used. The loss will also determine the power of laser source required to deliver the necessary power to a certain position along the waveguide. Although very high power lasers are available at the wavelength used (1066nm), the more powerful the laser, the higher the cost.

Waveguide losses have been measured in many ways with no method dominating. The two losses are generally measured together and the coupling loss inferred from the propagation loss. For example, the propagation loss can be measured by the cut-back method [139]. Here either many similar waveguides are fabricated with the only difference being in their path length. The total losses of these waveguides is plotted as a function of

their lengths. The loss should scale linearly with length with the intercept giving the coupling loss. Another method is by observing the scatter of light along the waveguide as a function of its position along the waveguide. The intensity of light scattered as a function of position along the waveguide should fit an exponential curve with the decay rate giving the propagation loss. This can be done by imaging with a camera if the substrate is lossy, or it can be done with photographic film close to the waveguide [140].

In this project propagation loss is calculated by comparing the difference in loss of waveguide of approximately 4cm length to a length of 3cm by repolishing one end of the waveguide. The difference in the loss gives the propagation loss directly.

The loss of a waveguide at a single wavelength is discussed above. However a measure of the loss at a range of wavelengths gives more detailed information about a waveguide. As has been seen in chapter 3 the number of modes a waveguide supports is dependent on its size. For an asymmetric waveguide there is a wavelength above which a waveguide will cease to guide the fundamental mode. This is called the waveguide's 'cut-off' wavelength, at which point the theoretical loss of the waveguide will be infinite. This cut-off wavelength can be measured and used to help characterise a waveguide.

The experiment involves coupling radiation from a broad-band light source into a waveguide and measuring the loss of the waveguide over a range of wavelengths using a monochromator or optical spectrum analyser (OSA) to select narrow wavelength ranges. The apparatus used is shown in figure 5.6. White light from a bright tungsten source is coupled into standard SMF fibre with a 40x lens. Initially white light from the fibre is collimated with a lens positioned such that a narrow beam is incident on the monochramator slit. The computer controls the monochromator, slowly scanning in steps through a defined wavelength range. The output from a photodetector is simultaneously measured by a lock-in amplifier (LIA) and this is logged by the computer. An optical chopper positioned midway between the output of the fibre and the monochromator provides the reference signal for the lock-in amplifier (LIA). The measurement is then repeated for the case of the light being coupled through the sample waveguide and the output of the waveguide being directed into the monochromator. The loss (in dB) as a function of wavelength can be calculated using the following equation:

$$Loss(\lambda) = -10 \times \log_{10} \frac{P_{wg}(\lambda)}{P_f(\lambda)}, \tag{5.3}$$

where P_{wg} is the power measured out of the waveguide and P_f was the power measured in the fibre.

Depending on the cut-off wavelength of a waveguide either a silicon (range ∼400nm and ∼950nm) or an InGaAs (range ∼950nm and ∼1700nm) detector was used. The InGaAs detector was preferred between the wavelengths of 900nm and 1100nm due to its greater sensitivity with lower noise at the wavelength to be used for trapping experiments. In

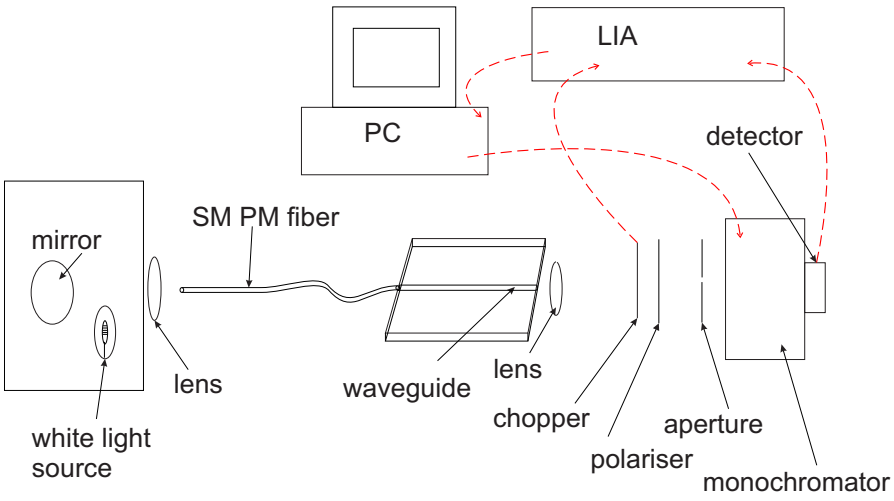

FIGURE 5.6: Experimental apparatus used for white light measurements also showing data interconnects (– →).

this project the cut-off wavelength is defined as the wavelength at which the loss rises to 3dB greater than the background level of loss.

5.4.4 Spot-size measurements

Chapter 3 showed that the modal intensity distribution is of interest in calculating the proportion of power in the superstrate. It may also be used to determine if a waveguide is single moded or multimoded and to quantify a coupling loss. The method for measuring this is to magnify the near-field image of the mode exiting the waveguide into free-space. A high magnification lens is used for this and the mode is focussed on a digital camera. To check whether the waveguide is monomode (at that wavelength) the input beam is moved slightly. In the case of a multimode waveguide a difference in the intensity distribution will be observed whereas for a single mode waveguide the total power will change but the distribution will remain the same.

In this project modal spot-sizes were measured both by using a standard digital camera and exporting the data to Matlab and using a commercial solution involving a digital camera and software designed for this purpose (Coherent, Beamview analyser).

In both cases it is necessary to have a standard to calibrate the measurements. Rather than calculating the magnification, a graticule placed where the output of the waveguide was to be positioned, was back-illuminated and imaged. The modal spot-size was calculated by fitting a Gaussian beam to the data through the intensity peak in the two orthogonal directions. The spot-sizes are given as the full-width of $1/e^2$ of the peak intensity values.

5.5 Characterisation results

Many waveguides were fabricated in the project and a representative sample of the results is shown below. The results show data concerning both K^+ and Cs^+ ion-exchanged waveguides. These were fabricated in a range of substrates for times ranging from 6 to 24 hours and at temperatures ranging between 350 and 530^0C. Typically waveguides were fabricated with a mask having openings from 1μm to 10μm and the effect of this varying width is also examined.

The temperatures used had to be above the melt temperatures of the salts (330°C for potassium nitrate and 414°C for cesium nitrate). The temperature should not be too high as very short times would be required (which are hard to reproduce accurately), the aluminium coating may become damaged (or oxidise) and the melt may decompose. At too low a temperature the ion-exchange time taken would be impractically long.

5.5.1 Composition measurements

Figure 5.7 shows the results of EDX composition measurements of a range of candidate substrate glasses. The glasses were chosen based on their wide range of expected compositions and for their quality (i.e. they should preferably be optical glasses).

As can be seen Menzel contained both sodium and calcium in (relatively) large proportions, as would be expected for a soda-lime glass. BK7 and K5 both contained less sodium, but much higher proportions of potassium. BK7 and pyrex both contained significant proportions of boron making them borosilicate glasses.

Figure 5.8 shows an EDX linescan across a waveguide made in a Menzel glass. This verifies that it was the Na^+ ions that were being exchanged in Menzel glass. It shows that, at the position of the waveguide the proportion of caesium in the glass increases from a very low value and that the proportion of sodium decreases by a similar amount. To quantify this data more accurately is hard due to the 'bulb' into which the X-rays penetrate being comparable to the expected depth and width of the waveguide.

5.5.2 Effective refractive index results

The glasses mentioned above were all immersed in molten $CsNO_3$ at various temperatures and times in order to assess their suitability for making planar waveguides. A selection of the results of the measured effective indices is shown below in table 5.2.

The glasses that did not form waveguides were discarded as the ion exchange temperature and time that would be required to form waveguides would be too great to be practicable and may not be possible. These results agree with those from the measurements of the

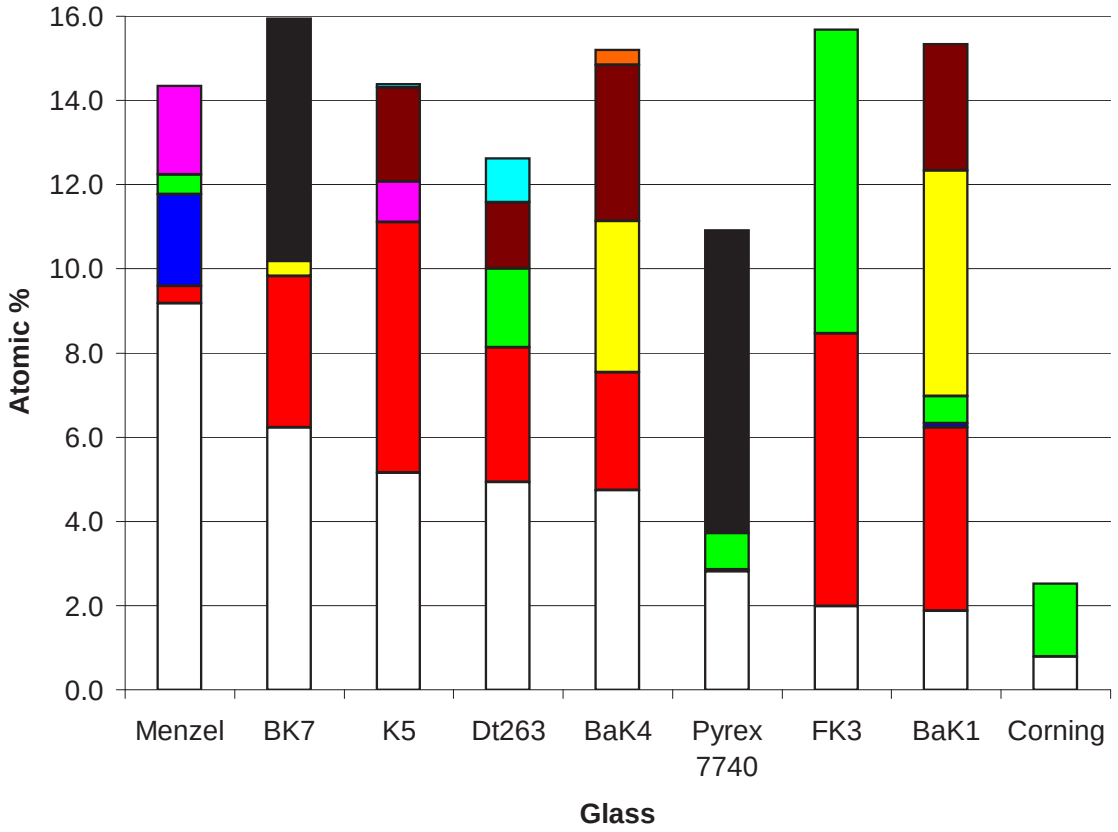

FIGURE 5.7: Composition of a range of glasses listed in order of sodium composition. SiO_2, the major component in all the glasses is omitted for clarity, the proportion of the Na (□), K (■), Mg (■), Al (■), Ca (■), B (■), Ba (■), Zn (■), Pb (■) and Ti (■) oxides is shown.

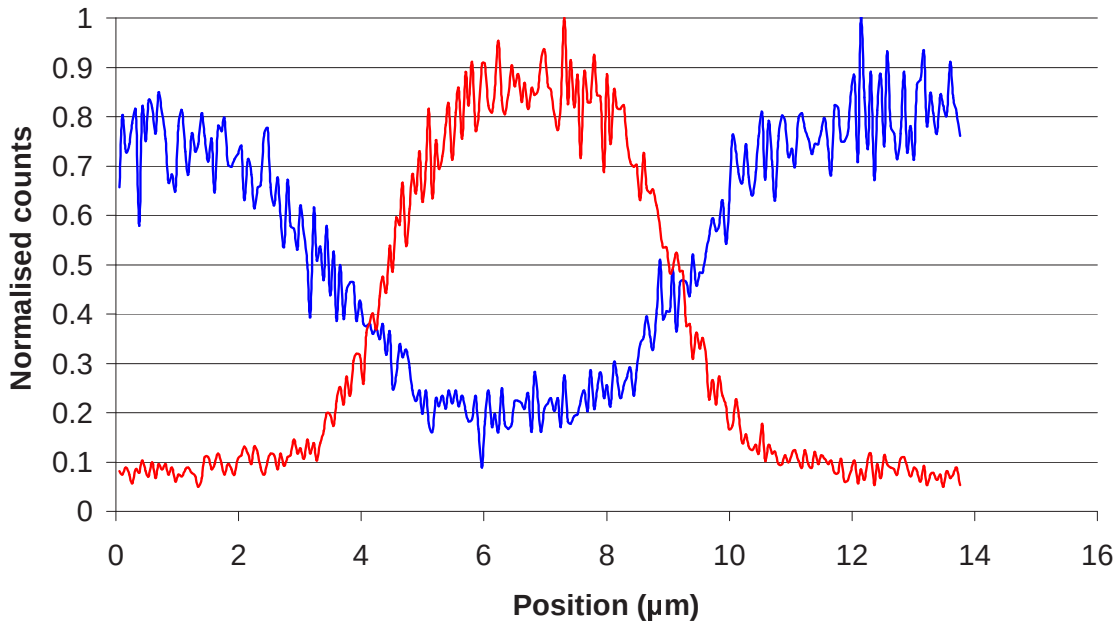

FIGURE 5.8: An EDX linescan scanned laterally across a Cs^+ ion-exchanged waveguide. The normalised proportions of Na (■) and Cs (■) are shown as a function of the position across the waveguide.

Substrate	IE temperature (^0C)	IE time (h)	Substrate index	Fundamental n_{eff}
Menzel	450	17	1.509	1.528
BK7	450	20	1.517	1.530
K5	450	20	1.522	1.527
DT263T	534	19	1.523	1.540
BaK4	450	40	1.569	x
FK3	450	20	1.465	1.485
BAK1	493	63	1.573	x
Corning 7056	500	20	1.487	x

TABLE 5.2: Measured effective indices of planar waveguides at 633nm in a range of glasses along with substrate indices that were all taken from literature apart from that of Menzel glass which was measured (at 633nm). An x indicates that a waveguide was not formed in these glasses.

glass compositions presented in the previous section. The glasses with lower proportions of sodium and potassium generally did not form waveguides. FK3 was unsuitable as it became mechanically unstable and would deform at high temperatures; prism coupling was only possible in a part of the substrate that remained flat. From these results it was decided that Menzel glass substrates should be used for the optical trapping experiments. These were chosen due to the ease with which waveguides could be fabricated and the high index change induced in the glass. In addition the glass is a fraction of the cost of the other (optical) glasses.

Cs^+ and K^+ ion-exchanged channel waveguides were fabricated as described in section 5.3. The modal effective indices were measured for both TE and TM polarisations and with a HeNe laser (633nm wavelength) and an Yb fibre laser (1066nm wavelength) for a range of ion-exchange times and temperatures.

In order to compare both BK7 and Menzel substrates, it is more useful to plot Δn_{eff}, the difference between the effective refractive index of the mode and the refractive index of the substrate. In order to do this the substrate refractive indices were measured and found to be 1.517 for BK7 at 633nm and 1.5098 and 1.5000 for Menzel at 633nm and 1066nm respectively.

Figure 5.9 shows results for K^+ ion-exchanged waveguides at 633nm in both Menzel and BK7 substrates. The ion exchanges in Menzel were for between 2 and 12 hours at 350^0C and in BK7 the ion exchange was at 400^0C for 4 hours. This plot and those below use smoothed lines between points as a visual aid, they do *not* represent lines of best fit. So as not to clutter the graphs results for the fundamental modes only are plotted.

From figure 5.9 it can be seen that there is a general trend for a longer ion-exchanged waveguide mode to have a higher Δn_{eff} as expected by diffusion theory. In addition, narrower waveguides have smaller effective refractive index changes as predicted theoretically (see section 3.5.4.1). It also shows that the effective index change in the BK7 substrate is much less than in the Menzel substrate, despite the BK7 substrate being

ion-exchanged at the higher temperature than the Menzel substrate. Finally, from the observation that the results for the 9 hour and 12 hour ion-exchanged waveguides do not differ significantly it is not likely that a much larger Δn_{eff} is possible than that obtained with these waveguides suggesting a maximum index change of less than 0.005 for a K^+ ion exchange in Menzel glass.

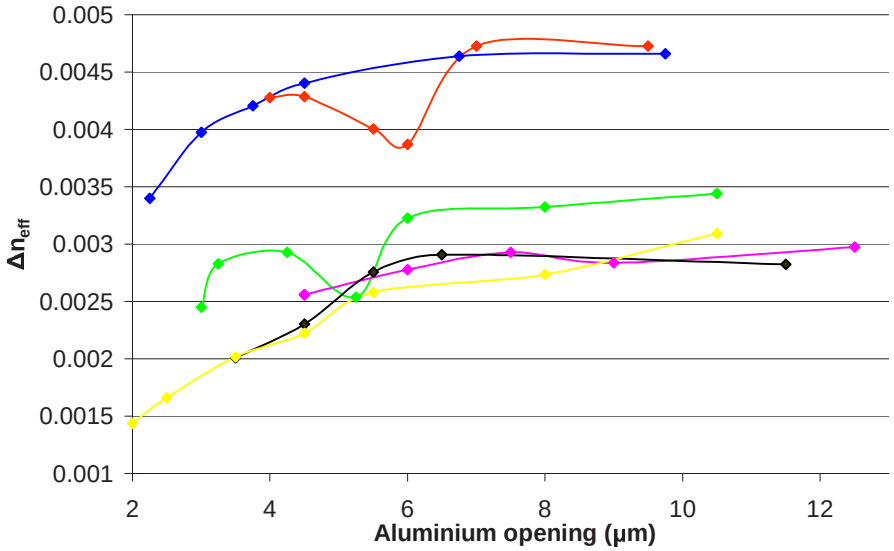

FIGURE 5.9: Increase in TM effective refractive indices of K^+ waveguides with respect to the substrate index for a variety of widths at a wavelength of 633nm. Results show Menzel waveguides ion-exchanged at 350^0C for 12(♦), 9(♦), 6(♦), 4(♦) and 2(♦) hours and in BK7 at 400^0C for 4(♦) hours.

Figure 5.10 shows effective index changes for Cs^+ ion-exchanged waveguides, ion-exchanged for between 7 and 10 hours at 450^0C in Menzel glass. The superscripts in the figure legend are for future reference to the same substrates. Although the correlation with time is not as expected the effective refractive index changes are consistently much higher with values ranging between 0.006 to 0.024 for Cs^+ ion-exchanged waveguides which compared to values less than 0.005 for K^+. There is again the minor tendency for narrower waveguides to have similar but lower effective indices than those from the same substrate with wider openings. Comparing the values of the effective refractive index change from this graph to the results from simulated waveguides in figure 3.14 shows that the depth parameter, w varies from approximately 0.8 to 2.5μm for these fabricated waveguides. As the ideal waveguide for trapping was determined to have a depth of approximately 1.1μm in section 3.5.5 this demonstrates that it is possible to fabricate an optimised waveguide with this depth.

The effective refractive index change for the K^+ ion-exchange waveguides in Menzel glass at 1066nm, that guide at this wavelength, is shown in figure 5.11. It shows a similar trend to the values taken at 633nm, with the main difference being that the shorter ion exchanges have lower values of Δn_{eff} which is as expected as these waveguides become closer to cut-off.

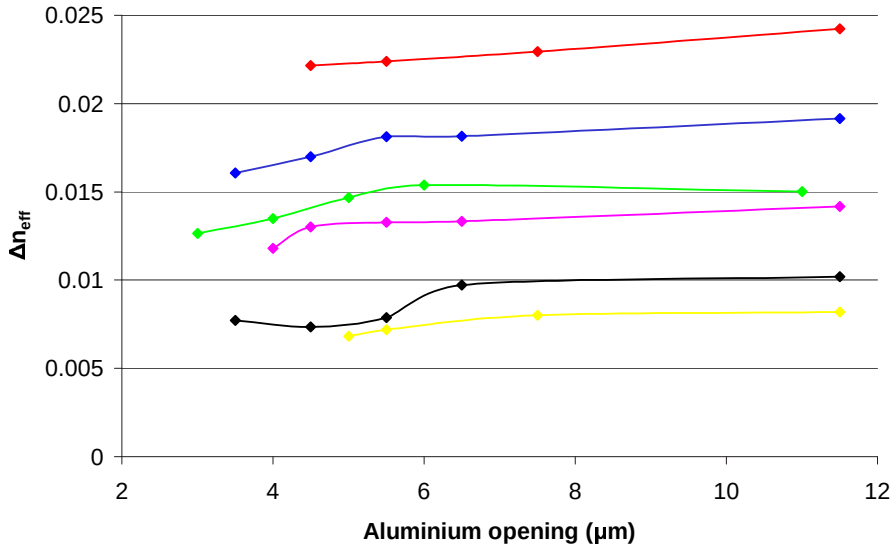

FIGURE 5.10: Increase in TM effective refractive indices of Cs^+ waveguides for a variety of widths at a wavelength of 633nm. Results show Menzel waveguides ion-exchanged at 450^0C for $9^{(1)}$ (♦), 8.5 (♦), 10(♦), $9^{(2)}$ (♦), 6(♦) and 7 (♦) hours.

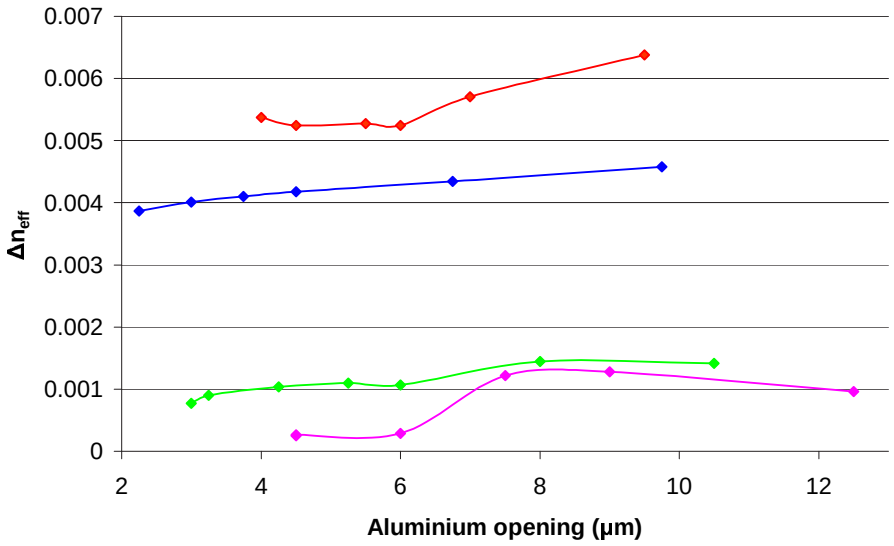

FIGURE 5.11: TM effective indices for K^+ ion-exchanged waveguides in Menzel at 1066nm at 350^0C and with times 12 (♦), 9 (♦), 6 (♦) and 4 (♦) hours.

The difference in Δn_{eff} for TE and TM polarisations for both K^+ and Cs^+ ion-exchanged waveguides were very small (typically <0.001), less than the error in the measurement.

These results have shown that a BK7 substrate does not produce as high values of Δn_{eff} for similar conditions (as would be predicted from the results in table 5.2). It has confirmed that, in general, the effective index increases with width, as expected. The refractive index change for Cs^+ ion-exchanged waveguides, although not consistent in terms of the ion-exchange time, did give much larger values of Δn_{eff} than those measured for K^+ ion-exchanged waveguides. The values of w used in chapter 3 to describe the depth of diffusion varied from approximately 0.8μm to 2.5μm. In terms of trapping

it was shown in section 3.5.5 that a value of approximately w=1.1μm is optimum for trapping in this project. This relates to a value of Δn_{eff} of approximately 0.014 for a waveguide with width of 10μm at 633nm. This is given by the second substrate ion-exchanged for 9 hours in figure 5.10. Therefore it is expected that this waveguide will be optimised for trapping particles.

5.5.3 Spectral attenuation results

Typical spectral loss measurements for K^+ ion-exchanged waveguides of varying width are shown in figure 5.12. The sharp increase in loss in these measurements defines the cut-off wavelength of the waveguide. The sharpness of the increase is dependent on the band pass of the slits of the monochromator which was set to have a bandwidth of approximately 2nm. The figure shows results for both the TE and TM polarisations and shows that they are very similar, indicating a low birefringence. Figure 5.12 also compares waveguides with widths of 3, 7 and 12μm. From the graph it can be seen that the wider the opening in the aluminium, the higher the cut-off wavelength, as predicted (section 3.5.4.3).

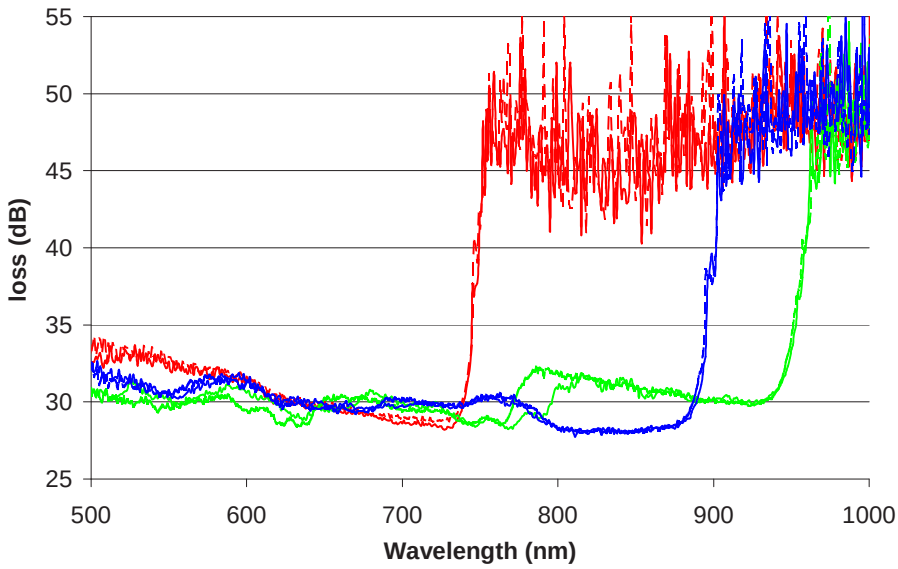

FIGURE 5.12: Results from a K^+ ion-exchanged waveguide ion-exchanged at 400^0C for 1 hour in a BK7 substrate with nominal openings of 3 (■),7 (■) and 12 μm(■). Dashed lines represents TE loss whereas solid lines represent TM modes.

Data from many waveguides may be collected together by plotting their cut-off wavelengths. The cut-off wavelength for several widths and several times of K^+ ion-exchanged waveguides are shown in figure 5.13. Results are shown for both BK7 substrates ion-exchanged at 400^0C and for Menzel substrates at 350^0C. As predicted for both sets of results, as the ion-exchange time increases, so too does cut-off wavelength of the waveguide. The result for the 9 hour Menzel substrate shows only the results for three of the

more narrow waveguides, as the wider waveguides had cut-off wavelengths outside the wavelength range of the InGaAs detector.

Figure 5.13 also shows that K^+ ions have a larger effect in Menzel glass than in BK7 glass for similar ion-exchange conditions. This is evident from the two results showing four hour ion exchanges. Comparing these two cases the Menzel has a higher cut-off than the BK7 for a given wavelength and width despite the ion-exchange being carried out at a lower temperature. This is due either to a greater peak refractive index change or depth of diffusion.

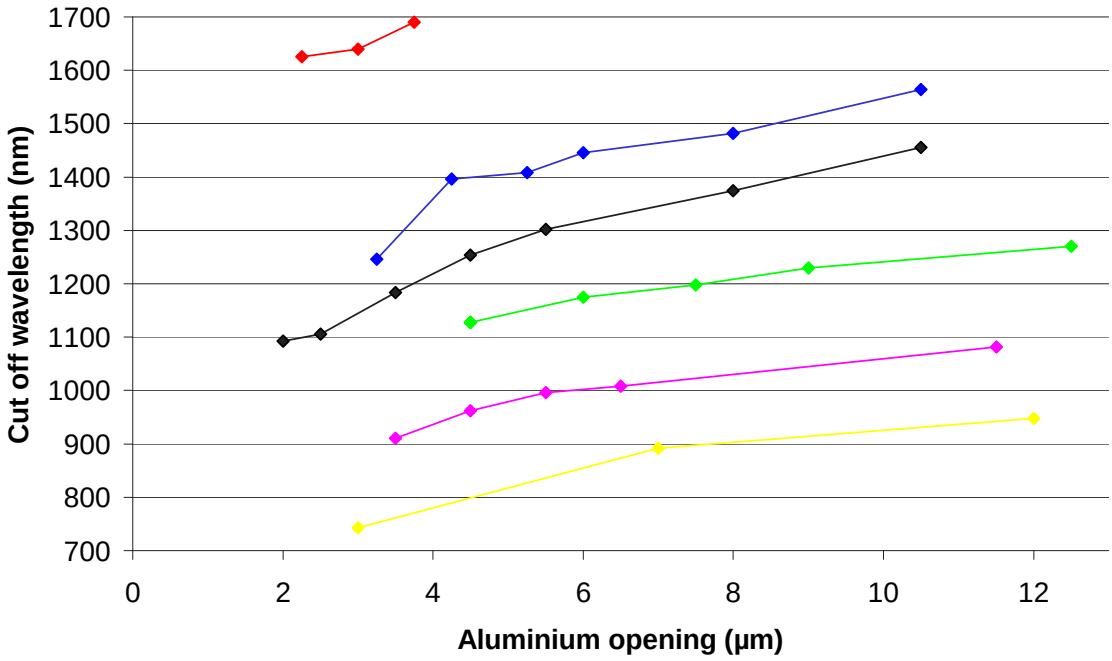

FIGURE 5.13: TE cut-off wavelengths for K^+ ion-exchanged waveguides in Menzel glass ion-exchanged at 350^0C for 9(♦), 6(♦), 4(♦) and 2(♦) hours and in BK7 at 400^0C for 4(♦) and 1(♦) hours.

Figure 5.14 shows typical loss spectra for a Cs^+ ion-exchanged waveguide. These are similar to those seen for the K^+ ion-exchanged waveguide (figure 5.12) but show a marked difference between the TE and TM results. In all cases the TE cut-off wavelength is substantially higher than the TM cut-off wavelength for any given Cs^+ ion-exchanged waveguide. This implies a much higher birefringence than the K^+ ion-exchanged waveguides and may be indicative of extra stress caused by the (much larger) Cs^+ ions when compared to the K^+ ions. Further, it can be seen that these spectral plots have much more gradual increases around the cut-off wavelength than those for K^+ ion-exchanged waveguides. This could be an indication of the quality of the waveguide as, if the quality is high the refractive index profile will be constant for the whole length of the waveguide, thus each point along the waveguide will have the same cut-off wavelength. If the waveguide edges are rough then different positions along the waveguide will have differing theoretical cut-off wavelengths.

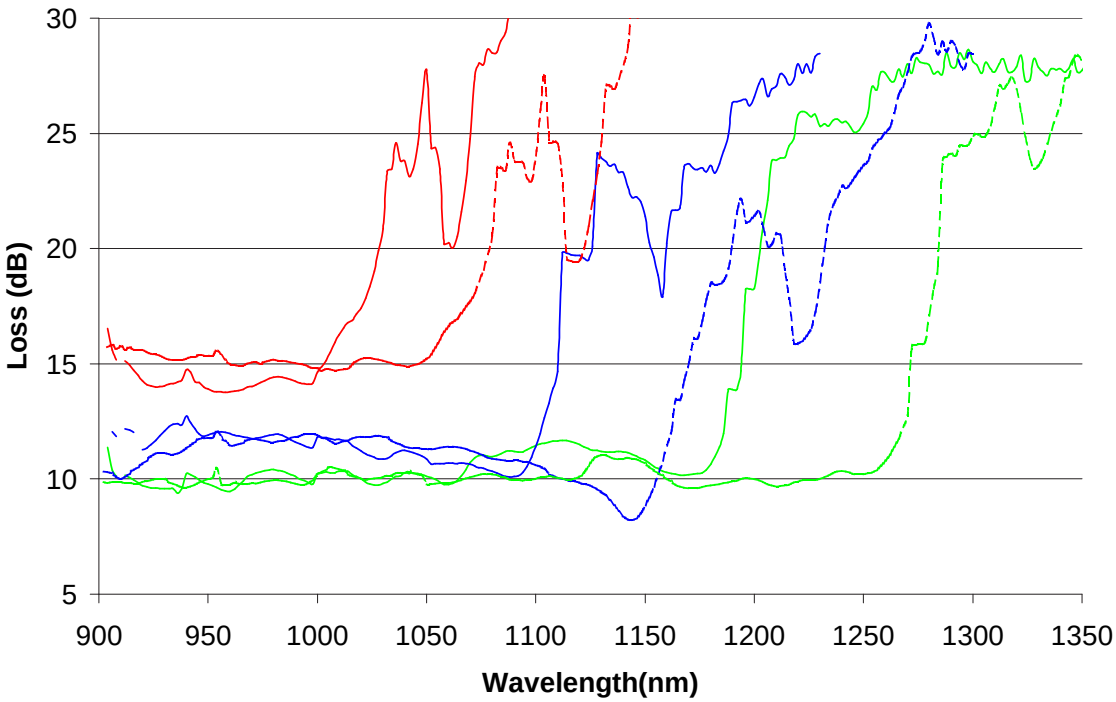

FIGURE 5.14: Typical waveguide spectral loss plots for a Cs^+ ion-exchanged waveguides. This Menzel substrate was ion-exchanged at 450^0C for 11 hours with nominal openings of 4 (■), 6 (■) and 11μm (■). TM polarisation results are shown as solid lines, TE polarisation are dashed.

As with the K^+ ion-exchanged waveguides, results were collated for Cs^+ waveguides and are shown below in figure 5.15. This shows the cut-off wavelengths, for TM polarisation, for the same Cs^+ ion-exchanged waveguides described above in section 5.5.2. In addition, the interpolated values for the effective index change Δn_{eff} of a waveguide with a width of 10μm from figure 5.10 are listed for comparison in the legend.

Figure 5.15 shows the same lack of correlation between the ion-exchange time and the cut-off wavelength as was seen for the effective index results. Results from other substrates have reinforced this oddity and confirmed that, unlike K^+ ion-exchanged waveguides, the cut-off wavelengths of Cs^+ ion-exchanged waveguides can not be predicted from the ion-exchange time. The reason for this is not yet known, however several potential explanations are proposed here. Firstly a depletion or decomposition of the melt could be the cause. However this is not thought to be the case as there would be some correlation with the order of the samples made. It could also be due to a variation in the melt temperature. Again this is not thought to be the reason as the tolerance on the temperature detector should be below 1^0C and the variation recorded of the temperature of the melt was never observed to be greater 1^0C meaning a total possible error of 2^0C which is thought to be insufficient to cause the error observed. A variation in the glass is thought unlikely as this should have shown an error in the K^+ ion exchange results also, however different levels of cracking due to the larger Cs^+ ion size may enhance the effect of this. Lastly the effect could be due to the higher temperature required

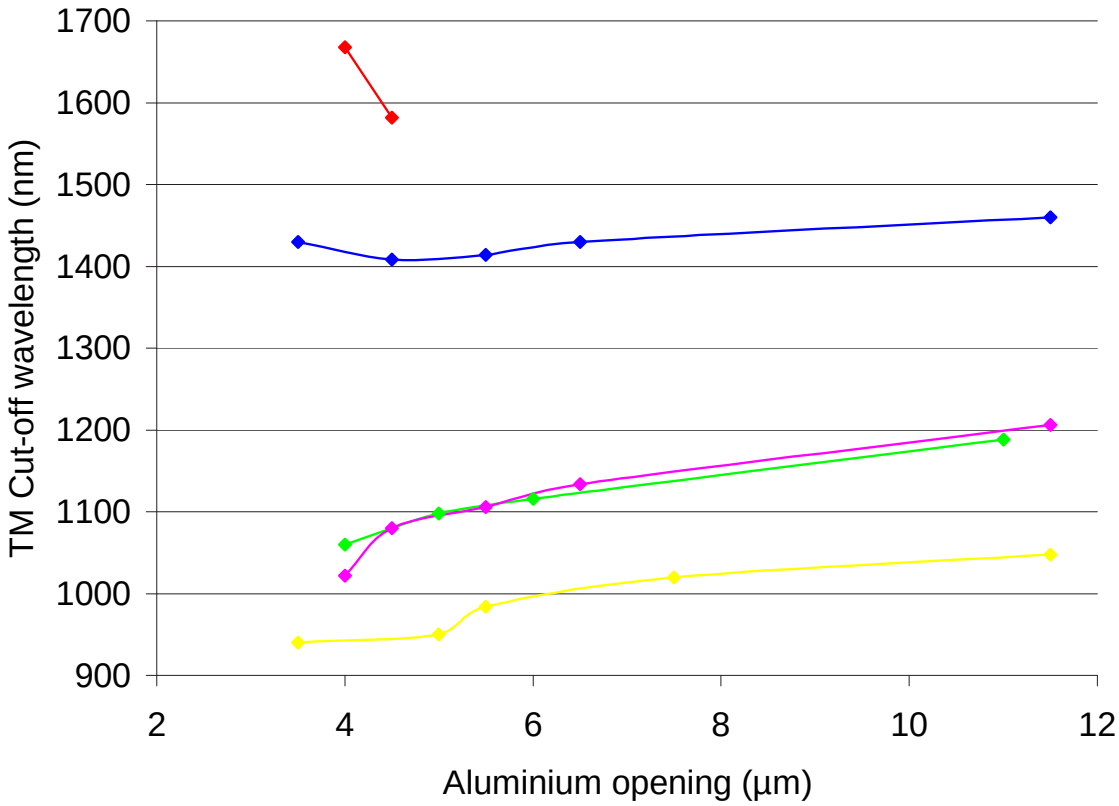

FIGURE 5.15: TM cut-off wavelengths for Cs^+ ion-exchanged waveguides in Menzel at 450^0C (with TM Δn_{eff} at a wavelength of 633nm) for $9^{(1)}(\Delta n_{eff}$=0.0237)(♦), 8.5 (0.0188)(♦), 10 (0.0151)(♦), $9^{(2)}$(0.0138)(♦) and 7(0.0082) hours (♦) as a function of their width.

to fabricate Cs^+ ion-exchanged waveguides than for the smaller and more mobile K^+ ions. This may lead to some additional damage to the glass that may be caused by an unmonitored parameter such as the cooling rate of the substrate after ion-exchange. Due to this discrepancy it is necessary to characterise a Cs^+ ion-exchanged waveguide by some optical parameter and not just the ion-exchange time used.

Comparing the results obtained here for the Cs^+ ion-exchanged waveguides to those theoretically simulated in section 3.5.4.3 shows that for the range of cut-off wavelengths obtained here (1050nm to >1700nm) a depth of waveguide, w, from approximately 0.85μm to greater than 1.5μm (which has a cut-off wavelength of approximately 1.85μm) is estimated. This is in rough agreement with the depth range determined from the measurements of the effective refractive indices of the same waveguides in the previous section.

Using the cut-back method (see section 5.4.3) on several sample substrates reducing the length of the sample from 4cm to 3cm it was found that K^+ waveguides have around 0.5dB/cm propagation loss whereas Cs^+ waveguides have around 1-1.5dB/cm of propagation loss. This was used to calculate the coupling loss and it was found that well-polished K^+ ion-exchanged waveguides generally have approximately 2dB loss whereas

well-polished Cs^+ ion-exchanged waveguides have a coupling loss closer to 3-4dB. These coupling losses are in agreement with what would be expected, as K^+ ion-exchanged waveguides have a larger spot-size (see next section) and thus have a better overlap between their mode profile and that of the fibre (approximately 6μm waist).

This section has confirmed the expected results that wavelength cut-off increases with width and with ion exchange time for a K^+ ion-exchanged waveguides. For Cs^+ ion-exchanged waveguides it has shown the same trend with width but that the cut-off wavelength correlates better with Δn_{eff} than it does with ion-exchange time. It also shows that this is a sensitive measurement determining a wavelength that varies over many hundreds of nanometers to within a couple of nanometers. It has again shown that waveguides optimised for trapping are within the range of waveguides made and thus are feasible. Lastly both the coupling and propagation loss of the waveguides has been shown to be greater for Cs^+ ion-exchanged waveguides compared to those formed by K^+ ion-exchange.

5.5.4 Spot-size measurements

Figure 5.16a shows an example of a typical mode intensity distribution obtained experimentally along with a fitted Gaussian distribution in both the lateral (figure 5.16b) and transverse (figure 5.16c) dimensions.

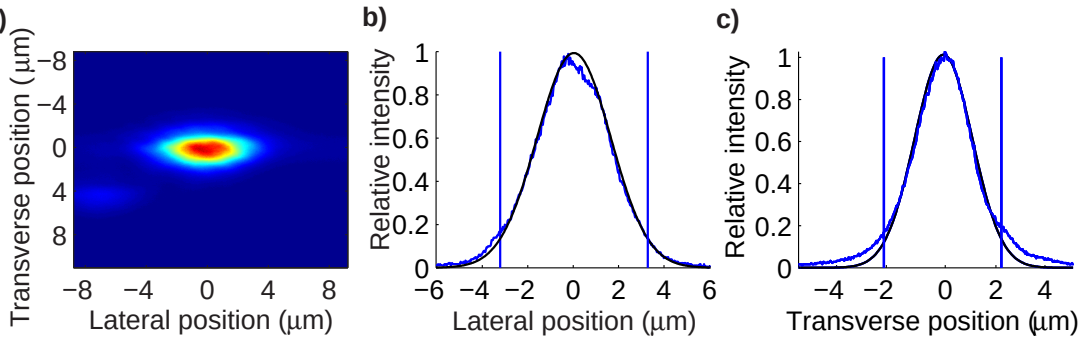

FIGURE 5.16: a) Fundamental mode profile of a K^+ ion-exchanged, 6μm opening, channel waveguide at 350^0C for 6 hours. The normalised b) lateral and c) transverse cross sections through the peak. b) and c) show the experimental data (■) and the Gaussian fit (■), whilst the vertical lines show the points at which the Gaussian has value of $1/e^2$.

Results from many waveguides were collected and are plotted for the case of K^+ ion-exchanged waveguides in figure 5.17. The results shown are for the TM fundamental mode however in the case that the waveguide is not monomode it was not always possible to only excite the fundamental mode. This problem has the greatest effect on the determination of the lateral widths of the spot-size. Figure 5.17 shows that as the waveguide gets wider so too does the beam spot-size, and that the mode height does not

change substantially in agreement with theoretical results in section 3.5.4.2. The mode height varies between approximately 4 and 5μm and the mode width varies between 6 and 11μm.

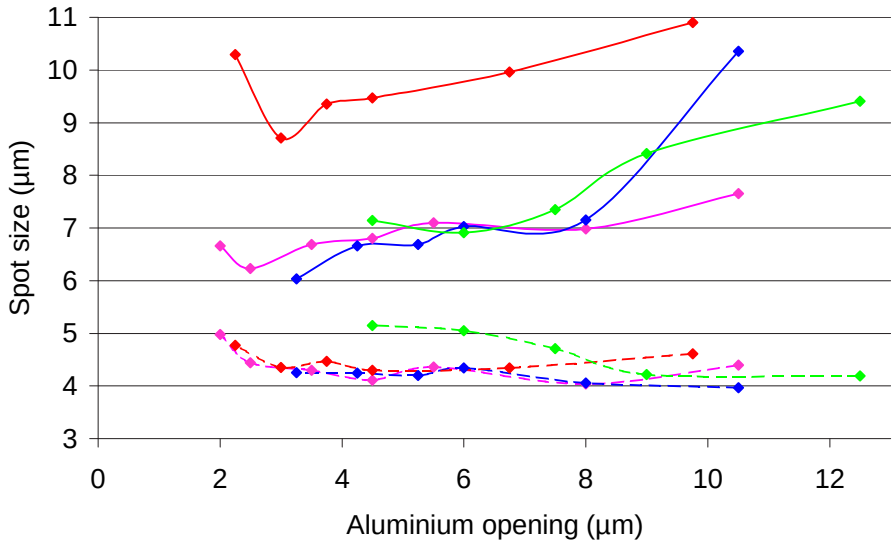

FIGURE 5.17: Spot-sizes at a wavelength of 1066nm for TM polarisation for K^+ ion-exchanged waveguide in Menzel at 350^0C for 9 (♦), 6(♦) and 4(♦) hours and in a BK7 substrate at 400^0C for 4 hours (♦). In all cases the dashed line represents the spot-size perpendicular to the surface, whereas the solid line shows the beam spot-sizes in the plane of the surface (and perpendicular to the waveguide).

Similar to figure 5.17, figure 5.18 shows beam spot-sizes for Cs^+ ion-exchanged waveguides. These results show a notable reduction in spot-size in both dimensions compared to K^+ ion-exchanged waveguides. Spot-sizes perpendicular to the substrate are generally between 2 and 3.5μm and in the plane of the substrate they are approximately 4 to 4.5μm.

In order to compare these results to those simulated in figure 3.19 the transverse height of the mode should be considered (as there is little theoretical difference to the lateral mode size as a function of ion exchange time). In addition it is more useful to compare the values for the more narrow waveguides (due to the problem of exciting higher order modes mentioned above). As can be seen, the experimentally determined heights (of between about 2 and 3.5μm) are very similar to those obtained by simulation (mainly in the range of 2 to 3μm). The only waveguide that has a modal height above 3μm for a waveguide width of less than 6μm is the waveguide that gave the lowest refractive index change at 633nm (whilst still guiding at 1066nm). Thus the greater modal height here can be explained by the waveguide approaching its cut-off wavelength causing the mode to expand.

These results can also be used to emphasise the advantage of using an ion that can induce a large refractive index change in the substrate. By taking the average of the ranges of the transverse and lateral spot-sizes for the two cases of Cs^+ and K^+ ion-exchanged waveguides it can be seen that the spot-size is over two times smaller in area for a Cs^+

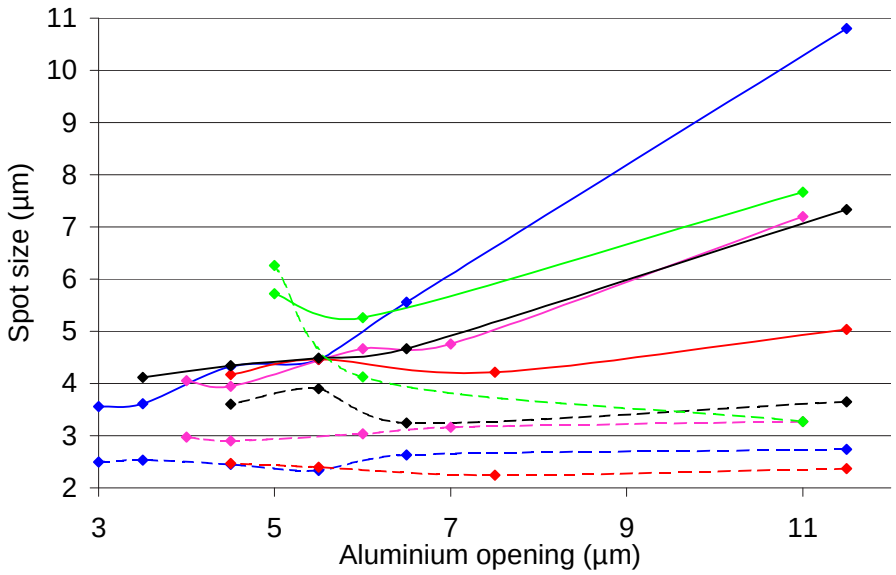

FIGURE 5.18: Spot-sizes at a wavelength of 1066nm for TM polarisation for Cs^+ ion-exchanged waveguide at 450^0C (with TM Δn_{eff} at a wavelength of 633nm) for $9^{(1)}$ (Δn_{eff}=0.0237) (♦), 8.5 (0.0188) (♦), 10 (0.0151) (♦), $9^{(2)}$ (0.0188) (♦) and 6 (0.0101) (♦) hours. In all cases the dashed line represents the spot-size perpendicular to the surface, whereas the solid line shows the spot-sizes in the plane of the surface (and perpendicular to the waveguide).

ion-exchanged waveguide with a narrow opening in the aluminium mask when compared to that of a similar K^+ waveguide. For a given modal power a smaller spot-size will lead to greater peak intensity. As shown in chapter 3 it can also lead to an even greater enhancement in the surface intensity, which is the key factor for particle trapping and manipulation.

5.6 Conclusion

This chapter first discussed the choice of waveguide configuration and identified that a diffused ion-exchanged waveguide was suitable due to its materials flexibility, the flatness of the surface provided, low propagation loss and ease of integration with biological systems amongst others. It then showed that the Cs^+ ion was a suitable ion due to its relatively large index change, its property of not precipitating to form its metallic form and its low toxicity.

In choosing a suitable substrate to use for the ion exchange process various glasses were trialled, resulting in Menzel glass being chosen for its high sodium content allowing waveguides to be fabricated with high index changes. In addition a Menzel substrate has the advantage of being approximately a hundred times cheaper than an optical glass, for example, BK7. The one disadvantage of choosing this glass therefore is that (as it is not an optical glass) the optical and surface quality is in no way guaranteed.

K^+ and Cs^+ ion-exchanged channel waveguides were fabricated and characterised for their effective index differences, cut-off wavelengths and spot-sizes. The expected trends were all found to agree with theory with the exception of the relation between the ion exchange time and the properties of Cs^+ ion-exchanged waveguides. Several potential explanations for this were put forward. In addition to the trends, the absolute values of the effective refractive indices, cut-off wavelengths and spot-sizes were found to be in reasonable agreement with those predicted by the simulations described in chapter 3.

Given the approximate agreement in parameters with the theory this suggests that the model described in chapter 3 was reasonable and thus the characteristics of the optimum waveguide as predicted by theory stand. Due to the lack of correlation between ion-exchange time and optical characteristics of the Cs^+ ion-exchanged waveguides, individual characterisation of a waveguide is necessary to distinguish the properties of the waveguides used, for the interpretation of trapping and propulsion measurements.

Chapter 6

Propulsion of Particles on Channel Waveguides

6.1 Introduction

Having fabricated waveguides that are theoretically close to optimum for the process of trapping particles, the aim is now to characterise the trapping and propulsion of both gold and latex particles on these waveguides.

This chapter describes the fundamental trapping and propelling experiments for both latex microparticles and gold nanoparticles. Firstly the experimental apparatus used to take the measurements is described. Secondly how the data is gathered and the methods used to analyse the data are discussed. Examples of the non-optical forces described in chapter 4 are shown. Characterisation of both the position and speed of particles propelled above a waveguide is shown.

Finally the effects of polarisation and modal power are shown and a comparison between the speeds of different sized particles on the same waveguide is given.

6.2 The experimental apparatus and procedure for trapping

The apparatus used for the experiments described in this chapter is shown in figure 6.1. The description and explanations of the experimental method is separated into three sections. These are the optical apparatus, describing the control and monitoring of the optical path of the laser, the imaging apparatus describing the microscope operation and the fluidic apparatus that describes the containment of the particles in a suitable cell above the waveguide.

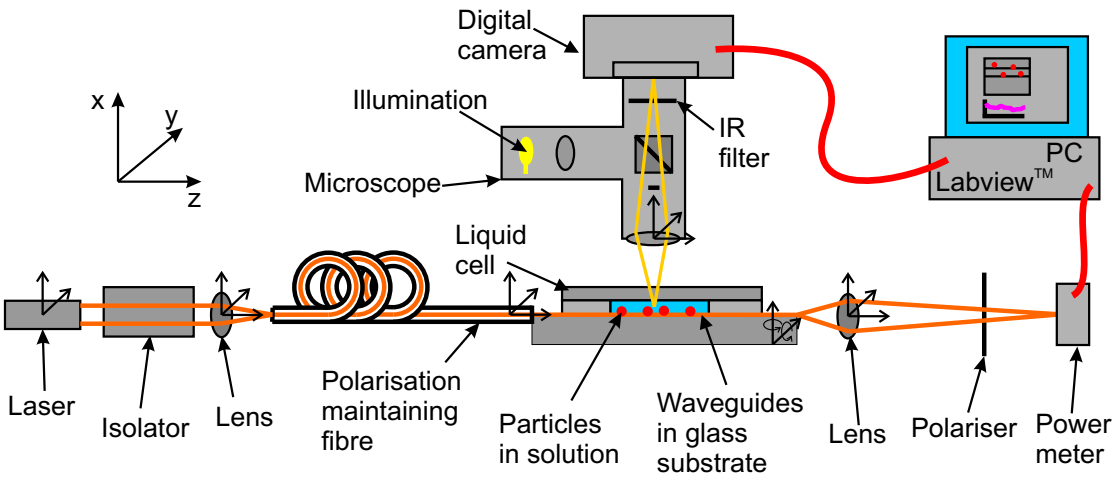

FIGURE 6.1: Schematic diagram of the experimental setup used for trapping. The arrows (→) indicates a degree of freedom offered by a manipulator in that dimension. Coloured lines indicate the optical path of the laser beam (■), the imaging path of the microscope (■) and a data link to a PC (■).

6.2.1 Optical apparatus

The laser source used for most of the experiments was a 5W, continuous wave, linearly polarised, Ytterbium doped, diode pumped, fibre laser (IPG-Photonics, PYL-5-1064-LP) with an output collimator. It supplied a Gaussian output beam with a 1.6mm waist. The beam is incident on an isolator (OFR, IO-5-1067-VHP) and coupled via a 40x microscope objective lens into single-mode polarisation maintaining fibre (Fibercore, HB980-T). The fibre is held in a rotatable chuck at both ends and a coupling efficiency of approximately 40% is achieved, whilst a degree of polarisation of greater than 30dB is maintained. The fibre is butt-coupled to the channel waveguides both with the aid of the microscope and by imaging the output of the waveguide. The substrate is held by a vacuum chuck. The power emerging from the waveguide is monitored by focussing the light out of the waveguide onto a power meter. The input and output translation stages, holding the fibre and the output lens, are three-axis positioners and the substrate stage has motion in two orthogonal axes perpendicular to the input fibre. It also has the ability to tilt around these two axes. The stages are manufactured by Melles Griot. This apparatus allows the fibre to be well aligned to the waveguide and also enables the waveguide to be horizontally levelled by translating the microscope across the substrate and observing the change in focus with position.

6.2.2 Fluidic apparatus

The substrate has a cell attached to its surface to contain the particles. This also facilitates the easy change of the fluid samples above the waveguides without the need to remove the substrate and cell, clean the substrate, reapply the cell and realign the

substrate. Instead the cell can be cleaned by flowing deionised water through it for a minute at high speed.

There are two design limitations for the cell. Firstly the part of the cell in contact with the waveguide must be of lower refractive index than the effective index of the modes supported by the waveguides. If this is not the case the waveguide would cease to contain the light at that point and the light would leak into the superstrate making the waveguide very lossy. Secondly the superstrate should have low loss so as to not increase the loss of the waveguide as a whole. However more importantly, if the superstrate is not transparent to the wavelength used, then at the high powers used, damage to the superstrate is likely to occur due to overheating. Typically the damage would in itself lead to change of form of the material e.g. by burning and thus make it much more lossy. These two conditions rule out most photoresists, many coatings, many glues and many tapes. The four options considered were: evaporated Teflon AF (with a refractive index of ∼1.31), poly-dimethyl siloxane (PDMS) (∼1.45), HS-2 UV-curing glue (∼1.45) and sputtered silica (∼1.45).

Three approaches were regularly used, each for slightly different reasons. The easiest design for rapid trials was to use a cell made of PDMS. This sealed well to the waveguide surface and would typically cause approximately 1dB of extra loss. This was fabricated by thoroughly mixing a 10:1 ratio of PDMS to hardener, pouring over a mould and allowing to settle for at least one hour (see figure 6.2). The mould design typically used was a coverslip of approximate dimensions 30×10×0.2 mm glued on top of a microscope slide. In order to remove the air bubbles the sample was then exposed to a weak vacuum (∼0.1bar) for some hours. Finally it was removed and baked for approximately one hour at 80^0C until set. The cell was then cut with a scalpel and could be peeled off the mould.

Two holes could be punched in either end of the cell in order to allow liquid in and air out. Teflon tubes (Ismatec) with an inner diameter of 1mm and an outer diameter of 1.8mm may be inserted into these holes. If inlet and outlet tubes were both used then it was required that they be positioned at least 35mm apart in order that microscope objectives could approach close enough without touching these tubes. A peristaltic pump (Pharmacia, LKB Pump, P-1) could be used to pump the required solutions over the waveguides.

The advantages of this cell were that it was easy to clean and apply. In addition, the processing of PDMS is a well known technology that can be defined much more accurately photolithographically [141]. This would require much more processing time, however it would also allow the use of much smaller samples (as may be required in a process involving the analysis of a biological sample where the sample volume is often very small). The main disadvantage with PDMS was that in order for it to be strong enough not to tear and so that the cell did not cave in, a thickness of a least two millimetres was required. This meant that the imaging was not optimal as microscope

objectives are typically adjusted for imaging through a coverslip, which has a standard thickness of approximately 180μm. This was more of a problem in imaging the gold particles than the latex particles, due to their smaller size.

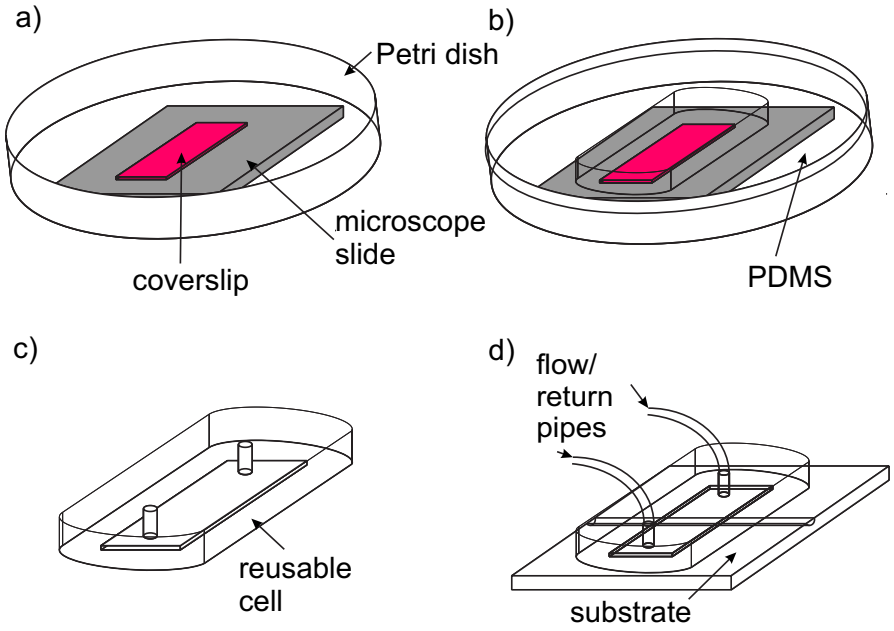

FIGURE 6.2: Fabrication and use of PDMS cell. a) Mould is made by gluing a coverslip, microscope slide, and petri dish together, b) PDMS is poured over mould, degassed, baked and cut, c) the cell can be pulled out of the mould and d) the cell is applied to the substrate. Tubes can then be pushed into the cell to allow the pumping of fluid over the waveguides.

A second design consisted of a cell made by glueing thin segments of a coverslip to the substrate with UV-curing, optically-clear glue (see figure 6.3). The segments of coverslip are made by marking with a diamond scribe using a ruler and then breaking. A microscope slide is cut to size and two holes of diameter 1.8mm are drilled with an ultrasonic drill. The required shape of a waxy film (Parafilm) is cut out with a scalpel and is used to affix the slide to the substrate to form the cell. The substrate, Parafilm cut out and the drilled microscope slide are heated to 70^0C, pressed firmly together and allowed to cool (with the pressure still applied). This produced a watertight cell of approximate thickness 230μm, equal to the thickness of the coverslip (180μm) plus the thickness of the Parafilm cut-out (50μm). Tubes could then be attached to the holes with superglue and a solution pumped through, as before.

There were three principal problems with this method. Firstly it was impossible to wipe away any excess glue when gluing the coverslips as this would lead to streaks of glue being left on the substrate. This meant the beam encountered multiple changes in the superstrate refractive index and thus increased the loss. Wiping with acetone that acted as a solvent improved this, however it also left an opaque film when it dried that drastically increased the loss. Secondly the damage threshold of the glue was not high and led to observations of burnt glue above waveguides which had suddenly become very

lossy at the high powers required for trapping. Lastly, it was very hard to remove the coverslips once they had been glued down.

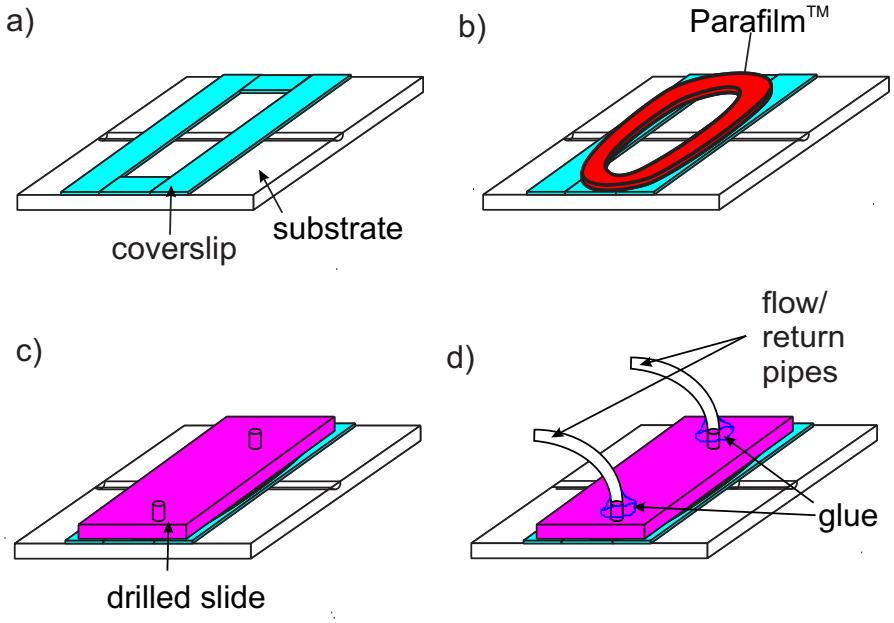

FIGURE 6.3: Fabrication and use of cell using UV-curing glue. a) Segments of coverslip are glued to the substrate, b) a cut-out sheet of Parafilm is laid over coverslips, c) the microscope slide fixed to top by heating the substrate and pressing together and d) the tubes glued in with superglue.

The most satisfactory method for the liquid cell was with the use of a silica (SiO_2) isolation layer defined with photoresist on top of the waveguides (see figure 6.4). A film of thickness 1.5μm SiO_2 was sputtered over the whole surface. The substrate was then washed in acetone that lifted off the photoresist leaving a gap in the silica film. This allowed the particles access to the superstrate of the waveguide. A Parafilm film cut-out and the same cut and drilled microscope slide as above then formed the cell. The thickness of this cell was therefore approximately 50μm. The sputtered silica was found to give no measurable extra loss.

Unless otherwise stated results presented in this thesis were collected using one of the latter two cells. The PDMS cell was only used for screening samples and quick tests. The method using the sputtered silica was the preferred method, however acceptable sputtering conditions for silica were not developed until part way through the project.

6.2.3 Imaging apparatus

A microscope (Nikon, Universal Epi-illuminator 10) is held by a custom-built holder above the substrate and has a digital camera (Qimaging, Monochrome Retiga 1300) attached for recording digital images to a computer. The microscope has three axes of motion (a focus and two orthogonal axes that allowed translation both parallel and

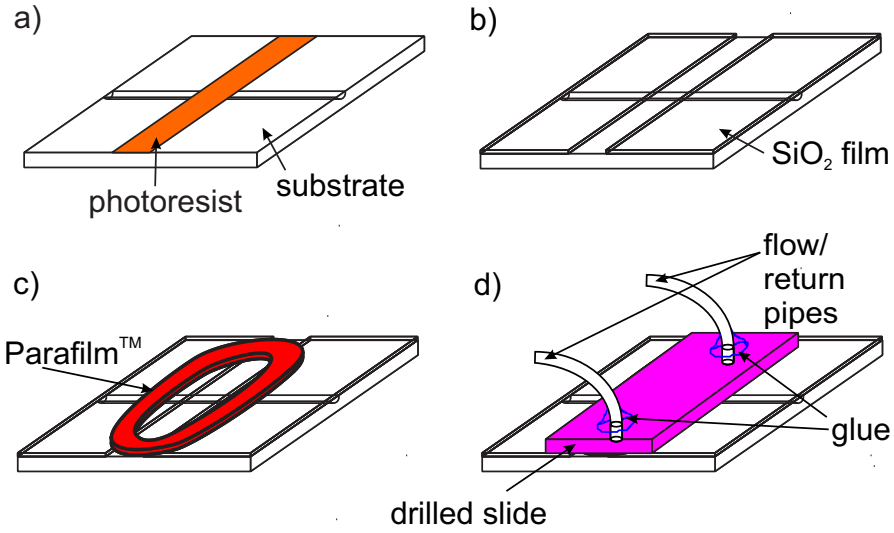

FIGURE 6.4: Fabrication method for a cell using sputtered silica. a) Photoresist is defined, b) silica is sputtered and lifted-off where the photoresist previously was, c) a cut-out sheet of Parafilm laid over coverslips and d) a microscope slide is fixed to top by heating the substrate and pressing together. Tubes can subsequently be glued in with superglue.

perpendicular to the waveguide axis). The microscope can be operated in either bright field mode or dark field mode. Bright field mode is the normal mode of operation for a microscope. In dark field mode the microscope cuts out all of the microscope's on-axis rays and passes oblique rays. This is carried out with an opaque light stop beneath the condenser lens. For microscopes operating in reflection (as in this case) this has the effect of changing both the illumination and the light that is allowed for viewing, thus making the images generally much darker. Images formed in dark field mode only consist of light that is either scattered or reflected from objects held at an angle greater than the effective numerical aperture of the dark field stop. Thus, in contrast to images taken in bright field mode, the majority of an image is black since reflections from interfaces orthogonal to the imaging axis are cut out. This feature is of great use since in bright field mode the relatively small amount of scattering from a nanoparticle is much smaller than the reflection from the interfaces of the air-coverglass, the coverglass-water, the water-substrate and the substrate-air interfaces. In dark field mode typically much longer integration times are therefore required for the digital camera.

The reason the vacuum holder is used to hold the substrate is to allow the substrate to be supported along one edge. In this way the area being imaged has air underneath the substrate. This eliminates the scattering from the surface of a holder that would increase the background light in images taken in dark field mode.

6.3 Gathering and analysis of images

The quantity of data that is gathered is too great to analyse particle motion in real time (typically a minimum of 100Mb in 4 minutes). Therefore the data is stored on a PC during the experiment to be analysed later. The acquisition and analysis are described below.

6.3.1 Data acquisition

Labview is used to gather all data in one integrated program. There are three parts to the data stored. Firstly a sequence of images is stored as soon as they are acquired. Simultaneously a record of the waveguide power as monitored by the power meter is updated. The file recording this data updates in batches. Lastly at the end of the recording a list of data about the particular experiment such as the particle size, concentration, laser polarization etc. is recorded.

A screenshot of the custom-written program is shown in figure 9.1 in Appendix A.

At the start of each experiment various parameters to control the camera must be input. These are:

- the integration time. This is the length of time that the camera has its electronic shutter open for, for each frame. In order to do effective subsequent analysis this must be set such that the brightest pixel is not saturated. The brighter the image the shorter the integration time required.
- the binning level. This is a method of sacrificing the resolution of the camera by grouping pixels together in order to increase the sensitivity of the camera. This also has the beneficial effect of reducing the data size of each frame. The camera used has the option of grouping together square arrays of 1,4,9 or 16 pixels giving resolutions of 1280×1024, 640×480, 420×340 and 312×240 respectively.
- the region of interest. It is possible to specify a rectangle of pixels that should be transferred from the camera to the computer. This is relevant if the image of interest has a different aspect ratio to that of the camera. Waveguides which are much narrower than their length can be imaged using this function as an area with width 10μm either side of the waveguide and a length of several hundred microns may be imaged. The advantage of reducing the region of interest is that less data is required to be transferred to the PC, thus a higher rate of acquisition of frames is available.
- the rate at which images should be recorded. As described above the camera has a user-defined integration time, however before it can start recording the next image

the data from the previous image must be sent to and stored on the PC. As this is not instantaneous the stored frame rate has to be slower than the integration time. For example, it has been found that, with 4×4 binning, in order to store a complete frame (312×240 pixels) at a rate of 20 Hz (i.e. a new picture every 50ms) the integration time cannot exceed 15ms. This demonstrates the importance of considering the region of interest and level of binning required as, using 1×1 binning, the frame rate is restricted to 1.7Hz, which is too slow to be able to track fast travelling particles.

The camera is controlled with one program using subroutines supplied by the camera's manufacturer. The images were transferred to the PC via a Firewire connection to a manufacturer-supplied board and are stored in a user-defined directory with the filename being a number indicating the position of the image in the sequence of the files.

The data for the power at the waveguide output is measured by a power meter (Newport, 835-C). The analogue output from this is recorded by a data acquisition board (National Instruments, S1840) and is multiplied by a constant to obtain the output power in milliwatts. The signal is sampled at a rate of 500Hz and all values are averaged over 1 second with the power being recorded and a text file appended to every second. This data was a fraction of that used by the camera so that although quite a high rate is used, it had no observable effect on the acquisition rate of the camera.

Data about the particle size and concentration, the salt concentration (see section 6.4.2), power of laser input, the initial waveguide output power, polarization of the laser input, the magnification of the microscope and which filter is inserted (either none, a neutral density or a 1μm wavelength high-pass filter), whether the microscope is in BF or DF mode and the total amount of time for which the whole programme ran is stored in a separate, automatically generated, file as a log file of the experiment. A box is also provided for any relevant user comments particular to that run. This program records an accurate, high temporal resolution record of the experiments where all the data regarding the conditions of the experiment must be provided to allow the experiment to start.

6.3.2 Analysis of data

Having collected a large amount of data (typically 5000 images were recorded for a single data point) it was necessary to have an automated and reasonably sophisticated method for analysing it. The following was required from the software:

- To make a movie containing sufficient data to be able to visualize particle motion. The movie should be enhanced in any way that would improve its clarity.

- To analyse the images firstly by identifying and recording the position of each particle in each image.
- From this data to use a nearest-neighbour approximation to identify the same particles in sequential images, thus giving the ability to track the particles, and to record this data.
- To collate these results to give an overall description of the motion of the particles.
- To display these results in a way that will demonstrate, or otherwise, the hypothesis being tested.

Custom-written programs were required and all of the analysis programs were implemented using Matlab. In later chapters the modular design of programming used demonstrates how the program is easily modified to explore new phenomena. This is one significant advantage of using a self-written program over using commercial software.

6.3.2.1 Making a movie

The process for making the movie was similar for all movies. Frames were opened in the order they were recorded. They were made into an image with the axes labeled with the scale and the title being the time point of the frame. The only enhancements that were added to this basic procedure were:

- Brighten. In order to record at as high an image rate as possible, rather than using the complete static range of the camera the images tended to be dark. Therefore images were rescaled in terms of brightness to use the complete range of the screen.
- Background removal. Sometimes, especially when recording scattered laser light images, there would be a constant background to all the frames. By summing all the frames and dividing by the number of these frames an average frame is obtained. Note that the method used gives an average frame rather than the average of all frames. The difference being that the average frame will contain position-dependent features whereas the average of the frames is a single value.
- Region of interest selection. Although the frames were recorded in a certain region of interest, occasionally only a certain part of the area recorded was required.

6.3.2.2 Identification of position of particles

The identification of the position of particles in a frame, was perhaps the most complicated aspect of the programming and still has limitations. The basic method followed was to:

- Calculate the average frame. This is as described above, however for very long recordings the average frame (or the background) will change over time. In this case it was necessary to split the background into shorter segments, for example, 500 frames. Ideally it would have been better to calculate an average image that comprised, for example, the previous 100 frames and the next 100 frames. However this method would have been much more computationally demanding.

- Limit pixels. Having subtracted the average frame from the frame being considered an intensity limit was placed on the image. The coordinates of all pixels in the image (minus the background) that were above this limit were recorded.

- Collate pixels. Pixels were collated so that if there were two or more pixels that had been found that were adjacent to each other, they were grouped together.

- Particle identification. Another threshold was used so that to be considered a particle an object must contain more than a certain number of grouped pixels (typically three). This drastically diminished the effect of noise as the probability of three or more pixels being randomly above the limit and adjacent to each other was highly unlikely. The particle position was then calculated as the average of the coordinates of the points that made up this object. No intensity weighting was used.

- Record and repeat. These positions were recorded for this frame and then repeated for all frames.

6.3.2.3 Particle tracking analysis

Having a data structure containing the positions of the particles in each frame, in order to track the particles, it was necessary to interrogate this data. This was carried out as follows:

- Particle positions from a pair of sequential frames were compared. A matrix was calculated giving the distance from every particle in the first frame to every particle in the next frame.

- This matrix was repeatedly interrogated to obtain the minimum value, the associated pair of particles were given the same label and the elements in this column and row set at a very high value. This was repeated until a user-defined separation between the particles was exceeded. This was a distance beyond which it was judged highly unlikely for a particle to travel in the given time interval. Clearly this became more of a problem as particle speeds increased. In this case unambiguous results were obtained by reducing the particle concentration.

- A displacement was calculated for each particle that was also found in the previous frame.
- Particles in the second frame that had not been identified as having an associated particle in the first frame were given a new label.

It is clear that using this process, there is a great advantage in keeping the number of particles in any given frame reasonably low so as to vastly reduce the processing time required to analyse the data. Countering that was the wish to obtain data about as many particles as possible.

6.3.2.4 Checking, collection and presentation of results

It was necessary to check that particles had been accurately identified and that the tracking process produced plausible results. As a first check a program was written that loaded and displayed a small number of frames. It would highlight the identified particles and show the displacements between any similar particles that were identified. This could be visually checked and led to a simple pass-fail test. If it failed, the previous programs would have to be rerun with different parameters, or in the worst case, if the data was not good enough for the program to complete the analysis reliably the experiment would be discarded and repeated. This could be due to a number of causes. Firstly the background could be too noisy for the program to be able to locate the particles. Secondly too many particles could be present making particle tracking unreliable. Lastly, it could be that the background was changing too quickly to be compensated for.

The previous check ensured that the results were not likely to be catastrophically wrong, however it would have been prohibitively time-consuming to check every displacement individually. Therefore another type of filter is applied. Here the position transverse to the waveguide is plotted against the velocity in the direction of the waveguide. As mentioned above a user defined limit is put on the displacement that a particle can have. This is chosen to allow propelled particles travelling at their peak speed to be accepted, but reject displacements where, for example a particle leaves the region of interest at the same instant another particle enters, in another area of the frame. The filter used here was simple and consisted of rejecting large displacements not in the region of the waveguide. This may seem to be an unreliable filter as only data that is expected is retained. However typically there are very few such displacements amongst many thousands and by checking these points on a number of sample analyses manually, this has been observed to be a reasonable filter (i.e. it was clear that the pair of particles in contention should not be considered the same).

From this large amount of data it is possible to produce many different graphs automatically and these will be explained as they are introduced both in this and later chapters.

6.4 Non-optical experimental results

6.4.1 Brownian motion of particles

As described in section 4.4, Brownian motion is always present, and little can be done to reduce the effect of it, other than cooling the sample. This was considered unlikely to be successful as a minimum temperature of approximately 0^0C was possible, however it would be very hard to maintain this temperature close to the waveguide especially considering the heat absorbed from the laser light. To quantify the motion of particles in the absence of laser light, results demonstrating how the Brownian motion of particles increases with decreasing particle radius are given.

A cell was fixed to a glass slide and particles were injected at a suitable concentration and a sequence of 5000 images was recorded at 20Hz using dark-field imaging. Typical images of five different particle sizes, 6μm and 3μm latex particles (Duke Scientific, 4000 series) and 250nm, 150nm and 100nm gold particles (British Biocell International, GC series) are shown in both their raw form and with their background removed in figure 6.5. The images of the 6μm and 3μm particles were sufficiently bright that background removal was unnecessary.

Using the method of analysis described above it was possible to plot the displacement vector diagram, samples of which are shown below in figure 6.6 for the 3μm latex and the 250nm gold particles. This plots every displacement in a 50ms time frame of every particle on the same plot. As can be seen the particles move about randomly with particles equally likely to travel in all directions. This confirms that the cell is suitable in terms of preventing drift.

Root-mean-squared (RMS) distance was used to compare with theory rather than velocity, due to the low sampling rate. RMS distance is not a function of the sampling speed and may be compared to theory using equation 4.10. As can also be seen from equation 4.10 the Brownian motion should solely be a function of the particle size, thus comparing latex and gold samples as like-for-like, should not affect the results. The measurement is made more accurate by sampling a greater number of images and recording over a longer time.

This data was analysed and compared to theoretical values. Rather than using the data from figure 6.6 directly, displacements from the point at which a particle is first observed until it is lost are used. This reduces the effect of quantization error due to pixellation

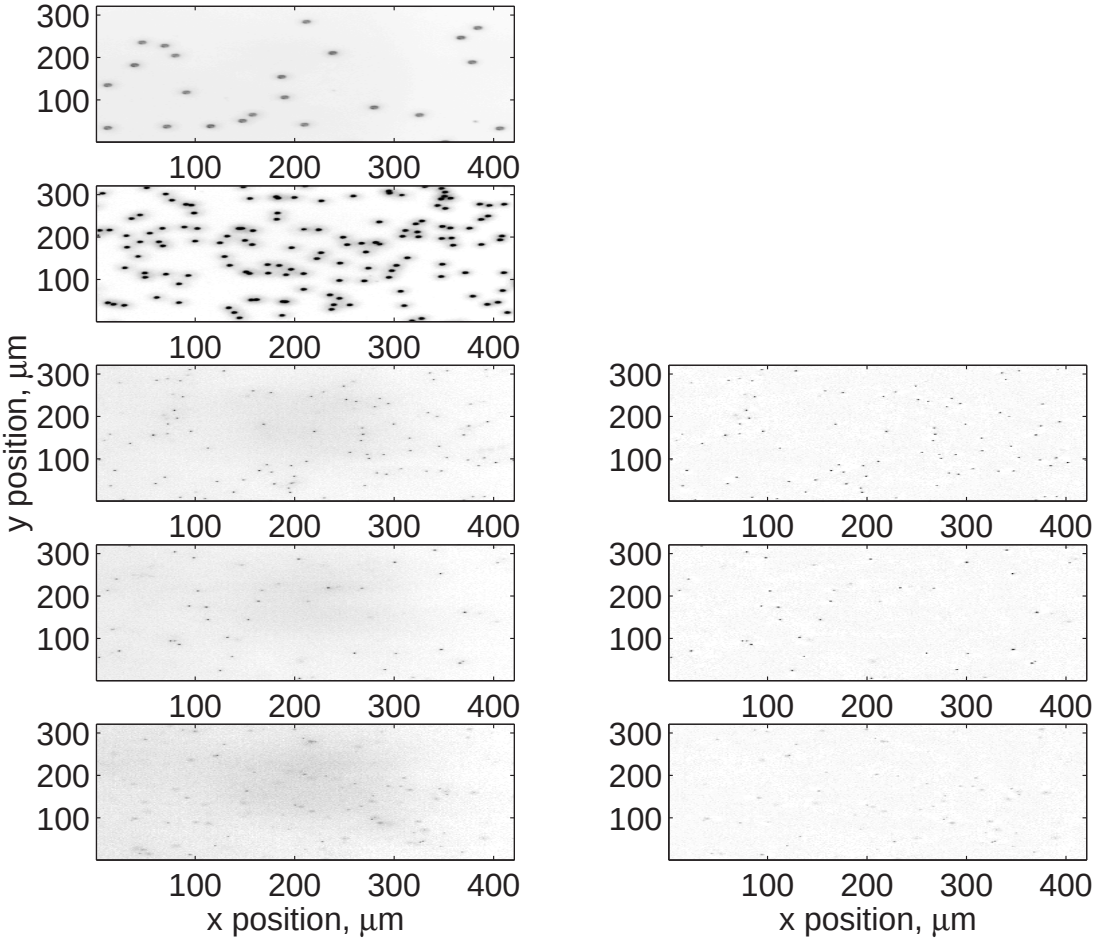

FIGURE 6.5: Particle images of 6μm, 3μm, 250nm, 150nm and 100nm from the top down respectively, with the left images being the raw images and the right images being the background-corrected images. Images inverted for clarity.

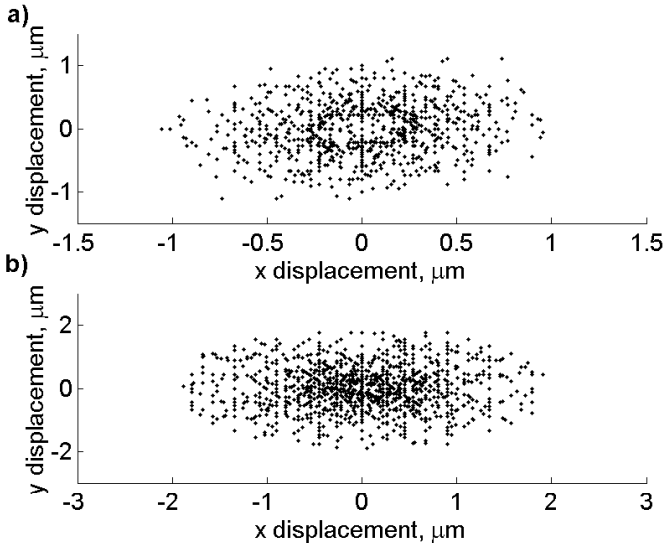

FIGURE 6.6: All displacements of all particles in a 50ms time interval recorded over 5000 frames for a) 3μm particles and b) 250nm particles.

that can be observed in figure 6.6. Therefore as particles were tracked for a varied length of time equation 4.10 was slightly modified to the following form:

$$Br = \frac{\overline{(x,y)^2}}{t} = \frac{2kT}{3\pi a\eta} \tag{6.1}$$

The function, Br, is plotted from the experimental data using the first half of the equation and theoretically using the last part of the equation. Figure 6.7 shows a graph comparing experiment and theory in this way for the five particle sizes.

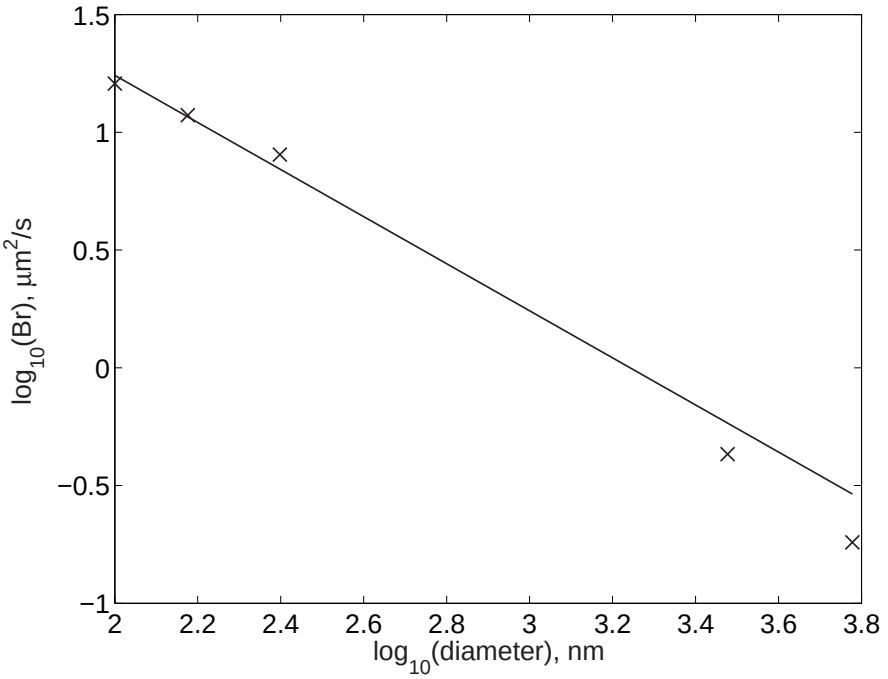

FIGURE 6.7: Comparison of Brownian motion experimentally measured (×) compared to that calculated theoretically (–) for particles of different radii.

Figure 6.7 shows a good fit especially for the smaller particles. In this graph the value of η used was 1×10^{-3}Pas. This is the bulk value for water and does not take into account the effect of the surface described in section 4.3. This may therefore explain the deviation for larger radii particles where the increased weight of the particles may cause them to sit closer to the surface and thus reduce the Brownian motion. This good fit of the data for the gold particles helps validate the method of analysis of particle tracking used and confirms the destabilising effect of Brownian motion that the optical trap will be required to overcome.

6.4.2 The effect of ion concentration

As described in section 4.5, by increasing the ion concentration in the cell it was believed that the electric double-layer repulsive force could be reduced by screening the

effectiveness of the particle and the waveguide to repel each other.

It was observed experimentally that with a high concentration of sodium chloride (NaCl) added to the solution of gold particles injected over the cell, the particles would become stuck immediately on contact with the surface. These particles could be removed, but only by removing the cell and pumping pressurised water over the surface or physically rubbing the surface.

In order to examine this effect, solutions were prepared containing 250nm gold particles diluted with water to a concentration of 7×10^6 particles/ml. To this a variable volume of a sodium chloride solution was added and the solution thoroughly mixed. A planar waveguide was selected (the whole surface being ion-exchanged) and a cell affixed (using a microscope slide to form the top of the cell). The solutions with different concentrations of NaCl were injected over the surface and observed. Between each test the cell was removed, the surfaces cleaned with acetone, IPA and copious amounts of deionised water and the surfaces were blown dry. Images of the particles were recorded every second for ten minutes and a movie subsequently made. The movie was examined noting the number of particles stuck to the surface at the start (if any), the number of particles stuck after 200 seconds and the number of particles stuck after 400 seconds. The fraction of particles free at these times (discounting those initially stuck) are plotted for a range of concentrations, as shown below in figure 6.8.

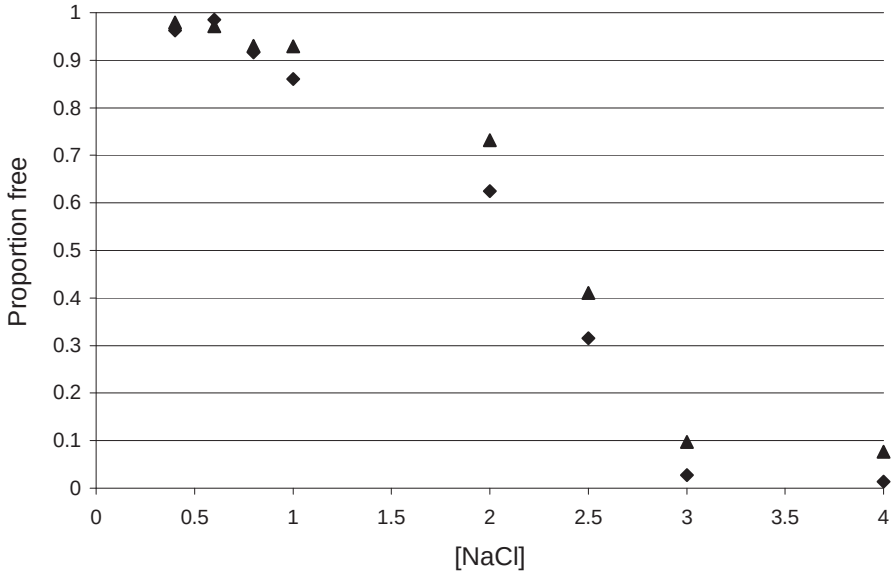

FIGURE 6.8: The proportion of particles free after 200 (▲) and 400 (♦) seconds.

Figure 6.8 shows that the proportion of particles free after 400 seconds are shifted to slightly lower values than the proportion after 200 seconds (as would be expected). At concentrations above 3×10^{-3}M almost all particles were stuck within 400 seconds. In addition, at NaCl concentrations below approximately 0.6×10^{-3}M virtually no particles became attached to the surface. In fact, although particles did become attached, often with time they would be released and move around again with Brownian motion.

Although the concentration at which particles start to become stuck was not predicted theoretically the trend is as expected. The periods of time chosen are comparable to those required to run one analysis.

The choice of sodium chloride was not arbitrary. Firstly the salt should be monovalent (in order to be compared more easily with theory). To reduce the number of variables the substance should not be an acid or alkali. NaCl maintains the pH at approximately 7. NaCl also dissociates totally (meaning that the concentration of ions may be simply calculated). Lastly it was chosen as the solution did not introduce any new ions. Na^+ ions are already present (in very low concentrations) due to the dissociation from the surface of the glass and Cl^- ions are present on the surface of the gold to prevent agglomeration of the particles.

As a consequence of these results, in the experiments conducted below with gold particles, a NaCl concentration of 0.4×10^{-3}M, slightly less than the lower value determined above, was used both to ensure that a constant concentration of ions were present and to aid the gold particles in approaching the surface (see section 4.5) whilst preventing them from becoming attached.

6.4.3 The minimization of drift on the surface

During the project, two types of drift have been observed. The first was due to evaporation from open cells. Initially the cells that were used were exposed along the edges perpendicular to the waveguides. This reduced the loss of the waveguide and was much simpler to construct. However it was found that this type of cell was not ideal as water held at the edges of the thin film could evaporate dragging the remaining water by surface tension. This led to a very fast drift of the particles, making them much harder to trap. This therefore necessitated a closed cell which (as seen above) resolved this problem.

The second type of drift was caused by the laser and is thought to be due to absorption causing heating. As has been discussed in section 4.6 absorption by the waveguide is expected to lead to a water flow perpendicular to the waveguide above the surface of the substrate. In the most extreme case boiling of water above the waveguide has been observed. However this was only a very localised effect, and is therefore thought to be due to a very absorbing contaminant being present, for example, aluminium left over from the ion-exchange mask.

Figure 6.9 shows the first image of a movie (drift.avi) that demonstrates an extreme case of how 250nm particles are attracted laterally towards the waveguide due to heating in a cell. In this case a K^+ ion-exchanged waveguide with an output power of approximately 1W is used.

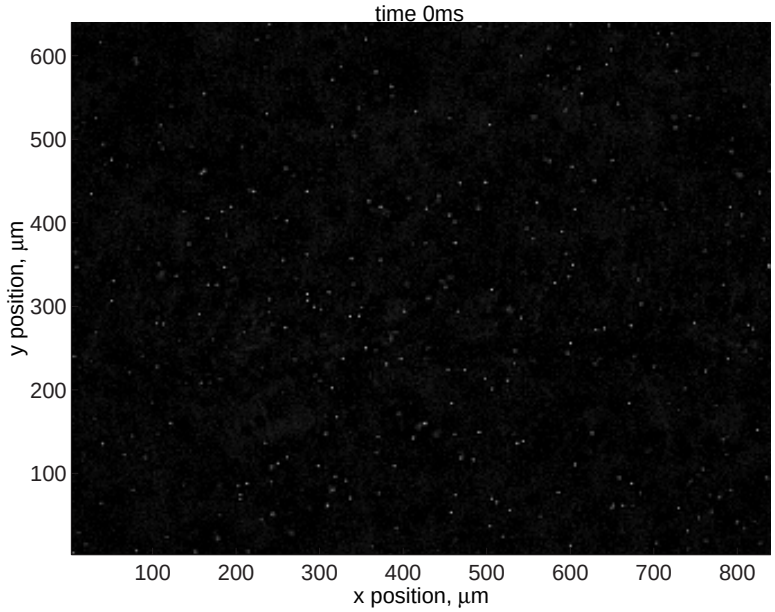

FIGURE 6.9: The first image of a movie (drift.avi) showing 250nm gold particles drifting due to convection currents caused by absorption of laser radiation.

The movie shows particles with speeds of up to about 40μm/s being attracted towards the waveguide. When they approach the waveguide they appear to slow down laterally as they start to be lifted vertically upwards as was predicted in section 4.6. This can be observed in the particles starting close to the waveguide (at the centre of the figure). After a time they appear to disappear which can physically only be explained by them travelling upwards out of the focus of the microscope. Individual particles can be tracked by adjusting the focus and are shown to follow the path predicted by natural convection shown in [116]. It was found that drift was reduced by using lower modal powers and by the use of a thinner cell.

6.5 Particle propulsion results

6.5.1 Positional propulsion results

The experiments in this section use Cs^+ ion-exchanged waveguides fabricated in Menzel glass at 450^0C for 6.5 hours. 250$\pm$20nm gold particles were diluted to 10^6 particles/ml and were injected into the cell.

The first image of a movie (goldprop.avi) showing the motion of the particles is shown in figure 6.10. The temporal resolution is 50ms and a 20x magnification objective was used. This experiment uses a waveguide with an aluminium opening of 3μm and a measured spotsize of approximately 5.0μm width x 2.4μm depth, an effective index of 1.5042 $\pm$ 0.0005 and was single-mode at 1066nm. The two weak parallel lines show the edges of the waveguide. In this movie false colours have been used to aid viewing.

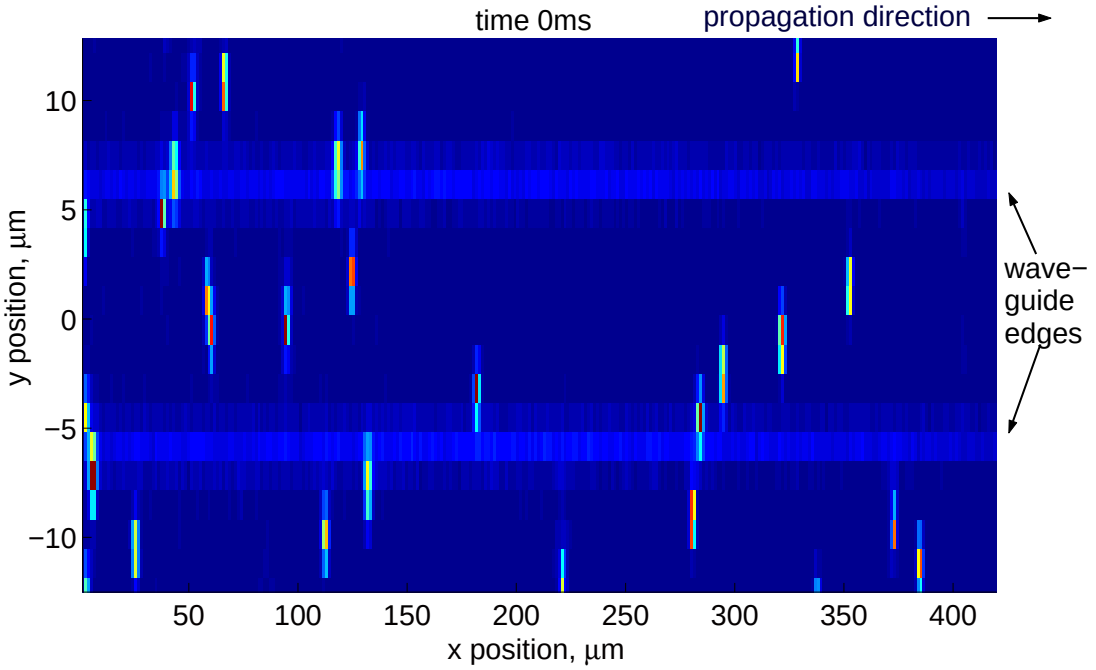

FIGURE 6.10: First image of a movie (goldprop.avi) showing particles above a 3μm wide, single-mode waveguide. The movie shows the motion of the particles - some of which are propelled along the waveguide.

Figure 6.11a shows the same small region within three consecutive images separated by 50ms, illustrating the motion of three particles on this single-mode waveguide. While the images appear cluttered due to imperfections in the surface of the glass, this background is removed in the analysis; it is not removed here to allow the edges of the waveguide to be seen. It is clear that the particles do not move at a steady rate, for example the right particle (R) moves much further in the first 50ms than in the second 50ms, during which the left particle (L) shows no more than Brownian motion. The difference in the speed of the propelled particles is believed to be due to fluctuations in both the height and lateral position of particles above the waveguide resulting in them being exposed to differing evanescent field strengths.

Figure 6.11b shows the 2-D trajectory of an individual particle on the same waveguide for a duration of approximately 10s before it is propelled out of the field of view. It was extracted from a sequence of images containing many tens of particles. Alternating full and dotted lines connect the centre of the particle from sequential frames (every 100ms in this case). Brownian motion can be observed at the extreme left of the graph, as random meandering until the particle encounters the evanescent field of the waveguide. It is then propelled at a speed proportional to the intensity at that point. The vector lines represent a velocity and can be represented as a distribution of velocities as shown in figure 6.11c.

Figure 6.11c may be considered as two groups of points; the first is a near-circular distribution centered near the origin that represents random Brownian motion as seen

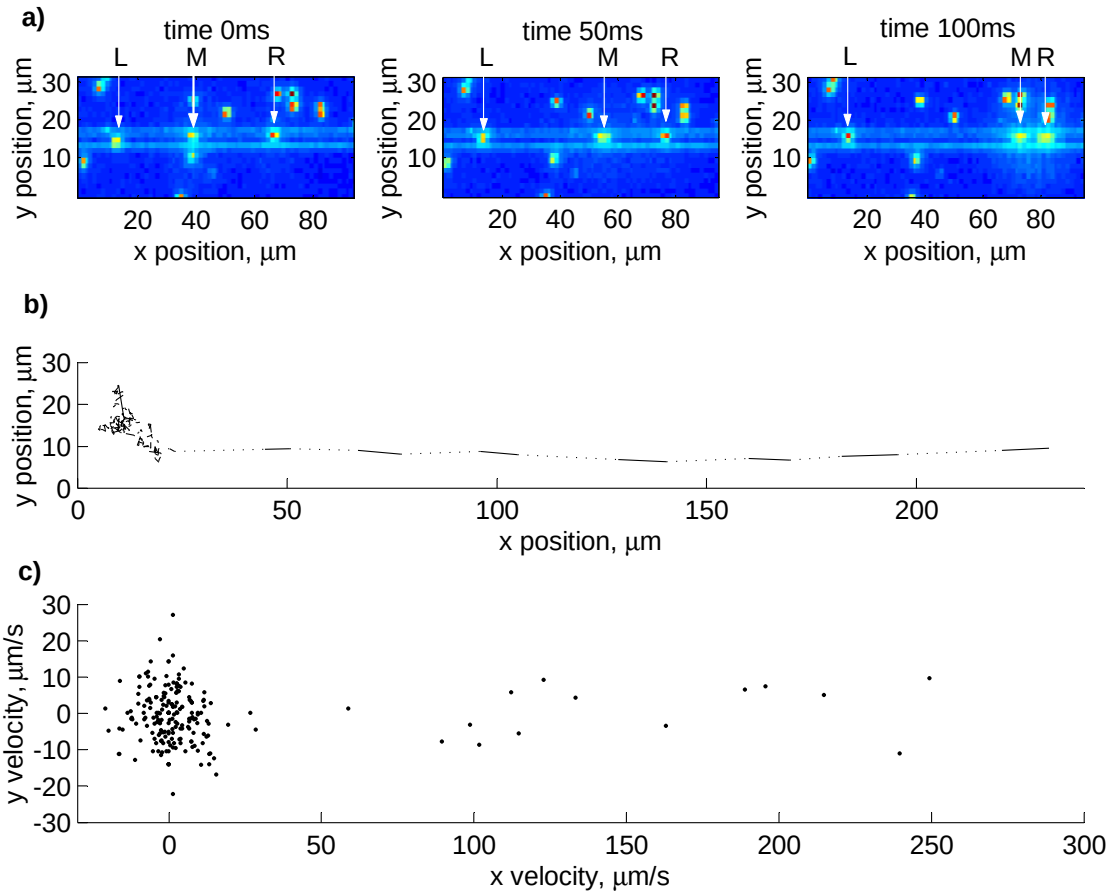

FIGURE 6.11: a) Three consecutive images of three 250nm gold particles propelled along the waveguide b) A typical trace of a particle initially traveling randomly due to Brownian motion until it is propelled along the waveguide c) the velocity diagram of the particle in b.

in section 6.4.1 and any temperature-induced macro flow. The second group forms a lobe in the positive x direction. This represents the particle being propelled along the waveguide by the evanescent field of the mode. The transverse speed, compared with that under purely Brownian motion, is reduced slightly due to the restoring force from the lateral gradient of the optical trap.

Figure 6.12 shows the positions of all particles moving along the waveguide at a speed of at least 40μm/s, for (a) the monomode waveguide described in figures 6.10 and 6.11 and (b) a laterally dual-moded waveguide, formed by ion-exchange on the same substrate through an 11μm wide stripe. For the dual-moded waveguide the input fibre is butted off-axis to excite both modes, which were measured (in air) to have effective indices of 1.5075 $\pm$ 0.0005 and 1.5090$\pm$0.0005. These plots show that in the case of a single mode waveguide the particles follow a straight line along the waveguide, whereas in the case of the dual-moded waveguide the particles are only propelled in the areas following the beat pattern of the intensity. The linear structure in these plots parallel to the waveguide is an artifact due to pixellation.

The beat-length is the spatial period of the sinusoidal pattern caused by the interference of two modes of a waveguide. It is given by $\frac{2\pi}{\Delta\beta}$ where $\Delta\beta = k_0(n_1 - n_2)$ and where n_1 and n_2 are the effective indices of the two modes being considered [142]. In figure 6.12 it can be seen that the measured beat length is approximately 540μm. This would result from the beating between the fundamental and first order modes with a difference in effective refractive indices of $\Delta N_{eff} \sim 0.002$, in reasonable agreement with the measured effective indices. Particles travel on the high-intensity side of the waveguide until the intensity on both sides becomes similar, when they cannot cross over the waveguide as abruptly as the beat pattern does. Tanaka and Yamamoto demonstrated similar behaviour with 4μm diameter latex beads, but with much lower resolution due to the size of the beads [69].

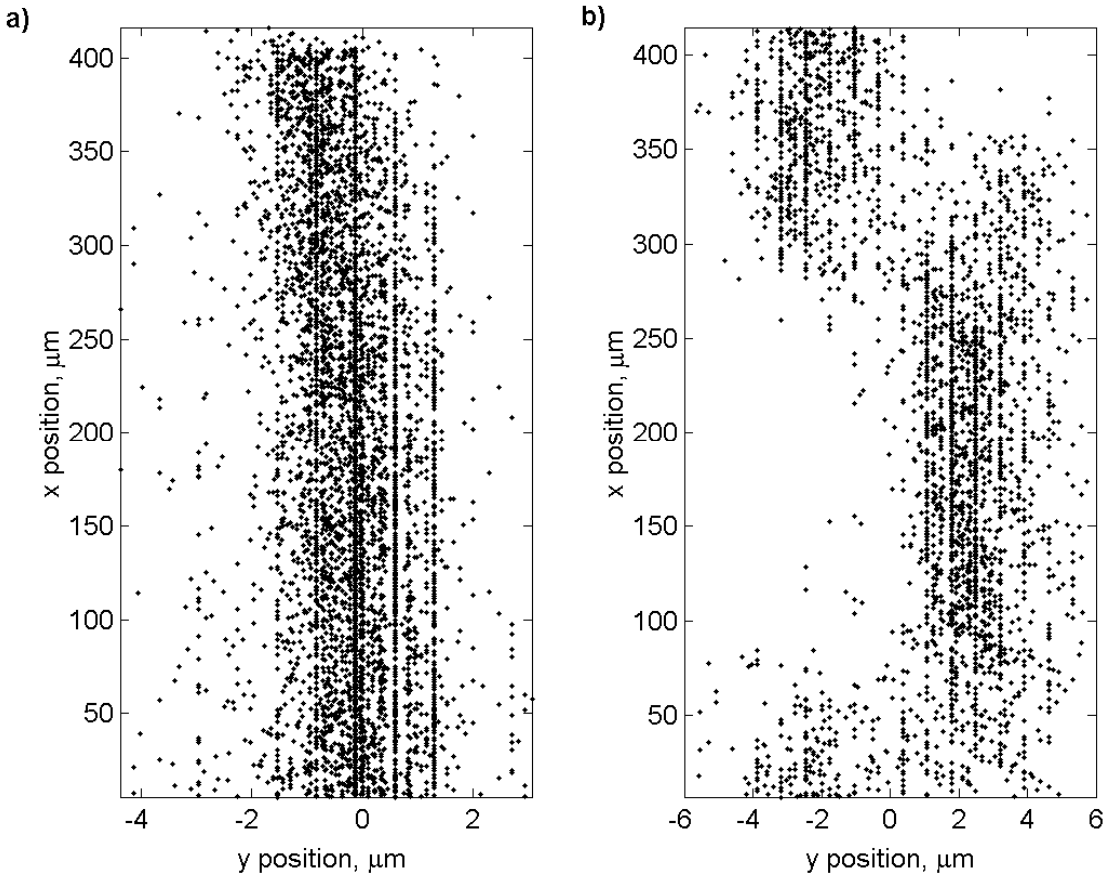

FIGURE 6.12: Position of propelled particles for a) a single mode waveguide b) a dual-moded waveguide.

Figure 6.13a and b shows the speed of particles along the waveguide as a function of their position across the waveguide for both the single mode and dual-mode waveguides. These graphs represent a large number of particles observed over a waveguide length of approximately 425μm for approximately eight minutes. Figure 6.13a shows the case for the single mode waveguide while figure 6.13b shows the case for the dual-moded waveguide. Figure 6.13a clearly shows that at the centre of the waveguide, where the intensity is expected to be the greatest, the particles travel at the greatest speed. Figure 6.13c and

d shows the measured mode profiles of the waveguides. The width of the distribution of the propelled particles for the single mode waveguide (4.4μm) shows that the propelled particles are confined within the 5.0μm width of the mode, as expected. In Figure 6.13d only the fundamental mode is shown, to give an indication of the intensity distribution in comparison with the velocity distribution of the particles. In the experiment, both the fundamental and the first order mode are excited.

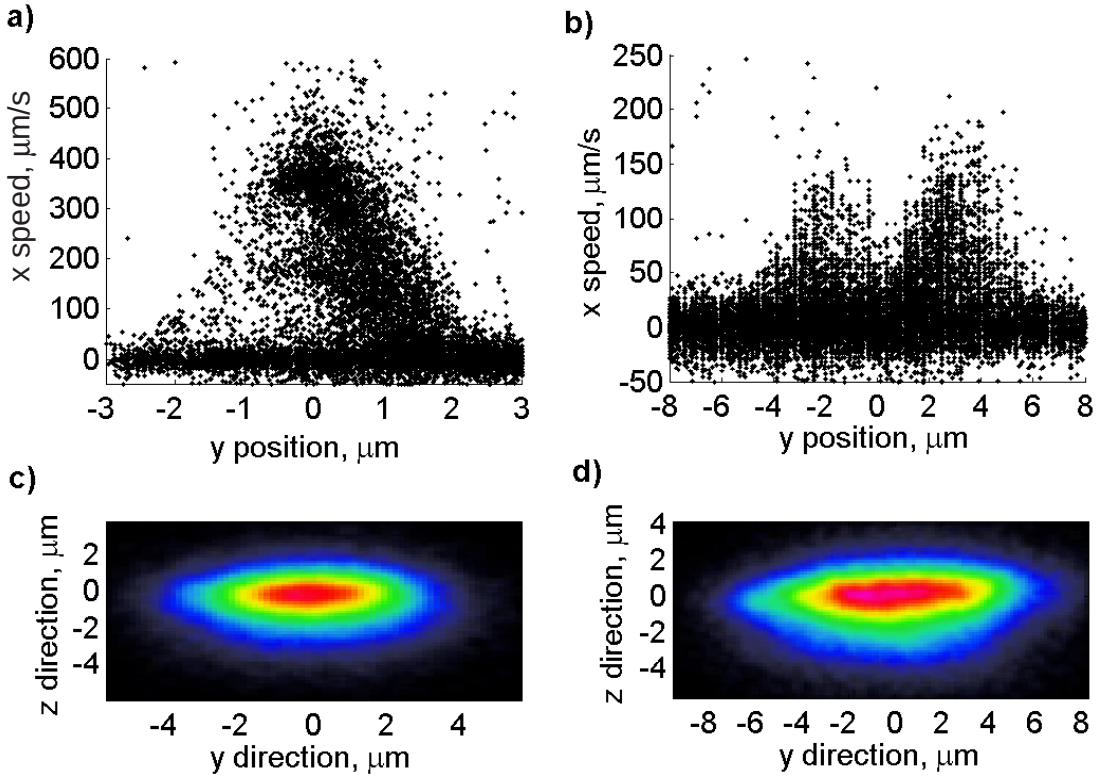

FIGURE 6.13: Plot of lateral position against speed of particles for a) single mode waveguide b) dual-moded waveguide, and their respective beam profiles c),d).

The envelopes of these data points represent the maximum velocity experienced by particles very close to the surface of the waveguide. The envelopes are "filled in" with data points at lower velocities as, at any instant, a particle may be at a different height above the waveguide, experiencing a weaker evanescent field and thus being propelled more slowly. The observed asymmetry in figure 6.13a is thought to be due to greater drift of particles from the right hand side onto the waveguide. A potential cause for this drift could be the absorption of light from the fibre that was not coupled into the waveguide causing off-axis heating and thus leading to natural convection currents as discussed in section 4.6. Figure 6.13b shows two maxima where the constructive interference of the modes gives a higher intensity than is obtainable at the centre of the waveguide.

In the case of the monomode waveguide, the maximum speed is approximately 500μm/s. In order to compare this to theory the peak intensity is estimated from figure 3.23. In the evanescent field of a channel waveguide with an aluminium opening of 3μm the peak intensity is approximately 30 GWm^{-2} per Watt of propagating modal power. The

modal power used (140mW) was estimated from the waveguide loss (∼1dB/cm) and the output power. This leads to a predicted velocity of 940μm/s for a 250nm diameter particle. However the particles have a wide size tolerance, and the predicted velocity for a 270nm particle is 1283μm/s and for a 230nm particle it is 667μm/s emphasising the size sensitivity of the calculation. This theoretical over prediction of the speed can be explained by a number of factors. Firstly the average intensity over the particle must be less than the intensity at the surface used in this calculation. Secondly, the intensity is unlikely to be the maximum theoretical intensity as the depth of the waveguide may not be precisely optimum. The agreement between theory and experiment (speeds up to 1283μm/s predicted, with speeds of 500μm/s observed) is much improved on previous comparisons [39].

6.5.2 Power and polarisation dependence on particle speed

In this section both the effect of power and polarisation on the speed of particles are considered. It is clear that as the intensity of the evanescent field increases so too should the mean particle speed, as the optical forces in the direction of the waveguide will increase linearly with power.

The 250nm gold particles used for this experiment were diluted to a concentration of 7×10^6 particles/ml. A salt (sodium chloride, NaCl) concentration of 4×10^{-4}M was used. Here the scattered laser light from the particles was imaged which had the advantage of only imaging the particles that were in the evanescent field, vastly reducing the amount of data processing that was required and allowing a higher concentration of particles to be used. One of two neutral density filters, a 20dB or a 25dB was used in the microscope depending on the modal power to attenuate this scattered light. Images were recorded at a rate of 20Hz with 4×4 binning and for 5000 frames. The rotatable chuck that held the fibre made it possible to control the polarisation in the waveguide. A polarisation extinction efficiency of greater than 25dB was obtained in all the following experiments.

For this and following experiments a histogram of the speed of the particles was calculated from the analysed results. A typical histogram is shown below in figure 6.14, with a best-fit Gaussian overlaid.

Although the physical reason for using a Gaussian fit has not been established this gave a reasonable fit in all instances. The Gaussian curve is defined by three parameters, an amplitude, a velocity offset, and a width. The amplitude is the peak frequency. The offset is used as the mean speed for trapped particles and in the case shown this is 38μm/s. The broadening will be a factor of a number of parameters, such as the particle size distribution and the distribution of the position of the particle above the waveguide.

The results for the two polarisations TE and TM are shown below in figure 6.15.

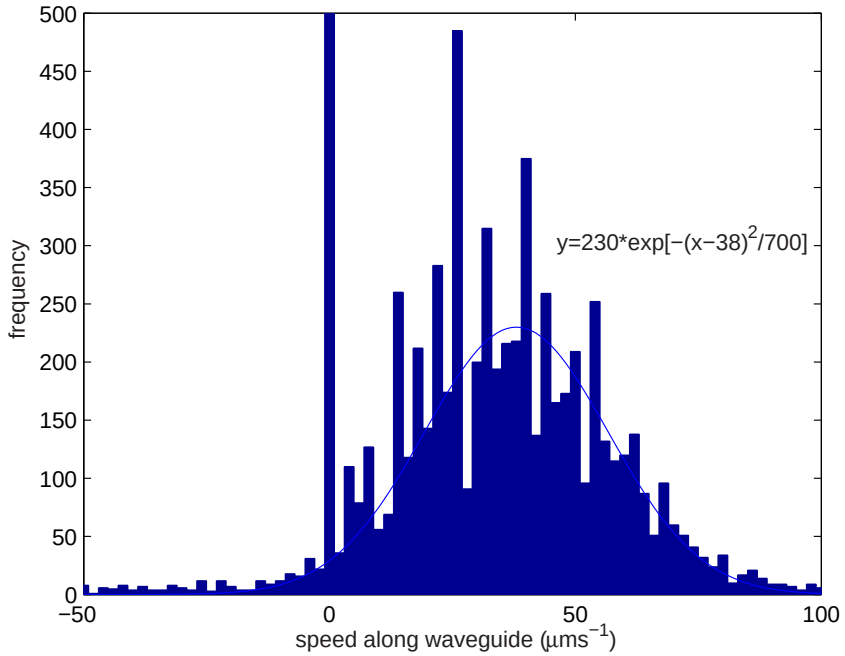

FIGURE 6.14: A typical speed histogram of the trapped particles, with a Gaussian best fit curve (−) and its equation shown.

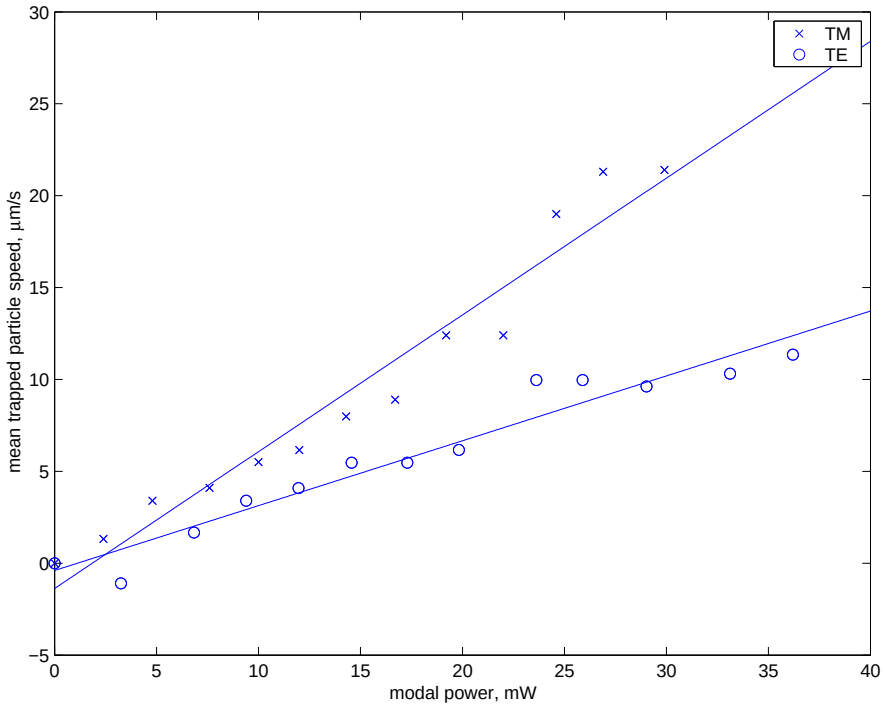

FIGURE 6.15: Plot of particle speed against power output for the two polarisations, TE and TM and the best fit lines for these.

In both cases the speed increases roughly linearly with the power, as expected. It was, however, considered possible that the effect of power may not be entirely linear as the particle speed will be dependent on the mean height of a trapped particle above a waveguide. As the gradient force is greater at higher power, thus the particle would be expected to be closer to the waveguide. However this effect was not observed.

The velocity for the TM polarisation shows the greater gradient meaning that this polarisation exhibits the higher surface intensity. This is in agreement with the results published by Ng, however in that case a K^+ ion-exchanged waveguide was used [39]. Therefore TM polarisation has been used in the experiments presented below and for subsequent chapters of this thesis.

This result can be explained by differing cut-off wavelengths observed between the two polarisations. As was seen in section 3.5.5 (in figure 3.23) a small change in depth of waveguide can lead to a large change in surface intensity for the case of the waveguide mode being close to cut-off. This same effect would be expected to be caused by the combination of a small birefringence and the differing boundary conditions for the waveguide mode for the differing polarisations. As the waveguide was chosen for optimised trapping, the fundamental mode of the waveguide was operating close to its cut-off wavelength, thus this explanation is plausible.

6.5.3 The effect of particle size

In this section the particle velocity is investigated as a function of the particle size for both latex and gold particles. In order to ensure that the intensity distribution that a particle is subjected to is the same in all cases, the same waveguide was used for all experiments. The waveguide used here was a 4μm single mode waveguide that was ion-exchanged in $CsNO_3$ for 9 hours at 450^0C with a cut-off wavelength of 1110nm (for TM polarisation).

The same method was used as in the previous section and the speeds of 250nm and 500nm gold particles were analysed as above. The latex particles were analysed differently due to the low number of particles observed. For these the average speed of a small number of particles (typically 2 or 3) was calculated at each speed. The average speed was calculated by recording the time taken to travel a fixed distance (typically 300μm). Figure 6.16 shows the particle speeds obtained in these ways.

Figure 6.16 demonstrates that for the latex particles, as the particle size increases so too does the velocity of the particles. However the variability of speeds also increases. This is in agreement with the results published in collaboration with the University of Tromsø [137] and has been shown to be expected due to the increased effects of Mie resonances with larger particle size [73].

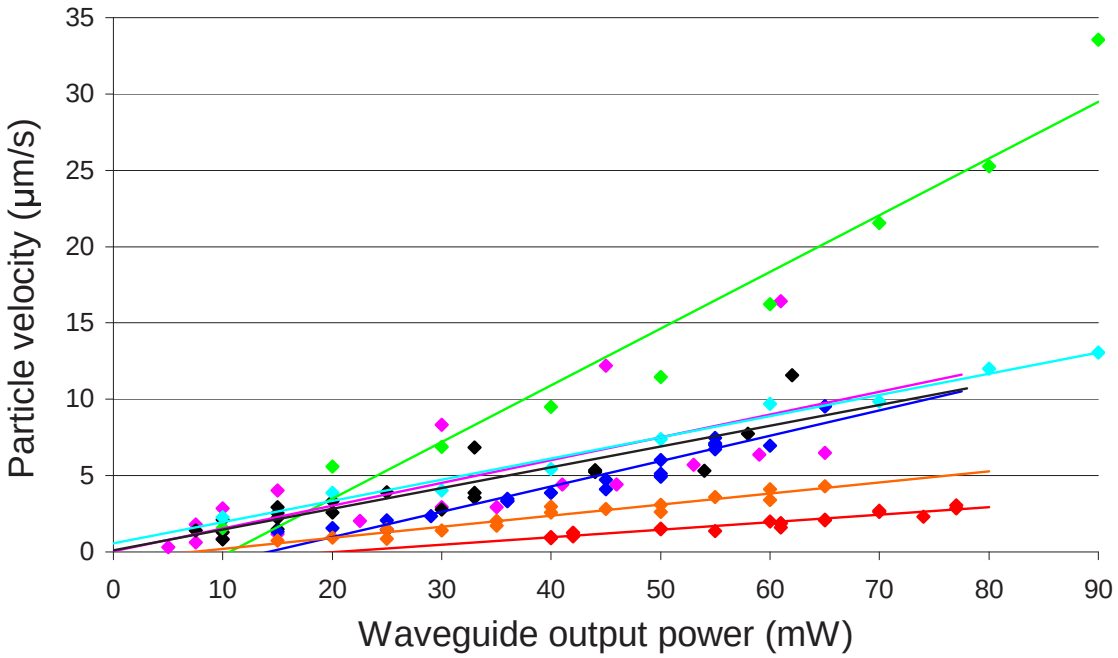

FIGURE 6.16: Plot of particle speed against power for a range of particle sizes and their lines of best fit. The sizes are 15μm, (♦), 10μm, (♦), 7μm, (♦), 5μm, (♦), 3μm and (♦) latex particles and 500nm, (♦) and 250nm, (♦) gold particles.

Recording speeds for more latex particles was not possible for two reasons. As larger latex particles have much less Brownian motion a much longer time was required for a particle to randomly come close enough to the optical field to become trapped. In addition, a higher concentration could not be used as trapped particles added significant loss to the waveguide. Whilst hardly noticeable for a single particle, it became apparent if many particles were trapped.

With regard to the gold particles, although some effect of propulsion of the smaller 100 and 150nm particles was very weakly observed the data was not of high enough quality to be analysed. This is due both to the very small amount of light that these particles scatter and the very short time for which they are propelled, making position detection unreliable. The results show that the 500nm gold particles are propelled at slower velocities than those of the 250nm gold particles in contrast to theoretical predictions in section 4.7.2. Clearly there will be an increased drag force on the 500nm particles due to their larger size. However theory has shown that this factor would have been expected to be at least balanced out by the increase in the scattering force applied to the larger particles. A potential reason for this is that of the breakdown in the applicability of Rayleigh theory for the larger particles, where the optical forces would be expected to deviate towards lower than predicted forces for a large particle size. It should also be mentioned that, unlike the other particles, the 500nm particles were non-standard and were supplied with no guarantee.

6.6 Summary

In this chapter firstly the apparatus used in this project has been described. Three processes of forming a cell which was optically clear and watertight were described. These caused varying amounts of additional loss to the waveguide and the optimal cell was found to be one that used silica sputtered on to the substrate to isolate the waveguides.

The programs used to record and analyse the data were all custom written in Labview for data acquisition and Matlab for data analysis. They were therefore shown to be highly flexible in terms of the results that could be obtained.

Brownian motion was observed and found to broadly agree with the theoretical values predicted. This gave extra validity to the particle analysis programs. In addition the effect of adding NaCl to the solution containing the particles showed that a concentration of 4×10^{-4}M NaCl could be added to 250nm gold particles without the particles adhering to the substrate. The drift of particles due to the heating caused by the laser as predicted by modelling in chapter 4 was shown and highlighted that there was a limit to the modal power that could be used.

The motion of 250nm gold particles above a Cs^+ ion-exchanged channel waveguide was monitored and the particles were found to be propelled with speeds of up to 500μm/s with a modal power of 140mW. This however was an extreme case as in most cases the particles travelled at much slower velocities than this. This value was comparable to that predicted by theory giving a slower experimental speed than the theoretically calculated speed and potential reasons for this discrepancy were explained.

The distribution of the speeds of the particles was found to follow that of the predicted intensity of the particles, peaking at the centre for the single mode waveguide, whilst showing a peak either side of the centre for a multimode waveguide. In addition, a plot of the position of the propelled particles was shown to be straight for single mode waveguides, whilst it alternated either side of the waveguide for a multimode waveguide with the wavelength of the expected beat pattern between the first two modes observed.

A range of gold and latex particle sizes could be propelled. It was shown for the case of gold that a TM polarised fundamental mode propelled particles faster than the TE polarised mode. Results of particle speeds as a function of modal power for various particle sizes were as expected except in the case of 500nm gold particles travelling slower than 250nm particles contrary to theory. This was believed to be due to the breakdown in the Rayleigh theory for this particle size.

Having developed the apparatus and analysis methods and having investigated the fundamentals of the propulsion of both gold and latex particles, this chapter has paved the way for the development of devices based on Cs^+ ion-exchanged waveguides.

Chapter 7

Sorting of Particles along Optical Waveguides

7.1 Introduction

This chapter builds on the previous chapter by extending the techniques and conditions obtained for trapping and propulsion of particles along straight waveguides to sorting particles down Y-branched waveguide splitters. In order for a device using the technology of evanescent wave trapping to be useful it is preferable that as much as possible of the manipulation of the particles is done optically. The ability to separate the particles would be a significant function, for which there are many uses that may be envisaged, for example, as a miniaturised fluorescently activated cell sorting (FACS) [143].

In the first section, the potential methods for carrying this out are discussed and the requirements for the chosen method are investigated. Separation of latex particles is characterised and shown to work with 100% success rate provided that certain conditions are satisfied. Gold particles are also sorted in the same manner, although the results are less conclusive due to the weaker lateral trapping of the smaller gold particles. The limits of the method, ways to improve it and a summary are discussed in the conclusion.

7.2 Choice of separation method

Three principal methods for separating particles were considered. These are discussed below along with their advantages and potential problems.

A single driving waveguide with multiple perpendicular waveguides could be used as shown below in figure 7.1a. The single waveguide would provide a stream of particles from which particles would be tapped off by modulating light power in perpendicular

waveguides. The main technical drawback is the requirement to provide multiple high power sources. One laser for each waveguide could be used and the powers modulated individually. However this would be a very costly solution. In principal, a single laser could be used to provide multiple beams either using an 'all-fibre' method or via a free-space method. A single laser could be coupled into a fibre splitter that could have any number of outputs. Modulation of the power in the waveguides would be possible by moving the fibres butted to the waveguides with manipulators such that the coupling efficiency was modulated. This would require multiple programmable stages. Alternatively the proportion of light in each fibre could be modulated, however this would require the added complication of external electro-optic switches, for example.

In the free-space case the laser beam could be split in free space, subsequently coupling the beams into fibres, or directly into the waveguides. Modulation of the power of the free-space beams is then trivial with neutral density filters. However to accurately control the powers at high speed could be expensive. The advantage of this method is that the number of waveguides is limited only by the power of the laser source.

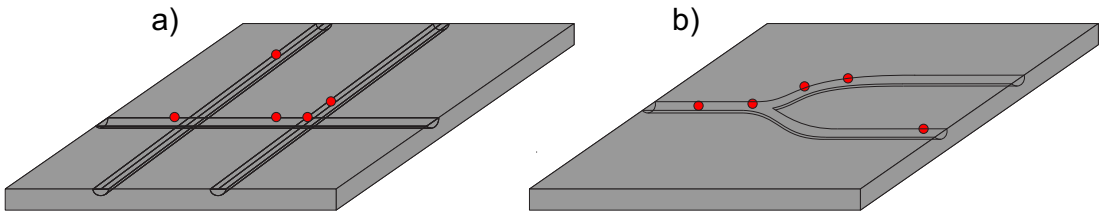

FIGURE 7.1: Two methods for optically sorting particles. a) The power in perpendicular waveguides is modulated in order to separate desired particles. b) The power can be modulated down either of two branches by controlling the beat pattern with either input fibre position or wavelength.

The second conceived method uses a Y-junction down which particles can be sorted in one of two directions (figure 7.1b) by a bimodal waveguide excited eccentrically thus forming a beat pattern. This would lead to a peak intensity that alternates from one side of the waveguide to the other. A Y-junction is positioned a sufficient distance along the trunk of the waveguide. If the wavelength of light were changed so too would the beat length. This would then make it possible to switch the proportion of light that travels down each branch as shown below (figures 7.2a and 7.2b). If the particles remain trapped above the point of highest intensity then clearly the particles will travel down the branch that has the higher intensity in it. Again the main problem with this method is the requirement of sufficiently high power, which is tuneable.

The last potential method for sorting involves translating the fibre across the waveguide. This will also cause the beat pattern to move (as shown in figure 7.2a and 7.2c). This was believed to be the most feasible experiment to demonstrate sorting as only one high power non-tuneable laser is required. However more integrable approaches are feasible in the longer term.

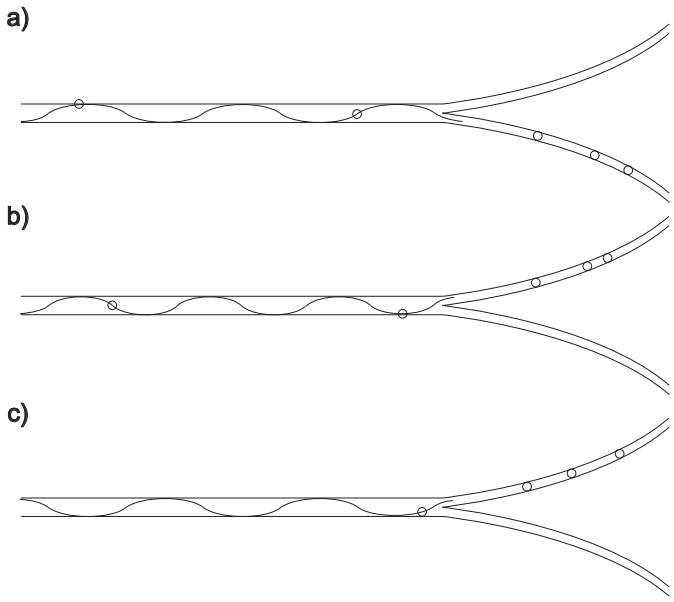

FIGURE 7.2: Sorting of particles. In a) the beat pattern guides the particles to travel down the lower branch, in b) the wavelength is lowered to introduce an extra half wavelength and the particles are sorted into the upper branch and in c) the position of the input is shifted to a symmetrically opposite position on the other side of the waveguide, the beat pattern is now opposite to that in a) and the particles are sorted to the upper branch.

7.3 Bend loss measurements

In order for the particles to be separated by sorting down a Y-junction, particles will be required to travel around bends. Therefore the light will also have to propagate around the bend. There is a limit to the radius around which light can travel [144], thus it is necessary to investigate this.

For this two masks were used. The first had varying radii bends with the input and output at 90^o to each other and thus a bend length of a quarter of a circumference as shown in figure 7.3a. The bends varied in radii from approximately 5mm to 20mm and were used to measure the bend loss of K^+ ion-exchanged waveguides. The waveguides were measured at two wavelengths, 633nm and 1066nm. The results for this are shown below in figure 7.4. The loss for the waveguides at 1066nm is similar to that at 633nm for shallow bends of 20mm, but increases significantly as the bends become tighter. Therefore, to make Y-junctions from K^+ waveguides a bend radius of at least 20mm should be used. It should be noted that the waveguides illuminated with light of wavelength 633nm were not single-moded.

For Cs^+ ion-exchanged waveguides a different mask was used as no difference was observed for the loss of each of the bends with the first mask. This had straight channels and bends of radii 2,4,6,8 and 10mm as shown in figure 7.3b. In this case the measured waveguide losses were not affected by the bends even for radii as low as 2mm as shown

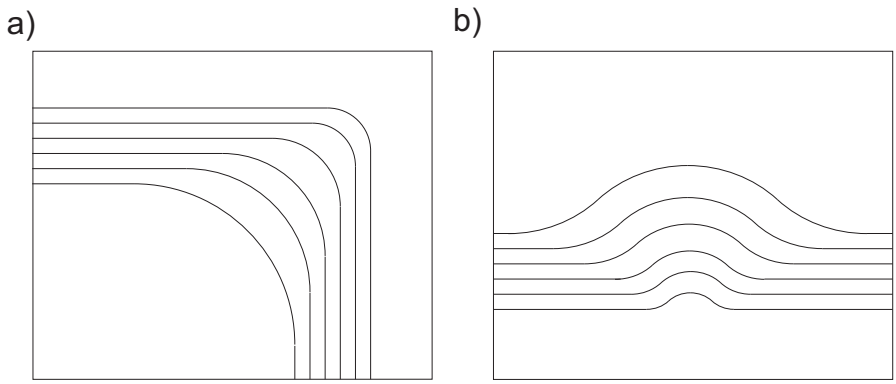

FIGURE 7.3: Two masks used to obtain an indication of the bend losses for a) K^+ and b) Cs^+ ion-exchanged waveguides.

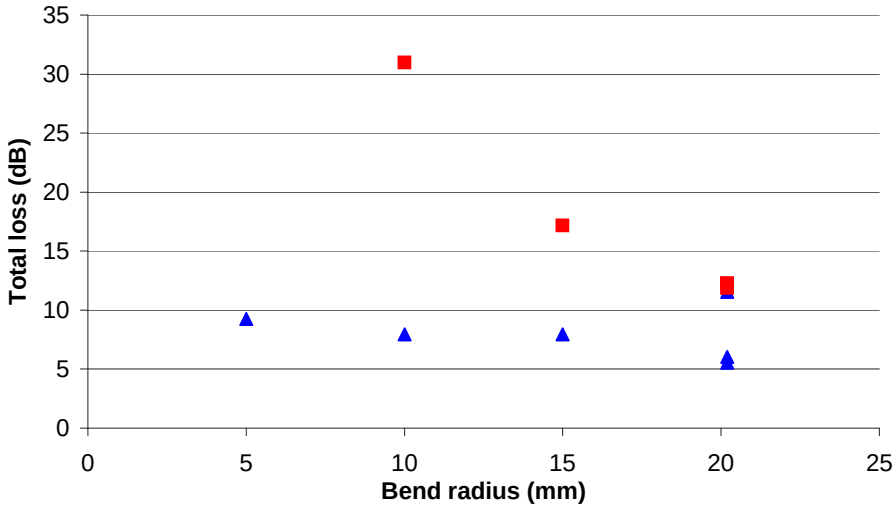

FIGURE 7.4: An indication of a K^+ ion-exchanged waveguides' bend losses at 1066nm (■) and 632nm (▲).

in table 7.1 showing a summary of the lengths and losses for both the K^+ and Cs^+ ion-exchanged waveguides at a wavelength of 1066nm.

Both the K^+ and Cs^+ ion-exchanged waveguides had a nominal opening of 3μm and the coupling efficiencies for all of the waveguides in each substrate can thus be assumed to be the same. Although the length of the waveguide changes (the waveguides containing the tighter bends being longer in the case of the K^+ ion-exchanged waveguides and shorter for Cs^+ ion-exchanged waveguides), this is not considered to be as significant as the loss due to the bend loss as can be seen from the results for the K^+ ion-exchanged waveguide bends at a wavelength of 633nm.

Thus, making bends by Cs^+ ion exchange allows a much smaller radius of curvature than a K^+ ion-exchanged waveguide. The advantage of this is twofold - less space on the substrate and a shorter length of waveguide is required in order to turn through a certain angle. Less space can be critical for the ability to multiplex and to keep components short therefore incurring less propagation loss.

Ion	Radius (mm)	bend length (mm)	total length (mm)	loss (dB)
K^+	∞	0	45	6.5
K^+	20.2	31.7	69.3	12.3
K^+	20	31.4	70.2	12.3
K^+	15	23.6	72.8	17.2
K^+	10	15.7	75.3	31.0
K^+	5	7.9	77.9	> 40
Cs^+	∞	0	45	10.0
Cs^+	10	31.4	48.1	10.0
Cs^+	8	25.2	47.5	11.6
Cs^+	6	18.9	46.9	10.3
Cs^+	4	12.6	46.3	9.5
Cs^+	2	6.3	45.6	10.1

TABLE 7.1: A summary of waveguide lengths and losses (at a wavelength of 1066nm) for Cs^+ and K^+ ion-exchanged waveguides.

7.4 Routing light in Y-junctions by varying input coupling

It was decided to trial two types of waveguiding Y-junction structures. The first (figure 7.5a) had a trunk with an opening of 6μm resulting in it being bimodal in the lateral dimension of the waveguide. This splits into two 3μm single mode waveguides that separated with various radii of curvature (from 2mm to 10mm) to a distance of 200μm. The second type (figure 7.5b) had a trunk with a 10μm opening that also split into two 3μm waveguides. These waveguides were aligned with the outside edges of the 10μm waveguide and thus there is a butt in the centre that is 4μm long. The expected advantage with the 6μm trunk was that particles would not have to travel a long distance laterally to cross the waveguides - ideal if the lateral trapping proved weak. The advantage of the 10μm branch was that a larger contrast between the power in each branch could be obtained by this method.

7.4.1 Modelling of Y-junctions

Having obtained a model for the straight waveguides used in this project (chapter 3) it is now possible to apply this model to the two structures that will be used experimentally, in order to predict the expected characteristics of the Y-junctions. Models of the waveguides were set up in the Beamprop CAD program. The diffusion depth, w, was set to a value of 1.1μm, d was set to 0.125μm, the polarisation set to TM and all the global parameters were the same, apart from the width of the area simulated, which was set 5μm either side of the outer edges of the branches. The length of the trunk was set to 2mm, to allow the modes sufficient distance to be unaffected by the non-coupled light from the input. The radii of the bends was 4mm, which has been shown above not to incur significant excess loss. First the modes of the trunk were solved. These are shown below in figure 7.6. The 10μm trunk was found to support three modes, whereas the

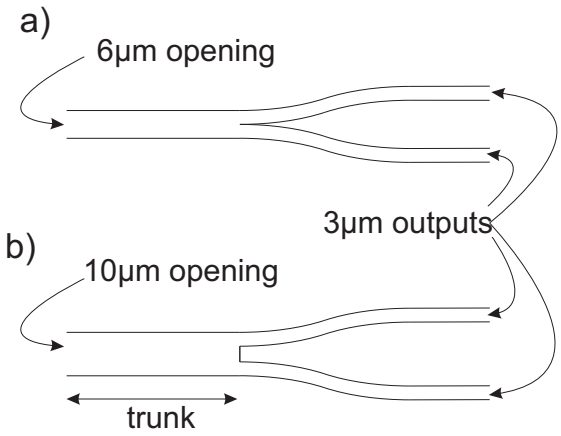

FIGURE 7.5: The two designs used to separate particles - a) has a 6μm opening, whilst b) has a 10μm opening.

6μm waveguide is bimodal. The effective refractive indices of these modes are tabulated in table 7.2.

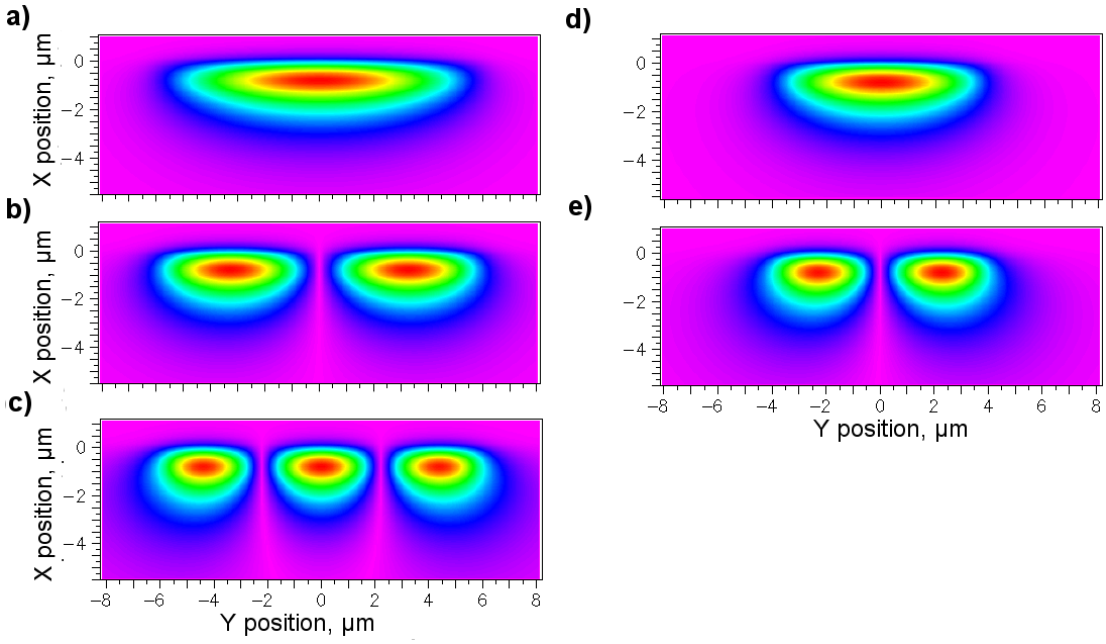

FIGURE 7.6: Mode profiles of the a) zeroth, b) first and c) second order modes of a 10μm waveguide and the d) zeroth and e) first modes of a 6μm waveguide.

Mode	6μm	10μm
0	1.50509	1.50568
1	1.50182	1.50404
2	-	1.50141

TABLE 7.2: Effective refractive indices of the modes for a 6μm and 10μm waveguide.

Fibre butt-coupling into the trunk was simulated by a 3μm Gaussian beam centred at x=-0.66μm (the approximate transverse position of peak intensity of the modes described

above). The lateral position could be varied and instances illustrating preferential coupling into one of the waveguides are shown for both the 6μm trunk (figure 7.7) and 10μm trunk (figure 7.8) Y-junctions are shown below.

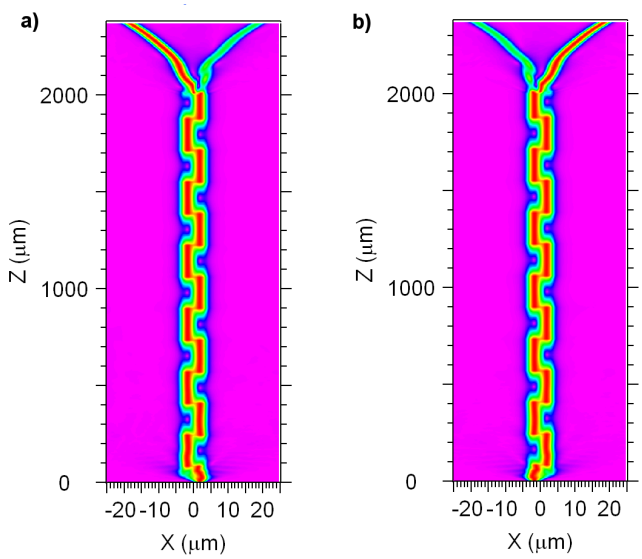

FIGURE 7.7: Propagation of the beam with the input beam positioned at a) y=+1.75μm and b) y=-1.75μm with respect to the centre of a 6μm waveguide.

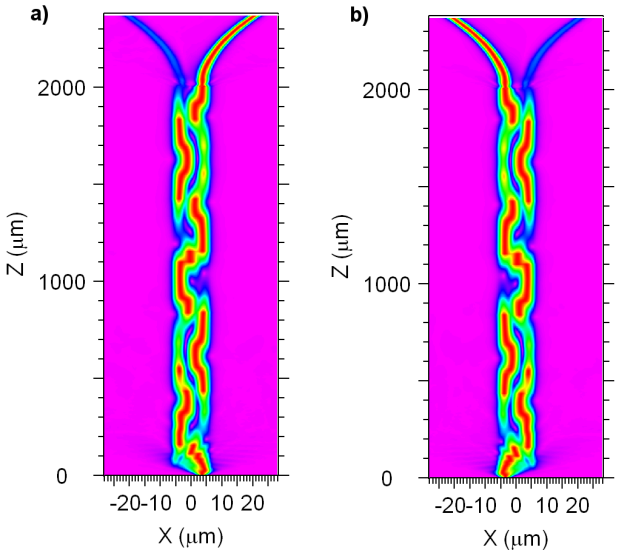

FIGURE 7.8: Propagation of the beam with the input beam positioned at a) y=+3.5μm and b) y=-3.5μm with respect to the centre of a 10μm waveguide.

A range of lateral positions of the fibre was simulated and the proportion of power in each branch monitored. The results for this are shown below in figure 7.9.

This shows that the 10μm trunk Y-junction has the ability to couple a greater proportion of light into a branch than is possible with the 6μm trunk Y-junction. It also shows that a greater contrast between the powers in each of the branches is possible using the wider trunk Y-junction.

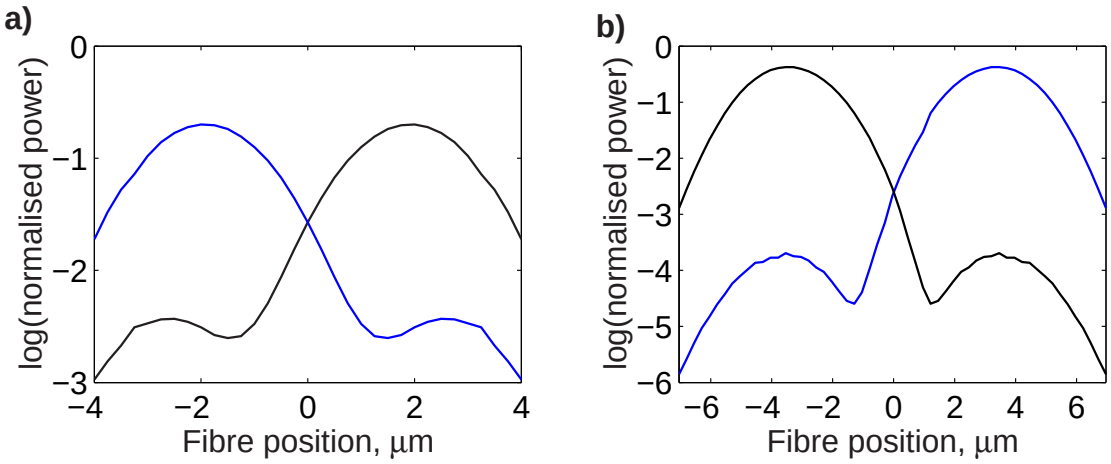

FIGURE 7.9: Proportions of light propagating in the left (■) and right (■) branches as a function of the fibre position for the case of a) a 6μm and b) a 10μm width trunk.

7.4.2 Experimental results

A mask was designed and waveguides were fabricated with Y-junctions of the types described above.

The same apparatus used for the experiments in chapter 6 was used for the following experiments. The only difference was that the fibre rotator was held on a micromanipulator that itself was attached to a computer-controlled stage. A screw-driven stage was used (Newport, PM500-LW) and was controlled through a controller (Newport, PM500-C6). This was integrated with the computer using a modification to the Labview program described in chapter 6 and added the ability to move the fibre laterally across the waveguide, with a step-size of 50nm. This changed the proportion of the light coupled to the available modes, thus changing the beat pattern. Figure 7.10 below shows typical results for the output of the two branches of the waveguide as a function of the lateral position of the fibre for a Y-junction with a 10μm multimode input waveguide taken at 0.5μm step intervals.

This shows the same small peak in the branch more weakly coupled to as predicted in figure 7.9b. It also shows that it is possible to achieve a good contrast with approximately 10dB less power in the weaker branch if the fibre is positioned so as to maximize the power in the other branch. This was better than could be achieved with the 6μm opening. Indeed some of the Y-junctions made with the 6μm openings were single-moded. Therefore only waveguides with 10μm trunks were used in the experiments described below.

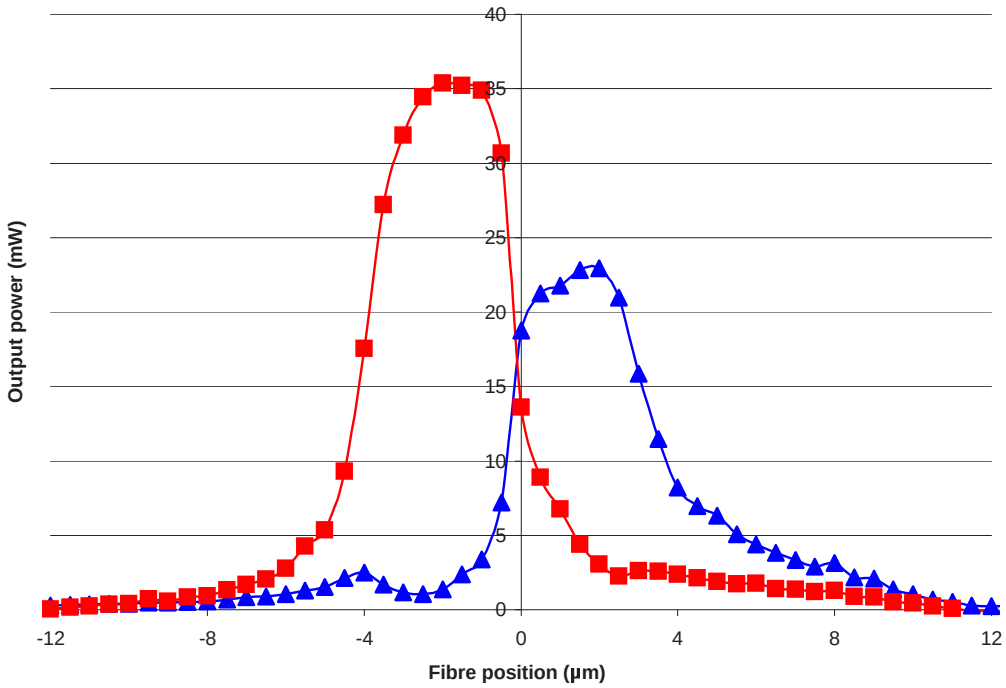

FIGURE 7.10: The output power of the upper branch (■) and the lower branch (▲) of the Y-junction as the fibre is traversed across the input of the multimode waveguide.

7.5 Particle meandering above a multimode waveguide

The initial experiments in separating particles were carried out using 6μm latex particles. These were found to be much easier to trap and propel due to their reduced Brownian motion and are also easier to image. To check that particles would be able to cross the waveguide following the beat pattern, particles were observed being propelled along a straight multimode waveguide ion-exchanged through a 10μm opening.

Particles were imaged and recorded at 10x magnification. Analysis was run on a sequence of approximately 1000 images taken with a 200ms time resolution. Figure 7.11a shows the speed distribution of particles travelling along a straight multimode waveguide. This graph represents approximately 6500 individual particle displacements. This image is made by using a simple spline to interpolate speeds between points at positions shown in figure 7.11b. It shows primarily that the maximum speed of particles alternates from side to side as does the beat pattern. In addition, the beat length of this pattern (approximately 500μm), may be used to calculate a difference in effective indices of the first two modes (as in section 6.5.1). Using this gives an approximate n_1-n_2=0.0021 whereas the difference in the simulated modes shown in table 7.2 gives a n_1-n_2=0.0016. This difference can readily be explained by considering that the waveguide is expected to support three modes, thus the beat pattern is not expected to be periodic on the length scale shown, and is therefore only indicative. However the proximity to the predicted value further validates the theory that the speed distribution of the particles is controlled by the beat pattern.

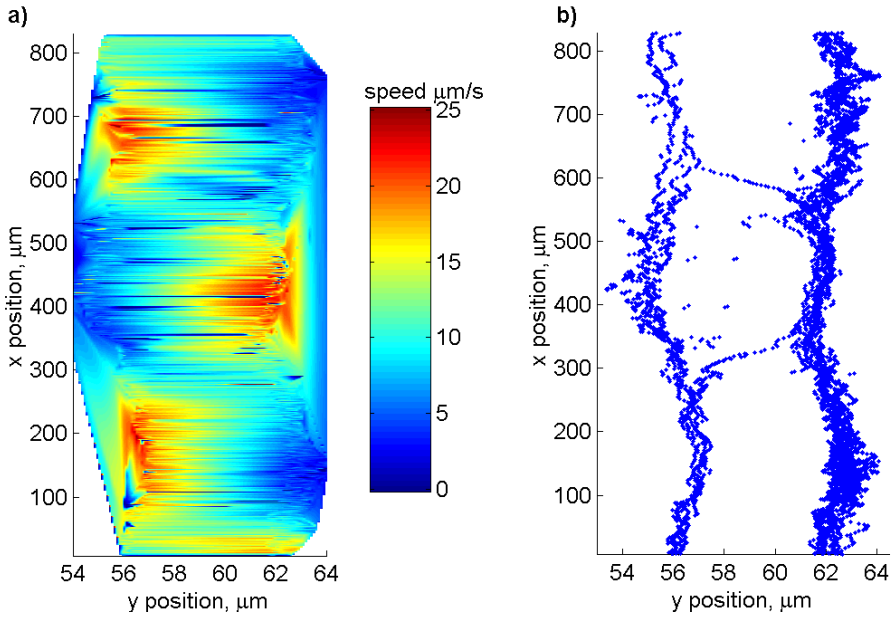

FIGURE 7.11: Position of latex particles travelling on multimode waveguide showing a) an interpolated speed map showing that particles on either side of the waveguide alternatively travel faster and b) the positions from which a) was formed.

Figure 7.12 shows the tracks of the particles described above. Both figures 7.11b and 7.12 show that most of the particles do not cross from one side of the waveguide to the other as the beat pattern does, instead just speeding up and slowing down along the one side. However when using Y-junctions the coupling can be optimised so as to ensure a maximum contrast between each of the two branches involving coupling strongly into the second order mode. As the experiments below show this has allowed successful selection of latex particles to be obtained.

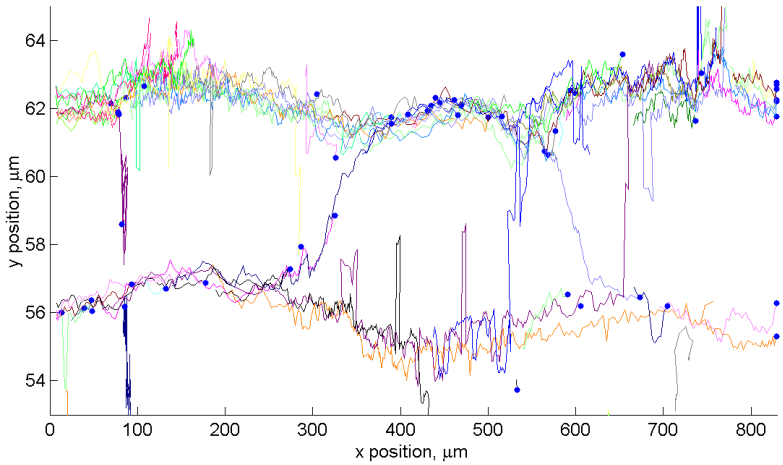

FIGURE 7.12: Traces of all the particles viewed in figure 7.11. (•) represents the end of a trail where the next position of the particle was uncertain.

Figure 7.13 is a plot of the speed of the particles as a function of their lateral position across the waveguide. This shows how the maximum speed of the particles is increasing towards the centre of the waveguide, but that at a certain point the particles slow down

when in a band approximately 5μm wide directly on top of the waveguide - in agreement with figure 7.9.

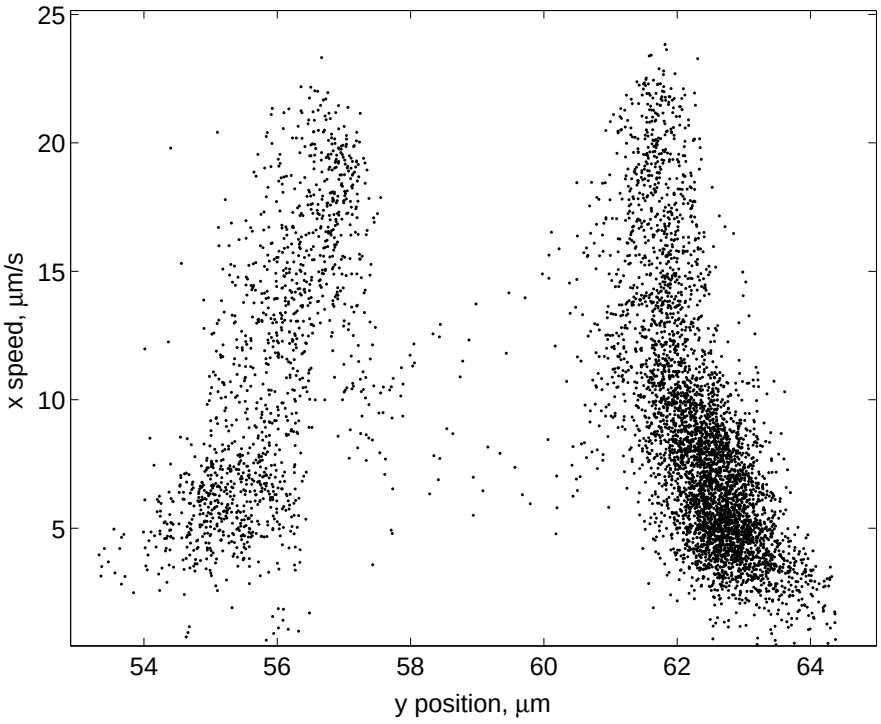

FIGURE 7.13: The instantaneous axial speed as a function of the lateral position of the particles represented in figure 7.11.

7.6 Sorting of latex particles along a Y-branch

The work done in this section was carried out in the ORC, University of Southampton, in collaboration with Katarina Grujic, a visiting PhD. student from the Department of Physics at the Universitetet i Tromsø.

7.6.1 Characterisation of sorting

In this experiment the initial aim was to set a power ratio between the two branches and monitor the proportion of particles that travelled down each of the branches. However this was not possible as at intermediate power ratios (e.g. 1:1 ratio between the two branches) the powers were very unstable. This was believed to be due to a slight drift of the fibre with respect to the waveguide input. As can be seen from figure 7.10, around this ratio the gradient of power with lateral fibre position is very steep so that a very small perturbation of the fibre causes a large change in the ratio of the power in the output branches. Therefore the experiment was modified. Rather than controlling the power, the fibre position was set to give approximately a 1:1 ratio and the recording

of images was started. The power was then allowed to drift either way and after some time was restored manually. After a representative time the recording was stopped and a time-labelled movie made. Figure 7.14 shows the first image of a movie (latsort1.avi) that is a sample of the total movie. The whole movie was then examined, noting down the time at which a particle travelled past the junction, which branch it travelled down and the power in each branch. The time-labeled powers in each branch at these instances were also noted (see the relevant powers from the movie in figure 7.14 in figure 7.15).

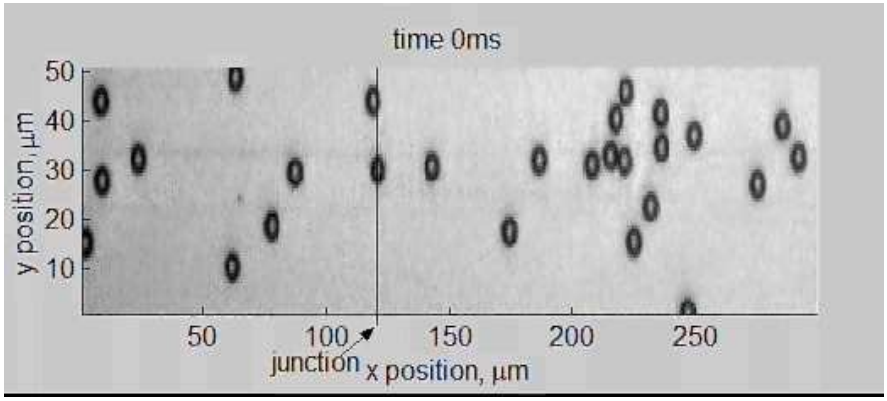

FIGURE 7.14: The first image of the start of a movie (latsort1.avi) that shows latex particles travelling down the branches. In this movie the power is not controlled.

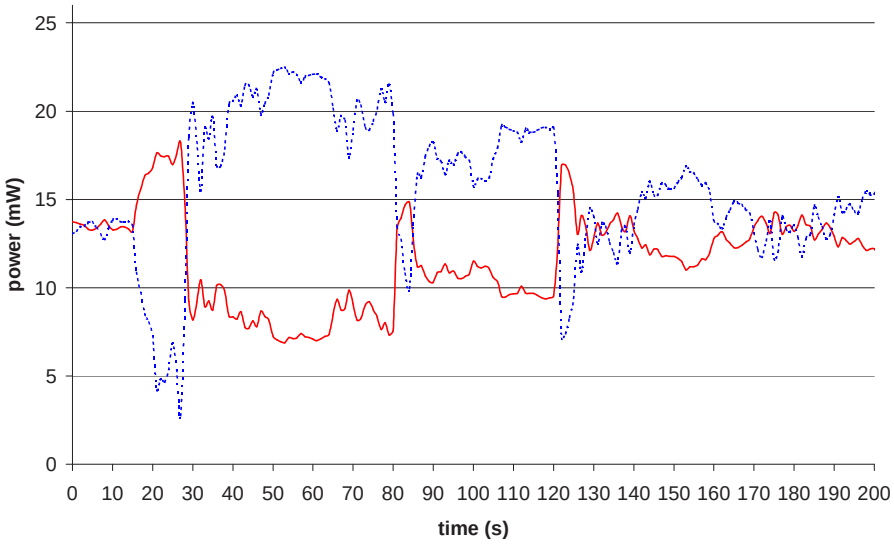

FIGURE 7.15: The powers in the upper (■) and lower (■) waveguide for a greater duration than shown in the above movie.

These data are plotted in figure 7.16 as a graph of the power in the upper branch versus the power in the lower branch where the form of data points is dependent on which branch the particle travelled down. If the power was much greater in one branch than the other, the particles would almost always travel down that branch as expected. Exceptions to the rule were examined more closely and found to occur at points when a particle was within $\sim 20\mu$m of the junction at the time that the power was readjusted.

In this case the particles may not have had time to cross the waveguide and so carried on down the branch that had less power in at the instant the particle crossed the junction. For an intermediate contrast between the power in each branch, the branch that the particle travelled down was less predictable.

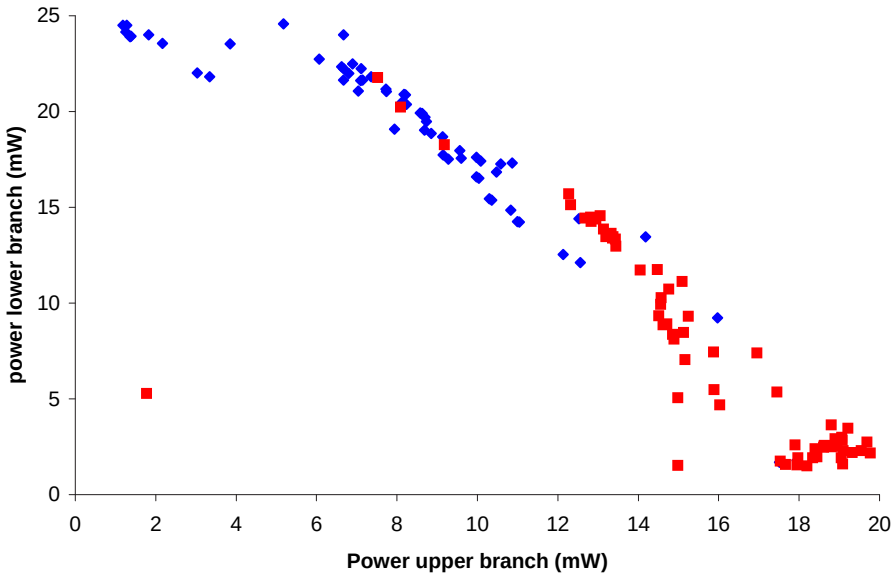

FIGURE 7.16: A plot showing the particles that were sorted into the upper branch (■) and those that were sorted to the lower branch (♦) as a function of the powers in these waveguides at the instant the particle crossed the junction.

These results show that in general a particle will travel down the more strongly illuminated branch but that, as expected, as the contrast becomes weaker so too does the accuracy of the sorting.

7.6.2 Programmable sorting of latex particles

The experiment described in section 7.6.1 characterised the behaviour of the particles. However in order to make a useful device based on this it is necessary to be able to control a particle to direct it down a certain branch. To enable this, two fibre positions that gave a large difference in power between the two output branches are obtained. A new program was written in Labview designed to demonstrate that particles could be specifically controlled to be diverted down a certain branch. The program provides a button that could be pressed at any point in time. This would then toggle the position of the fibre between the two positions obtained above. Using this program it was possible to investigate the effect of switching the particle position at different positions ahead of the junction. An example of this control can be seen in the movie (latsort2.avi) for which figure 7.17a is the first image [66]. Simultaneously figure 7.17b shows the powers in the two branches.

At the start of the movie a particle is approaching the junction on the lower side of it. After about 25 seconds when the particle is approximately 50μm from the junction

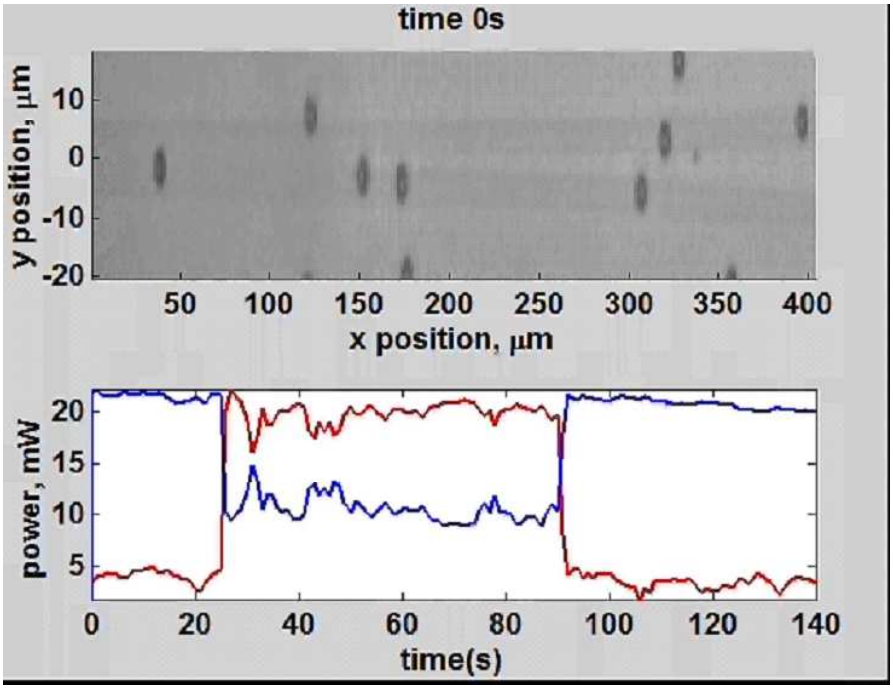

FIGURE 7.17: The controlled sorting of a particle, a) shows the first image of movie (latsort2.avi) whilst b) simultaneously shows the power in the upper (■) and lower (■) branches as a function of the time. The vertical bar in the movie represents the time point that is being shown in the movie.

the button is pressed and the peak power shifts to the upper branch. The particle (which had been aiming towards the lower branch), crosses over the waveguide and travels along the upper branch. Another particle subsequently approaches the junction and again approximately 50μm prior to the particle reaching the junction the power is switched again and the particle crosses over the waveguide and is sorted down the lower branch.

It was found that for the kind of powers and the waveguide used a distance of approximately 40μm was sufficient to guarantee that the particle travelled down the correct path. In addition, the power could not be switched back until the particle had travelled at least 10μm along the desired branch otherwise it could cross over and be propelled along the other branch. This is believed to be due to the particle being within the field of the other guide and so can be pulled across the waveguide.

It was also found that the Y-junctions with the tightest bends worked better in terms of obtaining a larger contrast in the powers of the branches. This may be due to coupling between the two waveguides after the junction which would decay more rapidly for tighter bends.

It is also worth noting that the ratio between the two powers is not maximised, rather one of the powers is maximised and the other is still significant. This is preferable to keep particles on the more weakly illuminated branch trapped and propelled.

7.7 Sorting of gold particles along a Y-branch

Having successfully separated latex particles very reliably, separation of 250nm gold particles was now studied. Due to the fact that particles were trapped for much shorter times, statistics for the particles were built over a longer time and using a better time resolution (100ms). In addition, rather than continuously switching the power between branches, two separate sets of data result were obtained - one with one branch strongly coupled to, and a second with the other branch more strongly illuminated. The data were analysed and were filtered as described in section 6.3.2 and the positions and displacements of particles that travelled in the waveguiding direction with a speed of at least 30μm/s are plotted below in figure 7.18. This condition was sufficient to select only particles propelled by the waveguide. The relatively short lengths of the lines compared to those in figure 7.12 show that in general the particles are not trapped for a long time.

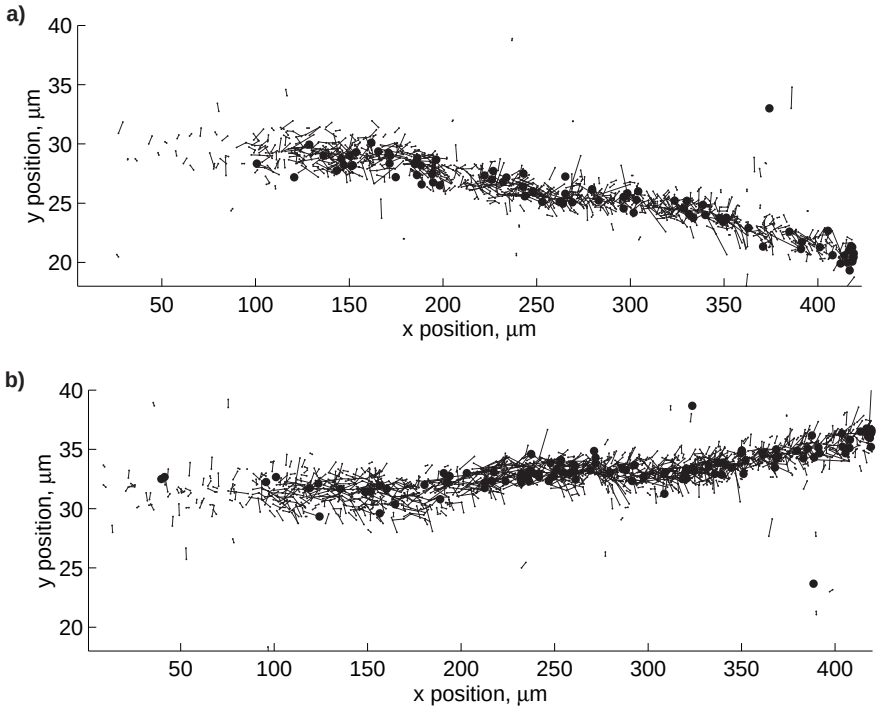

FIGURE 7.18: Trace of 250nm gold nanoparticles with the a) lower branch and b) upper branch more strongly coupled to.

Figure 7.19 shows analogous data to figure 7.11b demonstrating the positions of the particles propelled in figure 7.18 and again shows that particles are only propelled if trapped above the more strongly illuminated waveguide.

The results for gold are less conclusive than the latex and certainly the gold particles do not exhibit the same property as the latex spheres of being trapped and propelled along the more weakly illuminated branch. Analysing data at the junction confirms that particles will only be propelled down the correct branch. This may, however, take some

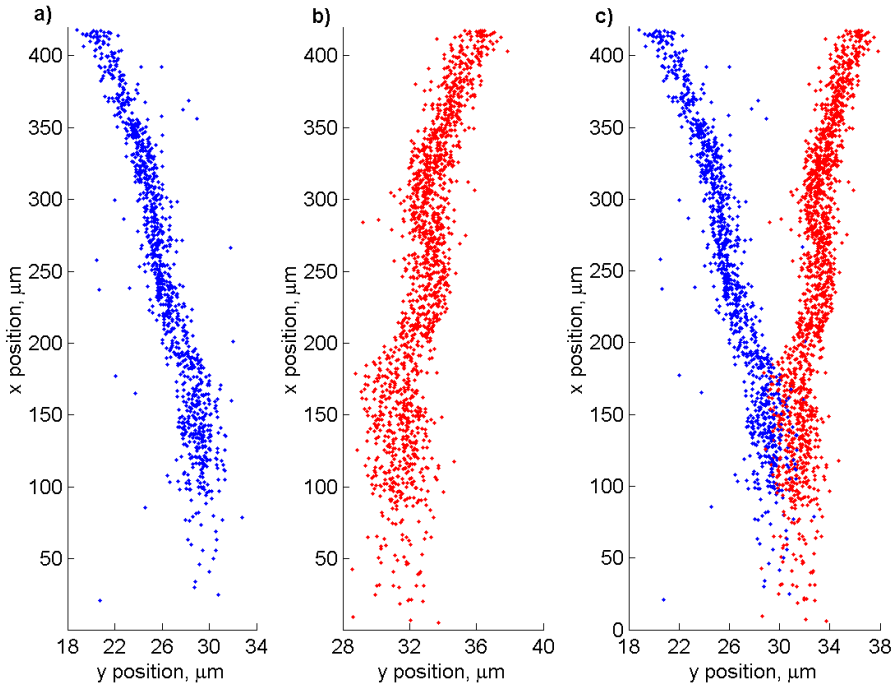

FIGURE 7.19: The position of particles travelling at least 30μm/s with a) the left branch and b) the right branch illuminated. c) shows the two images superimposed on each other for clarity.

time to occur, before they interact sufficiently strongly with the field to be propelled down the branch.

7.8 Conclusion and discussion

This chapter has shown that using Cs^+ ion-exchanged waveguides allows much tighter bends to be used to guide light (to a bend radius of below 2mm) compared to K^+ ion-exchanged waveguides. It also shows that Y-junctions can be fabricated that allow light to be split down two branches without excessive losses. If a Y-junction of a non-orthodox type is used (i.e. with a butt-ending) better control of the proportion of light propagating down each branch can be achieved as was predicted by theory. The junctions were characterised for 6μm latex particles and it was shown that in general particles will travel down whichever branch is more strongly coupled to. However it is necessary to allow a particle some distance before the branch is reached in order to cross the waveguide. It is believed possible that this distance could be decreased by a more gradual traversing of the fibre across the input as this could gently drag the particle across the waveguide. Currently the method is an instantaneous shift in the beat pattern that is used. The current method illustrates that approximately 40μm prior and 10μm beyond the waveguide junction is required to 'sort' a particle. With a particle's mean speed of approximately 10μm/s this would translate to a maximum throughput of a particle every 5 seconds or 720 particles/hour. This would probably be

too slow for most biological applications, although this rate could possibly be accelerated by increasing the power or using using larger particles. However these changes may, in turn, change the distance required to sort the particle.

Gold particles travelling at speeds over 30μm/s were also shown to be propelled into the waveguide branch that was more strongly illuminated. However due to the short distance for which they were laterally trapped, it was not possible to draw conclusions analogous to those for the latex particles. With stronger lateral trapping this process should work equally well as for the latex particles, with the higher speeds giving potential for much higher throughput and the use of a tuneable laser removing the necessity for moveable parts.

Chapter 8

Control of Particles using a Counter-propagating Wave

8.1 Introduction

The propagating evanescent wave created by light travelling through the waveguide needs to be of sufficient power to trap particles both laterally and transversely. This power is also sufficient to axially propel particles along the waveguide. The method described thus far for trapping particles is only able to propel the particles in one direction - the direction of the propagating light. It would be advantageous to have the ability to position a particle at any point along the waveguide. This could then be used to more effectively measure trapping strengths and to allow other forms of interrogation, such as probing for Mie resonances of a particle. This type of control may be achievable by having light propagating in both directions simultaneously in a waveguide. In this chapter the theory of a standing wave in a waveguide is described along with experimental results from several different methods used to gain greater control of particles.

In the first method a mirror is attached to the end of the waveguide to test the principle of using a counter-propagating wave. Secondly a monomode waveguide that splits into a loop is used. Finally a more flexible solution using a fibre-coupler to split light into two equal components in separate fibres is tested. In this method light is coupled into each end of a straight waveguide and by varying the coupling efficiency to the waveguide it is found that very good control of the position of a particle can be obtained.

This concept is not entirely new; the use of a standing wave to create an optical trap has been investigated by Zemanek et al [145] for holding latex particles in a standing wave formed by a reflected focussed Gaussian beam.

8.2 Theory for particles in a standing wave

8.2.1 Introduction

In this section the well-known form of the fields and intensity formed by a perfect standing wave is derived. This is then expanded in order to take into account both the reflectivity of the mirror and the loss of the waveguide. The theory for the optical forces due to a propagating evanescent wave has already been described in some detail in chapter 2 and this can be built on in order to theoretically predict the effect of the counter-propagating wave on the axial forces.

8.2.2 Intensity of a standing wave

A standing wave formed by the total reflection of a plane wave at a dielectric mirror positioned at z=0 has forward, E_f, and backward, E_b travelling field components given by [82], [146]:

$$E_f = E_0 e^{i(kz-wt)} \tag{8.1}$$

$$E_b = RE_0 e^{i(-kz-wt+\pi)} \tag{8.2}$$

where R^2 is the reflectivity of the mirror and the introduction of π in the reflected wave describes the phase shift of the field upon reflection. The resultant field is simply obtained by adding the two individual waves (principal of superposition). The energy density or intensity is therefore given by [146]:

$$I = \frac{\epsilon_r \epsilon_0 c}{2} EE^* \tag{8.3}$$

$$= \frac{\epsilon_r \epsilon_0 c}{2}(E_f + E_b)(E_f^* + E_b^*) \tag{8.4}$$

$$= \frac{\epsilon_r \epsilon_0 c}{2}(E_f + E_b)(E_f^* + E_b^*) \tag{8.5}$$

$$= I_f + I_b + 2\sqrt{(I_f I_b)}[-\cos(2kz)] \tag{8.6}$$

where the * represents the complex conjugate and I_f and I_b represent the intensity of the forward and backwards travelling wave.

The form of the evanescent wave of a channel waveguide is (see section 3.2.2):

$$E_i(x,z) = E_0 e^{-qx} e^{-i(\omega t + k_1 z)} e^{-\gamma z} \tag{8.7}$$

where the dependence on the y dimension is more complex. As the dependence of both the plane and evanescent wave on the z dimension is the same, equation 8.6 is equally applicable to standing wave created by a reflected evanescent wave.

The case described above is for a loss-less waveguide. However to generalise this to that of a waveguide with loss 2γ is possible and requires the adjustment of the two intensities I_f and I_b as follows:

$$I_f = I_0 e^{-2\gamma z} \tag{8.8}$$

$$I_b = R^2 I_0 e^{2\gamma z} \tag{8.9}$$

where I_0 is now the intensity of the forwards travelling wave at the position z=0. The model and intensities are shown below in figure 8.1.

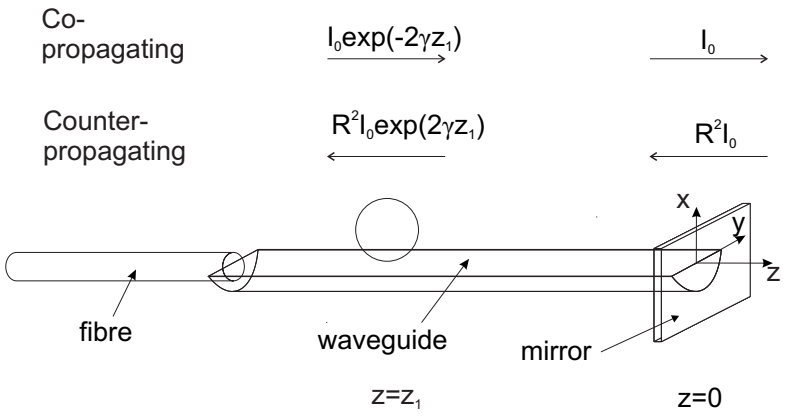

FIGURE 8.1: Geometry for evanescent standing wave analysis of a lossy waveguide.

For the case of the lossless standing wave the amplitude of the oscillation is $2I_0R$, where R is the contrast of the incident to the reflected field. Here therefore we define an effective reflectivity, $R^2_{eff}(z)$, given by I_b/I_f. Using this expression in equation 8.6 gives:

$$I = I_f + I_b - 2RR_{eff}\cos(2kz)I_0 \tag{8.10}$$

$$= I_f + I_b - 2R^2 e^{2\gamma z}\cos(2kz)I_0 \tag{8.11}$$

The form of this is plotted below in figure 8.2 shown with a greatly exaggerated loss, for illustrative purposes. The parameters used for this case were light of wavelength, 1.06μm, an effective waveguide refractive index of 1.51, a reflectivity (R^2) of 0.6 and a waveguide loss of 2.6×10^4dB/cm. The incident beam is normalised such that it has unity intensity at z=0.

From this figure a number of points should be emphasised. Here, as with any standing wave, the period of the intensity is half that of the wavelength of light in the medium ($\lambda/2n_{eff}$), which equates to a period of 350nm. There is an oscillation that is decaying with distance from the mirror as the reflected beam decays. This decaying oscillation is superimposed on a DC component that will grow as with the sum of the incident and reflected beams. At the interface where the mirror is placed (z=0) there is a minimum in the intensity that is given by 1-R^2, thus close to the surface, for a perfect reflectivity

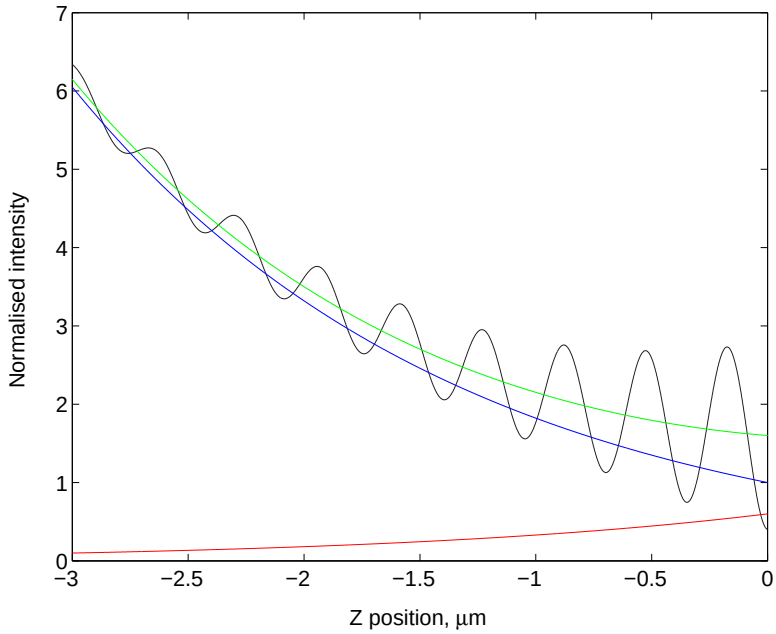

FIGURE 8.2: Intensity as a function of position for the partial standing wave (■). Included are the incident (■) and reflected (■) waves and the sum of the incident and reflected waves (■).

the intensity has maximum magnitude up to four times greater than the intensity of the forward propagating wave.

For more realistic parameters for our case, at a distance of 1cm from the mirror, with a waveguide loss of 2dB/cm and a reflectivity of 0.6, the forward travelling wave has an intensity of 1.58 whilst the backward intensity is 0.38. This gives an approximate amplitude of oscillation of 1.71 with the same period.

8.2.3 Effect of standing wave on optical forces

Having obtained an expression for the intensity of a partial standing wave for a lossy medium this can now be applied to the axial forces calculated previously in chapter 2 to see if a particle may be trapped axially and thus in three dimensions above a waveguide.

The Rayleigh force consists of three components: a scattered, an absorbed and a gradient force. For the gradient force the intensity in the z-direction can be used directly. For the scattered and the absorbed forces the direction in which the wave is travelling is clearly important. For this, therefore, despite the coherent interference, the resultant amplitude of the two intensities in either direction is used.

The gradient force is obtained from equations 2.89 and 8.11:

$$F_{grad,z} = -\frac{\epsilon_1}{n_{eff}c}\alpha'[-2\gamma e^{-2\gamma z} + R^2 2\gamma e^{2\gamma z} - 2R^2 e^{2\gamma z}(2\gamma z\cos 2kz - 2k\sin 2kz)]I_0 \tag{8.12}$$

$$\approx -\frac{\epsilon_1}{n_{eff}c}\alpha'[4kR^2 e^{2\gamma z}\sin 2kz]I_0 \tag{8.13}$$

The first two terms of equation 8.12 refer to the force caused by the propagating parts of the wave and have been shown to be many orders of magnitude smaller than the scattering force. The third term is clearly much smaller than the fourth for realistic values of γ and z.

The scattering and absorption forces are as given in equation 2.76 and equation 2.90 and are only modified by the intensity of the reflected wave:

$$F_{scat,z} = \frac{n_{eff}\beta_0^4}{6\pi c}|\alpha|^2(e^{-2\gamma z} + R^2 e^{2\gamma z})I_0 \tag{8.14}$$

$$F_{abs,z} = \frac{\epsilon_1}{n_{eff}c}\beta\alpha"(e^{-2\gamma z} + R^2 e^{2\gamma z})I_0 \tag{8.15}$$

The effect that this standing wave has on a gold particle of radius 100nm in shown in figure 8.3. The conditions are that the distance from the particle to the mirror is 1cm, the waveguide loss is 2dB/cm, the output modal power is 100mW and thus surface intensity of 3×10^9W/m^2, placed in a standing wave and where the reflectivity of the mirror used is 0.8.

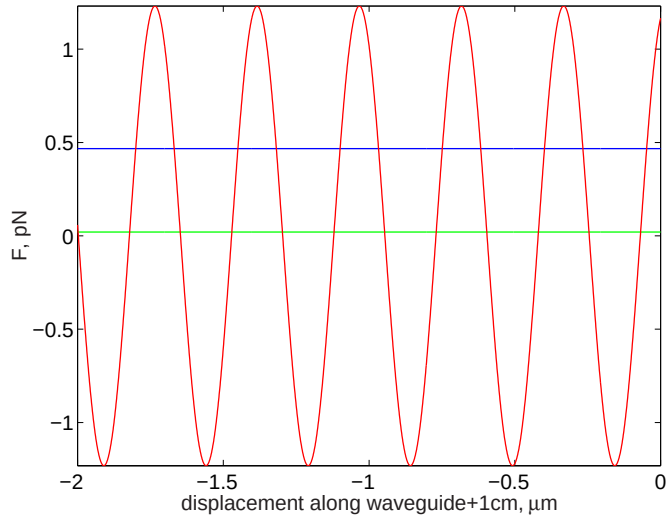

FIGURE 8.3: Comparison of scattering (■), gradient (■) and absorption (■) axial forces on a 125nm radius gold particle in an evanescent standing wave of a waveguide.

From figure 8.3 it can be seen that the sign of the gradient force changes. This is because where the intensity is increasing with z, the gradient force acts to accelerate the particle in the direction of the forward propagating wave, and vice versa. As the maximum magnitude of the gradient force is greater than that of the scattering force (which itself

is over an order of magnitude greater than the absorption force), the gradient force is sufficiently strong to create a region where the particle is held stationary i.e. trapped axially above the waveguide. However the length over which this gradient force acts must be considered. The standing wave part of the intensity was shown to have a period of approximately 350nm. The gradient force is negative over a length of 175nm therefore and the force is greater than the scattering force (which may be considered constant over the particle) for 132nm in this case. Integrating the force over the diameter of the particle is not sufficient to calculate whether this size of particle will be trapped as the force only acts at the permittivity discontinuity (i.e. at the surface). However the case is much clearer for smaller particles, for example, for a 150nm particle the gradient force is a factor of ten greater than the scattering force and, due to the added factor of its smaller size, it would be expected that there is a position at which the particle is stably axially trapped.

This section has therefore shown that it is theoretically possible to trap particles axially with a modest reflection coefficient of 60%. In this case the axial gradient force can (at the correct axial position) be greater than the scattering force over the vast majority of the diameter of the particle. However it has also shown that there is a limit to the particle size that may be trapped by this method.

8.3 Experimental methods

8.3.1 Introduction

The experimental results for this chapter were gathered in a four month visit to the Department of Physics at Tromsø University, Norway. This was necessary, as, in order to create a standing wave, the laser had to be single moded longitudinally to provide a sufficiently long coherence length. The laser used in these experiments, was therefore different and had a slightly longer wavelength (1083nm) (IPG Photonics). It delivered single mode, in both transverse and longitudinal directions, linearly polarised emission with a peak continuous power up to approximately 1.4W and was spliced directly to a fibre isolator that terminated in a fibre.

Three types of experiments will be described below all of which were used to create a standing wave with varying degrees of success. The first used a dielectric mirror attached to the output of a straight waveguide as described theoretically above. The second method involved using photolithographically defined back to back Y-junctions where the outputs from the second Y-junction formed a loop. The last method involved injecting light into both ends of a waveguide, using two output fibres from a 2x2 fibre coupler.

8.3.2 Dielectric mirror method

The method for the experiments using a standing wave created by a mirror was similar to the method for the straight waveguides described in chapter 6. However in this case the end of the substrate had to be machine polished and a very flat edge perpendicular to the waveguides was required. In addition an SiO_2 layer was sputtered onto the surface of the waveguide with a window close to the machine-polished edge (approximately 3mm away and with dimensions of 15mm by 40mm). This was to allow the cell, and thus particles, to be as close to the mirror as possible, so as to reduce the effect of waveguide losses. A Parafilm layer was cut to size, and a microscope slide with holes drilled in was bonded to create a cell as described in section 6.2.2. Both a small sample (approximately 3mm square) of a high-reflectivity, dielectric-stack mirror, with reflectivity of 99.98% at 1083nm, and the machine-polished end of the waveguide were cleaned with filter paper moistened with acetone. A fine paintbrush was dipped in Fluorinert then continuously wiped to reduce the amount of Fluorinert on the paintbrush to an absolute minimum. The brush was then drawn across the end of the waveguide in one smooth movement and the segment of mirror pushed up against the waveguide (ensuring the coated side was against the waveguide). This was then held by surface tension to the end of the substrate. Lastly the mirror was aligned to the waveguide to be used and pushed hard against the substrate with folded filter paper.

In this case the coupling could be optimised as normal. Despite the high-reflectivitiy mirror, the 0.02% transmission was sufficient to monitor the coupling of the light to the waveguide.

8.3.3 Optically diffused loop method

A mask was designed with a structure as shown below in figure 8.4. Light is injected in

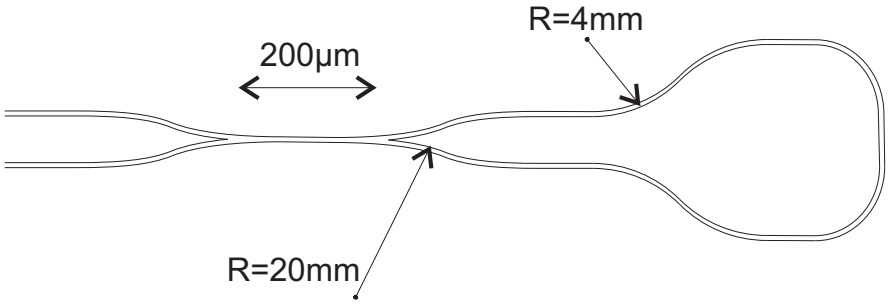

FIGURE 8.4: Design for production of a standing wave using a loop. The width of all waveguiding parts was 3μm

one of the branches at the left by fibre butt-coupling (as usual). Two back-to-back Y junctions with a separation of 200μm are used and all waveguiding areas are 3μm wide (with the exception of the points where the splitting takes place). Light is coupled into

one of the single-mode branches, and a loss of 50% is incurred at the first junction [147]. This is then split again at the second junction with 50% light coupled into each branch (assuming the interaction area between the two Y-junctions is single mode). The second input branch (although not used in this project) could have been used to monitor the power in the loop. Instead the coupling was optimised by roughly aligning the fibre to the waveguide input, aided by the microscope. The microscope was then moved to observe the particles inside the cell. The coupling could be fine-tuned by maximising the scattering of light by the particles.

8.3.4 Bi-coupling fibre method

A connectorised fibre splitter was used to inject light from both ends of a straight channel waveguide as shown in figure 8.5.

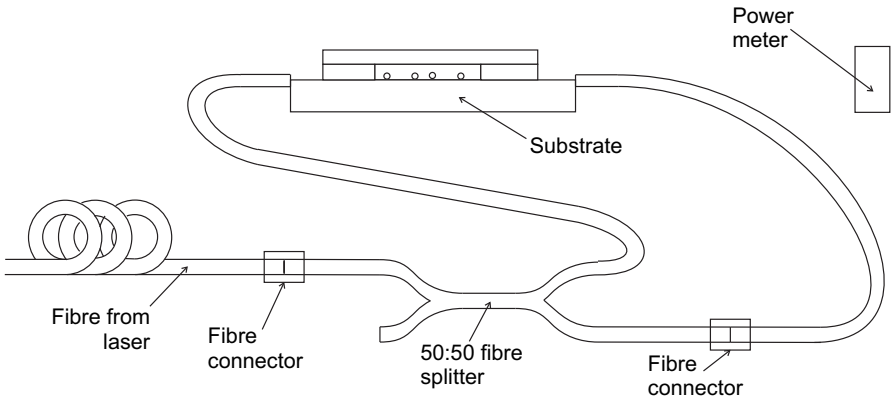

FIGURE 8.5: Creation of a standing wave by injecting light from the laser into both ends of the waveguide.

The fibre splitter split light with approximately 50% of light coupled into each output fibre. Alignment was carried out for one fibre as normal. The unconnectorised end of the second fibre was then aligned roughly using the microscope at the other end. The connectorised end was disconnected from the fibre splitter and monitored using a power meter and the power was optimised. This end was then connected back on to the fibre splitter with the knowledge that the coupling between the waveguide and the fibre was optimised.

8.4 Experimental results

8.4.1 Dielectric mirror results

A single-mode waveguide formed by ion-exchange through a 4μm aluminium opening was selected for its low loss and 5μm latex particles, diluted to an approximate concentration

of 10^6 particles/ml, were injected into the cell and the mirror attached as described.

Figure 8.6 shows the first image of a movie (mirroroff.avi) where the scattered light from a 5μm latex particle is imaged. Initially a mirror is attached to the output of the waveguide. At time, t=247s, the mirror is knocked off by flicking it off with tweezers. The suction of the vacuum holder was sufficient to ensure that it was possible to do this without the coupling changing. This was an important point for comparing the two cases of the mirror on and the mirror off and is the reason the experiment was carried out in this order.

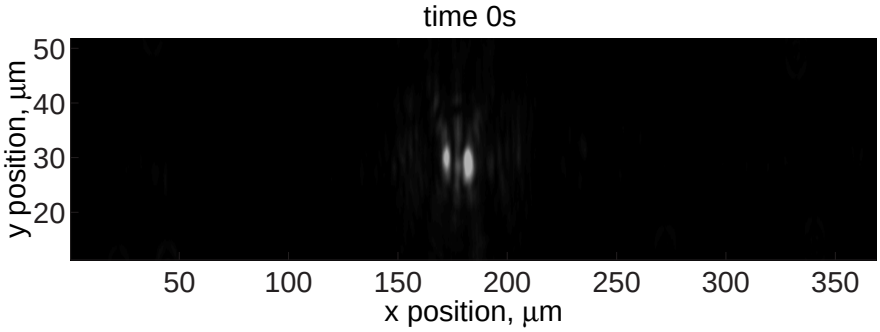

FIGURE 8.6: First image of a movie (mirroroff.avi) showing the scattered light from a trapped latex sphere. The attached mirror is knocked off at t=247seconds.

A number of points can be observed from this experiment. Firstly it is clear that the particle speeds up after the mirror is knocked off, as expected. Analysis showing this is shown below in figure 8.7. The position of the front lobe of the front particle is plotted over a period of 270 seconds is shown in figure 8.7a. The sudden changes at t=47, 133 and 216 is where the microscope is translated as the particle is about to leave the area observed by the microscope, as can be seen from the movie. Figure 8.7b shows the gradient of 8.7a (i.e. it shows the speed of the particle). At the point that the mirror is knocked off, the particle noticeably increases velocity from approximately 4μm/s to approximately 10μm/s.

It is also interesting to note that whereas previously with no mirror attached the scattering from a latex particle is centred at the front of the sphere, with the mirror on the particle scatters light both at the front and the rear of the sphere. This is shown schematically in figure 8.8. A similar form of light distribution in a sphere has been observed for Gaussian illuminated spheres at their Mie resonance [15]. It can be confirmed that this is the case (and that it does not represent two particles in close proximity) by repeating the experiment with the mirror on and alternating the use of white light imaging or scattered light imaging. It is reasonable to assume that the brightness of these 'bulbs' at the front/rear of the particle is proportional to the intensity of the forwards/backwards travelling waves respectively.

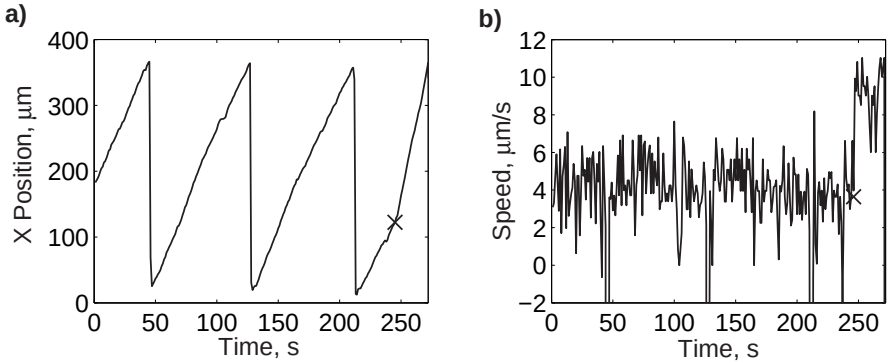

FIGURE 8.7: a) The 'x' position in the image and b) the speed of particle as a function of time. The × represents the point at which the mirror was knocked off.

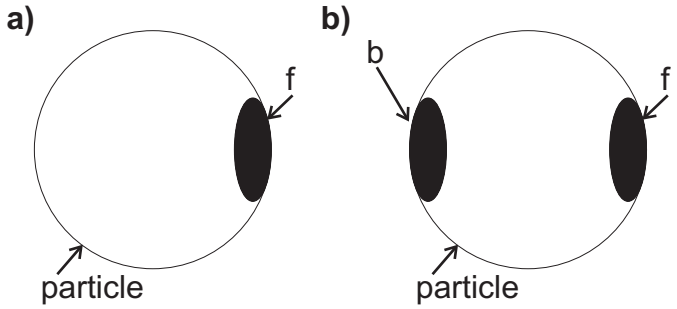

FIGURE 8.8: Diagram showing the approximate positions of scattering lobes on a latex particle for the case of a) no reflection and b) some reflection at the output of the waveguide. f and b refer to the bulbs caused by the forward travelling and backwards travelling wave respectively where the direction of forward propagating light is from left to right.

By recording the scattered light from particles at a range of distances from the mirror it was possible to plot both the speed of the particle and the ratio of the intensity of the rear bulb to that of the front bulb as a function of distance from the mirror.

For this experiment the same waveguide and concentration of 5μm latex particles were used. The power of the laser was set to approximately 0.4W. The camera was focussed on the scattering from particles and the integration time set to 1ms (low enough to ensure that no pixels would be saturated). Images of the particles were recorded at a rate of approximately one per second for approximately an hour. When a trapped and moving particle was found by translating along the length of the waveguide, the frame number, waveguide output power and position along the waveguide was recorded. The position was recorded from the graduated manual linear stage that is used to translate the microscope. The power was measured by imaging the output of the waveguide as normal through the dielectric mirror. After half an hour the mirror was removed as before and particles were imaged and recorded as before.

A movie was made of the entire period and studied to identify the relevant frames. A program written in Matlab identified the position of the maxima from each frame. This was invariably due to the front lobe of the particle. The pixel values enclosing

a square area around the (mean) maximum point were integrated, I_f, and taken to be representative of the forwards intensity. Similarly two more squares of the same size were integrated; firstly, one positioned a constant number of pixels behind the maximum that enclosed the bulb from the backwards travelling wave, I_b, and one positioned a set number of pixels above this square that represented the background intensity, I_n. The ratio was then calculated as:

$$Ratio = \frac{I_b - I_n}{I_f - I_n} \tag{8.16}$$

Figure 8.9 shows the results for the experiment described above.

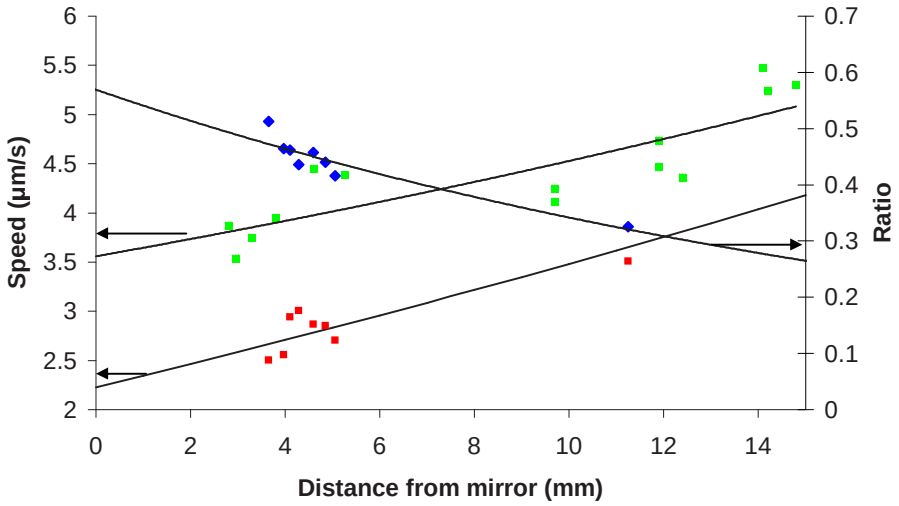

FIGURE 8.9: The speed (left axis) of particles plotted as a function of their distance from the end of the waveguide with the mirror on (■), and removed (■). The right axis shows the ratio between the intensity of forward 'bulb' and the rear 'bulb' (◆). The best fit curves are also shown.

From figure 8.9 it is possible to infer some data about the waveguide loss and how much light is reflected back into the waveguide by the mirror. As has been shown above (section 8.2.2) the forward, I_f, and backward, I_b, travelling waves and the scattering force with the mirror on, $F_{sc,on}$ and off, $F_{sc,off}$ will have intensity in the form:

$$F_{sc,off} = I_f = Ae^{-2\gamma z} \tag{8.17}$$

$$I_b = AR^2e^{2\gamma z} \tag{8.18}$$

$$F_{sc,on} = I_f - I_b = A[e^{-2\gamma z} - R^2e^{2\gamma z}] \tag{8.19}$$

Where A is a constant, 2γ is the waveguide loss, R^2 is the coefficient for reflection back into the waveguide and the origin is the position of the mirror. The best-fit to this form of equation (by least squares) for the speed of particles with the mirror off gives A=3.56μm/s and 2γ=0.024mm^{-1} directly. This value of γ gives a loss equivalent to 1.03dB/cm, within the bounds stated in section 5.5.3. Using these values in equation 8.19 a best-fit value for the reflection coefficent, R^2 as 0.37. The ratio of I_b/I_f=$R^2e^{-4\gamma z}$ and the best fit curve for the ratio in figure 8.9 gives R^2=0.57 and 2γ=0.025mm^{-1}.

These two values of 2γ as calculated by the ratio of intensities and the speed measurements are very close. However the value for R^2, the reflection coefficient, calculated by the intensity ratio of 0.57 is quite different to that calculated by the speed of the particles, 0.37. A potential reason for this discrepancy is that the first method assumes that the backwards travelling wave has no effect on a trapped particle other than to slow it down. However the increased average intensity gradient due to the reflected wave will have the effect of holding a particle laterally closer to the centre and transversely closer to the surface of the waveguide. Here the intensity of the evanescent wave and thus the expected speed of the particle is maximum. Therefore, with the mirror on, a particle would be expected to have a greater speed than that simply predicted from the resultant intensity. This would, in turn, result in a lower than expected extrapolated ratio of the speeds at the mirror (z=0) which is the ratio used to calculate the reflection coefficient.

It was generally not possible to record a single particle traveling the whole distance of the waveguide as particles regularly became stuck to the waveguide. Also in order to limit the loss of the waveguide caused by the particles a low concentration of particles had to be used so that not too many particles were trapped. This had the effect that it was hard to collect a large amount of data. Unfortunately it was not possible to image particles closer than approximately 3mm to the mirror as the Parafilm cut-out required this length in order to form a cell with an effective seal.

Figure 8.9 does not show I_b/I_f for the case of the mirror off. It was roughly an average of 5x lower than that for the mirror on. The fact that it is not much lower than this can partly be explained from a 4% reflection due to the Fresnel reflection of the end face, but more likely is due to a small proportion of the scattered light from the forward travelling wave, being subsequently scattered into the area from where the backward scattered intensity is calculated.

The non-perfect fit of the points to the data can be explained by variation in particle diameter and surface quality and the variation in separation between the waveguide surface and the particle [137]. In addition, there is light scattered by the waveguide, an unknown quality of the waveguide at the regions measured, uncertainty about the intensity at a point along the waveguide at a given time due to particles trapped further along the waveguide, etc. The errors are also likely to be due to the intensity of the lobes being sampled for only 1ms each second. Therefore if the scattering from the lobes is not constant, as is clearly the case (see movie mirroroff.avi), errors are going to be introduced. This could potentially have been improved by using an optical filter to allow the integration time of the camera to be increased or by analysis at a higher temporal resolution.

The effect of the reflected wave was also investigated for the smaller gold particles. A solution of 250nm gold particles with a concentration of 7×10^6 particles/ml and a NaCl concentration of 4×10^{-4}M was prepared and injected into the cell. The same single mode

waveguide as above was imaged 4.5mm from the output end of the waveguide, and the output power of the waveguide was 72mW (without the mirror attached). Observing the effect of the mirror on the gold particles was significantly harder due to their not being trapped for as long a duration. However analysis as described in section 6.3.2 could be carried out. Figure 8.10 below shows the comparison of the velocities both before and after the mirror was knocked off and where no other conditions were, knowingly, changed.

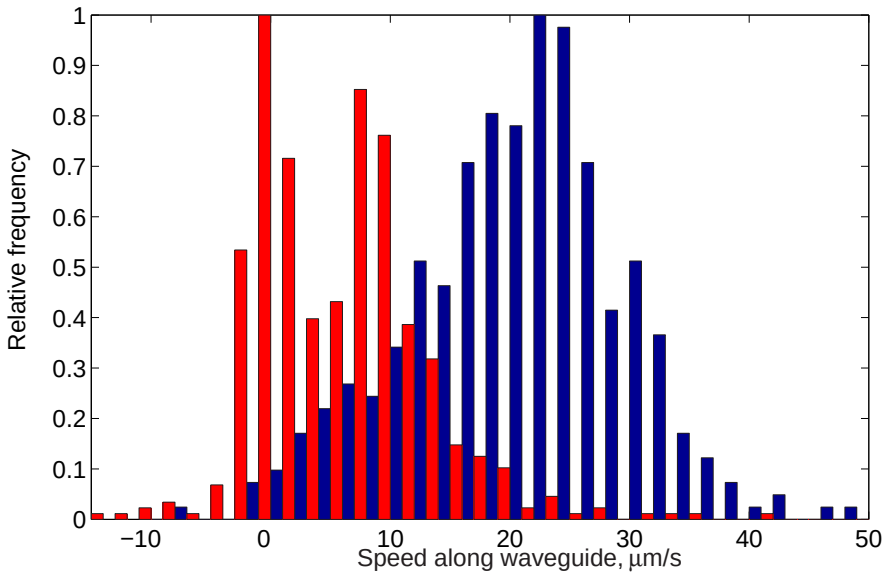

FIGURE 8.10: The axial speed histogram for gold particles above a single mode waveguide with a mirror attached to (■)and after knocking off (■) the output end of the waveguide.

The peak frequency of the speed of the particles is approximately 23μm/s without and 8μm/s with the mirror attached. This ratio, 0.35, is approximately the same as found for the latex particles above for the same distance from the mirror.

The fact that the gold particles still moved shows that the effect of the standing wave was not sufficient to hold the particles stationary. This may be due to the particles having a diameter much larger than the half period of the intensity pattern as shown in section 8.2.3 and the efficiency of the reflection back into the waveguide being 57% or lower. Smaller 150nm particles also did not show stationary trapping although typically their lateral trapping was much weaker and therefore may not have been noticed.

8.4.2 Optically diffused loop results

As has been seen, it was impossible to render particles stationary using a mirror due to the losses of the waveguide and poor reflectivity. The loop, described in section 8.3.3, is expected to ensure that the intensities are matched in each direction where light has travelled an equal distance along each branch from the point at which it is split.

5μm latex particles were injected into a cell and the scattered laser light from the particles imaged as described previously. The brightness of the forward and backward scattering bulbs and the position of particles was recorded. The brightnesses were used to calculate an intensity ratio of each of the components of propagating light and this was plotted as a function of the distance from the lower branch. Typical results are plotted below in figure 8.11.

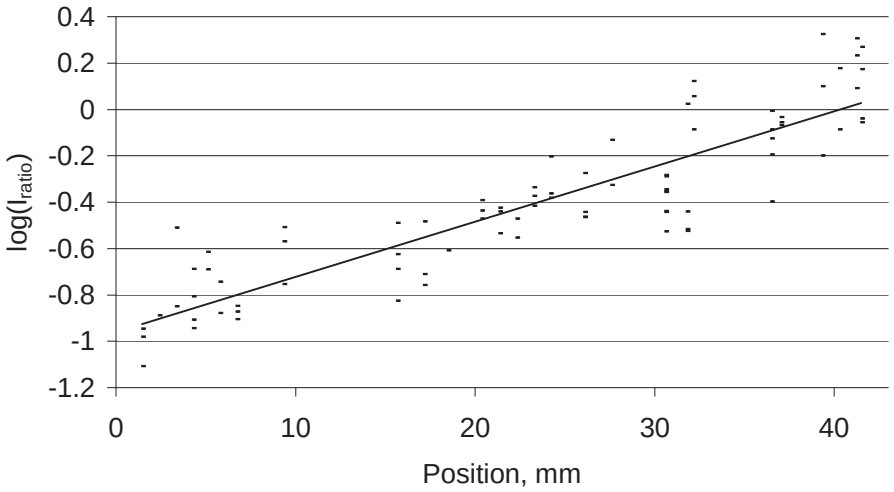

FIGURE 8.11: The $\log_{10}$ of the ratio of the brightness of the front to backward lobes as a function of the distance (along the waveguide) from the Y-junction split.

Figure 8.11 shows that the log of the ratio of the particle speed is approximately linear with position, as expected. The point at which the ratio is 1 ($\log_{10}$(ratio)=0) is approximately 40mm along the waveguide in one direction. Observing particles at this point of equal forward and backward intensities confirmed that particles were indeed stationary. This is virtually the whole distance around loop, which had a length of approximately 45mm (i.e. not opposite to the Y-junction as would be expected). This was found to be the case for a number of the waveguides fabricated in different substrates and implies that the splitter did not evenly split the power down the two branches. A potential reason for this is that the length of the interaction region (between the two Y-junctions) was insufficient to allow total mixing of the wave. This could have led to radiative modes formed at the first junction coupling back into the waveguide after the second Y-junction. More likely however is the case that there could have been an error in the mask used for these Y-junctions, which could explain the consistant difference observed. This is supported by the observation that the total power in the waveguide appeared to be much lower than would be expected (from observing the brightness of the lobes).

8.4.3 Bi-coupling fibre results

Latex particles (5μm diameter) were injected above the same waveguide used in section 8.4.1 and fibres aligned to both ends as described in section 8.3.4. The laser power was

set to approximately 0.8W (or 400mW in each output fibre). Again the scattered light from the particles was imaged.

Figure 8.12 below is the first image in a movie (matched.avi) showing seven particles being held stationary by the matched power in each direction. After 31 seconds the fibre at the left hand side of the waveguide is moved slightly and the coupling is reduced. Therefore the particles move left.

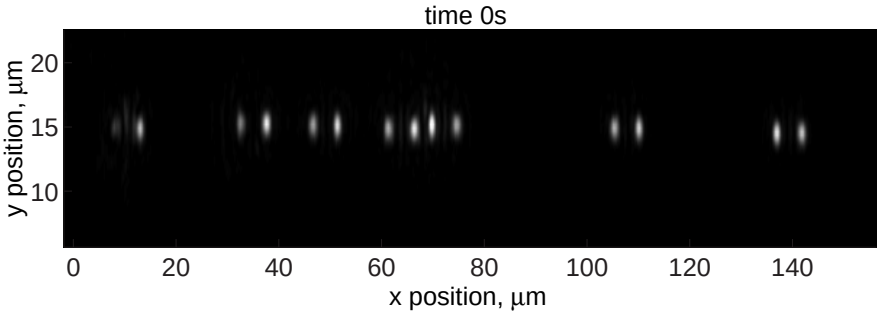

FIGURE 8.12: First image from a movie (matched.avi) showing the scattering from seven latex particles with equal forward and backward components of intensity. At t=31s the fibre at the left hads side is moved.

As can be seen in this case the particles are very stably trapped. Thus by analysing the particles as before, by examining the ratio of the intensity of the bulbs to the resultant particle speed, a plot similar to figure 8.9 is obtained and is shown below in figure 8.13.

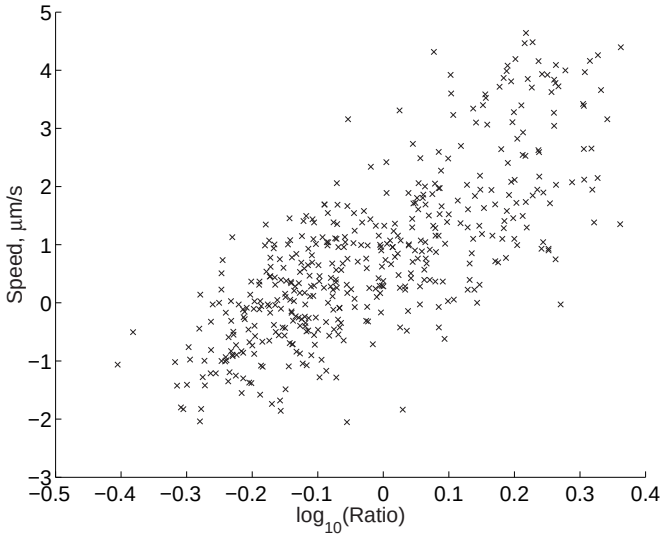

FIGURE 8.13: The axial speed of particles as a function of the ratio of the intensity of the forward to backward scattering 'bulbs'.

It again shows the trend of the particles moving in the direction with the brighter bulb, as expected. However again the spread of the speeds is large, and this is believed to be due to the same reasons stated above for the case of the mirror. It may also be partly to do with having a fibre at each end which may drift slightly changing the coupling between the fibre mode and the waveguide mode.

Finally figure 8.14 shows the first image in a movie (latcont.avi) which demonstrates that the position of a particle can be accurately positioned [148]. In this movie the manipulators holding the two fibres are moved manually. The particle at the top right is clearly under control. The fibre could be more accurately positioned and thus the particle position controlled by mounting both (or just one) of the fibres on the motorised nanomanipulator used in chapter 7. This could potentially be further integrated by

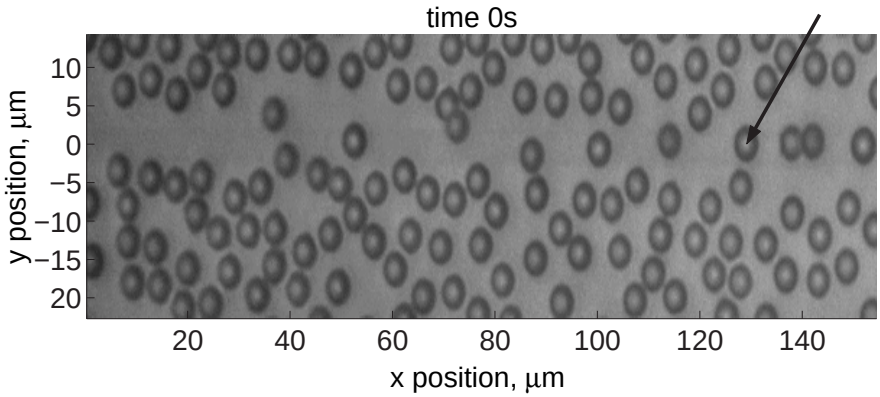

FIGURE 8.14: The first image of a movie (latcont.avi) showing the axial control of the latex particle indicated by the black arrow.

fibre-pigtailing (permanently fixing) both ends of the fibre to the waveguide. An electro optical switch could then be used to reduce the proportion of light in one branch using an optical coupler (see for example [149]).

8.5 Conclusion

This chapter has studied the theory of the intensity of an evanescent standing wave with a non-unity reflection coefficient in a lossy waveguide. It showed the well-known result that a standing wave can cause an intensity four times that of the propagating wave, and that the intensity is periodic with a period of $\lambda/2n_{eff}$. It also showed the effect of the contrast between the forwards and backwards travelling components of the field. The intensity distribution was applied to describe theoretically how the forces in the axial direction are changed due to the reflected wave and showed that a particle could (theoretically) be efficiently axially trapped by a non-perfect standing wave providing the particle was sufficiently small.

Three methods of creating an evanescent standing wave were implemented. A dielectric mirror attached to the output edge of the waveguide was shown to considerably slow down both latex and gold particles, but that due to the loss caused by the coupling of the reflected light back into the waveguide, and their size, the particles could not be held stationary. It was shown that the loss and fraction reflected back into the waveguide could be inferred and the values of loss calculated agreed well with what was previously

believed to be the case. An integrated optical loop was used to create a standing wave, and a plot of the ratio of the forward to backward travelling wave intensities against the position of the particles showed that the waveguides were consistantly coupling more light into the lower branch than the upper branch.

Finally, by injecting light from fibres at both ends of a straight waveguide, it was demonstrated, for the first time, that the axial position of latex particles could be accurately controlled along a diffused waveguide. It is hoped that this may lead to an integrated electro-optical approach thus miniaturising the apparatus required and allowing accurate control of the particle position without the use of moving parts.

Chapter 9

Conclusion and Future Work

9.1 Summary

In this thesis the evanescent trapping and propulsion of gold and latex particles above a channel waveguide, along with two alternative configurations to the standard approach of injection of light at one end of a straight waveguide, have been theoretically and experimentally studied.

In order to predict the intensity distribution above the waveguide, thus allowing theoretically optimised waveguides to be designed, to generate results to which waveguides could be compared experimentally and to allow better calculation of the optical forces, the waveguides were modelled. The modelling was carried out using two independent methods. The first, an analytical transfer-matrix model, was derived and implemented in conjunction with the effective index method. The second was a commercial beam propagation method (BPM) software package. The two models were compared and found to agree well for planar waveguides and for effective indices of wide, channel waveguides. However the analytical method was not suited to predicting the fields of channel waveguides, so that the BPM software was used for design and analysis.

The form of the refractive index profile used for the Cs^+ ion-exchanged waveguides in a Menzel glass was approximated to that of a Fermi function and the parameters for this were obtained. A peak refractive index difference of 0.03 was found in agreement with previously published values. The model was used to calculate mode profiles and the effective indices, spot-sizes and cut-off wavelengths of waveguides were obtained. In addition, parameters that affect the optical forces on particles in the superstrate, namely the maximum intensity, the maximum intensity gradient, the length over which the intensity gradient deviates less than 20% from the maximum and the superstrate power were investigated. It was shown that the increase in refractive index of the medium from 1 (air) to 1.33 (water) gave increases in both the intensity and intensity gradients

of a factor of approximately two. It was also shown that generally a shallow and narrow waveguide was preferred with an approximate depth of 1.1μm and width of 3μm. For larger waveguides these values result in a gradual decrease in intensity and intensity gradients due to increased spot-sizes. Smaller waveguides result in the fundamental mode of the waveguide approaching cut-off, resulting in a sharp decrease in the trapping parameters.

The thesis presented the theoretical aspects of the optical forces caused by laser light in an evanescent field. It derived the well-known Mie theory for the case of plane wave excitation, and explained how this may be expanded to the case of evanescent wave excitation. Mie resonances are found to be much stronger for a high contrast in refractive indices between a particle and the medium in which it is held. Thus latex particles in water are expected to have much weaker Mie resonances than the same particles in air. Mie resonances were shown to be much sharper for larger particles, due to the higher Mie mode contributions.

The comparison between Mie theory and the Rayleigh approximation was discussed and it was concluded that gold particles with radii up to 70nm are reasonably modelled by Rayleigh theory. The Rayleigh theory was derived and shown to be much simpler (both conceptually and in terms of computation) than the Mie theory. Gradient, scattering and absorption forces were calculated using Rayleigh theory and it was shown that these forces had maxima at a wavelength of 550nm, near the gold plasmon frequency.

Using the maximum predicted values of intensity (30GW/m^2 per Watt of modal power) and intensity gradients (200×10^{15} and 20×10^{15}W/m^3 per Watt of modal power for the transverse and lateral dimensions respectively) optical forces for a 125nm radius particle were predicted to be 0.1pN, 12pN, 0.13pN and 1.6pN for the absorption, scattering, and lateral and transverse gradient forces respectively. The axial forces lead to the prediction of the maximum speed of 250nm gold particles of 940μm/s per Watt of modal power.

In addition to the optical forces acting on the particle, non-optical forces were also found to be of significant importance. The well understood forces of gravity, buoyancy, drag and Brownian motion were analysed. It was found that the greater difference in density between gold and water compared to latex and water (by a factor of approximately 370) meant that a gold particle had a resultant downwards force due to gravity and buoyancy equivalent to a latex particle with an approximately 7$\times$ greater radius. It was shown that the system should follow Stokes' law, and thus the drag force on a particle was directly proportional to the speed of the particle. However the effect of the surface meant that there was an increase in the effective viscosity of the water. This effect decreased with distance from the surface and the decrease was more rapid for smaller particles.

The effect of the surface charges on the particles and glass surface was studied for the first time in this field of application. All the surfaces (latex, gold and glass) have a

negative surface charge, thus the two surfaces would be expected to repel each other. This double-layer force was derived along with the van der Waals force for which it was shown that although the energy decays rapidly (r^{-6}) with separation for two molecules, the decay is more gradual for the case of a sphere and a wall (r^{-2}). The combination of these forces was found to reach a peak force of approximately 20pN for a 200nm gold particle and 1.5nN for a 3μm latex particle at separations of approximately 3nm and was shown to be dependent on the ion concentration of the supporting medium.

The effect of heating of the bodies by the incident laser radiation was also investigated to describe an experimentally observed drift. A natural convection model was proposed to explain for this and has been shown to be a plausible explanation to the phenomena observed.

Having explored theoretically the properties predicted for an optimised waveguide, K^+ and Cs^+ ion-exchanged waveguides were fabricated according to standard procedures and were characterised. K^+ ion-exchanged waveguides were found to follow all the expected trends, however Cs^+ ion-exchanged were found not to follow the expected correlation between optical parameters and ion-exchange time and potential reasons for this were explained. The Cs^+ ion-exchanged waveguides did however follow the predicted trends within the measured optical properties (a waveguide mode with a high effective refractive index, was also found to have a high cut-off wavelength, for example).

Sophisticated software was written in Labview that automated the process of acquiring images from a CCD camera, recording the power output of the waveguide and keeping a record of the details of a particular run. Matlab programs were written to semi-automatically analyse the images by using background substraction, a particle identification algorithm and a tracking algorithm. This led to greater flexibility in the ability to analyse particular features and in displaying the data in a suitable form than offered by commercial particle identification software. Typically 5000 frames would be recorded to analyse approximately 60,000 particle displacements with a temporal resolution of 50ms.

The optical and imaging apparatus used was standard, however the design of the fluidic cell was found to have limiting criteria that were overcome with the use of a sputtered silica layer to protect and isolate the superstrate of the waveguide.

Thermophoretic natural convection induced by the laser was demonstrated where lateral speeds of up to 40μm/s were observed for a waveguide output power of 1W. The effect of increasing the concentration of monovalent ions in the solution was studied and it was found that approximately 50% of particles became attached to the surface in a time period of 400s with a sodium chloride concentration of 2.25mM. Brownian motion of both gold and latex particles was measured and agreed well with the theoretically predicted values.

Gold nanoparticles trapped above a single mode channel waveguide were found to have a velocity comparable to that predicted by theory and at 500μm/s is over an order of magnitude greater than previously reported for evanescently propelled particles. They were also shown to have a speed distribution that varied across the waveguide as expected (i.e. with a maximum speed at the centre of the waveguide). A multimoded waveguide was shown to propel particles in lateral positions with an axial periodicity along the waveguide that concurred with the hypothesis that this was due to the beating between the first two modes of the waveguide.

Surface intensities of TE and TM modes would be expected to be different and it was shown that particles were propelled faster with the TM fundamental mode than the TE fundamental mode. Like-for-like experiments were carried out to measure how the velocity of different particle sizes varied. It showed that for latex particles, larger particles generally had a higher, but more varied speeds that was believed to be due to weak Mie resonances.

Having characterised how particles are trapped and propelled along a straight waveguide the first particle sorter using optical evanescent wave trapping was described. A computer-controlled actuator translated a fibre across the end face of a channel waveguide. This has the effect of changing the beat pattern in the waveguide and thus altering the proportion of light coupled into each output branch. Particles trapped above the waveguide would be sorted into the branch that had the higher power at the time the particle arrived at the junction. This was found to have a 100% success rate providing the particle power was set when the particle was 40μm before the junction and was not switched until the particle had travelled 10μm down the junction.

Finally, the effect of using a counter-propagating wave in a range of configurations with the aim of allowing better control of particles on the waveguide was demonstrated. The basic theory of a standing wave was adapted to the case of a partial standing wave caused by a lossy waveguide. The configurations evaluated involved using a mirror, a loop and by injecting light into both ends of the waveguide simultaneously. Both gold and latex particles on a waveguide with a mirror attached to the end were demonstrated to be propelled faster upon the removal of the mirror, as expected. It was noted that there were two 'bulbs' visible from the scattering of the laser light by the particle when the mirror was attached. These corresponded to the scattering from the front and rear of the particle due to the forwards and backwards travelling components of the beam, respectively. The ratio of the intensity of these two bulbs was expected to be proportional to the ratio of the intensities of the forwards and backwards travelling waves, and this was further confirmed by the analysis, that led to the proportion of light coupled back into the waveguide and the loss of the waveguide being calculated. The experiments using the optically diffused waveguide loop also showed a similar effect and the point at which the beams were equal in each direction being identified.

Two fibres were used to demonstrate, for the first time, that the axial position of a latex particle on a waveguide could be accurately controlled by controlling the relative coupling of the fibres at each end into the waveguide. This result leads to the expectation that an electro-optic switch may be used to produce an integrated optical method for controlling a particle's axial position.

9.2 Future work

The results presented in this thesis provide a strong basis on which to build more robust evanescent wave traps. Theoretically however, further analysis of the optical forces should be obtained by extending the application of Mie theory to evanescent wave excitation, Rayleigh theory being only a guide for all but the smallest particles used.

Experimentally the major obstacle has not been in the propulsion of particles, but in the trapping of gold nanoparticles on the waveguide due to their small size (and thus the greater effect of Brownian motion). There are a number of possibilities that should be further investigated to address this problem. The most obvious solution to this problem would be to change the type of waveguide used. The reasons for the choice of Cs^+ ion-exchanged waveguides have been explained earlier, and still stand, however a higher effective index waveguide, such as those produced by thallium ion exchange (not chosen here for their toxicity), would be expected to improve the trapping duration.

Negating the forces countering the trapping force would also lead to improved trapping. To this end further studies regarding the equilibrium proximity of particles to the surface could be done. This could be carried out by, for example, total internal reflection fluorescence microscopy, TIRFM, whereby the intensity of fluorescence measured from a labelled (gold) particle could be used to infer the height of the particle above the surface. This could potentially be coupled with results using an optical tweezer configuration to measure the force required to bring the particle closer to the surface in a system similar to that used by Sasaki et al. [150, 151]. This may allow the characterisation of surface chemistry that could be carried out to modify the surface of the glass or, the use of different (potentially acidic) ions in the solution and thus controlling more accurately the height to which the particle will approach. In addition the cell should be made with smaller dimensions as this would suppress the effect of the natural convection.

Brownian motion may still limit the trapping time and in this case an entirely different geometry may be required. An example of a potential solution would be that of using photolithographically defined etched channels in a low refractive index medium. The sample could be injected into this and the water in the sample used as the waveguide core. This would clearly have a large advantage in that the vast majority of the power of the light would be used in propelling the particles and they would be structurally trapped. The materials considerations for this would be much more restricting although

a potential solution could be with Teflon AF coated on glass forming the cladding for the waveguide (as shown in [152], for example).

With stronger evanescent trapping of particles by whatever method chosen, this thesis has found that this technique should be applicable and useful to biological applications of sorting/counting of biological matter. The high speeds of gold particles obtained indicates that a rapid high-throughput process may be possible. The advance made in the work on Y-junctions leads to a confidence in the ability to sort with 100% accuracy whilst the work with the counter-propagating wave will allow sample cells, particles etc. to be held steadily whilst probing (for example by SERS) takes place. Indeed these processes could be integrated to form a complete lab-on-a-chip all-optical system for manipulation, characterisation, counting and sorting of biological matter. By integration with microfluidic processes this could be further enhanced to run un-aided through a series of tests to carry out batch processing of very small volumes of sample.

Appendix A: Screenshot of Labview Program

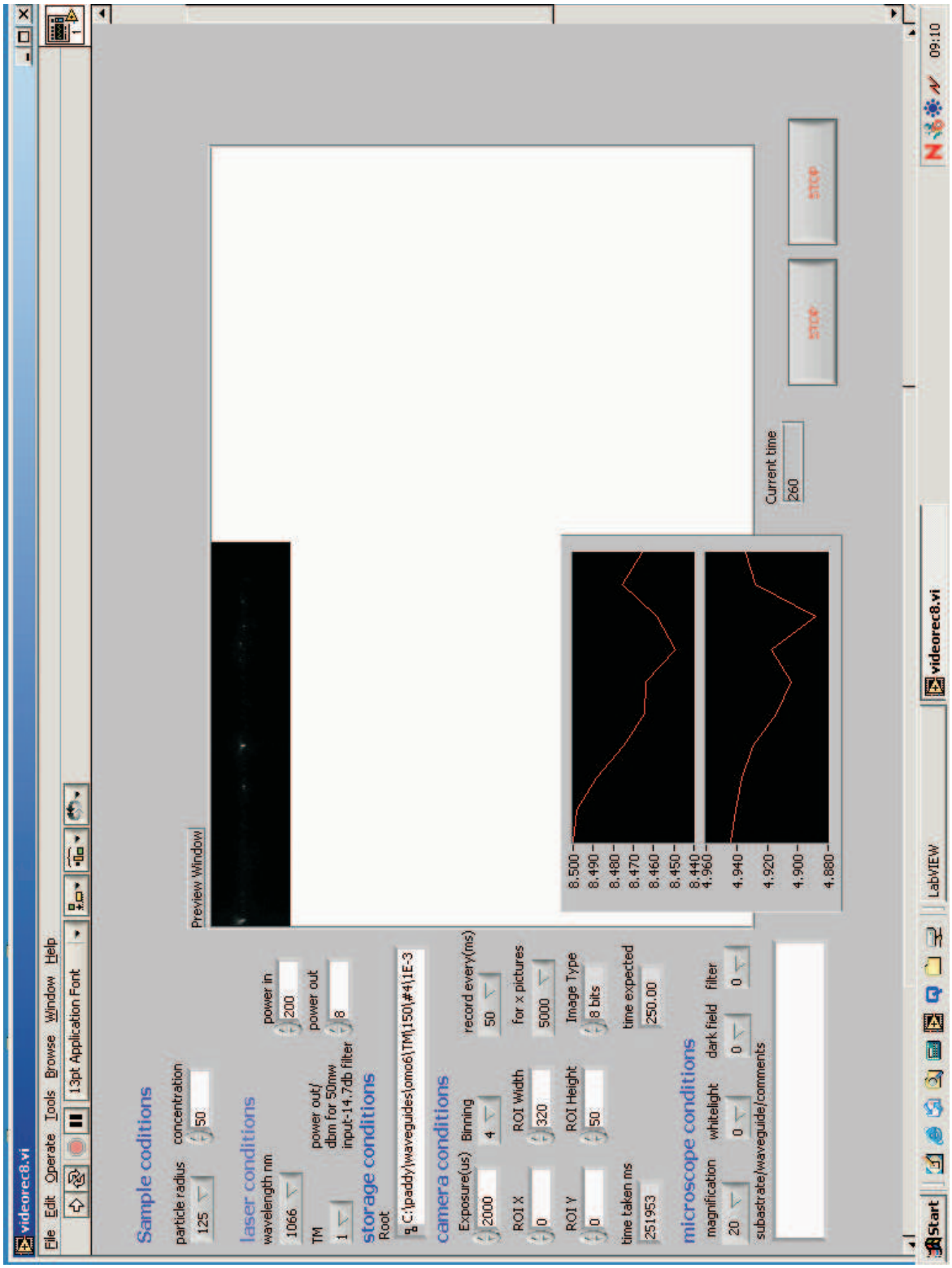

FIGURE 9.1: A screenshot of the Labview program used for the acquisition of images and experimental conditions.

Bibliography

[1] J. J. Storhoff, A. A. Lazarides, R. C. Mucic, C. A. Mirkin, R. L. Letsinger, and G. C. Schatz. What controls the optical properties of dna-linked gold nanoparticle assemblies? *Journal of the American Chemical Society*, 122(19):4640–4650, 2000.

[2] M. C. Daniel and D. Astruc. Gold nanoparticles: Assembly, supramolecular chemistry, quantum-size-related properties, and applications toward biology, catalysis, and nanotechnology. *Chemical Reviews*, 104(1):293–346, 2004.

[3] M. A. van Dijk, L. C. Kapitein, J. van Mameren, C. F. Schmidt, and E. J. G. Peterman. Combining optical trapping and single-molecule fluorescence spectroscopy: Enhanced photobleaching of fluorophores. *Journal of Physical Chemistry B*, 108(20):6479–6484, 2004.

[4] M. Y. Han, X. H. Gao, J. Z. Su, and S. Nie. Quantum-dot-tagged microbeads for multiplexed optical coding of biomolecules. *Nature Biotechnology*, 19(7):631–635, 2001.

[5] P. Nakroshis, M. Amoroso, J. Legere, and C. Smith. Measuring boltzmann's constant using video microscopy of brownian motion. *American Journal of Physics*, 71(6):568–573, 2003.

[6] K. Svoboda and S. M. Block. Biological applications of optical forces. *Annual Review of Biophysics and Biomolecular Structure*, 23:247–285, 1994.

[7] E. Hecht. Electromagnetic theory, photons and light. In B. Spatz, editor, *Optics*, volume 1, page 675. Addison Wesley, New York, 2nd edition, 1987.

[8] E.F. Nichols and G.F. Hull. *Physical Review*, 13:293, 1901.

[9] P.N. Lebedev. Untersuchungen uber die druckkrafte des lichtes. *Annalen der Physik*, 6:433, 1901.

[10] C.H. Townes. *How the laser happened*. Oxford University Press, Oxford, 1999.

[11] A. Ashkin. Acceleration and trapping of particles by radiation pressure. *Physical Review Letters*, 24(4):156–159, 1970.

[12] A. Ashkin and J.M. Dziedzic. Optical levitation by radiation pressure. *Applied Physics Letters*, 19(8):283–285, 1971.

[13] A. Ashkin and J.M. Dziedzic. Optical levitation in high vacuum. *Applied Physics Letters*, 28(6):333–335, 1975.

[14] A. Ashkin and J.M. Dziedzic. Observation of resonances in the radiation pressure on dielectric spheres. *Physical Review Letters*, 38(23):1351–1354, 1977.

[15] A. Ashkin and J. M. Dziedzic. Observation of optical resonances of dielectric spheres by light-scattering. *Applied Optics*, 20(10):1803–1814, 1981.

[16] A. Ashkin. Trapping of atoms by resonance radiation pressure. *Physical Review Letters*, 40(12):729–732, 1978.

[17] J. E. Bjorkholm, R. R. Freeman, A. Ashkin, and D. B. Pearson. Observation of focusing of neutral atoms by the dipole forces of resonance-radiation pressure. *Physical Review Letters*, 41(20):1361–1364, 1978.

[18] A. Ashkin, J. M. Dziedzic, and P. W. Smith. Continuous-wave self-focusing and self-trapping of light in artificial kerr media. *Optics Letters*, 7(6):276–278, 1982.

[19] P. W. Smith, A. Ashkin, and W. J. Tomlinson. 4-wave mixing in an artificial kerr medium. *Optics Letters*, 6(6):284–286, 1981.

[20] A. Ashkin and J. M. Dziedzic. Optical trapping and manipulation of viruses and bacteria. *Science*, 235(4795):1517–1520, 1987.

[21] A. Ashkin, J. M. Dziedzic, and T. Yamane. Optical trapping and manipulation of single cells using infrared-laser beams. *Nature*, 330(6150):769–771, 1987.

[22] A. Ashkin and J. M. Dziedzic. Internal cell manipulation using infrared-laser traps. *Proceedings of the National Academy of Sciences of the United States of America*, 86(20):7914–7918, 1989.

[23] A. Ashkin. Applications of laser radiation pressure. *Science*, 210(4471):1081–1088, 1980.

[24] A. Ashkin. Optical trapping and manipulation of neutral particles using lasers. *Proceedings of the National Academy of Sciences of the United States of America*, 94(10):4853–4860, 1997.

[25] A. Ashkin. History of optical trapping and manipulation of small-neutral particle, atoms, and molecules. *IEEE Journal of Selected Topics in Quantum Electronics*, 6(6):841–856, 2000.

[26] R. A. Flynn, A. L. Birkbeck, M. Gross, M. Ozkan, B. Shao, M. M. Wang, and S. C. Esener. Parallel transport of biological cells using individually addressable

vcsel arrays as optical tweezers. *Sensors and Actuators B-Chemical*, 87(2):239–243, 2002.

[27] S. Sato, Y. Harada, and Y. Waseda. Optical trapping of microscopic metal particles. *Optics Letters*, 19(22):1807–1809, 1994.

[28] H. Furukawa and I. Yamaguchi. Optical trapping of metallic particles by a fixed gaussian beam. *Optics Letters*, 23(3):216–218, 1998.

[29] M. Gu and P. C. Ke. Image enhancement in near-field scanning optical microscopy with laser-trapped metallic particles. *Optics Letters*, 24(2):74–76, 1999.

[30] S. Kawata, Y. Inouye, and T. Sugiura. Near-field scanning optical microscope with a laser trapped probe. *Japanese Journal of Applied Physics Part 2-Letters*, 33(12A):L1725–L1727, 1994.

[31] K. Svoboda and S. M. Block. Optical trapping of metallic rayleigh particles. *Optics Letters*, 19(13):930–932, 1994.

[32] A. Terray, J. Oakey, and D. W. M. Marr. Microfluidic control using colloidal devices. *Science*, 296(5574):1841–1844, 2002.

[33] L. Sacconi, G. Romano, R. Ballerini, M. Capitanio, M. De Pas, M. Giuntini, D. Dunlap, L. Finzi, and F. S. Pavone. Three-dimensional magneto-optic trap for micro-object manipulation. *Optics Letters*, 26(17):1359–1361, 2001.

[34] T. N. Buican, M. J. Smyth, H. A. Crissman, G. C. Salzman, C. C. Stewart, and J. C. Martin. Automated single-cell manipulation and sorting by light trapping. *Applied Optics*, 26(24):5311–5316, 1987.

[35] T. Tanaka and S. Yamamoto. Optically induced propulsion of small particles in an evenescent field of higher propagation mode in a multimode, channeled waveguide. *Applied Physics Letters*, 77(20):3131–3133, 2000.

[36] S. Kawata and T. Tani. Optically driven mie particles in an evanescent field along a channeled waveguide. *Optics Letters*, 21(21):1768–1770, 1996.

[37] S. Kawata and T. Sugiura. Movement of micrometer-sized particles in the evanescent field of a laser-beam. *Optics Letters*, 17(11):772–774, 1992.

[38] L. N. Ng, B. J. Luff, M. N. Zervas, and J. S. Wilkinson. Propulsion of gold nanoparticles on optical waveguides. *Optics Communications*, 208(1-3):117–124, 2002.

[39] L. N. Ng, M. N. Zervas, J. S. Wilkinson, and B. J. Luff. Manipulation of colloidal gold nanoparticles in the evanescent field of a channel waveguide. *Applied Physics Letters*, 76(15):1993–1995, 2000.

[40] J.E. Curtis, B.A. Koss, and D. G. Grier. Dynamic holographic optical tweezers. *Optics Communications*, 207:169–175, 2002.

[41] D. Cojoc, S. Cabrini, E. Ferrari, R. Malureanu, M. B. Danailov, and E. Di Fabrizio. Dynamic multiple optical trapping by means of diffractive optical elements. *Microelectronic Engineering*, 73-74:927–932, 2004.

[42] V. Garces-Chavez, D. McGloin, H. Melville, W. Sibbett, and K. Dholakia. Simultaneous micromanipulation in multiple planes using a self- reconstructing light beam. *Nature*, 419(6903):145–147, 2002.

[43] M. P. MacDonald, L. Paterson, K. Volke-Sepulveda, J. Arlt, W. Sibbett, and K. Dholakia. Creation and manipulation of three-dimensional optically trapped structures. *Science*, 296(5570):1101–1103, 2002.

[44] J. M. Tam, I. Biran, and D. R. Walt. An imaging fiber-based optical tweezer array for microparticle array assembly. *Applied Physics Letters*, 84(21):4289–4291, 2004.

[45] K. Sasaki, M. Koshioka, H. Misawa, N. Kitamura, and H. Masuhara. Optical trapping of a metal-particle and a water droplet by a scanning laser-beam. *Applied Physics Letters*, 60(7):807–809, 1992.

[46] S. D. Collins, R. J. Baskin, and D. G. Howitt. Microinstrument gradient-force optical trap. *Applied Optics*, 38(28):6068–6074, 1999.

[47] R. J. Oetama and J. Y. Walz. Translation of colloidal particles next to a flat plate using evanescent waves. *Colloids and Surfaces A-Physicochemical and Engineering Aspects*, 211(2-3):179–195, 2002.

[48] M. Gu, J. B. Haumonte, Y. Micheau, J. W. M. Chon, and X. S. Gan. Laser trapping and manipulation under focused evanescent wave illumination. *Applied Physics Letters*, 84(21):4236–4238, 2004.

[49] H. Jaising, K. Grujic, and O. G. Hellesø. Simulations and velocity measurements for a microparticle in an evanescent field. *Optical Review*, 12(1):4–6, 2005.

[50] B. A. Brown and P. R. Brown. Optical tweezers: Theory and current applications. *American Laboratory*, 33(22):13–+, 2001.

[51] S. Chu. Laser manipulation of atoms and particles. *Science*, 253(5022):861–866, 1991.

[52] J. E. Molloy, K. Dholakia, and M. J. Padgett. Preface: Optical tweezers in a new light. *Journal of Modern Optics*, 50(10):1501–1507, 2003.

[53] D. G. Grier. A revolution in optical manipulation. *Nature*, 424(6950):810–816, 2003.

[54] J. P. Burke, S. T. Chu, G. W. Bryant, C. J. Williams, and P. S. Julienne. Designing neutral-atom nanotraps with integrated optical waveguides. *Physical Review A*, 65(4):art. no.–043411, 2002.

[55] M. Hammes, D. Rychtarik, B. Engeser, H.C. Nagerl, and R. Grimm. Evanescent-wave trapping and evaporative cooling of an atomic gas at the crossover to two dimensions. *Physical review letters*, 90(17):173001, 2003.

[56] Z. P. Luo, Y. L. Sun, and K. N. An. An optical spin micromotor. *Applied Physics Letters*, 76(13):1779–1781, 2000.

[57] B. A. Koss and D. G. Grier. Optical peristalsis. *Applied Physics Letters*, 82(22):3985–3987, 2003.

[58] M. E. J. Friese, T. A. Nieminen, N. R. Heckenberg, and H. Rubinsztein-Dunlop. Optical alignment and spinning of laser-trapped microscopic particles. *Nature*, 394(6691):348–350, 1998.

[59] F. V. Ignatovich, A. Hartschuh, and L. Novotny. Detection of nanoparticles using optical gradient forces. *Journal of Modern Optics*, 50(10):1509–1520, 2003.

[60] R. Lugowski, B. Kolodziejczyk, and Y. Kawata. Application of laser-trapping technique for measuring the three-dimensional distribution of viscosity. *Optics Communications*, 202(1-3):1–8, 2002.

[61] J.P. Hole, J.S. Wilkinson, K. Grujic, and O.G. Hellesø. Velocity distribution of gold nanoparticles trapped on an optical waveguide. *Optics Express*, 13(10):3896, 2005.

[62] S. C. Kuo and M. P. Sheetz. Force of single kinesin molecules measured with optical tweezers. *Science*, 260(5105):232–234, 1993.

[63] J. T. Finer, R. M. Simmons, and J. A. Spudich. Single myosin molecule mechanics - piconewton forces and nanometer steps. *Nature*, 368(6467):113–119, 1994.

[64] J. Guck, R. Ananthakrishnan, C. C. Cunningham, and J. Kas. Stretching biological cells with light. *Journal of Physics-Condensed Matter*, 14(19):4843–4856, 2002.

[65] A. Ashkin and J. Prost. Forces of a single beam gradient laser trap on a dielectric sphere in the ray optics regime. *Biophysical Journal*, 61:569–582, 1991.

[66] K. Grujic, O.G. Hellesø, J.P. Hole, and J.S. Wilkinson. Sorting of polystyrene microspheres using a y-branched optical waveguide. *Optics Express*, 13(1):1, 2005.

[67] M. L. Bennink, O. D. Scharer, R. Kanaar, K. Sakata-Sogawa, J. M. Schins, J. S. Kanger, B. G. de Grooth, and J. Greve. Single-molecule manipulation of double-stranded dna using optical tweezers: Interaction studies of dna with reca and yoyo-1. *Cytometry*, 36(3):200–208, 1999.

[68] I. Brevik, T. A. Sivertsen, and E. Almaas. Radiation forces on an absorbing micrometer-sized sphere in an evanescent field. *Journal of the Optical Society of America B-Optical Physics*, 20(8):1739–1749, 2003.

[69] T. Tanaka and S. Yamamoto. Optically induced meandering mie particles driven by the beat of coupled guided modes produced in a multimode waveguide. *Japanese Journal of Applied Physics Part 2-Letters*, 41(3A):L260–L262, 2002.

[70] C.F. Bohren and D.R. Huffman. *Absorption and scattering of light by small particles*. John Wiley and sons, Inc, New York, 4th edition, 1998.

[71] J. Y. Walz. Ray optics calculation of the radiation forces exerted on a dielectric sphere in an evanescent field. *Applied Optics*, 38(25):5319–5330, 1999.

[72] R. Wannemacher, A. Pack, and M. Quinten. Resonant absorption and scattering in evanescent fields. *Applied Physics B-Lasers and Optics*, 68(2):225–232, 1999.

[73] H. Y. Jaising and O. G. Helleso. Radiation forces on a mie particle in the evanescent field of an optical waveguide. *Optics Communications*, 246(4-6):373–383, 2005.

[74] W.J. Wiscombe. Improved mie scattering algorithms. *Applied optics*, 19:1505–1509, 1980.

[75] S. Stenholm. Light forces put a handle on the atom - to cool and trap atoms by laser-light. *Contemporary Physics*, 29(2):105–123, 1988.

[76] S. Stenholm. The semiclassical theory of laser cooling. *Reviews of Modern Physics*, 58(3):699–739, 1986.

[77] L. N. Ng, B. J. Luf, M. N. Zervas, and J. S. Wilkinson. Forces on a rayleigh particle in the cover region of a planar waveguide. *Journal of Lightwave Technology*, 18(3):388–400, 2000.

[78] Y. Harada and T. Asakura. Radiation forces on a dielectric sphere in the rayleigh scattering regime. *Optics Communications*, 124(5-6):529–541, 1996.

[79] P.B. Johnson and R.W. Christy. Optical constants of noble metals. *Physical Review B*, 6(12):4370–4379, 1972.

[80] H.J. Hagemann, W. Gudat, and C. Kunz. Optical constants from the far infrared to the x-ray region: Mg, al, cu, ag, au, bi, c, and al_2o_3. *DESY Report, Hamburg*, SR-74/7, 1974.

[81] D.W. Lynch and W.R. Hunter. Optical properties of metals and semiconductors. In E.D. Palik, editor, *Handbook of optical constants of solids*, pages 275–367. Academic Press, Orlando, 1985.

[82] M. Born and E. Wolf. *Principles of Optics*. Cambridge University Press, Cambridge, 7^{th} edition, 1999.

[83] D.L. Lee. *Electromagnetic principles of integrated optics*. Wiley, New York, 1986.

[84] L. M. Walpita. Solutions for planar optical waveguide equations by selecting zero elements in a characteristic matrix. *Journal of the Optical society of America A*, 2(4):595–602, 1985.

[85] G.B. Hocker and W.K. Burns. Mode dispersion in diffused channel waveguides by the effective index method. *Applied Optics*, 16(1):113–118, 1977.

[86] Rsoft Incorporated. Beamprop user manual, 2001.

[87] J. Crank. *Mathematics of diffusion*. OUP, Oxford, 347 edition, 1957.

[88] J. Chilwell and I. Hodgkinson. Thin-films field-transfer matrix-theory of planar multilayer waveguides and reflection from prism-loaded waveguides. *Journal of the Optical Society of America a-Optics Image Science and Vision*, 1(7):742–753, 1984.

[89] D.G. Ashworth, R. Oven, and M.C. Page. The influence of the pseudo-mixed-alkali effect on the field-assisted diffusion of silver ions into glass for optical waveguides. *Journal of Physics D-Applied Physics*, 28:657–664, 1995.

[90] V. Neuman, O. Parriaux, and L. M. Walpita. Double alkali effect, influence on index profile of ion exchanged waveguides. *Electronics Letters*, 15(22):204–206, 1979.

[91] L.B. Glebov, S.K. Evstrop'ev, N.V. Nikonorov, and G.T. Petrovskii. Planar optical waveguides formed in glass by ion-exchange diffusion of cesium. *Soviet physical and tecnological physics*, 34(8):629–631, 1989.

[92] J. M. White and P. F. Heidrich. Optical waveguide refractive index profiles determined from measurement of mode indexes, a simple analysis. *Applied Optics*, 15(1):151–155, 1976.

[93] G. B. Hocker and W. K. Burns. Modes in diffused optical-waveguides of arbitrary index profile. *IEEE Journal of Quantum Electronics*, QE11(6):270–276, 1975.

[94] L. B. Glebov, S. K. Evstropev, N. V. Nikonorov, and G. T. Petrovskii. Planar optical wave-guides formed by cesium ion-exchange diffusion in glasses. *Zhurnal Tekhnicheskoi Fiziki*, 59(6):72–75, 1989.

[95] L. Zhenhua, W. Shu, and D.J. Harrison. The refractive index-profiles and diffusion analysis of cs^+ - na^+ ion-exchange waveguides. *17th International Congress on Glass*, pages 97–102, 1995.

[96] R. Hayami and R. Terai. Diffusion of alkali ions in na2o-cs2o-sio2 glasses. *Physics and Chemistry of Glasses*, 13(4):102, 1972.

[97] A.M. Howatson, Lund P.G., and Todd J.D. *Engineering tables and data.* Chapman Hall, London, 2nd edition, 1995.

[98] Duke Scientific. Polymer microsphere, 4000 series, msds, 2004.

[99] D. Auerbach. Some limits to stokes-law. *American Journal of Physics*, 56(9):850–851, 1988.

[100] A. Pralle, Florin E.L., Stelzer E.H., and Horber J.K. Local viscosity probed by photonic force microscopy. *Applied physics A*, 66:S71S73, 1998.

[101] J. Happel and H. Brenner. *Low Reynolds Number Hydrodynamics.* Prentice Hall, Englewood Cliffs, 1965.

[102] C. Kittel. *Elementary Statistical Physics.* John Wiley and sons, New York, 3 edition, 1964.

[103] A. Einstein. Uber die von der molekularkinetischen theorie der warme geforderte. bewegung von in ruhenden flussigkeiten suspendierten teilchen. *Annalen der Physik*, 17:549–560, 1905.

[104] J.N. Israelachvili. *Intermolecular and surface forces.* Academic Press, London, 1991.

[105] British Biocell international. Technical data sheet for gold colloids. Technical report, British Biocell international, 2000.

[106] R. M. Richardson, R. M. Dalgliesh, T. Brennan, M. R. Lovell, and A. C. Barnes. A neutron reflection study of the effect of water on the surface of float glass. *Journal of Non-Crystalline Solids*, 292(1-3):93–107, 2001.

[107] W. L. W. Hau, D. W. Trau, N. J. Sucher, M. Wong, and Y. Zohar. Surface-chemistry technology for microfluidics. *Journal of Micromechanics and Microengineering*, 13(2):272–278, 2003.

[108] R.H. Doremus, editor. *Ion exchange in glass*, volume 2 of *Ion Exchange-A Series of advances.* New York, New York, 1969.

[109] B.V. Derjaguin and L. Landau. some stuff. *Acta Physica URSS*, 144:633, 1941.

[110] E.J.W. Verwey and J.T.G Overbeek. *Theory of stability of Lyophobic Colloids.* Elsevier, Amsterdam, 1948.

[111] Y. Gu and D. Liy. The zeta-potential of glass surface in contact with aqueous solutions. *Journal of Colloid and Interface Science*, 226:328–339, 2000.

[112] D. J. Shaw. *Introduction to Colloid and Surface Chemistry.* Butterworths, London, 1 edition, 1966.

[113] H. Zhao, B. Yuan, and X. Dou. The effects of electrostatic interaction between biological molecules and nano-metal colloid on near-infrared surface-enhanced raman scattering. *Journal of Optics A: Pure and Applied Optics*, 6:900–905, 2004.

[114] S.Y. Shulepov and G. Frens. Surface roughness and particle size effect on the rate of perikinetic coagulation: Experimental. *Journal of Colloid and Interface Science*, 182:388–394, 1996.

[115] S.C. McCutcheon, J.L Martin, and T.O. Barnwell. Water density as function of temperature and concentration. In D.R. Maidment, editor, *Handbood of Hydrology*, page 11.3. McGraw-Hill, New York, 1993.

[116] S. Duhr and D. Brauna. Two-dimensional colloidal crystals formed by thermophoresis and convection. *Applied physics letters*, 96:131921, 2005.

[117] K. Shen, X. Chena, M. Guob, and J. Cheng. A microchip-based pcr device using flexible printed circuit technology. *Sensors and actuators B*, 105:251–258, 2005.

[118] M.P. Hughes and H. Morgan. Dielectrophoretic trapping of single sub-micrometre scale bioparticles. *Journal of Physics D-Applied Physics*, 31:2205–2210, 1998.

[119] N.P. Bansal and R.H. Doremus. Chapter 3. In *Handbook of glass properties*. Academic Press, Orlando, 1986.

[120] G.H. Chartier, P. Jaussaud, A.D. de Oliveira, and O. Parriaux. Fast fabrication method for thick and highly multimode optical waveguides. *Electronics letters*, 13:763, 1977.

[121] C. R. Lavers, B. J. Ault, and J. S. Wilkinson. Characterization of secondary silver ion-exchange in potassium- ion-exchanged glass wave-guides. *Journal of Physics D-Applied Physics*, 27(2):235–240, 1994.

[122] P. G. Noutsios and G. L. Yip. Characterization and modeling of planar surface and buried glass wave-guides made by field-assisted k+ ion-exchange. *Applied Optics*, 31(25):5283–5291, 1992.

[123] B. J. P. daSilva, R. P. deMelo, E. L. FalcaoFilho, and C. B. deAraujo. Potassium source for ion-exchange glass waveguide fabrication. *Applied Optics*, 36(24):5949–5950, 1997.

[124] J. Spirkova, P. Nebolova, I. Jirka, K. Mach, V. Perina, A. Mackova, and G. Kuncova. Copper doped waveguides in glass substrates. *Fiber and Integrated Optics*, 21(1):63–74, 2002.

[125] R. Oven, M. Yin, and P. A. Davies. Characterization of planar optical waveguides formed by copper- sodium, electric field assisted, ion exchange in glass. *Journal of Physics D-Applied Physics*, 37(16):2207–2215, 2004.

[126] T. Izawa and H. Nakagome. Optical waveguide formed by electrically induced migration of ions in glass plates. *Applied Physics Letters*, 21(12):584, 1972.

[127] R. Ramaswamy. ion-exchanged glass waveuides: a review. *Journal of Lightwave Technology*, 6(6):984–1001, 1988.

[128] T. Findakly. Glass wave-guides by ion-exchange - a review. *Optical Engineering*, 24(2):244–250, 1985.

[129] A. Opilski. Technology of ion exchange in glass and its application in waveguide planar sensors. *Optical engineering*, 36(6), 1997.

[130] M. Abouelleil. Ion exchange in glasses and crystals. *Annual Review of Materials Science*, 23:255–268, 1993.

[131] R. Terai and R. Hayami. Ionic diffusion in glasses. *Journal of Non-Crystalline Solids*, 18:217–264, 1975.

[132] T.G. Giallorenzi, E. J. West, R. Kirk, R. Ginther, and R. A. Andrews. Optical waveguides formed by thermal migration of ions in glass. *Applied Optics*, 12(6):1240–1245, 1973.

[133] L. Holland. *The properties of glass surfaces*. Chapman and Hall, London, 1 edition, 1964.

[134] M. Abouelleil and F. Leonberger. Model for ion-exchanged wave-guides in glass. *Journal of the American Ceramic Society*, 71(6):497–502, 1988.

[135] L.B. Glebov, I.S. Morozova, and G.T. Petrovskii. *Fiz. Khim. Stekla*, 10(2):194–198, 1984.

[136] R.A. Betts, C.W. Pitt, K.R. Riddle, and L.M. Walpita. A comparative study of the dopant profiles in diffused planar optical waveguides by sims and guided wave probe. *Applied physics A*, 31:29, 1983.

[137] K. Grujic, O.G. Hellesø, J.S. Wilkinson, and J.P. Hole. Optical propulsion of microspheres along a channel waveguide produced by cs^+ ion-exchange in glass. *Optics Communications*, 239(4-6):227–235, 2004.

[138] J. Hlavac. *The technology of glass and ceramics, an introduction*, volume 4 of *Glass science and technology*. Elsevier scientific publishing company, Oxford, 1 edition, 1983.

[139] T. Yamashita, M. Kagami, and I. Ito. Waveguide shape control and loss properties of light-induced self-written (lisw) optical waveguides. *Journal of lightwave technology*, 20(8):1556–1562, 2002.

[140] L. A. Hornak and T. W. Weidman. Propagation loss of index imaged poly(cyclohexylsilyne) thin- film optical wave-guides. *Applied Physics Letters*, 62(9):913–915, 1993.

[141] S. K. Sia and G. M. Whitesides. Microfluidic devices fabricated in poly(dimethylsiloxane) for biological studies. *Electrophoresis*, 24(21):3563–3576, 2003.

[142] H. Gnewuch, J. E. Roman, M. Hempstead, J. S. Wilkinson, and R. Ulrich. Beat-length measurement in directional couplers by thermo-optic modulation. *Optics Letters*, 21(15):1189–1191, 1996.

[143] A. Y. Fu, C. Spence, A. Scherer, F. H. Arnold, and S. R. Quake. A microfabricated fluorescence-activated cell sorter. *Nature Biotechnology*, 17(11):1109–1111, 1999.

[144] O. G. Helleso, P. Gerard, P. Benech, and R. Rimet. Low-loss bends in k+ ion-exchanged wave-guides. *Ieee Photonics Technology Letters*, 6(10):1241–1243, 1994.

[145] P. Zemanek, A. Jonas, L. Sramek, and M. Liska. Optical trapping of rayleigh particles using a gaussian standing wave. *Optics Communications*, 151(4-6):273–285, 1998.

[146] H.J. Buchner, H. Stiebig, V. Mandryka, E. Bunte, and G. Jager. An optical standing-wave interferometer for displacement measurements. *Measurement science and technology*, 14:311–316, 2003.

[147] M. Izutsu, Y. Nakai, and T. Sueta. Operation mechanism of the single mode optical waveguide y junction. *Optics Letters*, 7(3):136–138, 1982.

[148] J.P. Hole, J.S. Wilkinson, O.G. Hellesø, and K. Grujic. Guiding and sorting of micro and nano-particles with integrated optics. In *CLEO Europe*, pages CK6–2, ICM, Munich, Germany, 2005.

[149] W. H. Steier, A. Chen, S. S. Lee, S. Garner, H. Zhang, V. Chuyanov, L. R. Dalton, F. Wang, A. S. Ren, C. Zhang, G. Todorova, A. Harper, H. R. Fetterman, D. T. Chen, A. Udupa, D. Bhattacharya, and B. Tsap. Polymer electro-optic devices for integrated optics. *Chemical Physics*, 245(1-3):487–506, 1999.

[150] K. Sasaki, J. I. Hotta, K. Wada, and H. Masuhara. Analysis of radiation pressure exerted on a metallic particle within an evanescent field. *Optics Letters*, 25(18):1385–1387, 2000.

[151] K. Sasaki, M. Tsukima, and H. Masuhara. Three-dimensional potential analysis of radiation pressure exerted on a single microparticle. *Applied Physics Letters*, 71(1):37–39, 1997.

[152] A. Datta, E. In-Yong, A. Dhar, P. Kuban, R. Manor, I. Ahmad, S. Gangopadhyay, T. Dallas, M. Holtz, H. Temkin, and P.K. Dasgupta. Microfabrication and characterization of teflon af-coated liquid core waveguide channels in silicon. *IEEE Sensors*, 3(6):788–795, 2003.